Standard Model Extensions with Neutral Leptons:

Addressing Dark Matter, Neutrino Oscillations and the Flavor Anomalies

---

DISSERTATION

zur Erlangung des akademischen Grades
DR. RER. NAT.
im Fach
PHYSIK

vorgelegt von

DOMINIK DÖRING

geboren in Dorsten

Lehrstuhl für theoretische Physik III
Fakultät Physik
Technische Universität Dortmund
2021

1. Gutachter: Prof. Dr. Heinrich Päs
2. Gutachterin: Prof. Dr. Gudrun Hiller
Vorsitzender der Prüfungskommission: Prof. Dr. Jan Kierfeld
Mitglied der Prüfungskommission: Prof. Dr. Zhe Wang

Datum des Einreichens der Arbeit: 13.09 2021
Datum der mündlichen Prüfung: 01.12.2021

This thesis contains work based on the following articles published by the author:

- [1] *Sterile neutrinos with altered dispersion relations as an explanation for neutrino anomalies*
  D. Döring, H. Päs, P. Sicking and T. J. Weiler
  Eur.Phys.J.C 80 (2020) 12, 1202 ; arXiv:1808.07460

- [2] *Fermionic Singlet Dark Matter in One-Loop Solutions to the R_K Anomaly: A Systematic Study*
  M. Becker, **D. Döring**, S. Karmakar and H. Päs
  Eur.Phys.J.C 81 (2021) 12, 1053 ; arXiv:2103.12043

Abstract

In this thesis, we study two different Standard Model extensions involving neutral leptons aiming to explain current anomalies in the neutrino sector, as well as to explain the flavor anomalies in combination with the dark matter abundance in the universe. At first, we develop a model that introduces additional sterile neutrino states featuring altered dispersion relations in order to explain the longstanding short baseline neutrino oscillation anomalies and the gallium/reactor anomalies, while also staying in accordance with high energy data from atmospheric and long baseline accelerator experiments. Furthermore, we systematically analyze a model class of one-loop solutions to the B-anomalies in the context of fermionic singlet dark matter candidates. We study the dark matter phenomenology for both Dirac and Majorana fermions in all five models that contain a fermionic singlet. In our analysis, we include different hierarchies between the new Yukawa couplings to Standard Model quarks and also examine different mass ratios in the dark sector. Our study shows that especially direct detection limits can probe such solutions of the B-anomalies.

Zusammenfassung

In dieser Dissertation untersuchen wir zwei verschiedene Standardmodellerweiterungen mit neutralen Leptonen, die darauf abzielen, die Anomalien im Neutrinosektor zu erklären, sowie eine Erklärung der Flavoranomalien mit der Existenz Dunkler Materie im Universum zu verknüpfen. Zunächst entwickeln wir ein Modell, das zusätzliche sterile Neutrinos mit veränderten Dispersionsrelationen einführt, um die Neutrino-Oszillationsanomalien, sowie die Gallium- und Reaktoranomalien zu erklären, während es gleichzeitig mit den Hochenergie-Daten aus atmosphärischen aus Beschleuniger-Experimenten in Übereinstimmung steht. Darüber hinaus präsentieren wir eine systematische Analyse einer Modellklasse von Ein-Schleifen-Lösungen für die B-Anomalien im Kontext von fermionischen Dunkle-Materie-Kandidaten in der Eich-Singulett-Darstellung. Wir untersuchen die Dunkle-Materie-Phänomenologie sowohl für Dirac- als auch für Majorana-Fermionen in allen fünf Modellen, die ein fermionisches Eich-Singulett enthalten. In unserer Analyse prüfen wir unterschiedliche Hierarchien zwischen den neuen Yukawa-Kopplungen an die Standardmodell-Quarks und analysieren zudem verschiedene Massenverhältnisse im dunklen Sektor. Unsere Studie zeigt, dass besonders direkte Detektionsexperimente solche Lösungen der B-Anomalien testen können.

Acknowledgements

First and foremost, I want to thank my advisor Prof. Dr. Heinrich Päs for his support, the weekly group meetings, the fruitful collaboration and also for sending me on conferences and seminars abroad. I am especially indebted to him for making my extended stay in India possible. I am grateful to Prof. Dr. Subhendu Rakshit and Prof. Dr. Gautam Bhattacharyya for hosting my stay at IIT Indore and SINP Kolkata respectively. I want to also thank Prof. Dr. Gudrun Hiller for reviewing this thesis.

In addition, I owe special thanks to Susanne Laurent for always being helpful with organizational issues and encouraging us to continue the department's football betting game.

Being at T III/T IV was a truly memorable period of my life. This was mainly due to all the amazing people that I was fortunate enough to meet during my PhD at this department. I thank my office mates Philipp Sicking and Tim Brune for enduring my presence for many hours a day and for random (physics) discussions! I think you could also say that I quite enjoyed working on a daily basis with my collaborator Mathias Becker, be it on successful or not quite so successful models (I want to mention the glorious Frank-Walter plot here, which somehow didn't manage to get into the thesis).

I also enjoyed all the non-physics activities that I was part of in the last years: I thank Peter Schuh, Stefan de Boer, Rigo Bause, Marcel Golz and Nico Adolph for being part of the ambitious department football team. Also, I wouldn't want to miss the extensive coffee break discussions with the aforementioned people and Dennis Loose, Maggi Zenglein, Clara Hormigos-Feliu, Stefan Bißmann, Sinan Zeißner, Dimitrios Skodras, Kevin Moch, Andrey Tayduganov, Fagner Cintra Correia and Héctor Gisbert-Mullor (although I don't even drink coffee). I also loved going to the annual DPG conferences with a subset of the people mentioned above, despite constantly stating the contrary. I'm also willing to forgive you the inflatable mattress and the barely isolated windows.

I'm also hugely grateful to all the people who proofread chapters of my thesis.

Probably the most memorable period of my PhD was the time I spent in India together with Mathias in 2018. I still fondly remember eating the super spicy food at *Café Zippy* that everyone warned us about, the trip to Indore city with the one-eyed auto rickshaw driver and the hike in the Himalayas with a spontaneous bath under the waterfall. I'm eternally indebted to Siddhartha Karmakar and also Sujata Pandey, who introduced us to Indian culture and regularly saved our lives. I am truly blessed to call you my friends. Furthermore, I am also grateful to Avik Banerjee and Prof. Palash Pal for giving us guided tours through Kolkata.

During the last one and a half years of my PhD, the Covid-19 pandemic struck the world and prevented me from getting to know the 'new people' at the department better, but I have to say that the online coffee breaks played a huge part in keeping me sane during the times of isolation.

Last but not least, I want to thank my nonphysicist friends, my family and my wife Christin for their magnificent support during the completion of this thesis.

Contents

Abbreviations and Mathematical Notation

Abbreviations and Acronyms

Acronyms of Physical Concepts

SM	Standard Model
QFT	Quantum Field Theory
QCD	Quantum Chromodynamics
EW	Electroweak
GWS	Glashow-Weinberg-Salam
QED	Quantum Electrodynamics
SSB	Spontaneous Symmetry Breaking
EWSB	Electroweak Symmetry Breaking
vev	Vacuum Expectation Value
CKM	Cabbibo-Kobayashi-Maskawa
FCCC	flavor-changing charged current
FCNC	flavor-changing neutral current
BSM	Beyond the Standard Model
NP	New Physics
GR	General Relativity
EFE	Einstein Field Equations
FLRW	Friedmann-Lemaître-Robertson-Walker
CMB	Cosmic Microwave Background
BBN	Big Bang Nucleosynthesis
ΛCDM	Cosmological Constant - Cold Dark Matter
DM	Dark Matter
MOND	Modified Newtonian Dynamics
BAO	Baryonic Acoustic Oscillations
LFU	Lepton Flavor Universality
LHC	Large Hadron Collider
GUT	Grand Unified Theory
PMNS	Pontecorvo-Maki-Nakagawa-Sakata
NO	normal ordering
IO	inverted ordering
au	astronomical unit
2HDM	two-Higgs-doublet model
SUSY	supersymmetry
MSW	Mikheyev-Smirnov-Wolfenstein
PREM	Preliminary Reference Earth Model
MCM	Mantle-Core-Mantle
WIMP	Weakly-Interacting Massive Particle

ALP Axion-like Particle

EFT Effective Field Theory

DD direct detection

RD relic density

DMRD dark matter relic density

ID indirect detection

SI spin-independent

SD spin-dependent

dSphs dwarf spheroidal satellite galaxies

VIB virtual internal bremsstrahlung

FSR final state radiation

LFV lepton flavor violation

SBL short baseline

LBL long baseline

UV ultraviolet

RAA Reactor Antineutrino Anomaly

PDF parton distribution function

DV displaced vertex

ADR altered dispersion relation

BMP benchmark point

Acronyms of Experiments

SK SuperKamiokande

SNO **S**udbury **N**eutrino **O**bservatory

KATRIN **Kar**lsruhe **Tri**tium **N**eutrino Experiment

T2K **T**okai to **K**amioka

NOνA **N**uMi **O**ff-Axis ν_e **A**ppearance Experiment

DUNE **D**eep **U**nderground **N**eutrino **E**xperiment

JUNO **J**iangmen **U**nderground **N**eutrino **O**bservatory

LSND **L**iquid **S**cintillator **N**eutrino **D**etector

MiniBooNE **Mini Boo**ster **N**eutrino **E**xperiment

KamLAND **Kam**ioka **L**iquid Scintillator **A**ntineutrino **D**etector

RENO **R**eactor **E**xperiment for **N**eutrino **O**scillation

LEP **L**arge **E**lectron-**P**ositron **C**ollider

SLC **S**tanford **L**inear **C**ollider

NEOS **N**eutrino **E**xperiment for **O**scillation at **S**hort baseline

DANSS **D**etector of the reactor **AntiN**eutrino based on **S**olid **S**cintillator

GALLEX **GALL**ium **EX**periment

SAGE **S**oviet-**A**merican **G**allium **E**xperiment

LUX **L**arge **U**underground **X**exnon Experiment

CRESST **C**ryogenic **R**are **E**vent **S**earch with **S**uperconducting **T**hermometers

CDMS **C**ryogenic **D**ark **M**atter **S**earch

LAT **L**arge **A**rea **T**elescope

HESS **H**igh **E**nergy **S**tereoscopic **S**ystem

MINOS **M**ain **I**njector **N**eutrino **O**scillation **S**earch

KARMEN **KA**rlsruhe **R**utherford **M**edium **E**nergy **N**eutrino experiment

Mathematical Notation

- Einstein summation

$$X_a Y^a \equiv \sum_a X_a Y_a$$

- Conjugation

$$\begin{aligned} \Psi^* &\equiv \text{complex conjugation,} \\ \Psi^\dagger = (\Psi^*)^T &\equiv \text{hermitian conjugation,} \\ \bar{\Psi} = \Psi^\dagger \gamma^0 &\equiv \text{Dirac conjugation} \end{aligned}$$

- Feynman slash

$$p_\mu \gamma^\mu \equiv \not{p}$$

- (Anti)Commutation

$$\begin{aligned} [A,B] &\equiv A \cdot B - B \cdot A && \text{commutator,} \\ \{A,B\} &\equiv A \cdot B + B \cdot A && \text{anti commutator} \end{aligned}$$

- Derivatives

$$\begin{aligned} \partial_x &\equiv \frac{\partial}{\partial x}\,, \\ \partial_\mu &\equiv \frac{\partial}{\partial x^\mu} \end{aligned}$$

Chapter 1

Introduction

1.1 The Standard Model of Particle Physics

In this section, we briefly review the Standard Model (SM) of particle physics. As this discussion does not feature great detail in all calculations, we refer the reader to the standard literature, e.g. References [3, 4, 5, 6, 7, 8], for in-depth information. The theory aims to describe the non-gravitational interactions of fundamental particles within a mathematical framework of a renormalizable gauge Quantum Field Theory (QFT), in which the gauge group is given by

$$SU(3)_C \otimes SU(2)_L \otimes U(1)_Y \,, \tag{1.1.1}$$

where $SU(N)$ stands for the special unitary group of degree N, C stands for *color*, L for *left-handed* and Y denotes the *weak hypercharge.* Here, $SU(3)_C$ represents the theory of Quantum Chromodynamics (QCD) describing the strong interaction, whereas $SU(2)_L \otimes U(1)_Y$ is the gauge group of the Electroweak (EW) theory. The former is the theory describing interactions between quarks and gluons as well as dynamics of hadrons, which are bound states of these particles enforced by a property called *color confinement.* The latter is spontaneously broken to the abelian symmetry group $U(1)_{\text{em}}$ of Quantum Electrodynamics (QED) at the EW scale via so-called the Higgs mechanism, which will be discussed later in this chapter. This framework is often referred to as Glashow-Weinberg-Salam (GWS) theory. Since the SM is a QFT, it also respects the principles of special relativity and, therefore, entails invariance under the Lorentz group, strictly speaking the proper orthochronous Lorentz group $SO(3{,}1)$.

The field content of the SM can be broadly categorized into fermionic matter fields and bosonic force carriers with the exception of the Higgs field, which belongs into a category of its own: the bosonic scalar fields. The matter field content and the corresponding representations under the SM gauge group are listed in Table 1.1. Matter fields can be further divided into two distinct categories: quark fields $Q = (u_L, d_L)^T$, d_R and u_R, which are in the fundamental representation of $SU(3)_C$ and can be categorized into up- (u) and down-type (d) quarks, as well as lepton fields $L = (\nu_L, l_L)^T$ and l_R, which are color-neutral and further divided into charged leptons (l) and neutrinos (ν) after spontaneous symmetry breaking. It is important to note that it was empirically discovered that each of these fields comes in three different versions, the so-called *generations.* In the traditional counting scheme we consequently obtain six quarks [up (u), down (d), charm (c), strange (s), top (t), bottom (b)] and six leptons [electron (e), muon (μ), tau-lepton (τ) and the corresponding neutrinos ν_e, ν_μ, ν_τ]. The index L/R denotes a left-/right-handed *chirality*[1]. A spinor with pure chirality can be produced by acting the

---

[1] In the literature, *right/left-handed* sometimes refers to *helicity* instead of chirality. In this thesis, the term

Field	$SU(3)_C$	$SU(2)_L$	$U(1)_Y$
Q	**3**	**2**	$1/6$
u_R	**3**	**1**	$2/3$
d_R	**3**	**1**	$-1/3$
L	**1**	**2**	$-1/2$
l_R	**1**	**1**	-1

Table 1.1: Matter fields of the SM and their representations under the SM gauge groups.

left-/right-handed projector $P_{L/R}$ on a Dirac 4-spinor ψ as

$$P_{L/R}\psi = \frac{1 \mp \gamma^5}{2}\psi \equiv \psi_{L/R}\,, \tag{1.1.2}$$

where $\gamma^5 = \mathrm{i}\gamma^0\gamma^1\gamma^2\gamma^3$ is the fifth Dirac γ-matrix. The common γ-matrices are defined by the Clifford anticommutation algebra

$$\{\gamma^\mu, \gamma^\nu\} = \gamma^\mu\gamma^\nu + \gamma^\nu\gamma^\mu = 2\eta^{\mu\nu}\mathbb{1}_{4\times 4}\,. \tag{1.1.3}$$

With these prerequisites in mind, we can construct the kinetic part of a renormalizable, Lorentz- and gauge-covariant Lagrangian as follows

$$\mathcal{L}_{\text{kin}} = \sum_{i\in\text{fermions}} \bar{\psi}_i \not{D}\psi_i + \frac{1}{4}\left(W^a_{\mu\nu}W^{\mu\nu}_a + B_{\mu\nu}B^{\mu\nu} + G^b_{\mu\nu}G^{\mu\nu}_b\right)\,, \tag{1.1.4}$$

where $G^b_{\mu\nu}$ is the gluon field strength tensor, $W^a_{\mu\nu}$,$B_{\mu\nu}$ are the field strength tensors associated with $SU(2)_L \otimes U(1)_Y$. The field strength tensors are defined as

$$F^i_{\mu\nu} = \partial_\mu F^i_\nu - \partial_\nu F^i_\mu + g_F \sum_{j,k} f^{ijk} F^j_\mu F^k_\nu\,, \tag{1.1.5}$$

where g_F denotes the coupling constant and f^{ijk}, defined via the commutation relation $f^{ijk}t_k = \left[t^i, t^j\right]$, are the structure constants of the corresponding Lie algebra. We require the introduction of the covariant derivative

$$D_\mu = \partial_\mu - \mathrm{i}g_s t_a G^a_\mu - \mathrm{i}g\tau_b W^b_\mu - \mathrm{i}g' Y B_\mu\,, \tag{1.1.6}$$

with the $SU(3)_C/SU(2)_L/U(1)_Y$ generators $t_a/\tau_b/Y$, to render the Lagrangian covariant under gauge transformations of the form

$$\psi(x) \to \psi'(x) = \exp\left(\mathrm{i}\,\alpha_a(x)\frac{\lambda^a}{2}\right)\exp\left(\mathrm{i}\,\beta_b(x)\frac{\sigma^b}{2}\right)\cdot\exp\left(\mathrm{i}\frac{\gamma(x)}{Y}2\right)\psi(x)\,. \tag{1.1.7}$$

The generators $\tau^a = \sigma^a/2$, $t^a = \lambda^a/2$ are expressed in terms of the Pauli matrices σ^a and Gell-Mann matrices λ^a, respectively.

An important property of particles is the concept of mass. Since they are structured as $\sim m\bar{\Psi}\Psi$, Dirac mass terms of fermions are generally forbidden as they violate $SU(2)_L$ gauge invariance. Furthermore, gauge bosons as they are described above do not have any mass. Since empirical observations clearly show that these particles in fact do have mass, there is a need for a dynamic mechanism within this formulation of the SM that provides an explanation for this

---

right-/left-handed always refers to chirality.

phenomenon. The widely accepted realization of this is the *Higgs mechanism* and the concept of Spontaneous Symmetry Breaking (SSB). Within the framework of Electroweak Symmetry Breaking (EWSB), an $SU(2)_L$-doublet complex scalar field H is introduced to the SM. We describe the Higgs Lagrangian as

$$\mathcal{L}_{\text{Higgs}} \supset \left(D^\mu H\right)^\dagger D_\mu H - \underbrace{\mu^2 H^\dagger H - \lambda\left(H^\dagger H\right)^2}_{:=V(H)}\,, \tag{1.1.8}$$

where μ^2 is the mass parameter, λ is the quartic coupling and $V(H)$ is the so-called scalar potential. If the parameters satisfy the conditions

$$\mu^2 < 0 \vee \lambda > 0\,, \tag{1.1.9}$$

the potential obtains a shape often referred to as the *Mexican hat* or *champagne bottle* profile. The Higgs field acquires a non-zero Vacuum Expectation Value (vev) of $\langle H \rangle = \frac{1}{\sqrt{2}}\begin{pmatrix} 0 \\ v \end{pmatrix}$ due to the shape of the scalar potential $V(H)$ and the vacuum state therefore breaks the $SU(2)_L$ symmetry. The Higgs field can thus be written as an excitation around this vev, yielding[2]

$$H = \frac{1}{\sqrt{2}}\begin{pmatrix} 0 \\ v+h \end{pmatrix}\,, \tag{1.1.10}$$

where $v = \sqrt{-\mu^2/\lambda}$ and h denotes the physical Higgs boson that describes the remaining degree of freedom in the radial direction of the potential. Since the complex scalar Higgs field has four degrees of freedom before EWSB, three degrees of freedom are attributed to the three *Goldstone bosons* that arise due to the breaking of a continuous symmetry according to Goldstone's theorem [9, 10]. Those Goldstone bosons are 'eaten' by three of the gauge bosons, giving them additional polarizations and therefore non-zero masses. In the Higgs Lagrangian we find

$$\mathcal{L}_{\text{Higgs}} \supset \frac{1}{2}\left[-2\lambda v^2 h^2 + \frac{v^2 g^2}{4}\left(W^1_\mu W^{1\,\mu} + W^2_\mu W^{2\,\mu}\right) + \frac{v^2}{4}\left(-gW^3_\mu + g'B_\mu\right)\left(-gW^{3\,\mu} + g'B^\mu\right)\right]\,, \tag{1.1.11}$$

from which we can infer that $m_h^2 = 2\lambda v^2$, $M_W^2 = \frac{v^2 g^2}{4}$, $M_Z^2 = (g^2 + g'^2)\frac{v^2}{4}$ and $M_A^2 = 0$, defining the linear combinations

$$\begin{aligned} Z_\mu &\equiv \frac{1}{\sqrt{g^2 + g'^2}}\left(gW^3_\mu - g'B_\mu\right)\,, \\ A_\mu &\equiv \frac{1}{\sqrt{g^2 + g'^2}}\left(gW^3_\mu + g'B_\mu\right)\,, \\ W^\pm_\mu &\equiv \frac{1}{\sqrt{2}}(W^1_\mu \mp \mathrm{i}W^2_\mu)\,. \end{aligned} \tag{1.1.12}$$

A practical definition proves to be the *Weinberg angle* θ_W, which is defined as the orthogonal rotation angle between the generator basis and the particle basis

$$\begin{pmatrix} Z_\mu \\ A_\mu \end{pmatrix} = \begin{pmatrix} \cos\theta_W & -\sin\theta_W \\ \sin\theta_W & \cos\theta_W \end{pmatrix}\begin{pmatrix} W^3_\mu \\ B_\mu \end{pmatrix} \tag{1.1.13}$$

---

[2] Here, the vev is chosen to lie in the real direction of the complex plane, which can be achieved by choosing a particular gauge transformation, fixing the gauge. The gauge chosen in this case is commonly called *unitary gauge*.

with $\cos\theta_W = {}^{g}/_{\sqrt{g^2+g'^2}}$ and $\sin\theta_W = {}^{g'}/_{\sqrt{g^2+g'^2}}$ and thus

$$\begin{aligned} A_\mu &= \cos\theta_W W^3_\mu + \sin\theta_W B_\mu\,, \\ Z_\mu &= \cos\theta_W W^3_\mu - \sin\theta_W B_\mu\,. \end{aligned} \tag{1.1.14}$$

While we have shown that within the framework of EWSB the EW gauge boson and the Higgs boson acquire their masses from a non-zero vev of the Higgs field, it is still left to show how fermions acquire their mass. Writing down all renormalizable, Lorentz- and gauge-invariant interaction terms in the Lagrangian, involving the newly introduced Higgs field and fermionic fields, yields

$$\mathcal{L}_\text{Yuk} = -Y^d_{ij}\bar{Q}^i H d^j_R - Y^u_{ij}\bar{Q}^i \tilde{H} u^j_R - Y^l_{ij}\bar{L}^i H l^j_R + h.c.\,, \tag{1.1.15}$$

where Y^f_{ij} ($f \in [u,d,l]$) denote the up-type/down-type/leptonic Yukawa matrix elements with the generation indices i,j and we define $\tilde{H} \equiv \mathrm{i}\sigma_2 H^*$ as the hypercharge conjugated Higgs field. This type of interaction is called *Yukawa interaction*, involving two fermionic fields and a scalar at the vertex in question. After EWSB the Yukawa Lagrangian transforms to

$$\mathcal{L}_\text{Yuk} = -\frac{v}{\sqrt{2}}\left(\bar{d}^i_L Y^d_{ij} d^j_R + \bar{u}^i_L Y^u_{ij} u^j_R + \bar{l}^i_L Y^l_{ij} l^j_R\right) + h.c.\,, \tag{1.1.16}$$

from which we can extract that the mass matrix has the form $M^f_{ij} = {}^{vY^f_{ij}}/_{\sqrt{2}}$. In general, this matrix is non-diagonal, which indicates a mismatch between the eigenbasis of the weak interaction and the eigenbasis of physical mass. To obtain the masses of the physical quarks, we must perform a bi-unitary diagonalization of the mass matrix introducing the unitary matrices V_d,V_u,U_d and U_u as

$$\mathcal{L}_\text{Yuk} \supset -\underbrace{\bar{d}_L V^\dagger_d}_{\equiv \bar{d}'_L}\underbrace{V_d M^d U^\dagger_d}_{\equiv M'_d}\underbrace{U_d d_R}_{\equiv d'_R} - \underbrace{\bar{u}_L V^\dagger_u}_{\equiv \bar{u}'_L}\underbrace{V_u M^u U^\dagger_u}_{\equiv M'_u}\underbrace{U_u u_R}_{\equiv u'_R} + \text{h.c.}\,, \tag{1.1.17}$$

where $M'_{u/d}$ are the diagonal mass matrices, carrying the physical quark masses on the main diagonal and $u'_{L/R}$ as well as $d'_{L/R}$ denote quark mass eigenstates.

Using this language in the context of $W^\pm$-mediated charged-current interactions we can develop the equations that provide insight into the flavor changing nature of these interactions. Writing down the part of the kinetic Lagrangian in the mass basis reads

$$\mathcal{L}_\text{kin} \supset W^+_\mu \bar{u}'_L \underbrace{V_u V^\dagger_d}_{\equiv V_\text{CKM}} \gamma^\mu d'_R\,, \tag{1.1.18}$$

where we defined the Cabbibo-Kobayashi-Maskawa (CKM) matrix

$$V_\text{CKM} = V_u V^\dagger_d = \begin{pmatrix} V_{ud} & V_{us} & V_{ub} \\ V_{cd} & V_{cs} & V_{cb} \\ V_{td} & V_{ts} & V_{tb} \end{pmatrix}\,. \tag{1.1.19}$$

This shows that the SM exhibits a flavor-changing charged current (FCCC) already on tree-level, since the off-diagonal elements of the CKM matrix are known from experiment to be non-zero. Note that the Z-mediated neutral current is left invariant by the change in basis because of the spinor structure and the unitarity of the matrices $U_{u/d}$ and $V_{u/d}$. This means that on tree level there are no flavor-changing neutral currents (FCNCs) in the SM and this kind of interaction can appear at the earliest on the one-loop level, which is obviously suppressed in

	Parameter	Value		Parameter	Value
gauge	g_s	1.221	leptons	m_e	$0.5109989461 \pm 0.0000000031\,\mathrm{MeV}$
	g	0.357		m_μ	$105.6583745 \pm 0.0000024\,\mathrm{MeV}$
	g'	0.652		m_τ	$1.77686 \pm 0.00012\,\mathrm{GeV}$
CKM	$\sin\theta_{12}$	0.225 ± 0.001	quarks	m_u	$2.16^{+0.49}_{-0.26}\,\mathrm{MeV}$
	$\sin\theta_{13}$	0.003675 ± 0.000095		m_d	$4.7^{+0.48}_{-0.17}\,\mathrm{MeV}$
	$\sin\theta_{23}$	0.04200 ± 0.00059		m_s	$93^{+11}_{-5}\,\mathrm{MeV}$
	δ	1.167 ± 0.035		m_c	$1.27^{+0.02}_{-0.02}\,\mathrm{GeV}$
Higgs	m_H	$125.10 \pm 0.14\,\mathrm{GeV}$		m_b	$4.18^{+0.03}_{-0.02}\,\mathrm{GeV}$
	v	$246.22\,\mathrm{GeV}$		m_t	$172.76^{+0.30}_{-0.30}\,\mathrm{GeV}$

Table 1.2: Basis of SM parameters including quark and lepton masses [8], CKM parameters [11], gauge couplings.

perturbation theory. Due to its unitarity, the CKM matrix exhibits $3^2 = 9$ real, independent parameters that can be divided into three mixing angles and six phases. As each of the quark fields can be redefined and thus can absorb such a phase, and global phases are unphysical, it is possible to reduce the parameters of the CKM matrix to three mixing angles and one physical phase. The most common parametrization is given by

$$V_{\mathrm{CKM}} = \begin{pmatrix} c_{12}c_{13} & s_{12}c_{13} & s_{13}\exp(-\mathrm{i}\delta) \\ -s_{12}c_{23} - c_{12}c_{23}s_{13}\exp(-\mathrm{i}\delta) & c_{12}c_{23} - s_{12}s_{23}s_{13}\exp(-\mathrm{i}\delta) & s_{23}c_{13} \\ s_{12}s_{23} - c_{12}c_{23}s_{13}\exp(-\mathrm{i}\delta) & -c_{12}s_{23} - s_{12}c_{23}s_{13}\exp(-\mathrm{i}\delta) & c_{23}c_{13} \end{pmatrix}, \tag{1.1.20}$$

where $c_{ij} = \cos\theta_{ij}$ and $s_{ij} = \sin\theta_{ij}$ are the (co)sines of the three mixing angles θ_{12},θ_{13},θ_{23} and iδ is the complex CP-phase. This CP-phase is the only source of CP violation in the SM.

The leptonic part of the Yukawa Lagrangian in Eq. (1.1.16) has a similar, but not identical structure, as there is no right-handed leptonic $SU(2)_L$ singlet neutrino field in the SM. This automatically renders neutrinos massless. Constructing the analogous mixing matrix for leptons, we thus do not have to diagonalize two mass matrices M^l and M^ν, but rather only M^l. Drawing our attention to the kinetic part of the Lagrangian for leptons analogously to Eq. (1.1.18), this leads to the fact that the mixing matrix $V_{\mathrm{lept}} = V_\nu V_l^\dagger$ can always be chosen $V_{\mathrm{lept}} = \mathbb{1}$, as V_ν is unconstrained and can be chosen freely.

Altogether, the considerations of this chapter result in the astounding fact that the SM features 18 parameters[3], which cannot be predicted within the theory itself but rather have to be measured by experiment. One of the most common notions of this set of parameters is summarized in Table 1.2.

1.2 The Cosmological Standard Model

This section aims to outline the *Cosmological Standard Model*, sometimes also colloquially dubbed *Big Bang Theory*, describing the history of the universe. This model relies on the two corner stones of modern physics, the SM, describing the interactions of fundamental particles, and the theory of General Relativity (GR), describing the dynamics of gravity. The *cosmological principle*, which is the assumption that the universe is homogeneous and isotropic on large scales, can be considered a third column of this theory. As we do not present the calculations in detail,

---

[3] In the literature, sometimes the so-called QCD theta-parameter $\theta_{\mathrm{QCD}} \approx 0$ is added to this list. The seemingly unnatural smallness of this parameter is often referred to as the *strong CP problem*.

we refer the reader to e.g. [12, 13] for information about GR and e.g. [8, 14, 15, 16, 17] for more detailed information about Cosmology. This section is based on the aforementioned references.

1.2.1 The Cosmological Principle and the Expansion of the Universe

In this part of the section, we discuss the dynamics of the expansion of the universe and shortly outline the basic concepts.

In order to begin with our discussion, we present the Einstein Field Equations (EFE) or *Einstein's equations*

$$R_{\mu\nu} - \frac{1}{2} R g_{\mu\nu} + \Lambda g_{\mu\nu} = 8\pi G T_{\mu\nu} \, , \tag{1.2.1}$$

where $R_{\mu\nu}$ denotes the *Ricci tensor*, $R = R_{\mu\nu} g^{\mu\nu}$ is the Ricci scalar, Λ is the *cosmological constant*, G is Newton's constant and $T_{\mu\nu}$ represents the *stress energy tensor*. The Ricci tensor arises from the tensor contraction $R_{\mu\nu} = R^{\kappa}{}_{\mu\kappa\nu} = R_{\kappa\mu\lambda\nu} g^{\kappa\lambda}$ of the *Riemann curvature tensor*

$$R^{\kappa}_{\mu\lambda\nu} = \partial_\lambda \Gamma^{\kappa}_{\mu\nu} - \partial_\nu \Gamma^{\kappa}_{\mu\lambda} + \Gamma^{\sigma}_{\mu\nu} \Gamma^{\kappa}_{\sigma\lambda} - \Gamma^{\sigma}_{\mu\lambda} \Gamma^{\kappa}_{\sigma\nu} \, , \tag{1.2.2}$$

which describes the curvature of (pseudo-)Riemannian manifolds with the help of the *affine connection* or *Christoffel symbol*

$$\Gamma^{\kappa}_{\mu\nu} = \frac{1}{2} g^{\kappa\sigma} \left(\frac{\partial g_{\nu\sigma}}{\partial x^{\mu}} + \frac{\partial g_{\mu\sigma}}{\partial x^{\nu}} - \frac{\partial g_{\mu\nu}}{\partial x^{\sigma}} \right) . \tag{1.2.3}$$

The affine connection describes the incremental change of a vector during parallel transport along a smooth curve. Einstein's equations therefore describe the interplay of the geometry of spacetime with momentum, mass and energy. These two aspects often motivate to write down the EFE in the way they are presented in this work, partitioning the geometry-related part (left-hand side) from the energy-related part (right-hand side). Mathematically, the EFE are non-linear partial differential equations whose solutions are the components of the metric tensor $g_{\mu\nu}$, which effectively describe how distances in spacetime are measured according to the *line element*

$$\mathrm{d}s^2 = g_{\mu\nu} \mathrm{d}x^{\mu} \mathrm{d}x^{\nu} \, . \tag{1.2.4}$$

Confronted with the cosmological principle, the EFE can be solved and an exact solution, the Friedmann-Lemaître-Robertson-Walker (FLRW) metric, can be found[4]. It is most commonly formulated as a line element in spherical polar coordinates

$$\mathrm{d}s^2 = \mathrm{d}t^2 - a(t)^2 \left[\frac{\mathrm{d}r^2}{1 - kr^2} - r^2 \mathrm{d}\theta^2 - r^2 \sin^2\theta \mathrm{d}\phi^2 \right] , \tag{1.2.5}$$

where $a(t)$ is the Robertson-Walker scale factor of expansion and k is the curvature parameter. As $a(t)$ factorizes completely, notions of *proper distance* and *comoving distance* can be established. The proper distance is the distance of an object taking into account the expansion factor, meaning that this distance is fundamentally time dependent. The comoving distance on the other hand is the distance that factors out the expansion factor. Depending on the choice of the curvature parameter, the spacetime geometry can take one of three forms,

$$k = \begin{cases} 1, & \text{spherical/closed} \\ 0, & \text{flat} \\ -1, & \text{hyperbolic/open} \end{cases} . \tag{1.2.6}$$

---

[4] Note that the general form of the metric can be derived by using only the cosmological principle. The correct dynamic of the RW scale factor makes it a solution to the EFE.

Note further that in general the equations of dynamics of the expansion of the universe depend on an overall normalization factor for $a(t)$. In the special case of a flat universe this dependence is lifted and thus only the ratios of $a(t_i)$ are of physical importance.

Following the cosmological principle, we assume that the energy content of the universe behaves like a perfect fluid, whose stress-energy tensor takes the form

$$(T^{\mu}{}_{\nu}) = g^{\mu\sigma}T_{\sigma\nu} = \mathrm{diag}(\rho(t), -p(t), -p(t), -p(t))\,, \tag{1.2.7}$$

where $\rho(t)$ is the homogeneous energy density and $p(t)$ denotes the pressure. To obtain the dynamics of the scale factor, we apply the FLRW metric to the EFE and obtain the well-known *Friedmann equation*

$$H^2 = \frac{8\pi G}{3}\rho(t) - \frac{k}{a(t)^2} + \frac{\Lambda}{3}\,, \tag{1.2.8}$$

as well as the acceleration equation

$$\frac{\mathrm{d}H(t)}{\mathrm{d}t} + H(t)^2 = \frac{\mathrm{d}^2 a(t)}{\mathrm{d}t^2} = -\frac{4\pi G}{3}(\rho(t) + 3p(t)) + \frac{\Lambda}{3}\,, \tag{1.2.9}$$

where $H(t) \equiv {}^{\frac{\mathrm{d}a(t)}{\mathrm{d}t}}\!/_{a(t)}$ is the *Hubble parameter*. Note that Eqs. (1.2.8) and (1.2.9) are not linearly independent from the fluid equation that arises from requiring stress-energy conservation as

$$D_\mu T^{\mu}{}_{0} = 0 \tag{1.2.10}$$

$$\Leftrightarrow \frac{\mathrm{d}\rho(t)}{\mathrm{d}t} + 3H(\rho(t) + p(t)) = 0\,, \tag{1.2.11}$$

where $D_\mu T^{\mu}{}_{\nu} = \partial_\mu T^{\mu}{}_{\nu} + \Gamma^{\mu}_{\mu\lambda}T^{\lambda}{}_{\nu} + \Gamma^{\lambda}_{\mu\nu}T^{\mu}{}_{\lambda}$ is the covariant derivative of the stress-energy tensor. Note also that this equation is invariant under the redefinition

$$\rho(t) \to \rho(t) - \frac{\Lambda}{8\pi G} \tag{1.2.12}$$

$$p(t) \to p(t) + \frac{\Lambda}{8\pi G}\,, \tag{1.2.13}$$

simplifying the Friedmann equation by absorbing the cosmological constant into the energy density of the universe.

It is convenient to define the *density parameter* $\Omega(t)$ via the *critical density* $\rho_{\mathrm{crit}}(t)$ as

$$\Omega(t) = \frac{\rho(t)}{\rho_{\mathrm{crit}}(t)} \tag{1.2.14}$$

$$\rho_{\mathrm{crit}}(t) = \frac{8\pi G}{3H(t)^2} \tag{1.2.15}$$

and the curvature parameter

$$\Omega_k(t) = -\frac{k}{H(t)^2 a(t)^2}\,, \tag{1.2.16}$$

as the Friedmann equation breaks down to

$$1 = \Omega(t) + \Omega_k(t)\,. \tag{1.2.17}$$

Hence, the critical density is defined as the one energy density where the universe is flat, as $\Omega_k\,|_{k=0} = 0$, whereas $\rho(t) < \rho_{\text{crit}}(t)$ leads to a hyperbolic and $\rho(t) > \rho_{\text{crit}}(t)$ to a spherical universe.

We now shift our attention to the possible sources of energy density to determine the effect on the dynamics of expansion in relation to the contents of the universe. In order to do this, we must formulate an equation of state $p = p(\rho)$ for each species of energy density: (non-)relativistic matter and vacuum energy. As we applied the cosmological principle for the modeling of the perfect fluid, it is possible to find an equation of state of the form

$$p = w\rho\,, \tag{1.2.18}$$

with a constant parameter w_i that can be derived for each energy species $i \in [m,r,\Lambda]$ (matter, radiation, vacuum energy) via fundamental thermodynamical principles. Solving Eq. (1.2.11) using Eq. (1.2.18) leads to

$$\rho_i(a(t)) = \rho_0 \left(\frac{a(t)}{a_0}\right)^{-3(1+w_i)}\,, \tag{1.2.19}$$

where a_0 is an arbitrary normalization factor. Following these considerations, the dynamics of the energy density of the different species $\rho_i(a(t))$ yields

$$\rho_i(a(t)) \sim \begin{cases} a(t)^{-3}, & \text{non-relativistic matter} \quad (w_m = 0) \\ a(t)^{-4}, & \text{relativistic matter/ radiation} \quad (w_r = 1/3) \\ const, & \text{vacuum energy} \quad (w_\Lambda = -1) \end{cases}\,. \tag{1.2.20}$$

It is quite intuitive that non-relativistic matter dilutes with the third power of the scale factor in 3-dimensional space, while relativistic matter dilutes with one more power, as it is subject to additional energy loss due to relativistic redshift. Vacuum energy, however, is not diluted with the expansion of space[5]. This behavior also leads us to the ad-hoc assumption that the early universe was in a radiation dominated phase, which was displaced by a matter domination phase and ultimately ended in a vacuum energy dominated phase.

It proves to be convenient to formulate the Friedmann equation with the density parameters for curvature, matter, radiation and vacuum energy measured today, which is possible using the results from Eq. (1.2.20). The equation reads

$$H(t)^2 = H_0^2 \left[\Omega_{m,0}\left(\frac{a(t)}{a_0}\right)^{-3} + \Omega_{r,0}\left(\frac{a(t)}{a_0}\right)^{-4} + \Omega_{\Lambda,0}\left(\frac{a(t)}{a_0}\right)^{0} + \Omega_{k,0}\left(\frac{a(t)}{a_0}\right)^{-2}\right]\,, \tag{1.2.21}$$

where the subscript 0 stands for an evaluation of the quantity today as per $x_0 \equiv x(t)\,|_{t=t_0}$.

1.2.2 Experimental Observations and a Very Short History of the Universe

This part of the section deals with experimental evidence found to test the theory outlined in Section 1.2.1. We also shortly discuss a possible history of the universe that is implied by the Cosmological Constant - Cold Dark Matter (ΛCDM) model including the most important events .

---

[5] Note that this behavior implies that total energy is not a conserved quantity as the universe expands.

Parameter	value
H_0	$(67.4 \pm 0.5)\,{}^{\mathrm{km}}/_{\mathrm{s\cdot Mpc}}$
$\Omega_{m,0}$	0.3166 ± 0.0084
$\Omega_{\Lambda,0}$	0.6847 ± 0.0073
$\Omega_{k,0}$	0.0007 ± 0.0019
$\Omega_{r,0}$	$5.38(15) \cdot 10^{-5}$

Table 1.3: Experimental values of cosmological parameters provided by the Planck collaboration [8, 18].

The most precise determinations for those basic cosmological parameters come from the measurements of the Cosmic Microwave Background (CMB), performed by the Planck microwave telescope [18] built by the European Space Agency (ESA). The CMB is formed during the epoch of *recombination*, which we shortly describe later in this section. Experimental values for the cosmological parameters are summarized in Table 1.3. From these values, we can infer that the universe must be remarkably flat ($k = 0$), since $\Omega_{k,0}$ is consistent with zero.

Turning back time in the ΛCDM model - which means scaling down $a(t)$ - ultimately leads to a point where all proper distances in the universe vanish. This hypothetical instance is commonly called the *Big Bang*. We can estimate the age of the universe as $t_U \sim 13.8 \cdot 10^9$ years. From a theoretical point of view, however, this event is highly debated, as one of the cornerstones of the model, GR, breaks down at the *Planck scale* and there is no accepted theory of quantum gravity to replace it at this stage. Additionally, the Big Bang model comes with a series of problems like the *horizon problem* and the *flatness problem*. The horizon problem deals with the question why the temperature fluctuations in the CMB are so miniscule throughout although the distances between parts of the observable universe are bigger than their respective causal horizons. This implies that these regions cannot have been in thermal contact with one another and therefore there is no reason to assume that the temperature should be the same. The flatness problem deals with the aforementioned fact that the universe is surprisingly flat, although the dynamics of expansion suggest that the curvature term has a tendency to increase, as $\Omega(t)$ decreases faster than $a(t)^2$ increases[6] and thus an unnatural initial flatness has to be considered. These problems can be alleviated by introducing a different kind of 'first phase' called *inflation* [19].

Inflationary universes typically contain a scalar field ϕ called the inflaton responsible for a phase of exponential expansion. For this expansion to be sufficiently long (typically 50-60 *e-folds*), the scalar potential is required to have a certain shape, where $\dot{\phi} \ll V(\phi)$. The exponential expansion explains why there was indeed thermal contact between seemingly distinct areas of the universe and it also provides an explanation for the flatness due to the period of dominance of vacuum energy. Inflation also gives a compelling argument for a facilitated structure formation, as quantum fluctuations enlarged to macroscopic proportions act as gravitational seeds for the formation of galaxies. The inflationary phase typically ends with a phase called *reheating*, where the inflaton decays completely to SM particles and repopulates the completely diluted universe[7].

Both inflation and standard cosmology are in accordance that shortly after the respective beginning of the universe, a phase dominated by relativistic matter began. Once the temperature drops to $T \sim \mathcal{O}(100\,\mathrm{GeV})$, the EW phase transition occurs and at around $T \sim \mathcal{O}(1\,\mathrm{MeV})$ the first atomic nuclei begin to form. At this point in time, the average kinetic energy of particles

---

[6] This is true only in a matter/radiation dominated universe, which can be assumed as true for most of our universe's history.

[7] This dilution of particle species existent before the inflationary phase is sometimes used in the literature to explain the absence of *topological defects*.

in thermal bath is not high enough to reionize a forming nucleus anymore, i.e. $E \lesssim \mathcal{O}(\text{MeV})$. Within the framework of the ΛCDM model, precise predictions about the composition of light elements in the universe can be made, which depend crucially on the ratio of protons and neutrons present at this point in time. This mechanism is called *primordial nucleosynthesis* or Big Bang Nucleosynthesis (BBN).

As the temperature of the universe drops further, it eventually reaches the scale of the binding energy of hydrogen at around $\mathcal{O}(10\,\text{eV})$. For similar reasons as for the formation of nuclei, protons and electrons form electrically neutral hydrogen. At this point in the universes history, called *recombination*, the average kinetic energy of electrons is low enough for them to be captured by hydrogen nuclei and thus the amount of Thomson scattering of photons with free charged particles is significantly reduced for the universe to become transparent. This process can be modeled with the help of the *Saha ionization equation* [20]. The CMB therefore is the redshifted radiation that has been propagating ever since this epoch.

1.3 Evidence for New Physics Beyond the Standard Model

In Section 1.1, we discussed the foundations of the SM and hinted at some of the phenomenological consequences that they imply. In this section, however, we point out hints at possible Beyond the Standard Model (BSM) physics as well as outright shortcomings of this theory. In each subsection, we discuss the motivation behind the need for New Physics (NP) and we will shortly outline the most important attempts of explaining these phenomena present in the literature.

1.3.1 Neutrino Masses and Oscillation

An apparent shortcoming of the SM and therefore evidence for BSM physics is the existence of the *neutrino oscillation* phenomenon. After the discovery of solar neutrinos by the Homestake experiment, a 615t tetrachloroethylene tank buried in the Homestake mine designed to detect neutrinos via the inverse β-decay $\nu_e + {}^{37}\text{Cl} \longrightarrow {}^{37}\text{Ar} + e^-$ [21], and the emergence of other experiments dedicated to neutrino detection like GALLEX, SAGE (radiochemical Gallium detection) and Kamiokande (water Cherenkov experiment) the *solar neutrino problem* arose. The nature of this problem was a deficit of the measured neutrino flux compared to the solar neutrino flux theoretically calculated within the *standard solar model* [22].

This deficit can in principle be explained by neutrino oscillations [23], which are an effect of non-trivial leptonic mixing analogous to the CKM mixing in the quark sector. The mechanism describes a neutrino flavor conversion during propagation directly induced by quantum mechanical superposition and dispersion. The deficit is generated because a fraction of the ν_e-flux is converted to ν_μ or ν_τ, which eludes detection by early neutrino experiments [24, 25].

Today, neutrino oscillations are a well established experimental observation, first discovered by SuperKamiokande (SK) [26] and the SNO [27], whose detector design also allows for the reconstruction of ν_μ's.

For a more detailed discussion about the neutrino oscillilation formalism and some applications we direct the reader to Section 2.1.

There are efforts to determine the absolute scale of neutrino masses, e.g. via direct measurements performed with KATRIN or CMB measurements performed by the Planck collaboration. KATRIN is an experiment dedicated to measuring the high energy tail of the tritium beta decay spectrum and currently puts a bound of $\sum_i m_i < 1.1\,\text{eV}$ [28] on the sum of the masses of the neutrino mass eigenstates. Planck is able to establish an even more competitive bound of $\sum_i m_i < 0.12\,\text{eV}$ [18] from precision CMB measurements. Note here, that this bound, however, is relying on the assumptions made in ΛCDM model, while direct searches are generally model independent.

1.3.2 Energy Content of the Universe

One of the most pressing bits of evidence for the SM not being the most fundamental theory of nature is the energy content of the universe. The Planck measurement of the power spectrum of the CMB suggests that $\sim 68.9\%$ of the universe's energy density is made up of *Dark Energy* (see Table 1.3), which is responsible for the current vacuum-energy dominated era of the universe.

There is currently no accepted explanation for what this Dark Energy is. The simplest solution assumes Dark Energy to be largely comprised of the cosmological constant Λ and thus a fundamental property of spacetime. In this context, however, a fine-tuning problem commonly referred to as *cosmological constant problem* arises, when the observed value of the vacuum energy is confronted with theoretical predictions of vacuum energy contributions from QFT [29].

The remaining $\sim 31\%$ of the energy density of the universe stem from non-relativistic matter, as the energy density portions of curvature and radiation are vanishingly low.

Moreover, many experimental observations point towards the existence of a form of non-relativistic matter that does not interact via the electromagnetic force like 'ordinary', i.e. *luminous* or *baryonic*[8] matter. The purely gravitational effect of such non-luminous Dark Matter (DM) can e.g. be observed in rotation curves of galaxies.
According to classical mechanics, the tangential velocity of stars is expected to decrease with increasing distance from the galactic center. Astronomical Doppler measurements, however, show that the velocity flattens out with increasing distance [30, 31]. This can be explained by a DM *halo*[9] around the galaxy with a mass distribution $\rho \sim r^{-2}$.

A different kind of evidence stems from comparisons between the mass distribution measured in gravitational lensing experiments and optical telescopes. Gravitational lensing is an effect predicted by GR [33] that describes the deflection of the path of light in space by massive objects in the vicinity. In the famous example of the *Bullet Cluster* (1E 0657-558), which consists of two galaxy clusters colliding, optical telescopes register significant X-ray emission from the collision center, whereas gravitational lensing detects two halos of DM that passed through one another. These observations hint towards the existence of DM with very weak interaction with baryonic matter as well as weak self-interaction [34, 35].

The best evidence for DM, however, comes from the CMB, which also allows to differentiate baryonic matter and dark matter. Fundamentally, this is possible because in the primordial plasma of the early universe dark matter only interacts gravitationally, while baryonic matter interacts both gravitationally and electromagnetically. Small anisotropies in the plasma containing dark and baryonic matter attract more matter via the gravitational force leading to overdense regions, whereas electromagnetic interactions of the baryonic part of the matter create an outward pressure. These counteracting forces lead the plasma to perform the so called Baryonic Acoustic Oscillations (BAO). When the CMB formed, shortly after recombination, the electromagnetic pressure was released and the overdensities were effectively frozen at the scales of the oscillation, which is still visible in the power spectrum of the CMB today.

Combined with the measurement of gravitational lensing effects of galaxies, Planck states a

---

[8] As opposed to particle physics, leptons also count as baryonic matter in cosmologists' terms.

[9] An alternative explanation of DM proposed to solve this problem is Modified Newtonian Dynamics (MOND) [32]. However, this framework has great difficulties to explain other phenomena commonly associated to DM.

DM/baryonic matter distribution of [18]

$$\Omega_b \approx 0.049, \tag{1.3.1}$$

$$\Omega_{\mathrm{CDM}} \approx 0.261\,. \tag{1.3.2}$$

or sometimes expressed as

$$\Omega_b h^2 = 0.02233 \pm 0.00015, \tag{1.3.3}$$

$$\Omega_{\mathrm{CDM}} h^2 = 0.11933 \pm 0.00091, \tag{1.3.4}$$

with the dimensionless Hubble Parameter $h = {}^{H}\!/\!\left(100\,\frac{\mathrm{km}}{\mathrm{s\cdot Mpc}}\right) = 0.6766 \pm 0.042$.

The baryon abundance in Eq. (1.3.3) can also be determined via the relative abundances of light elements such as ^{2}H, ^{3}He, ^{4}He and ^{7}Li during the BBN [36]. The result is consistent with the CMB measurement stated above, which is additional evidence that DM is non-baryonic.

Although its existence is a widely accepted fact, the exact nature of DM is still unknown and subject to extensive efforts in the scientific community. There is a plethora of particle DM candidates including Weakly-Interacting Massive Particles (WIMPs) and e.g. Axion-like Particles (ALPs) [37].

We review the topic in more detail in Section 2.3 for the case of WIMP-DM.

1.3.3 Lepton Flavor Universality and the R_K Anomaly

As discussed in Section 1.1, lepton and quark fields come in three generations in the SM, which share the same quantum numbers. This property causes the fermionic fields to couple universally - meaning with the same coupling strength - to all gauge bosons. The only way to distinguish the different flavors is by their Yukawa interaction with the Higgs, i.e. their mass, ultimately leading to mixing effects.

FCNCs are only realized on loop level in the SM and therefore possible NP contributions can have sizable effects on the corresponding observables. For this reason, FCNCs provide a good basis to test the universality of fermion couplings for example at the Large Hadron Collider (LHC).

Particularly interesting due to recent experimental results are ratios of branching fractions of B-meson decays into lighter hadrons and lepton pairs, as they possess small theoretical uncertainties due to cancellations of hadronic effects. These observables are defined as [38]

$$R_H \equiv \frac{\int_{q^2_{\mathrm{min}}}^{q^2_{\mathrm{max}}} \mathrm{d}q^2 \frac{\mathrm{d}\Gamma(B\to H\mu^+\mu^-)}{\mathrm{d}q^2}}{\int_{q^2_{\mathrm{min}}}^{q^2_{\mathrm{max}}} \mathrm{d}q^2 \frac{\mathrm{d}\Gamma(B\to He^+e^-)}{\mathrm{d}q^2}}\,, \tag{1.3.5}$$

where q^2 is the invariant squared mass of the dilepton system and $\Gamma(B \to Hl^+l^-)$ is the partial width of the $B \to Hl^+l^-$ decay. In the SM, predictions of these ratios generally lie within $\mathcal{O}(1\%)$ of unity [39] in the q^2-region of $1.0\,\mathrm{GeV}^2 \leq q^2 < 6.0\,\mathrm{GeV}^2$ for B meson decays to kaons. This result is intuitive, since the only difference between the decays is the phase space occupied by masses of the lepton pairs, which is small compared to the mass of the bottom quark. The LHCb collaboration, however, reported on a 2.5σ deviation from the SM in the R_K observable of [40]

$$R_K = 0.846^{+0.060}_{-0.054}\mathrm{stat.}^{+0.016}_{-0.014}\mathrm{sys.} \tag{1.3.6}$$

in the $1.1\,\mathrm{GeV}^2 \leq q^2 < 6.0\,\mathrm{GeV}^2$ region, which is a hint towards a violation of Lepton Flavor Universality (LFU). This result was confirmed by a more recent analysis [41]

$$R_K = 0.846^{+0.042}_{-0.039}\mathrm{stat.}{}^{+0.013}_{-0.012}\mathrm{sys.}\,, \tag{1.3.7}$$

where the LHCb collaboration stated an improved $3.1\,\sigma$ significance of the anomaly in the same q^2-region, therefore providing the first evidence for LFUV in a single measurement.

In recent years, there has been a range of NP models attempting to resolve this anomaly including tree-level exchange of *leptoquarks* [42, 43, 44], Z' models [45, 46, 47] and also models introducing NP contributions at one-loop [48].

In this thesis, we study one-loop solutions to the R_K anomaly in more detail in Chapter 4 in the context of DM phenomenology.

1.3.4 Anomalous Magnetic Moment of the Muon

There are hints towards NP in the measurement of the magnetic moment of the muon performed at *Brookhaven National Laboratory* [49] and, more recently, *Fermilab* [50].

The magnetic moment of a particle species i is defined by

$$\vec{\mu}_i = g_i \frac{q_i}{2m_i}\vec{S}_i\,, \tag{1.3.8}$$

where $\vec{S}_i$ denotes the particle's spin, q_i the electric charge, m_i the mass and g_i the *spin g-factor*[10] of the particle. Based on the non-relativistic version of the Dirac equation, the *Pauli equation*, we can derive that for a fundamental, massive, electrically charged fermion that is coupled to an external electromagnetic field the g-factor is $g_i = 2$ (see e.g. [51, 52]). However, quantum corrections to this quantity can lead to an increase of this number. This *anomalous magnetic moment* is typically parametrized as

$$a_i = \frac{1}{2}(g_i - 2) \tag{1.3.9}$$

and commonly dubbed $(g-2)_i$.

Within the SM, contributions to this anomalous magnetic moment, depicted in Fig. 1.1 for the case of the muon, can arise from QED and weak processes at leading order on one-loop level and also by hadronic processes.

While QED correction are shown to be of the order $\sim \alpha/2\pi$ [53], generic corrections generated by heavy states are typically of the form $a_i \sim m_i^2/\Lambda^2$ [52, 54], where Λ is the scale of the heavy states, which can be e.g. the EW scale $\sim \mathcal{O}(100\,\mathrm{GeV})$ or the scale of potential NP. Since they are proportional to the mass m_i of the particle, loop corrections from EW physics and beyond are suppressed for electrons.

Muons, however, are experimentally interesting, since they possess a mass that is two orders of magnitude larger than the electron mass. At the same time, the muon's mean lifetime is approximately seven orders of magnitude larger than that of tau-leptons. These circumstances make the muon the ideal lepton candidate for an experiment that measures the difference between the cyclotron frequency $\vec{\omega}_c = -q\vec{B}/m\gamma$ and the spin precession frequency $\vec{\omega}_s = -g \cdot q\vec{B}/2m - (1-\gamma)\cdot q\vec{B}/\gamma m$ of the muon in a storage ring with an external magnetic field $\vec{B}$. This difference is thus proportional to the anomalous magnetic moment of the muon a_μ as [49]

$$\vec{\omega}_c - \vec{\omega}_s = -a_\mu \frac{q\vec{B}}{m_\mu}\,. \tag{1.3.10}$$

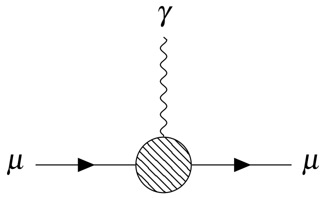

Figure 1.1: Feynman diagram[11] that contributes to the magnetic moment of the muon.

The result obtained at Brookhaven shows a 2.2 - 2.7 σ positive deviation from the SM prediction, while the Fermilab result deviates by 3.3 σ. Combined, the experimental measurement

$$\Delta a_\mu(\mathrm{Exp} - \mathrm{SM}) = (251 \pm 59) \times 10^{-11} \tag{1.3.11}$$

differs from the SM predicition by 4.2 σ [56].

This disagreement motivated extensive efforts of BSM model building, e.g. two-Higgs-doublet model (2HDM) solutions [57], leptoquark solutions [58, 59] and supersymmetry (SUSY) solutions [60, 61, 62]. For a recent review on NP solutions to the $(g-2)_\mu$ anomaly, see e.g. [63].

In Chapter 4, we address a possible one-loop solution to this anomaly [48] in the context of DM.

1.3.5 Additional Problems

There are additional problems of the SM pointing towards its incompleteness that are *not addressed* in this thesis. Note that the following (very short) list of shortcomings of the SM is *not* ordered in any sense.

- Gravity:
  As Section 1.1 suggests, the SM aims to describe all fundamental forces of nature as a renormalizable gauge QFT. However, to this day there is no accepted quantum theory of gravity, which renders the SM incomplete on a conceptual level.

- Grand Unification:
  Several theoretical hints such as e.g. the amount of free parameters in the SM and successful unification of the weak and electromagnetic forces point towards a possible Grand Unified Theory (GUT) at very high energies recovering the symmetry group of the SM at low energies via symmetry breaking. The most famous propositions are the *Georgi-Glashow* $SU(5)$-GUT [64], the *Pati-Salam* model [65] or the $SO(10)$-GUT [66], in which the first two are included as subgroups. These variants predict unobserved phenomena like proton decay (Georgi-Glashow) or magnetic monopoles (Pati-Salam).

- The Strong CP Problem:
  The question why QCD seems to be CP-invariant is commonly called the Strong CP Problem. In principle, there is no symmetry that forbids the CP-violating term $\mathcal{L}_{\mathrm{QCD}} \sim \theta G_{\mu\nu}\tilde{G}^{\mu\nu}$. However, measurements of the electric dipole moment of the neutron of $|d_n| \leq 1.8 \cdot 10^{-26} e \cdot \mathrm{cm}$ [67] indicate that the CP-violating parameter $\theta < 10^{-10}$. The most common propositions of an explanation for this problem invoke additional symmetries

---

[10] The g-factor is the dimensionless form of the *gyromagnetic ratio*, which is defined as the ratio of the magnetic moment to its spin.

[11] All Feynman diagrams in this work are created with the TikZ-Feynman package [55].

that naturally force the θ parameter to be small. The first and most prominent attempt is the *Peccei-Quinn* model involving a global $U(1)_A$ that lead to the introduction of the *axion* as a pseudo-Goldstone boson [68].

- The Baryon Asymmetry of the Universe:
  A fundamental puzzle of cosmology is the question why there is more matter than antimatter. According to the *Sakharov conditions* [69], a source of CP-violation is needed to generate an asymmetry from an initial symmetry of baryons and antibaryons. The CP-violation found in the SM, however, is not sufficient to accommodate the measured asymmetry parameter of $\eta = {}^{(n_B - n_{\bar{B}})}/_{n_\gamma} = (5.931 \pm 0.051) \cdot 10^{-10}$ [70]. Prominent theories to alleviate this problem are e.g. GUT-*baryogenesis* and *leptogenesis* [71, 72].

Chapter 2

Theoretical Groundwork Beyond the Standard Model

In this chapter, we introduce the most important BSM concepts that are a prerequisite for the Chapters 3 and 4. Most of the models and mechanisms presented here are used to solve problems that arise in the SM, both experimentally and theoretically.

In Section 2.1, we discuss the formalism of neutrino oscillations in vacuo and in matter. We also briefly discuss the current anomalies in neutrino oscillation data. In Section 2.2, we review the most popular neutrino mass generation mechanisms including the seesaw mechanism and radiative neutrino masses. Finally, we review the theory of DM production and detection in Section 2.3.

2.1 Neutrino Oscillations

In this section, we review the theory behind neutrino oscillations in vacuo as well as in matter. First, we derive the general neutrino flavor transition probabilities in vacuo and shortly discuss the experimental status. In the second part of the section, we aim to present the most important concepts of neutrino oscillations in matter and derive the neutrino flavor transition probability in a simplified two-flavor setup. We also discuss the implications of these results for a more realistic three-flavor scenario, taking into account the matter distribution of the Earth.

For in-depth discussions and comprehensible reviews about this topic see e.g. [73, 74, 75, 76]. Parts of this section loosely follow these reviews.

2.1.1 Neutrino Oscillations in Vacuo

As hinted in Section 1.3, neutrino oscillations are a direct consequence of leptonic mixing. As outlined in Section 1.1, mixing of this type can only occur if neutrinos are massive[1]. In analogy to the CKM matrix defined in Eq. (1.1.19), a leptonic mixing matrix, called Pontecorvo-Maki-Nakagawa-Sakata (PMNS) matrix, can be constructed if the Lagrangian contains a neutrino mass term[2].

---

[1] More elaborate scenarios can in principle get along without neutrino masses by invoking a certain kind of Lorentz violation (see e.g. [77]).

[2] The generation of such a mass term is discussed in Section 2.2.

The PMNS matrix is defined via the unitary mixing matrix

$$V_{\text{lept}} = V_\nu V_l^\dagger \equiv U_{\text{PMNS}}^\dagger \,, \tag{2.1.1}$$

where the common parametrization can be adopted from Eq. (1.1.20). As only the rotation by $V_\nu V_l^\dagger$ can be considered physical, the individual choice of V_l and V_ν is free as long as the other is chosen accordingly. In the literature it is common to choose $V_l = \mathbb{1}$ and thus $U_{\text{PMNS}} = V_\nu^\dagger$. This means that we implicitly interpret the charged leptons as mass eigenstates and interaction eigenstates, while neutrinos can be rotated from the mass eigenbasis to the weak eigenbasis (or flavor basis) with the help of U_{PMNS}. States in the mass basis $|\nu_i(x^\mu)\rangle$ are eigenstates of the free Hamiltonian and as such keep this property during propagation following

$$|\nu_i(\vec{x},t)\rangle = \exp(-\mathrm{i}p^\mu x_\mu)\,|\nu_i(0)\rangle \overset{p_i \gg m_i}{\approx} \exp\left(-\mathrm{i}\frac{m_i^2}{2E}t\right)|\nu_i(0)\rangle \,, \tag{2.1.2}$$

using the plane wave solution[3] and an expansion of the standard dispersion relation

$$E_i = \sqrt{m_i^2 + p^2} \approx p + \frac{m_i^2}{2p} \approx E + \frac{m_i^2}{2E} \,. \tag{2.1.3}$$

The phase factor $\exp(-\mathrm{i}Et)$ is the the same for each neutrino mass eigenstate, since we adopt the view point that the neutrino is created with a fixed energy in this formalism. An overall phase, however, does not play a role in neutrino oscillation phenomenology, as only phase differences are physical.

If we produce the neutrino in the weak eigenbasis e.g. via a decay of a W-boson, the neutrino state $|\nu_\alpha(\vec{x},t)\rangle$ is a superposition

$$|\nu_\alpha(\vec{x},t)\rangle = \sum_i (U_{\text{PMNS}})_{\alpha i}\,|\nu_i(\vec{x},t)\rangle \tag{2.1.4}$$

of different mass eigenstates $|\nu_i(\vec{x},t)\rangle$ and therefore the probability $P_{\nu_\alpha\to\nu_\alpha}(L)$ to find it in the same flavor state after some propagation distance $L \approx c\cdot t$ is generally ≤ 1. In more detail, the probability to find a neutrino that is initially in flavor state $|\nu_\alpha\rangle$ in a flavor state $|\nu_\beta\rangle$ after a baselength L is

$$\begin{aligned} P_{\alpha\to\beta}(L,E) &= |\langle\nu_\beta|\nu_\alpha(L)\rangle|^2 \\ &\approx \left|\sum_i U_{\beta i}^* U_{\alpha i}\exp\left(-\mathrm{i}\frac{m_i^2}{2E}L\right)\right|^2 \\ &\approx \sum_{i,j}\left(U_{\alpha j}^* U_{\beta j} U_{\alpha i} U_{\beta i}^* \exp\left(-\mathrm{i}\frac{m_j^2 - m_i^2}{2E}L\right)\right) \,, \end{aligned} \tag{2.1.5}$$

where we used Eqs. (2.1.2)-(2.1.4) and set $U \equiv U_{\text{PMNS}}$ for simplicity. As can be seen from Eq. (2.1.5), the probability is not dependent on the overall mass scale, but rather on the *mass squared differences* $\Delta m_{ji}^2 = m_j^2 - m_i^2$. This fact makes it conceptually impossible to extract an absolute neutrino mass scale from oscillation experiments.

---

[3] The plane wave formalism is conceptually flawed, as it proposes non-normalizable wave functions and infinite coherence lengths. A more accurate way of deriving the transition probability uses the wave packet formalism, where neither the momentum nor the energy of the initially created neutrino is fixed. This formalism is, however, much more computation-intensive and does not lead to fundamentally different results in the limit of non-astronomical baselengths. Detailed discussions about this topic can be found in e.g. [78, 79].

Parameter	Value (NO)	Value (IO)
Δm^2_{21}	$(7.42^{+0.21}_{-0.20}) \cdot 10^{-5}\,\mathrm{eV}^2$	$(7.42^{+0.21}_{-0.20}) \cdot 10^{-5}\,\mathrm{eV}^2$
$\Delta m^2_{13(23)}$	$(2.514^{+0.028}_{-0.027}) \cdot 10^{-3}\,\mathrm{eV}^2$	$(-2.497^{+0.028}_{-0.028}) \cdot 10^{-3}\,\mathrm{eV}^2$
$\sin^2\theta_{12}$	$0.304^{+0.013}_{-0.012}$	$0.304^{+0.013}_{-0.012}$
$\sin^2\theta_{23}$	$0.570^{+0.018}_{-0.024}$	$0.575^{+0.017}_{-0.021}$
$\sin^2\theta_{13}$	$0.02221^{+0.00068}_{-0.00062}$	$0.02240^{+0.00062}_{-0.00062}$
δ_{CP}	$(195^{+51}_{-25})^\circ$	$(286^{+27}_{-32})^\circ$

Table 2.1: Best fit points for neutrino parameters in the $1\,\sigma$ range for NO and IO [80, 81].

Moreover, the probability features a dependence on the quotient L/E, since the PMNS matrix elements do not feature any dependence on either of these quantities. Eq. 2.1.5 can be written in a form, that is more evocative of an oscillation. We obtain

$$\begin{aligned} P_{\alpha\to\beta}(L,E) \approx \delta_{\alpha\beta} &- 4\sum_{j>i} \Re(U^*_{\alpha j}U_{\beta j}U_{\alpha i}U^*_{\beta i})\sin^2\left(\frac{\Delta m^2_{ji}L}{2E}\right) \\ &+ 2\sum_{j>i} \Im(U^*_{\alpha j}U_{\beta j}U_{\alpha i}U^*_{\beta i})\sin\left(\frac{\Delta m^2_{ji}L}{2E}\right), \end{aligned} \tag{2.1.6}$$

where the constant values $\Delta m^2_{ji}/2$ can be interpreted as the oscillation frequencies for the argument L/E.

In the SM, we encounter three neutrino fields and thus the three-flavor case is a special consideration for a minimal extension. However, the equation for the three-flavor oscillation probability is non-trivial and does not provide the reader with any intuition of the physical effects. It is, however, advisable to consider the two-flavor case as limiting cases of a three-flavor world, as experimental determinations of mixing angles θ_i and mass-squared differences Δm^2_{ji} (cf. Table 2.1) suggest that there are parameter hierarchies, which can be used to simplify the equations for certain scenarios.

An obvious hierarchy lies e.g. in the mass-squared differences, where we observe

$$\left|\Delta m^2_{21}\right|^2 \ll \left|\Delta m^2_{31}\right|^2 \approx \left|\Delta m^2_{32}\right|^2 . \tag{2.1.7}$$

Note here that the signs of Δm^2_{31} and Δm^2_{32} are still unknown, while Δm^2_{21} is known to be positive. This means that there is still a possibility for two different orderings of mass eigenvalues: normal ordering (NO) ($m_3 > m_2 > m_1$) and inverted ordering (IO) ($m_2 > m_1 > m_3$), although NO is favored by global fits at $\sim 2.7\,\sigma$ [80]. The mass ordering can in principle be determined at experiments using *matter effects*. We direct the reader to Section 2.1.2 for more detail.

The two-flavor oscillation probability can be expressed as

$$P^{2\times 2}_{\nu_\alpha\to\nu_\beta}(L,E) = \sin^2 2\Theta \sin^2\left(\frac{\Delta m^2}{4E}L\right). \tag{2.1.8}$$

This equation approximately applies when we use the hierarchy in Eq. (2.1.7) for experiments, whose L/E does not compensate the smallness of Δm^2_{21} and the equations for the flavor transitions are dominated by contributions from Δm^2_{31}. In this limit, we do not see the modulation because the Δm^2_{21} 'frequency' is too low and we obtain

$$\lim_{\Delta m^2_{21}L/2E\to 0} P_{\nu_\alpha\to\nu_\beta}(L,E) = 4|U_{\alpha 3}|^2|U_{\beta 3}|^2\sin^2\left(\frac{\Delta m^2_{31}L}{4E}\right). \tag{2.1.9}$$

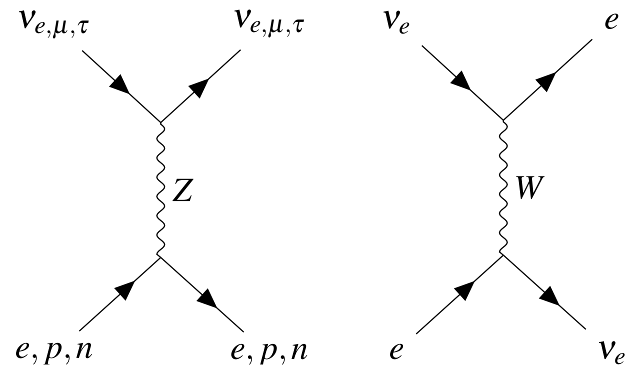

(a) Neutral current interaction (b) Charged current interaction

Figure 2.1: Neutrino scattering with ordinary matter via the weak interaction. (a) shows the interaction of all ordinary matter particles with all active neutrino flavors via the neutral current interaction. (b) shows the charged current interaction of electron neutrinos and electrons.

This behavior can be seen at e.g. atmospheric, reactor and accelerator experiments. The other extreme case is the scenario, where ${}^{\Delta m^2 L}\!/_{2E}$ is large, leading to fast oscillations. Once these oscillations become faster than the resolution of the experiment, an averaging effect occurs. This is the case at e.g. solar neutrino experiments, as they typically work with a baseline of $L \approx 1$ astronomical unit (au) and energies at around $\sim 10\,\mathrm{MeV}$. The ν_e survival probability in this case is [76]

$$P_{\nu_e \to \nu_e}(L,E) \approx \cos^4\theta_{13}\left(1 - \sin^2(2\theta_{12})\sin^2\left(\frac{\Delta m^2_{21} L}{4E}\right)\right) + \sin^4\theta_{13}\,. \tag{2.1.10}$$

2.1.2 Neutrino Oscillations in Matter

Neutrino interactions with ordinary matter (protons, neutrons, electrons) are generally only mediated by the weak force and thus typical cross sections are tiny. Furthermore, only coherent (momentum-conserving) forward scattering contributes to neutrino oscillations. All neutrino species scatter with ordinary matter via Z-boson exchange, while only ν_e's take part in W-mediated charged current interactions (see Fig. 2.1). The reason for this is the absence of muons and τ-leptons in ordinary matter, because of their higher mass and subsequent instability. As mentioned in Section 2.1.1, only relative phases lead to physical effects in neutrino oscillations, and thus neutral current interactions can be omitted from this discussion[4], since it creates a common phase for all neutrino species. The standard way of parametrizing matter effects in neutrino oscillations is using a Schrödinger-like evolution equation and formulate the interaction part as an additional effective potential in the Hamiltonian

$$\mathrm{i}\frac{\mathrm{d}}{\mathrm{d}t}\begin{pmatrix}\nu_e\\ \nu_\mu\end{pmatrix} = H\begin{pmatrix}\nu_e\\ \nu_\mu\end{pmatrix}\,, \text{where } H = H_{\text{vac}} + V_{\text{eff}}\,. \tag{2.1.11}$$

When taking into account matter effects, it is recommendable to work in the weak eigenbasis, as the effective potential V_{eff} is diagonal in this case. The effective charged current Hamiltonian

---

[4] In a scenario involving sterile neutrinos, neutral current interactions become important, as it creates a relative phase between active and sterile neutrinos.

for neutrino-electron scattering yields

$$\begin{aligned} H_{\text{eff}}^{\text{CC}} &= \frac{G_F}{\sqrt{2}} \left[\bar{e}\gamma_\mu \left(1-\gamma^5\right)\nu_e\right] \left[\bar{\nu}_e\gamma^\mu \left(1-\gamma^5\right) e\right] \\ &= \frac{G_F}{\sqrt{2}} \left[\bar{e}\gamma_\mu \left(1-\gamma^5\right) e\right] \left[\bar{\nu}_e\gamma^\mu \left(1-\gamma^5\right) \nu_e\right] \end{aligned} \tag{2.1.12}$$

in *Fermi contact theory* at low energies with the Fermi constant G_F. The second line of Eq. (2.1.12) can be obtained from the first line via a *Fierz transformation*[5]. In order to calculate the effective potential from this Hamiltonian, we have to integrate out the electron background. This leads to the form of the effective potential of [82]

$$V_{\text{eff}}^{\text{CC}} = \sqrt{2} G_F N_e \delta_{ei} \tag{2.1.13}$$

for electron neutrinos, where N_e is the electron number density and δ_{ei} is the *Kronecker delta*, fixing this potential to only electron neutrinos. This potential is added to the Hamiltonian in the flavor basis as

$$\begin{aligned} H &= U_{\text{PMNS}} H_{\text{mass}} U_{\text{PMNS}}^\dagger + V_{\text{eff}}^{\text{CC}} \\ \text{with } H_{\text{mass}} &= \frac{1}{2E} M^\dagger M \,, \end{aligned} \tag{2.1.14}$$

where the squared mass matrix $M^\dagger M$ can be written as

$$M^\dagger M = \begin{pmatrix} 0 & 0 \\ 0 & \Delta m^2 \end{pmatrix} . \tag{2.1.15}$$

Finding the neutrino flavor transition probability $P_{\nu_\alpha \to \nu_\beta}$ breaks down to finding the eigenvalues and eigenvectors of the Hamiltonian in Eq. (2.1.14)[6]. Using the eigenvalues and eigenvectors, we map the probability function onto the vacuum probability in Eq. (2.1.8) and construct an effective mixing angle and an effective mass-squared difference, yielding

$$\sin^2 2\tilde{\Theta} = \frac{(\Delta m^2)^2}{\left(\Delta m^2 \cos 2\Theta - 2\sqrt{2} E G_F N_e\right)^2 + (\Delta m^2)^2 \sin^2 2\Theta} \sin^2 2\Theta \tag{2.1.16}$$

$$\Delta\tilde{m}^2 = \Delta m^2 \sqrt{\sin^2 2\theta + \left(\cos 2\theta - \frac{2\sqrt{2} E G_F N_e}{\Delta m^2}\right)^2} . \tag{2.1.17}$$

In the effective parameters in Eqs. (2.1.16)-(2.1.17), we obtain a scaling of the vacuum amplitude by an energy-dependent factor. It becomes apparent that the amplitude term $\sin^2 2\tilde{\Theta}$ is maximal when the condition

$$E = \frac{\Delta m^2 \cos 2\Theta}{2\sqrt{2} G_F N_e} \tag{2.1.18}$$

is fulfilled. This is known as the *resonance condition* for matter effects (sometimes called the Mikheyev-Smirnov-Wolfenstein (MSW) condition), since the amplitude factor of the probability function reaches 1 and the effective mixing is maximal. At this particular energy (and/or electron number density), a resonant conversion of neutrino flavors is possible, even if the initial (vacuum) mixing angle is small [83, 84].

---

[5] For a definition of and short discussion about Fierz transformations see Section 2.3.3.4.

[6] This statement is especially true for approximately constant matter densities.

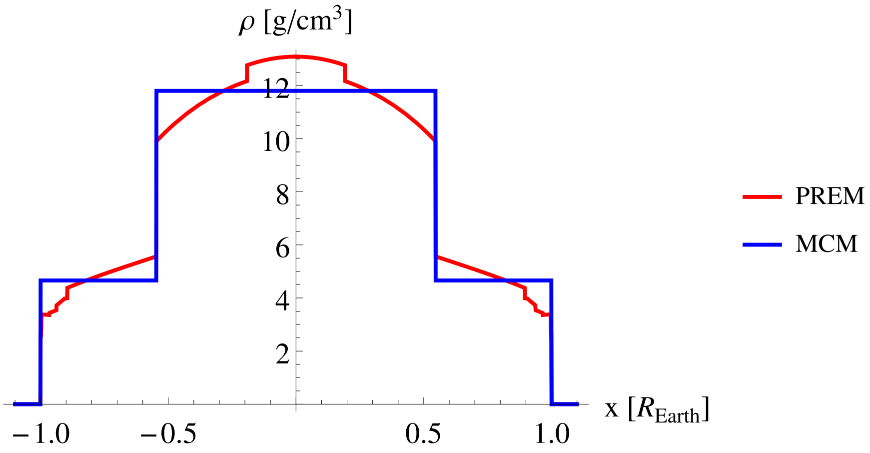

Figure 2.2: Density profiles of the PREM and the MCM model. Distances are given relative to the Earth's center.

Note that for antineutrinos, we have to make the shift $V_{\text{eff}}^{\text{CC}} \to -V_{\text{eff}}^{\text{CC}}$. For this reason, only either neutrinos or antineutrinos can experience resonant conversion in matter depending on the sign of the mass-squared difference. Hence, matter effects can help determine the mass ordering of neutrino mass eigenstates experimentally. long baseline (LBL) experiments with underground neutrino beams like T2K, NOνA and future experiments like DUNE and JUNO are able to test the mass hierarchy based on these foundations [85, 86].

In the case of experiments like SK and IceCube that measure neutrinos which are created via showers of cosmic particles in the atmosphere, neutrinos experience a varying matter density while traveling through the Earth. In this case, we rely on the Preliminary Reference Earth Model (PREM) or the more simplified Mantle-Core-Mantle (MCM) model of Earth's matter density to be able to predict the oscillation probabilities for upward-going neutrinos (meaning going upwards from the ground in the lab-frame, i.e. coming from the other side of the Earth). Figure 2.2 shows the density in relation to the distance from the Earth's center in the PREM and the MCM model. The PREM [87] is based on seismological data and interpolates Earth's density profile within several layers with the help of polynomials. The MCM model is a simplified version of this density profile, where we perform an average over the individual mantle and the core density profiles. Comparison of numerically obtained oscillation probabilities show that the main features of the oscillation probability are retained by the simplified MCM model [88]. Thus, we mainly use the MCM model in Chapter 3 for calculations of the oscillation probabilities at atmospheric neutrino experiments.

2.1.3 Anomalies in Neutrino Oscillations

Although the three neutrino paradigm is generally well accepted and most of the data accumulated by different experiments affirm this status quo, there are several anomalies suggesting that this picture is incomplete. The most prominent anomalies are *the short baseline anomaly* [89, 90, 91], *Reactor Antineutrino Anomaly (RAA)* [92] and *the gallium anomaly* [93, 94].

These anomalies, and especially the incompatibility of their commonly proposed solution - active-sterile neutrino oscillations in a $(3+N)\nu$ scenario - with other neutrino oscillation experiments are the main motivation for the model discussed in Chapter 3.

We base this brief discussion on the reviews [95, 96, 97] and the references given above.

2.1.3.1 The Short Baseline Appearance Anomalies

The short baseline (SBL) neutrino experiments are designed to probe neutrino oscillation at baselines $L \sim \mathcal{O}(10 - 1000\,\text{m})$. The most notable representatives of this kind of experiments are LSND and MiniBooNE.

LSND at *Los Alamos National Laboratory* uses a proton-accellerator-based stopped-pion source to generate muon antineutrinos via the reaction $\pi^+ \to \mu^+\nu_\mu \to \bar{\nu}_\mu \nu_\mu \nu_e e^+$. The $\sim 30\,\text{m}$ baseline to the 167 t mineral oil liquid scintillator detector is screened to let only the neutrinos pass. The typical neutrino energies of this experiment range from $20 - 60\,\text{MeV}$. This L/E design makes LSND sensitive to comparably large mass-squared differences of $\Delta m^2_{\text{LSND}} \sim 1\,\text{eV}^2$, while the regular mass-squared differences Δm^2_{21} and Δm^2_{31} are negligible is this context. The analysis of the experimental data found an excess of electron neutrino events at about $E \sim 25\,\text{MeV}$, which is commonly attributed to a non-standard neutrino oscillation of $\bar{\nu}_\mu$ to $\bar{\nu}_e$.

For the purpose of a cross check to the results found by LSND, the MiniBooNE collaboration performs an experiment at *Fermilab* with a similar L/E ratio. This experiment uses the *Booster proton accelerator beam* directed towards a beryllium target in front of a magnetic focusing horn to produce a focused beam of π and K-mesons of either positive or negative electric charge depending on the polarity of the horn. These mesons then decay in a 50 m decay pipe to (anti)neutrinos, which reach the 800 t mineral oil liquid scintillator detector located 541 m away from the beryllium target. The energy range of the MiniBooNE experiment is ca. $200\,\text{MeV} \leq E \leq 3\,\text{GeV}$. An analysis of the MiniBooNE data also found an excess of electron (anti)neutrino appearance in the muon (anti)neutrino beam. The energy range of this excess, however, lies at ~ 200-500 MeV.

2.1.3.2 The Reactor and Gallium Anomalies

Reactors have provided a reliable source of electron antineutrinos, which are created in beta-decay of unstable nucleus isotopes with typical energies of $\sim \mathcal{O}(\text{MeV})$. Reactor experiments typically feature detectors at comparably short baselines of $\mathcal{O}(10\,\text{m} - 1\,\text{km})$ [7], which detect neutrinos from the reactor source via inverse beta decay and thus effectively measure the electron antineutrino survival probability P_{ee} [8].

Their primary goals are a precise measurement of the neutrino fluxes of the radioactive isotopes and the measurement of PMNS mixing matrix elements, especially Δm^2_{21},θ_{12} in the case of e.g. KamLAND and Δm^2_{31},θ_{13} in the case of the RENO, (Double-)Chooz and DayaBay experiments. Analyses of the data collected in these experiments show that there is a disagreement of the theoretically predicted fluxes and the measurements, which is commonly referred to as the RAA [92].

Furthermore, gallium-based radio-chemical experiments that are designed to measure the solar neutrino flux like GALLEX at *Gran Sasso National Laboratory* and SAGE at *Baksan Neutrino Observatory*. The GALLEX detector, e.g. , is a tank filled with 101 t gallium trichloride/hydrochloric acid solution. A neutrino capture event triggers the reaction $\nu_e + {}^{71}\text{Ga} \to {}^{71}\text{Ge}^+ + e^-$, which implies that the effective counting of germanium atoms gives the number of captured neutrinos.

However, these experiments were also run with artificial ^{51}Cr and ^{37}Ar radioactive sources and a statistically significant deficit in the flux of electron neutrinos has been detected. This $2.3 - 3\,\sigma$ disagreement between observation and theoretical prediction is commonly called the *Gallium Anomaly* [93, 94].

---

[7] The most notable exception here is KamLAND, which is fueled by many power plants around the detector at an average baselength of $\sim 180\,\text{km}$.

[8] Because of CPT-invariance, the oscillation probabilities P_{ee} and $P_{\bar{e}\bar{e}}$ are the same [98].

2.1.4 eV^2-Scale Active-Sterile Neutrino Oscillations and its Problems

Individual analyses of reactor+gallium data as well as SBL appearance data suggest that scenario involving an additional, sterile neutrino with a large, additional mass-squared difference of $\sim 1\,\mathrm{eV}^2$ can provide a good fit and thus explain the anomalies presented in the sections above. Additionally, spectral distortions in the data of new generation experiments like NEOS and DANSS also hint towards an active-sterile oscillation [99]. In this section, we shortly review the physics of neutrino oscillations in the presence of a sterile neutrino flavor which mixes with the other neutrino states, commonly dubbed $(3+1)\nu$ scenario.

Any additional neutrino state is required to be sterile, since the measurement of the decay width of the Z-boson at LEP and the SLC restricts the number of active neutrinos states to be $N_\nu = 3$ [100][9]. Additional evidence against a fourth lepton doublet is the non-existence of a fourth charged lepton.

As derived in Eq. (2.1.6), the general neutrino oscillation probability of fully relativistic (light) neutrinos can be described by a sum of oscillatory sine (squared) terms weighted by a combination of mixing matrix elements. This is true for any $(3+N)\nu$ scenario. In the $(3+1)\nu$ case, this mixing matrix is not the PMNS matrix, but a unitary 4×4 matrix which contains the 3×3 PMNS matrix

$$U_{4\times 4} = \begin{pmatrix} & & & U_{e4} \\ & U_{\mathrm{PMNS}} & & U_{\mu 4} \\ & & & U_{\tau 4} \\ U_{s1} & U_{s2} & U_{s3} & U_{s4} \end{pmatrix} . \tag{2.1.19}$$

Neglecting potential CP violation, we can drop the imaginary part in Eq. (2.1.6). As suggested by the anomalies discussed above, the additional mass-squared difference $\Delta m^2_{41} \approx \Delta m^2_{42} \approx \Delta m^2_{43} \equiv \Delta m^2_{\mathrm{SBL}}$ is orders of magnitude larger than Δm^2_{21}, Δm^2_{31} and Δm^2_{32} and thus it is possible to express the oscillation probability as

$$\begin{aligned} P_{\alpha\to\beta}(E,L) &= \delta_{\alpha\beta} - 4\sum_j^3 \Re\left(U^*_{\alpha 4}U_{\beta 4}U_{\alpha j}U^*_{\beta j}\right)\sin^2\left(\frac{\Delta m^2_{4j}L}{4E}\right) \\ &= \delta_{\alpha\beta} - 4\underbrace{\sum_j^3 U_{\alpha 4}U_{\beta 4}U_{\alpha j}U_{\beta j}}_{\equiv -1/4\sin^2 2\theta_{\alpha\beta},\,\alpha\neq\beta} \cdot \sin^2\left(\frac{\Delta m^2_{\mathrm{SBL}}L}{4E}\right), \end{aligned} \tag{2.1.20}$$

where the unitarity condition $\sum_j^3 U_{\alpha j}U_{\beta j} + U_{\alpha 4}U_{\beta 4} = \delta_{\alpha\beta}$ applies for U. The effective amplitudes $\sin^2 2\theta_{\alpha\beta}$ for appearance and disappearance read [101]

$$\sin^2 2\theta_{\alpha\beta} = \begin{cases} 4|U_{\alpha 4}|^2|U_{\beta 4}|^2\,, & \alpha\neq\beta \quad \text{appearance} \\ 4|U_{\alpha 4}|^2(1-|U_{\alpha 4}|^2)\,, & \alpha=\beta \quad \text{disappearance} \end{cases} \tag{2.1.21}$$

and thus, for $|U_{\alpha 4}|^2 \ll 1 \wedge |U_{\beta 4}|^2 \ll 1$, the disappearance amplitude simplifies to $\sin^2 2\theta_{\alpha\alpha} \approx 4|U_{\alpha 4}|^2$ and thus we can relate appearance and disappearance via

$$\sin^2 2\theta_{\alpha\beta} \approx \frac{1}{4}\sin^2 2\theta_{\alpha\alpha}\cdot\sin^2 2\theta_{\beta\beta}\,. \tag{2.1.22}$$

---

[9] Since this is measured via the decay of the Z-boson, this statement is only true for all neutrinos with masses below the Z-boson mass.

As the data of e.g. LSND and MiniBooNE suggests, a significant appearance amplitude $\sin^2 2\theta_{e\mu}$ is required to explain these anomalies with $(3+1)\nu$ neutrino oscillation, while LBL atmospheric and accelerator data (e.g. of SK, IceCube and T2K) suggests that there is no significant disappearance in either $\overset{(-)}{\nu}_e \to \overset{(-)}{\nu}_e$ or $\overset{(-)}{\nu}_\mu \to \overset{(-)}{\nu}_\mu$. This contradiction shows that a $(3+1)\nu$ model is unable to explain the world neutrino data[10]. In fact, global analyses of neutrino oscillation data suggest that there is a strong tension between appearance and disappearance experiments in a $3+1\nu$ scenario. For this reason, global fits are often performed in a 'pragmatic' approach, neglecting e.g. the MiniBooNE excess [99, 103].

The appearance-disappearance relation in Eq. (2.1.22) is dependent on the mixing matrix elements being constants with respect to L and E. The strategy of the model proposed in Chapter 3 is lifting this condition by introducing an energy-dependent potential and thus effectively utilizing the fact that the experiments operate at different energy and baselength scales.

2.2 Neutrino Mass Generation

This section deals with the generation of neutrino masses that are consistent with the experimental data. As pointed out in Sections 1.3.1, the existence of neutrino oscillations necessitates neutrino masses, which are absent in the SM. In this work, we discuss the concepts of *Dirac mass terms*, *Majorana mass terms* and also *radiative neutrino masses* as possible solutions to the neutrino mass puzzle. All of these explanations for a non-zero neutrino mass require the introduction of additional degrees of freedom to the SM. This section is based on the review articles [8, 73, 104, 105, 106].

2.2.1 The Dirac Mass Term

Perhaps the simplest way to generate neutrino masses is to adopt the Higgs mechanism described in Section 1.1. In order to do this, we have to add right-handed neutrinos to the particle content, yielding a Yukawa interaction term

$$\mathcal{L}_{\text{Yuk}} \supset -(Y^\nu)_{ij} \bar{L}^i \tilde{H} \nu_R^j + \text{h.c.}\,, \tag{2.2.1}$$

leading to a Dirac mass matrix

$$(M^\nu)_{ij} = \frac{v}{\sqrt{2}} (Y^\nu)_{ij} \tag{2.2.2}$$

after EWSB. For this term to be gauge-invariant, we require the right-handed neutrinos to to transform as a singlet under the SM gauge group $\nu_R = (\mathbf{1},\mathbf{1},0)$.

Despite the simplicity of this mechanism, there are obvious questions that can be asked when taking a look at the experimental data. While the Yukawa couplings of the other fermions of the SM range from $\mathcal{O}(10^{-6})$ to $\mathcal{O}(1)$, the neutrino Yukawa couplings have to be $\mathcal{O}(10^{-13})$ to explain the masses of $\lesssim \mathcal{O}(0.1\,\text{eV})$. This discrepancy roughly seven orders of magnitude to the next smallest Yukawa coupling of the electron has sparked suspicions that the origin of the neutrino masses could be different. Furthermore, the fermion masses within a generation are usually within 1-2 orders of magnitude and the introduction of neutrinos completely changes this dynamic.

Moreover, as ν_R is a gauge singlet, there is no theoretical reason not to include a term $\sim (M_M^\nu)_{ij} \overline{\nu_R}^i ((\nu_R)^C)^j$ in the Lagrangian, since it is both Lorentz- and gauge-invariant. This

---

[10] Actually, this problem generally exists in $(3+N)\nu$ models [102].

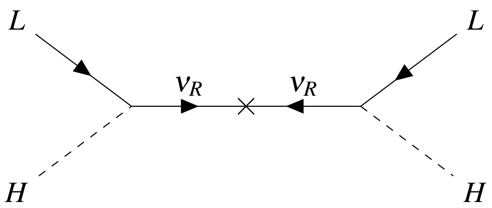

Figure 2.3: Feynman diagram for the type-I seesaw mechanism.

term is commonly referred to as the *Majorana mass term.* This consideration, however, leads to a different kind of mechanism, the so-called *type-I seesaw mechanism*, presented in Section 2.2.2.

Despite all these considerations, the Higgs mechanism for the generation of Dirac neutrino masses is a perfectly valid and indeed *technically natural* approach[11].

2.2.2 The Type-I Seesaw Mechanism

Additionally to the operator presented in Eq. (2.2.1), the introduction of a right-handed gauge singlet field allows for another Lorentz- and gauge-invariant term in the Lagrangian

$$\mathcal{L}_{\text{mass}} \supset -(M^\nu)_{ij}\overline{\nu_L}^i\nu_R^j - \frac{1}{2}(M_M^\nu)_{ij}\overline{\nu_R}^i((\nu_R)^C)^j + \text{h.c.}\,, \tag{2.2.3}$$

where $(\nu_R)^C = C\,\overline{\nu_R}^T$ is the charge conjugate of ν_R and M_M^ν is the so-called *Majorana mass matrix.* In the following, we derive an explicit expression for the active neutrino masses, which are induced by the Feynman diagram depicted in Figure 2.3.

For further details on the transformation properties of the charge conjugation operator C see Appendix A.2. The Majorana mass term is trivially gauge invariant, since the right-handed neutrino is a gauge singlet[12] and it is also Lorentz-invariant because $(\nu_R)^C$ is effectively a left-handed field. Writing this in a more compact way using the composite vector $\vec{\nu} = \begin{pmatrix}\vec{\nu}_L \\ \vec{\nu}_R^C\end{pmatrix}$, matrix notation and suppressing flavor indices, we arrive at

$$\mathcal{L}_{\text{mass}} \supset -\frac{1}{2}\overline{\vec{\nu}^C} M\,\vec{\nu} + \text{h.c.}\,, \tag{2.2.4}$$

$$\text{with } M = \begin{pmatrix} 0 & (M^\nu)^T \\ M^\nu & M_M^\nu \end{pmatrix}\,, \tag{2.2.5}$$

where $\vec{\nu}_L$ is a three-dimensional vector with the generation entries ν_L^i and $\vec{\nu}_R^C$ is an n-dimensional vector with the entries $((\nu_R)^C)^j$ for each generation, effectively rendering $\vec{\nu}$ a $(3{+}n)$-dimensional vector. A diagonalization of the matrix M leads to the identification of the neutrino mass eigenstates ν_m^i and the corresponding mass eigenvalues m_i^ν. Since we require M to be hermitian, we can always diagonalize it with a unitary matrix U^ν such that

$$(U^\nu)^\dagger\vec{\nu} \equiv \vec{\nu}_m\,. \tag{2.2.6}$$

To better illustrate the principles of the seesaw mechanism, we present the simple one-plus-one-generational case in the following, in which we assume the Majorana mass $M_{(M)}^\nu$ to be real.

---

[11] Technical naturalness, as defined by 't Hooft [107], is a property of a small parameter, which, when taken to zero, restores a higher symmetry of the theory. Sometimes, this rule is also reformulated as 'The β-function of a technically natural parameter is proportional to the parameter itself'.

[12] This property leads to the term 'sterile' sometimes used in the literature.

In this simple case, the unitary rotation matrix can be parametrized as

$$U = \begin{pmatrix} \cos\theta & \sin\theta \\ -\sin\theta & \cos\theta \end{pmatrix} \tag{2.2.7}$$

with the mixing angle θ given by

$$\tan 2\theta = \frac{2M^\nu}{M_M^\nu} \tag{2.2.8}$$

and the mass eigenvalues are

$$m_{1,2}^\nu = \frac{1}{2} M_M^\nu \mp \sqrt{\left(\frac{M_M^\nu}{2}\right)^2 + (M^\nu)^2}\,. \tag{2.2.9}$$

Rewriting Eq. (2.2.3) (or Eq. (2.2.4) for that matter), we obtain

$$\mathcal{L}_{\text{mass}} \supset -\frac{1}{2}\left(m_1^\nu\, \overline{(\nu_m^1)^C}\nu_m^1 + m_2^\nu\, \overline{(\nu_m^2)^C}\nu_m^2\right)\,. \tag{2.2.10}$$

In this equation it becomes apparent that both masses m_1^ν and m_2^ν are Majorana masses. This means that conversely to the mechanism presented in Section 2.2.1, the light neutrino masses are of the Majorana type.

In the limit $M_M^\nu \gg M^\nu$, which is the reason for the name *seesaw mechanism*, we approximately obtain the results

$$\theta \approx \frac{M^\nu}{M_M^\nu}\,, \tag{2.2.11}$$

$$m_1^\nu \approx -\frac{(M^\nu)^2}{M_M^\nu}\,, \tag{2.2.12}$$

$$m_2^\nu \approx M_M^\nu\,, \tag{2.2.13}$$

where the mixing angle θ is small and thus the mass eigenstates are either predominantly active (left-handed) or predominantly sterile (right-handed). m_1^ν belongs to the light, predominantly active neutrinos because of the suppression by the heavy Majorana mass, while m_2^ν belongs to the heavy, predominantly sterile neutrinos.

Since the Majorana mass M_M^ν is not protected by any symmetry because the right-handed neutrinos ν_R^i are gauge singlets, quantum corrections are expected to be proportional to the scale of NP particles running in the loop, e.g. the GUT scale at $\sim \mathcal{O}(10^{16}\,\text{GeV})$ or even the Planck scale M_{Pl}. This is a good justification for the seesaw condition, but it also allows the neutrino Yukawa couplings Y_{ij}^ν to be of order unity.

2.2.3 Beyond Type-I Seesaw

In ignorance of a ultraviolet (UV) realization, a neutrino mass term can e.g. be constructed from the dimension-5 Weinberg operator

$$\mathcal{L}_{\text{dimension}-5} = \frac{\mathcal{C}^{ij}}{\Lambda}\left(\overline{L_i^C}\tilde{H}^*\right)\left(\tilde{H}^\dagger L_j\right) \tag{2.2.14}$$

in an Effective Field Theory (EFT) approach, where Λ is the scale of NP and $\mathcal{C}^{ij}$ are the Wilson coefficients, which encompass the information about the UV-theory. Note that the Weinberg

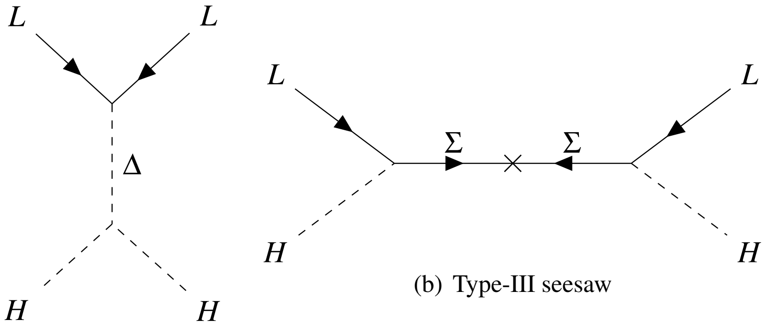

(a) Type-II seesaw

(b) Type-III seesaw

Figure 2.4: Feynman diagrams for the type-II and type-III seesaw mechanisms.

operator violates lepton number by two units ($\Delta L = 2$). However, the global $U(1)_L$ symmetry is only an *accidental symmetry* in the SM and thus lepton number violation does not violate the fundamental principles of a QFT.

In fact, the type-I seesaw mechanism presented in Section 2.2.2 is the most minimal UV realization of this operator, adding a fermionic singlet to the SM field content. Moreover, there are two more minimal realizations on tree-level, where only one additional field has to be added to the SM field content. These models are commonly called *type-II* and *type-III seesaw*. Loop-induced neutrino masses are shortly discussed in Section 2.2.4. In the case of the type-II seesaw, a heavy scalar $SU(2)_L$-triplet Δ is introduced, whereas in the type-III seesaw case a fermionic $SU(2)_L$-triplet Σ is introduced. Figure 2.4 shows the Feynman diagrams responsible for neutrino mass generation in these models.

The Yukawa part of the Lagrangian in the type-II seesaw reads [108, 109]

$$\mathcal{L}_{\text{Yuk}} = -\left(Y^{\Delta}\right)_{ij} \overline{L^C}^{i} \mathrm{i}\sigma_2 \Delta L^j + \text{h.c.}\,, \tag{2.2.15}$$

where $\Delta = \begin{pmatrix} \Delta^+/\sqrt{2} & \Delta^{++} \\ \Delta^0 & -\Delta^+/2 \end{pmatrix}$ is the newly introduced scalar triplet field with hypercharge 1. Since this model has an extended scalar sector, the scalar potential obtains additional terms

$$\begin{aligned} V(H,\Delta) \supset &+ M_\Delta^2 \operatorname{Tr}(\Delta^\dagger \Delta) + (\mu H^T \mathrm{i}\sigma_2 \Delta^\dagger H + \text{h.c.}) + \lambda_1 H^\dagger H \operatorname{Tr}(\Delta^\dagger \Delta) \\ &+ \lambda_2 (\operatorname{Tr}(\Delta^\dagger \Delta))^2 + \lambda_3 \operatorname{Tr}((\Delta^\dagger \Delta)^2) + \lambda_4 (H^\dagger \Delta)(\Delta^\dagger H)\,, \end{aligned} \tag{2.2.16}$$

where the couplings $\lambda_{1,2,3,4}, \mu$ can be w.l.o.g. assumed to be real. Once EWSB occurs and Δ and H acquire the non-zero vevs v_Δ and v_H in the neutral components, the neutrinos obtain a mass of [109]

$$m_\nu \approx Y^{\Delta} \sqrt{2} v_\Delta \approx \frac{Y^{\Delta} \mu v^2}{M_\Delta^2}\,. \tag{2.2.17}$$

Note that in general the EW vev v is a pythagorean sum of the vevs of H and Δ. However, v_Δ is constrained to be less than a few GeV, since it otherwise spoils the ratio of the gauge boson masses, sometimes parametrized with $\rho = M_W^2/\cos^2\theta_W M_Z^2 \approx 1$.

As Eq. (2.2.17) suggests, the neutrino mass is suppressed by two powers of the triplet scalar's mass, hence the label of a seesaw model.

In contrast to the type-I seesaw scenario, this model predicts charged scalars beyond the SM Higgs boson, which could in principle be produced at colliders. Depending on the magnitude of the vev v_Δ, signatures like same-sign dilepton decay channels ($Y^\Delta \sim \mathcal{O}(1)$) or lepton flavor violation (LFV), e.g. $\mu \to 3e$, can become observable [108].

The type-III seesaw mechanism is structurally similar to the type-I seesaw presented in Section 2.2.2, since the singlet and triplet fermions both induce the mass via virtually the same Feynman diagram, but with different couplings. The Lagrangian responsible for the mass generation reads

$$\mathcal{L}_\text{mass} = -\left(Y^\Sigma\right)_{ij} \overline{\Sigma}^i \sqrt{2}\tilde{H}^\dagger L^j - \frac{1}{2}\operatorname{Tr}\left(\overline{\Sigma} M_\Sigma \Sigma^C\right) + \text{h.c.}\,, \tag{2.2.18}$$

where $\Sigma = \begin{pmatrix} \Sigma^0/\sqrt{2} & \Sigma^+ \\ \Sigma^- & -\Sigma^0/2 \end{pmatrix}$ is the triplet fermion with vanishing hypercharge and M_Σ is the Majorana mass.

Because the mechanism is the same, the light neutrino mass follows the same pattern as in Eq. (2.2.12)

$$m_\nu \approx -\frac{(M^\nu)^2}{M_\Sigma}\,. \tag{2.2.19}$$

Since the triplet, conversely to the singlet fermions in the type-I seesaw, does directly interact with the gauge bosons due to it's non-trivial representation under $SU(2)_L$, Σ particles could e.g. be directly produced at the colliders [110, 111, 112]. This way, the parameters in this model can be constrained more tightly than in the type-I seesaw. The current lower limits at 95% confidence level on the heavy lepton mass is 790 GeV set by the ATLAS collaboration [113].

2.2.4 Radiative Neutrino Masses

In the previous sections, we focused the discussions on tree-level realizations of the Weinberg operator given in Eq. (2.2.14). However, neutrino masses can also be generated on loop-level. This class of models is often called *radiative neutrino mass models*. In these models, the smallness of the neutrino masses is partly explained by a loop suppression. A detailed review of radiative neutrino mass models can e.g. be found in [104].

One famous representative of these models is the *scotogenic model* [114]. In this model, the additional fields are three generations of fermionic gauge singlets N_i as well as a scalar $SU(2)_L$-doublet η with hypercharge $1/2$. All newly introduced field are also oddly charged under a discrete $\mathcal{Z}_2$ symmetry, whereas all SM fields are evenly charged. This symmetry forbids the standard Yukawa couplings with the SM Higgs field, hence preventing neutrinos from picking up a tree-level generated mass. The fermionic Lagrangian of the scotogenic model reads

$$\mathcal{L} \supset -\left(Y^N\right)_{ij} \overline{N}^i \eta L^j - \frac{1}{2}\left(M_N\right)_i \overline{N^C}^i N^i + \text{h.c.} \tag{2.2.20}$$

and the scalar potential yields

$$\begin{aligned} V(H,\eta) = -m_H^2 H^\dagger H + m_\eta^2 \eta^\dagger \eta + \frac{\lambda_1}{2}\left(H^\dagger H\right)^2 + \frac{\lambda_2}{2}\left(\eta^\dagger \eta\right)^2 + \lambda_3\left(H^\dagger H\right)\left(\eta^\dagger \eta\right) \\ + \lambda_4\left(H^\dagger \eta\right)\left(\eta^\dagger H\right) + \frac{\lambda_5}{2}\left[\left(H^\dagger \eta\right)^2 + \left(\eta^\dagger H\right)^2\right]. \end{aligned} \tag{2.2.21}$$

The neutrino masses, which are radiatively generated via the Feynman diagram depicted in

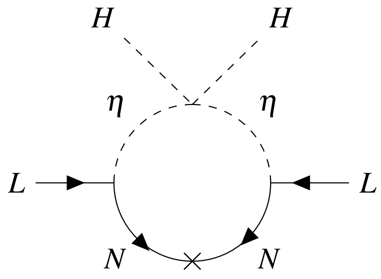

Figure 2.5: Feynman diagram for the neutrino mass generation in the scotogenic model.

Figure 2.5 in this model are given by

$$\begin{aligned}(M^{\mu})_{ij} = &\sum_k \frac{\left(Y^N\right)_{ki}\left(Y^N\right)_{kj}}{32\pi^2}\,(M_N)_k \\ &\times\left[\frac{m_{\eta^0}^2}{m_{\eta^0}^2-(M_N)_k^2}\ln\left(\frac{m_{\eta^0}^2}{(M_N)_k^2}\right)-\frac{m_{\eta'^0}^2}{m_{\eta'^0}^2-(M_N)_k^2}\ln\left(\frac{m_{\eta'^0}^2}{(M_N)_k^2}\right)\right],\end{aligned} \tag{2.2.22}$$

where m_{η^0} and $m_{\eta'^0}$ are the masses of the neutral scalar degrees of freedom that can expressed as

$$\begin{aligned} m_{\eta^0}^2 &= m_\eta^2 + \frac{v^2}{2}(\lambda_3+\lambda_2+\lambda_5) \\ m_{\eta'^0}^2 &= m_\eta^2 + \frac{v^2}{2}(\lambda_3+\lambda_2-\lambda_5)\,. \end{aligned} \tag{2.2.23}$$

Furthermore, note that Eq. (2.2.23) suggests that the neutral scalar masses are degenerate for a vanishing λ_5, which in turn leads to vanishing neutrino masses following Eq. (2.2.22). This is due to the cancellation of the diagrams involving η^0 and ${\eta'}^0$, which contribute with opposite sign.

In the case where $m_{\eta^0}^2 - m_{\eta'^0}^2 \ll m_{\eta^0}^2 + m_{\eta'^0}^2 \wedge m_{\eta^0}^2 + m_{\eta'^0}^2 \approx (M_N)_k^2$, we obtain

$$(M^\nu)_{ij} \approx \frac{\lambda_5 v^2}{2\cdot 16\pi^2}\sum_k \frac{\left(Y^N\right)_{ki}\left(Y^N\right)_{kj}}{(M_N)_k}\,, \tag{2.2.24}$$

where $m_{\eta^0}^2 - m_{\eta'^0}^2 = \lambda_5 v^2$.

The neutrino masses in Eq. (2.2.24) exhibit the same behavior as a type-I(III) seesaw mechanism, with an additional typical loop suppression factor. Due to this factor the viable parameter space is enlarged to with regards to the Yukawa couplings.

Note that there is a link between neutrino masses and DM in the scotogenic model[13]. The $\mathcal{Z}_2$ symmetry imposed in the model does not only prohibit tree-level Yukawa couplings with the SM Higgs, but it also stabilizes the lightest $\mathcal{Z}_2$-odd particle so that it qualifies as a potential DM candidate.

Besides others, radiative neutrino mass models that have generated interest of the community are e.g. the Zee model [115, 116] (one-loop, two additional scalars), the Zee-Babu model

---

[13] In fact, the scotogenic model received its name from the greek words σκότος (*scotos, eng.: darkness*) and γενής (*genes, eng.: offspring, kind*), meaning *generated by darkness.*

[117, 118] (two-loop, two additional scalars) and the Krauss-Nasri-Trodden model [119] (three-loop, two scalars and one fermionic singlet). We do not, however, discuss the details of these models in this work.

2.3 Dark Matter Theory

In this section, we present the fundamentals of WIMPs as a class of DM candidates. We discuss details of thermal production in the early universe as well as the physics of detection via direct and indirect searches of such a DM candidate.

2.3.1 Early Universe Thermodynamics

First of all, we introduce the important concepts of thermodynamics in the early universe to be able to formulate expressions for the production of DM. We base this discussion on [16, 120, 121, 122, 123, 124].

When speaking about the thermodynamics of the early universe, we need to define some characteristic quantities that sufficiently describe the state of the universe at any given point in time. Besides the temperature T, we also require a measure for the abundance of particles of a certain species. We therefore define the *phase space density* $f(\vec{x},t,\vec{p},E)$ [14]. In the case of *kinetic equilibrium*, i.e. for efficient energy transfer between particles in the plasma, this density can be approximated by their respective equilibrium distribution

$$f^{\mathrm{eq}}(E,t) = \frac{1}{\exp\left(\frac{E-\mu}{T}\right) \pm 1} \tag{2.3.1}$$

where $+1$ denotes *Fermi-Dirac distribution* (fermions) and -1 denotes *Bose-Einstein* (bosons) distribution and μ denotes the *chemical potential*, which usually is associated with a particular charge. Additionally, the number density n_k of a particle species k and its first moment, the density ρ_k are defined as

$$n_k = \frac{g_k}{(2\pi)^3} \int \mathrm{d}^3 p_k \, f_k(E_k,t)\,, \tag{2.3.2}$$

$$\rho_k = \frac{g_k}{(2\pi)^3} \int \mathrm{d}^3 p_k \, E \, f_k(E_k,t)\,, \tag{2.3.3}$$

where g_k are the *internal degrees of freedom* of the particle species in question. Using the definitions of the Fermi-Dirac and Bose-Einstein distributions from Eq. (2.3.1) and a coordinate transformation into spherical coordinates $\mathrm{d}p^3 \to \mathrm{d}p\,\mathrm{d}\Omega\,p^2$, the number density and mass-energy density yield

$$n_k = g_k T^3 \cdot \begin{cases} \zeta(3)/\pi^2 & \text{Bose-Einstein} \\ 3\zeta(3)/4\pi^2 & \text{Fermi-Dirac} \end{cases} \tag{2.3.4}$$

$$\rho_k = g_k T^4 \cdot \begin{cases} \pi^2/30 & \text{Bose-Einstein} \\ 7\pi^2/8\cdot 30 & \text{Fermi-Dirac} \end{cases} \tag{2.3.5}$$

for relativistic matter, where $\zeta(x)$ denotes the *Riemann ζ-function*. The assumption $E \gg m_k$ is justified in a radiation-dominated era, which is guaranteed before and during the formation

---

[14] Since we assume a FLRW universe, the phase space density f must be spacially homogeneous and isotropic and therefore does not depend on $\vec{x}$ and $\vec{p}$.

of the CMB in standard cosmological history. Note that based on Eq. (2.3.5) the *number of relativistic degrees of freedom* g_* can be defined as

$$g_*(T) = \sum_{b\in\text{bosons}} g_b \frac{T_b^4}{T^4} + \frac{7}{8} \sum_{f\in\text{fermions}} g_f \frac{T_f^4}{T^4} , \tag{2.3.6}$$

where T is the temperature of the thermal bath and T_i the temperature of the individual species. The relations in Eqs. (2.3.4) and (2.3.5) additionally rely on *thermal equilibrium*, which is achieved if kinectic equilibrium and *chemical equilibrium*

$$\sum_{i\in\text{initial states}} \mu_i = \sum_{f\in\text{final states}} \mu_f , \tag{2.3.7}$$

are simultaneously attained. In all models described in Chapter 4, this criterion is trivially fulfilled, as all chemical potentials are negligible due to the absence of particle asymmetries. Furthermore, we can define the *Boltzmann distribution*

$$f^{\text{eq}}(E,T) = \exp\left(-\frac{E-\mu}{T}\right) , \tag{2.3.8}$$

which approximates both the Fermi-Dirac and Bose-Einstein distributions in the limit ${}^{(E-\mu)}/{}_{T} \gg 1$. This limit applies to a good degree, as according to the *equipartition theorem* the average energy is $\langle E\rangle \sim 3T$. This enables us to neglect the slight differences of fermions and bosons from this point on. Due to the implications of the discussion of the chemical potential above, we can further approximate Eq. (2.3.8) to

$$f^{\text{eq}}(E,t) = \exp\left(-\frac{E}{T}\right) . \tag{2.3.9}$$

In general, we are particularly interested in the evolution in time of the quantities mentioned above, which are governed by the *Boltzmann equations*. These equations are generally written as

$$\hat{L}[f_k] = \hat{C}[f] , \tag{2.3.10}$$

where

$$\begin{aligned} \hat{L} &= p_k^\alpha \partial_\alpha - \Gamma^\alpha_{\beta\gamma} p_k^\beta p_k^\gamma \frac{\partial}{\partial p^\alpha} \\ \Rightarrow \hat{L}[f_k] &= E_k\, \partial_t f_k(E_k,t) - H(t) |\vec{p}_k|^2 \partial_{E_k} f_k(E_k,t) \end{aligned} \tag{2.3.11}$$

is the *Liouville operator* for the FLRW spacetime and $\hat{C}$ is the *collision operator*. Generally, the Liouville operator takes into account the spacetime effects on the change of phase space distribution, whereas the collision operator takes into account all changes from potential particle interactions. Note here that f_k is the phase space distribution of the species k in question, whereas f entails the phase space distributions for all particles that appear in collisions. Using the definition in Eq. (2.3.2), dividing by E_k, and integration by parts, a more evocative form can be formulated

$$\frac{\mathrm{d}n_k(t)}{\mathrm{d}t} + 3H(t) n_k(t) = \frac{g_k}{(2\pi)^3} \int \mathrm{d}^3 p_k \, \frac{\hat{C}[f]}{E_k} . \tag{2.3.12}$$

It becomes apparent that in the case where no collisions take place, the number density is diluted due to the expansion of the universe, while the absolute number of particles is a conserved quantity as

$$\begin{aligned} 0 &= \frac{\mathrm{d}n_k(t)}{\mathrm{d}t} + 3H(t)n_k(t) \\ &= \frac{\mathrm{d}n_k(t)}{\mathrm{d}t}a(t)^3 + 3n_k(t)\frac{\mathrm{d}a(t)}{\mathrm{d}t}a(t)^2 = \frac{\mathrm{d}(a(t)^3 n_k(t))}{\mathrm{d}t} \\ &= \frac{\mathrm{d}N_k}{\mathrm{d}t}\,. \end{aligned} \tag{2.3.13}$$

The Friedmann Equation (1.2.8) allows us to write the Hubble parameter H in terms of the mass-energy density as

$$H = \sqrt{\frac{8\pi G}{3}\rho} = \sqrt{\frac{8\pi^3}{90}\cdot\frac{g_*(T)}{M_{\mathrm{Pl}}^2}}\cdot T^2\,, \tag{2.3.14}$$

where $M_{\mathrm{Pl}} = {}^1\!/\!\sqrt{G} \approx 1.2\cdot 10^{19}\,\mathrm{GeV}$ is the *Planck mass.*

Neglecting effects such as *Pauli blocking* and *stimulated emission*, the collision term on the right hand side of Eq. (2.3.12) can be written as

$$\begin{aligned} \frac{g_k}{(2\pi)^3}\int \mathrm{d}p_k^3 \frac{\hat{C}[f]}{E_k} &= -\int \frac{g_k}{(2\pi)^3}\frac{\mathrm{d}^3 p_k}{2E_k}\prod_{a\in\text{all}}\frac{g_a}{(2\pi)^3}\frac{\mathrm{d}^3 p_a}{2E_a} \\ &\times (2\pi)^4\delta^{(4)}\left(p_k + \sum_{i\in\text{initial}} p_i - \sum_{f\in\text{final}} p_f\right)|\mathcal{M}_{\text{process}}|^2\left(f_k\prod_{i\in\text{initial}} f_i - \prod_{f\in\text{final}} f_f\right)\,, \end{aligned} \tag{2.3.15}$$

for the CP conserving process $k + \sum_{i\in\text{initial states}} i \rightarrow \sum_{f\in\text{final states}} f$, where the initial states are counted excluding the particle k in question[15]. Within Eq. (2.3.15), the delta distribution $\delta^{(4)}$ takes care of momentum conservation. Note here that potential symmetry factors are absorbed into the matrix element $\mathcal{M}$, while, conversely to a collider setup, both initial and final spin states are summed over.

As our primary concern is the time evolution of particle densities in a *comoving* volume, it is beneficial to define a quantity describing the particle density while not being affected by the expansion of the universe. For this purpose, we define the *yield* as

$$Y_k \equiv \frac{n_k}{s}\,, \tag{2.3.16}$$

where s is the entropy density

$$s = \frac{2\pi^2 g_{*s}(T)}{45}T^3\,. \tag{2.3.17}$$

The *entropy degrees of freedom* g_{*s} are defined analogously to the number of relativistic degrees of freedom (cf. Eq. (2.3.6)) as

$$g_{*s}(T) = \sum_{b\in\text{bosons}} g_b\frac{T_b^3}{T^3} + \frac{7}{8}\sum_{f\in\text{fermions}} g_f\frac{T_f^3}{T^3}\,. \tag{2.3.18}$$

---

[15] The more general form assuming Fermi-Dirac/Bose-Einstein distributions and potential CP non-conservation are described in [120, 16].

Furthermore, it is convenient for numerical calculations to define a dimensionless variable x that acts as a measure of time in the Boltzmann equation. The typical definition of this quantity is

$$x \equiv \frac{m_k}{T}\,, \tag{2.3.19}$$

where m_k is the mass of the particle in question[16].

In order to rewrite the Boltzmann equation in these variables, we use the conservation of entropy

$$\frac{\mathrm{d}S}{\mathrm{d}t} = \frac{\mathrm{d}(sa^3)}{\mathrm{d}t} \Rightarrow \frac{\mathrm{d}s}{\mathrm{d}t} = -3Hs \tag{2.3.20}$$

$$\Rightarrow \mathrm{d}t = \frac{1}{-3Hs}\frac{\mathrm{d}s}{\mathrm{d}T}\mathrm{d}T\,, \tag{2.3.21}$$

and also

$$\mathrm{d}T = -\frac{m_k}{x^2}\mathrm{d}x\,, \tag{2.3.22}$$

which leads to a formulation of the Boltzmann equation given by

$$\begin{aligned}\frac{\mathrm{d}Y_k}{\mathrm{d}x} &= -\frac{m_k}{3Hs^2x^2}\frac{\mathrm{d}s}{\mathrm{d}T}\int \frac{g_k}{(2\pi)^3}\frac{\mathrm{d}^3p_k}{2E_k}\prod_{a\in\mathrm{all}}\frac{g_a}{(2\pi)^3}\frac{\mathrm{d}^3p_a}{2E_a} \\ &\times(2\pi)^4\delta^{(4)}\left(p_k + \sum_{i\in\mathrm{initial}} p_i - \sum_{f\in\mathrm{final}} p_f\right)|\mathcal{M}_{\mathrm{process}}|^2\left(f_k\prod_{i\in\mathrm{initial}} f_i - \prod_{f\in\mathrm{final}} f_f\right)\,.\end{aligned} \tag{2.3.23}$$

2.3.2 Thermal Production of Dark Matter

In this section, we aim to calculate an expression for the DM yield today.

For all interaction rates Γ that are higher than the rate of the universe's expansion H, DM stays in strong thermal contact with the plasma and thus follows its equilibrium distribution. For the relic abundance to not be vanishingly small, DM must decouple from the thermal plasma as soon as $x \approx \mathcal{O}(10)$, as the equilibrium density in the non-relativistic limit is exponentially suppressed and the density thus depletes strongly if DM is kept in thermal equilibrium for longer. The decoupling from the thermal plasma is commonly called *freeze out* and typically occurs when the interaction rate drops below the Hubble rate

$$\Gamma < H\,. \tag{2.3.24}$$

For simplicity, we focus on 2-body annihilation processes in the following discussion, where two DM particles χ annihilate into two SM particles ψ ($\bar{\chi}\chi \leftrightarrow \bar{\psi}\psi$). In this case, it is a very good assumption that all SM particles are in thermal equilibrium $f_\psi = f_\psi^{\mathrm{eq}}$. Moreover, we assume kinetic equilibrium $f_\chi = \alpha \cdot f_\chi^{\mathrm{eq}}$ for χ. The energy conservation enforced by the δ function within the collision term of the Boltzmann equation leads to the so-called principle of *detailed balance*

$$f_{\bar{\psi}}f_\psi = f_{\bar{\psi}}^{\mathrm{eq}}f_\psi^{\mathrm{eq}} = \exp\left(-\frac{E_{\bar{\psi}}+E_\psi}{T}\right) = \exp\left(-\frac{E_{\bar{\chi}}+E_\chi}{T}\right) = f_{\bar{\chi}}^{\mathrm{eq}}f_\chi^{\mathrm{eq}}\,. \tag{2.3.25}$$

---

[16] Note that in the case of multiple coupled Boltzmann equations, we define x with the mass scale of one of the particles in questions (typically the DM mass).

With these premises, we can write the r.h.s. of Eq. (2.3.23) as

$$
\begin{aligned}
\frac{\mathrm{d}Y_k}{\mathrm{d}x} &= -\frac{m_k}{3Hx^2}\frac{\mathrm{d}s}{\mathrm{d}T}\langle\sigma v\rangle\left(Y_k^2 - (Y_k^{\mathrm{eq}})^2\right) && (2.3.26)\\
&= -\sqrt{\frac{\pi}{45}}\frac{M_{\mathrm{Pl}}\, m_k\, g_{*,\mathrm{eff}}^{\frac{1}{2}}}{x^2}\langle\sigma v\rangle\left(Y_k^2 - (Y_k^{\mathrm{eq}})^2\right)\,, && (2.3.27)
\end{aligned}
$$

where

$$
g_{*,\mathrm{eff}}^{\frac{1}{2}} \equiv \frac{g_{*,s}}{\sqrt{g_*}}\left(1 + \frac{T}{3g_{*,s}}\frac{\mathrm{d}g_{*,s}}{\mathrm{d}T}\right) \tag{2.3.28}
$$

is a combined function of the energy degrees of freedom g_* and the entropy degrees of freedom $g_{*,s}$. Furthermore, $\langle\sigma v\rangle$ is the *thermally averaged annihilation cross section*

$$
\begin{aligned}
\langle\sigma v\rangle \equiv \frac{1}{(n_\chi^{\mathrm{eq}})^2}\int & \frac{g_{\bar\chi}}{(2\pi)^3}\frac{\mathrm{d}^3p_{\bar\chi}}{2E_{\bar\chi}}\cdot\frac{g_\chi}{(2\pi)^3}\frac{\mathrm{d}^3p_\chi}{2E_\chi}\cdot\frac{g_{\bar\psi}}{(2\pi)^3}\frac{\mathrm{d}^3p_{\bar\psi}}{2E_{\bar\psi}}\cdot\frac{g_\psi}{(2\pi)^3}\frac{\mathrm{d}^3p_\psi}{2E_\psi}\\
&\times(2\pi)^4\delta^{(4)}\left(p_{\bar\chi}+p_\chi-p_{\bar\psi}-p_\psi\right)|\mathcal{M}|^2 f_{\bar\psi}^{\mathrm{eq}} f_\psi^{\mathrm{eq}}\,.
\end{aligned} \tag{2.3.29}
$$

In this context, the velocity $v = v_{\mathrm{Møller}} = \sqrt{|\vec v_1 - \vec v_2|^2 + |\vec v_1 \times \vec v_2|^2}$ is the *Møller velocity*, which is defined so that the product $v_{\mathrm{Møller}} n_1 n_2$ is Lorentz-invariant.

Note that in the general case, where the particle pair $\bar\psi\psi$ is a large set, we simply replace the single-process annihilation cross section with the total annihilation cross section.

In its temperature dependent form, $\langle\sigma v\rangle$ can be written as

$$
\begin{aligned}
\langle\sigma v\rangle(T) &= \frac{\int \mathrm{d}p_{\bar\chi}^3\mathrm{d}p_\chi^3\,\sigma v\exp\left(-{}^{(E_{\bar\chi}+E_\chi)}/_{T}\right)}{\int \mathrm{d}p_{\bar\chi}^3\mathrm{d}p_\chi^3\exp\left(-{}^{(E_{\bar\chi}+E_\chi)}/_{T}\right)}\\
&= \frac{1}{8m_\chi^4 T K_2^2\left(\frac{m_\chi}{T}\right)}\int_{4m_\chi^2}^{\infty}\mathrm{d}s\,\sigma(1-4m^2)\sqrt{s}K_1\left(\frac{\sqrt{s}}{T}\right)\,,
\end{aligned} \tag{2.3.30}
$$

where $\sqrt{s}$ is the center of mass energy and $K_i(x)$ is the *modified Bessel function* of order i.

As mentioned in the beginning of this section, we are mainly interested in freeze out temperatures at $\sim x = \mathcal{O}(10)$, meaning that the DM particles can be considered cold (non-relativistic). In this case, we can expand σv in powers of v^2, which can be related to an expansion of the thermally averaged cross section in powers of ${}^1/_x$ as

$$
\langle\sigma v\rangle = \left\langle a + bv^2 + cv^4 + \mathcal{O}\left(v^6\right)\right\rangle = a + \frac{3}{2}b\cdot\frac{1}{x} + \frac{15}{8}c\cdot\frac{1}{x^2} + \mathcal{O}\left(\frac{1}{x^3}\right)\,. \tag{2.3.31}
$$

The thermally averaged annihilation cross section is often approximated by its leading order contribution $\langle\sigma v\rangle \sim \sigma_0 x^{-n}$, where $n = 0$ corresponds to s-wave annihilation, $n = 1$ to p-wave, $n = 2$ to d-wave and so forth.

At this point, the Boltzmann equation can be solved numerically, e.g. with solvers such as MICROMEGAS [125, 126], which we use in Chapter 4, or MADDM [127]. In order to solve the resulting Boltzmann equation analytically to obtain parametric estimates, we assume the entropy degrees of freedom $g_{*,s}$ to be constant so that $g_{*,\mathrm{eff}}^{\frac{1}{2}} = {}^{g_{*,s}}/_{\sqrt{g_*}}$ and parametrize the departure from equilibrium as

$$
\Delta \equiv Y - Y^{\mathrm{eq}}\,. \tag{2.3.32}
$$

Inserting these premises into Eq. (2.3.27), we obtain

$$\frac{\mathrm{d}\Delta}{\mathrm{d}x} = -\frac{\mathrm{d}Y^{\mathrm{eq}}}{\mathrm{d}x} - \lambda x^{-n-2}(\Delta^2 + 2Y^{\mathrm{eq}}\Delta)\,, \tag{2.3.33}$$

where $\lambda \equiv \sqrt{\frac{\pi}{45}}\frac{M_{\mathrm{Pl}} m_\chi g_{*s}}{\sqrt{g_*}}\sigma_0$. It is justified to assume that at times $x \ll x_f$ before the freeze out, the DM yield follows its equilibrium distribution and thus Δ^2 and ${}^{\mathrm{d}\Delta}/_{\mathrm{d}x}$ are small. We obtain

$$\Delta \approx -\frac{\mathrm{d}Y^{\mathrm{eq}}}{\mathrm{d}x} \cdot \frac{x^{n+2}}{Y^{\mathrm{eq}} 2\lambda} \tag{2.3.34}$$

$$\overset{{}^{\mathrm{d}}/_{\mathrm{d}x} Y^{\mathrm{eq}} \approx -Y^{\mathrm{eq}}}{\Rightarrow} \quad \Delta_f \approx \frac{x_f^{n+2}}{2\lambda}\,. \tag{2.3.35}$$

For times $x \gg x_f$ after the freeze-out time, the departure from equilibrium can be well approximated as the yield itself, since the equilibrium yield is exponentially suppressed and therefore small. We thus obtain

$$\frac{\mathrm{d}\Delta}{\mathrm{d}x} \approx -\lambda x^{-n-2}\Delta^2\,, \tag{2.3.36}$$

which can be solved via separation of variables and subsequent integration. Using the expression for Δ_f from Eq. (2.3.35), we arrive at

$$Y_\infty \approx \Delta_\infty \approx \left(\frac{\lambda}{n+1} x_f^{-n-1} + 2\lambda x^{-n-2}\right)^{-1}\,. \tag{2.3.37}$$

The literature result [16]

$$Y_\infty \approx \frac{n+1}{\lambda} x_f^{n+1} \tag{2.3.38}$$

$$\Omega_{\mathrm{DM}} h^2 \approx \frac{m_\chi Y_\infty s_0 h^2}{\rho_{\mathrm{crit}}} \tag{2.3.39}$$

for the relic yield Y_∞ and the relic density $\Omega_{\mathrm{DM}} h^2$ can be obtained by the approximation of a small Δ_f, which is justified for typical freeze-out times $x_f \sim 20$. We define the freeze-out time x_f as the time when Δ becomes roughly of the order of the equilibrium yield Y^{eq} itself, indicating a significant deviation from equilibrium. We obtain the condition

$$\Delta(x_f) = k \cdot Y^{\mathrm{eq}}\,, \tag{2.3.40}$$

where k is a constant of $\mathcal{O}(1)$. Numerical solutions have shown that a result within 5% accuracy can be reached with the choice of $k(k+2) = n+1$ and we obtain

$$\begin{aligned} x_f = \ln\left[0.038(n+1)\frac{g_\chi M_{\mathrm{Pl}} m_\chi \sigma_0}{\sqrt{g_*}}\right] \\ -\left(n+\frac{1}{2}\right)\ln\left[\ln\left(0.038(n+1)\frac{g_\chi M_{\mathrm{Pl}} m_\chi \sigma_0}{\sqrt{g_*}}\right)\right]. \end{aligned} \tag{2.3.41}$$

The results presented in Eq. (2.3.38)-(2.3.41) are good approximations for most phenomenological applications in thermal DM models. However, if a model contains additional unstable dark sector particles, the annihilation cross section can be severely enhanced if the mass of these particles is within ~ 20% of the DM mass. This effect is known as *coannihilation* [128, 129] and is an important feature of the model classes discussed in Chapter 4 [17]. Considering N dark sector species χ_i, $i = 0,1,2,...,N-1$, where χ_0 is the DM candidate, the types of number changing processes can be

$$\begin{array}{lrl} \text{a)} & \chi_i\chi_j \to \psi\psi' & \text{annihilation,} \\ \text{b)} & \chi_i + \psi \to \chi_j + \psi' & \text{conversion,} \\ \text{c)} & \chi_{i\neq 0} \to \chi_j + \psi & \text{decay,} \end{array} \tag{2.3.42}$$

where ψ and ψ' are SM particles. In general, this leads to a coupled system of N Boltzmann equations, describing the evolutions with one equation for each dark sector species. However, we focus on the special case where the lightest dark sector particle, the DM candidate χ_0, is protected by a stabilizing symmetry. In this case, it is sufficient to monitor the sum of the densities (or yields) $\tilde{Y} = \sum_i^N Y_i$ of all dark sector particles in one effective Boltzmann equation, since all of them eventually decay into χ_0. Also, conversions and decays as shown in Eq. (2.3.42) do not need to be considered for the calculation of $\langle\sigma v\rangle$, as they are not number changing. They can, however, influence the number densities of the dark sector particles. Typically, conversions are efficient during freeze out and beyond, since the scattering with a relativistic SM particle from the thermal bath is not Boltzmann-suppressed compared to annihilations with a non-relativistic dark sector particle. This way, the individual number densities of the coannihilating particles remain the equilibrium distributions and we can calculate the thermally averaged annihilation cross section via

$$\langle\sigma v\rangle = \sum_{i,j} \langle\sigma_{ij} v_{ij}\rangle \frac{Y_i^{\text{eq}} Y_j^{\text{eq}}}{\tilde{Y}^{\text{eq}} \tilde{Y}^{\text{eq}}} \,, \tag{2.3.43}$$

if efficient conversion are assumed.

It becomes apparent from Eq. (2.3.43) that only small mass gaps can lead to significant contributions, since the equilibrium distributions $Y_i^{\text{eq}} \sim (m_i)^{3/2} \exp\left(-{}^{m_i}/_T\right)$ are exponentially suppressed with the mass of the particle χ_i.

2.3.3 Direct Detection

In this section, we discuss the direct detection (DD) of DM particles via scattering with heavy nuclei. This scattering is induced by Earth's trajectory through the DM halo of the galaxy. The experimental strategy of detecting this scattering is measuring the nuclear recoil of such an interaction. To this date, an ever increasing number of experimental collaborations are collecting and analyzing data searching for WIMP DM with dedicated detectors like liquid noble gas (Xe, Ar) detectors (e.g. XENON [130, 131] and LUX [132]), superheated phonon detectors (e.g. PICO60 [133]) or cryogenic solid state detectors (e.g. CRESST [134] or SuperCDMS [135]). The IceCube collaboration also performs DM searches with its multi-functional detector [136].

2.3.3.1 Fundamentals of Direct Detection

The expected rate of nuclear recoil events is given by [137]

$$\frac{\mathrm{d}R}{\mathrm{d}E_{\text{NR}}} = \frac{\rho_0 M}{m_{N'} m_\chi} \int_{v_{\min}}^{v_{\max}} \mathrm{d}v\, v\, f(\vec{v} + \vec{v}_{\text{Earth}}) \frac{\mathrm{d}\sigma}{\mathrm{d}E_{\text{NR}}} \,, \tag{2.3.44}$$

---

[17] There are two additional caveats: threshold effects and resonance effects. Threshold effects can play a role if there are annihilation products heavier than DM. Resonance effects play a role if the center of mass energy of the annihilation process is in the vicinity of an s-channel resonance. In this work, we neglect these effects. For more details see e.g. [120, 128].

where $E_{\mathrm{NR}} = {}^{q^2}\!/_{2m_{N'}}$ is the nuclear recoil energy, $m_{N'}$ is the mass of the nucleus, M is the target detector total mass and $\rho_0 = 0.3\,\mathrm{GeV}c^{-2}\mathrm{cm}^{-3}$ is the local DM energy density. The function $f(v)$ is the normalized velocity distribution, e.g. a Maxwell-Boltzmann distribution

$$f(v) \sim v^2 \exp\left(-\frac{3v^2}{2\sqrt{{}^3\!/_2} \cdot v_c(R)}\right) , \tag{2.3.45}$$

in the case of the ***standard halo model***[18], where $v_c(R)$ is the circular velocity of objects in the frame of the galactic center and $v_c(R_{\text{GC-Sun}}) \approx 220^{\mathrm{km}}\!/_{\mathrm{s}}$. Additionally, Earth's rotation around the Sun, which is an $\sim \mathcal{O}(10\%)$ effect since $v_{\text{Sun-Earth}} \approx 15^{\mathrm{km}}\!/_{\mathrm{s}} \cdot \cos\left(\frac{2\pi}{\mathrm{yr}}t\right)$, has to be taken into account.

The maximal velocity $v_{\max} \approx 544^{\mathrm{km}}\!/_{\mathrm{s}}$ [140] of a WIMP is the escape velocity of the Milky Way, meaning that the WIMP is not gravitationally bound to the galaxy if $v \geq v_{\max}$. The minimal velocity $v_{\min}$, however, is the smallest velocity required to transfer the energy E_{NR} to the nucleus. This amounts to [141]

$$v_{\min} = \sqrt{\frac{E_{\mathrm{NR}} m_{N'}}{2\mu^2_{\chi N'}}} , \tag{2.3.46}$$

where $\mu_{\chi N'} = {}^{(m_\chi + m_{N'})}\!/_{m_\chi m_{N'}}$ is the ***reduced mass*** of the DM-nucleus system.

In this thesis, we do not further discuss the astrophysical details of DD, but concentrate more on the particle physics aspect, i.e. the differential cross section. This cross section is typically parametrized as a linear combination of a spin-independent (SI) and spin-dependent (SD) part, yielding [142]

$$\frac{\mathrm{d}\sigma}{\mathrm{d}E_{\mathrm{NR}}} = \frac{m_{N'}}{2\mu^2_{\chi N'} v^2}\left[\sigma_0^{\mathrm{SI}} F^2_{\mathrm{SI}}(E_{\mathrm{eq}}) + \sigma_0^{\mathrm{SD}} F^2_{\mathrm{SD}}(E_{\mathrm{eq}})\right] , \tag{2.3.47}$$

where v is the relative velocity in the detector frame and $F_{\mathrm{SI/SD}}$ are form factors. Note here that the spin-(in)dependent cross section $\sigma_0^{\mathrm{SI/SD}}$ is evaluated at zero momentum transfer, since the momentum transfer dependence is shifted into the form factors. The strength of the interaction of a WIMP with a nucleon/nucleus is fundamentally dependent on its interaction with the nucleon's constituent particles: quarks and gluons. The nature of this interaction determines whether it contributes to the SI or SD cross section.

In the following section, we discuss how we obtain the WIMP-nucleon cross section from the fundamental interactions determined by a Lagrangian of a model. The discussion is primarily focused on interactions with fermionic singlet DM. Since DM is non-relativistic and the scattering occurs at low momentum transfer, we apply an EFT approach. This discussion is largely based on [143, 144].

Typical t-channel DD interactions with bosonic mediators have a the structure

$$\begin{aligned}
\mathcal{L}_{\mathrm{DD}} \supset{}& \mathcal{O}_{\mathrm{DM}} \Pi_{\mathrm{med}} \mathcal{O}_q \\
\overset{q^2 \ll m^2_{\mathrm{med}}}{\rightarrow}{}& \left(\frac{1}{m^2_{\mathrm{med}}}\mathcal{O}_{\mathrm{DM}}\right)\mathcal{O}_N \\
\rightarrow{}& \left(\frac{1}{m^2_{\mathrm{med}}}\mathcal{O}_{\mathrm{DM}}\right)\mathcal{O}_{N'} \\
\text{with } \mathcal{O}_{\mathrm{DM},i} ={}& \bar{\chi}\,\Gamma_i\,\chi\,, \quad \mathcal{O}_{q,j} = \bar{q}\,\Gamma_j\,q\,,
\end{aligned} \tag{2.3.48}$$

---

[18] Note that in the literature, also modifications of the standard halo model and subsequent modifications of the velocity distribution $f(\vec{v})$ are discussed, e.g. in the case of the *Navarro-Frenk-White profile* [138, 139].

describing an effective four-fermion interaction, where $\mathcal{O}_{\mathrm{DM/q/N/N'}}$ are the bilinear DM/quark/nucleon/nucleus operators and Π_{med} is the propagator of the mediator. The matrix $\Gamma_i \in [\mathbb{1},\gamma^5,\gamma^\mu,\gamma^\mu\gamma^5,\sigma^{\mu\nu}]$ is part of the basis of 4×4 matrices, representing *scalar (s), pseudoscalar (p), vector (v), axial vector (a)* and *tensor (t)* interactions respectively. Note that in this work, we choose an analysis for t-channel DD interactions, as DM and SM operators strictly factorize, as indicated in Eq. (2.3.48). Possible s-channel interactions can be related to this analysis via *Fierz transformations.*

A summation over the parton content of the nucleon is necessary, since we are interested in the interaction with protons and neutrons rather than quarks and gluons on their own. To obtain the description of an interaction of DM with the whole nucleus N', another summation over all nucleons $N = p,n$ is required. In an analysis of these operators, using that in the non-relativistic limit the fermion spinors can be expanded in small momenta as

$$\begin{aligned} u(p) &= \begin{pmatrix} \sqrt{p_\mu \sigma^\mu}\xi_f \\ \sqrt{p_\mu \bar{\sigma}^\mu}\xi_f \end{pmatrix} \\ &= \frac{1}{\sqrt{2m_f}} \begin{pmatrix} (2m_f - \vec{p}\cdot\vec{\sigma})\xi_f \\ (4m_f + \vec{p}\cdot\vec{\sigma})\xi_f \end{pmatrix} + \mathcal{O}(\vec{p}^2)\,, \end{aligned} \tag{2.3.49}$$

we find that different combinations of operators $\mathcal{O}_{\mathrm{DM},i}\,\mathcal{O}_{q/N/N',j}$ lead to different types of interaction, which are SI and SD interactions with different kinds of kinematic suppression factors. A detailed pedagogical derivation is shown in e.g. [145] on the nucleus level.

Interactions that are SD, as the name suggests, crucially depend on the spin of the nucleus J_N and the constituent particles S_N, but not on the overall mass of the target. As SI interactions are not sensitive to the nucleus' spin, we can simply sum over the nucleons and find that

$$\mathcal{O}^{\mathrm{SI}}_{N'} = Z\mathcal{O}_p + (A-Z)\mathcal{O}_n\,, \tag{2.3.50}$$

$$\mathcal{O}^{\mathrm{SD}}_{N'} = \left(\frac{\langle S_p\rangle}{J_{N'}}\mathcal{O}_p + \frac{\langle S_n\rangle}{J_{N'}}\mathcal{O}_n\right)\langle J_{N'}\rangle\,, \tag{2.3.51}$$

where Z is the *atomic number* and A is the total number of nucleons in the nucleus. In the following, we shortly present the transition from quark to nucleon operator for scalar, pseudoscalar, vector and axial vector interactions.

The scalar current $\mathcal{O}_q \supset \tilde{f}_q\bar{q}q \to \mathcal{O}_N \supset \tilde{f}_N\bar{N}N \equiv \mathcal{O}_{\mathrm{SI},s}$ leads to a contribution to the SI cross section, where the nucleon coefficient reads

$$\tilde{f}_N = m_N \sum_{q=u,d,s} f^N_{T_q}\frac{\tilde{f}_q}{m_q} + \frac{2}{27}m_N\left(1 - \sum_{q=u,d,s} f^N_{T_q}\right)\sum_{q=c,b,t}\frac{\tilde{f}_q}{m_q}\,, \tag{2.3.52}$$

where $f^N_{T_q} = {}^1\!/_{m_N}\cdot\langle N|m_q\bar{q}q|N\rangle$ are coefficients describing the quark content contributions to the nucleon mass. Their numerical values can be obtained from lattice calculations and can be extracted from Table 2.2.

The pseudoscalar current $\mathcal{O}_q \supset \tilde{t}_q\bar{q}\gamma^5 q \to \mathcal{O}_N \supset \tilde{t}_N\bar{N}\gamma^5 N \equiv \mathcal{O}_{\mathrm{SD},p}$ on the other hand contributes to the SD cross section and the coefficients can be written as[19]

$$\tilde{t}_N = \sum_{q=u,d,s}\tilde{t}_q\frac{m_N}{m_q}f^{(5N)}_q\,, \tag{2.3.53}$$

neglecting the sum over heavy quarks and gluons, as their contributions to the spin content of the nucleons are small.

---

[19] The pseudoscalar coefficients can also be related to the axialvector coefficients [146].

scalar coefficients	proton	$f^p_{T_u}$	$f^p_{T_d}$	$f^p_{T_s}$
		0.20	0.026	0.043
	neutron	$f^n_{T_u}$	$f^n_{T_d}$	$f^n_{T_s}$
		0.026	0.20	0.043
pseudoscalar coefficients	proton	$f_u^{(5p)}$	$f_d^{(5p)}$	$f_s^{(5p)}$
		0.43	-0.84	-0.50
	neutron	$f_u^{(5n)}$	$f_d^{(5n)}$	$f_s^{(5n)}$
		-0.42	0.85	-0.08
axial vector coefficients	proton	$\Delta_u^{(p)}$	$\Delta_d^{(p)}$	$\Delta_s^{(p)}$
		0.84	-0.43	-0.09
	neutron	$\Delta_u^{(n)}$	$\Delta_d^{(n)}$	$\Delta_s^{(n)}$
		-0.43	0.84	-0.09

Table 2.2: Numerical values of scalar, pseudoscalar and axial vector form factors [146, 147].

In the case of a vector current $\tilde{b}_q \bar{q}\gamma_\mu q \to \tilde{b}_N \bar{N}\gamma_\mu N \equiv \mathcal{O}_{\mathrm{SI},v}$, which leads to an SI contribution, only valence quarks contribute to the interaction. The coefficients are thus simply added up according to the nucleon's valence quark content

$$\tilde{b}_p = 2\tilde{b}_u + \tilde{b}_n \,, \quad \tilde{b}_n = \tilde{b}_u + 2\tilde{b}_n \,. \tag{2.3.54}$$

The axial vector current $\tilde{d}_q \bar{q}\gamma_\mu\gamma^5 q \to \tilde{a}_N \bar{N}\gamma_\mu\gamma^5 N \equiv \mathcal{O}_{\mathrm{SD},a}$ gives a contribution to the SD cross section. As is the case for the pseudoscalar current, heavy quarks and gluons can be neglected and therefore we only sum over the light quarks. The coefficients are

$$\tilde{a}_N = \sum_{q=u,d,s} \tilde{d}_q \Delta_q^{(N)} \,. \tag{2.3.55}$$

In the following, we discuss the SI/SD DM-nucleon cross section for different bosonic mediators. We choose to present the DM-nucleon cross section, since most DD experiments put bounds on this quantity in their analyses for both SI and SD interactions. In our analysis made in Chapter 4, we focus only on fermionic DM and we thus do not discuss scalar or vector DM here.

2.3.3.2 Fermionic Matter and Scalar Mediator

In the fermionic DM and scalar mediator case, the Lagrangian yields

$$\mathcal{L} \supset \left[\left(\frac{1}{2}\right)\bar{\chi}(\lambda_{\chi s} + \lambda_{\chi p} \mathrm{i}\gamma^5)\chi + \bar{q}(\lambda_{qs} + \lambda_{qp}\mathrm{i}\gamma^5)q\right] A \,, \tag{2.3.56}$$

where the factor of $1/2$ is applied in the case of χ being a Majorana fermion. In this type of interaction, the combinations (s,s), (s,p), (p,s) and (p,p) between the DM and the nucleon operators $\mathcal{O}_{\mathrm{DM}}$ and $\mathcal{O}_N$ arise. First, we turn our attention to the SI results, i.e. the combinations, which have a scalar interaction with the nucleus. After integrating out of the mediator, the corresponding SI DM-nucleus cross section reads

$$\sigma_{s,s}^{N',\mathrm{SI}} \approx \frac{\mu^2_{\chi N'}\lambda^2_{\chi s}}{\pi m_A^4}\left(Z\tilde{f}_p + (Z-A)\tilde{f}_n\right)^2 \tag{2.3.57}$$

$$\sigma_{p,s}^{N',\mathrm{SI}} \approx \frac{\mu^2_{\chi N'} v^2}{2m_\chi^2}\frac{\mu^2_{\chi N'}\lambda^2_{\chi p}}{\pi m_A^4}\left(Z\tilde{f}_p + (Z-A)\tilde{f}_n\right)^2 \,, \tag{2.3.58}$$

where $\tilde{f}_{p/n}$ are the coefficients defined in Eq. (2.3.52). In order to obtain the DM-nucleon cross section, we average over all nucleons of the nucleus and obtain

$$\sigma^{N,\mathrm{SI}}_{s,s} \approx \frac{\mu^2_{\chi N'}\lambda^2_{\chi s}}{\pi m_A^4}\left(\frac{Z\tilde{f}_p + (Z-A)\tilde{f}_n}{A}\right)^2 \tag{2.3.59}$$

$$\sigma^{N,\mathrm{SI}}_{p,s} \approx \frac{\mu^2_{\chi N'}v^2}{2m_\chi^2}\frac{\mu^2_{\chi N'}\lambda^2_{\chi p}}{\pi m_A^4}\left(\frac{Z\tilde{f}_p + (Z-A)\tilde{f}_n}{A}\right)^2 . \tag{2.3.60}$$

For the SD DM-nucleus cross sections, we obtain

$$\sigma^{N',\mathrm{SD}}_{s,p} \approx \frac{2\mu^2_{\chi N'}v^2}{4m^2_{N'}}\frac{4\mu^2_{\chi N'}\lambda^2_{\chi s}}{\pi m_A^4} J_{N'}(J_{N'}+1)\left(\frac{\langle S_p\rangle}{J_{N'}}\tilde{t}_p + \frac{\langle S_n\rangle}{J_{N'}}\tilde{t}_n\right)^2 \tag{2.3.61}$$

$$\sigma^{N',\mathrm{SD}}_{p,p} \approx \frac{4}{3}\left(\frac{2\mu^2_{\chi N'}v^2}{4m_\chi m_{N'}}\right)^2\frac{4\mu^2_{\chi N'}\lambda^2_{\chi p}}{\pi m_A^4} J_{N'}(J_{N'}+1)\left(\frac{\langle S_p\rangle}{J_{N'}}\tilde{t}_p + \frac{\langle S_n\rangle}{J_{N'}}\tilde{t}_n\right)^2 . \tag{2.3.62}$$

and thus for the DM-nucleus cross section

$$\sigma^{N,\mathrm{SD}}_{s,p} \approx \frac{2\mu^2_{\chi N'}v^2}{4m^2_{N'}}\frac{4\mu^2_{\chi N'}\lambda^2_{\chi s}}{\pi m_A^4}\left(\frac{S_N(S_N+1)}{J^2_{N'}}\tilde{t}^2_N J_{N'}(J_{N'}+1)\right) \tag{2.3.63}$$

$$\sigma^{N,\mathrm{SD}}_{p,p} \approx \frac{4}{3}\left(\frac{2\mu^2_{\chi N'}v^2}{4m_\chi m_{N'}}\right)^2\frac{4\mu^2_{\chi N'}\lambda^2_{\chi p}}{\pi m_A^4}\left(\frac{S_N(S_N+1)}{J^2_{N'}}\tilde{t}^2_N J_{N'}(J_{N'}+1)\right) . \tag{2.3.64}$$

Note that these results are obtained under the assumption that χ is a Dirac fermion. The Majorana results, however, are form-invariant with the substitution $\lambda \to \lambda/2$.

Note here that the SI (s,s) cross section is the only contribution that is not suppressed by powers of the small relative velocity v. Whereas the mixed terms (p,s) and (s,p) are suppressed by two powers of v, the diagonal term (p,p) is even suppressed with v^4. We thus find that the (s,s) contribution is dominant for scalar mediated SI DD, while for SD the (p,s) contribution is dominant.

2.3.3.3 Fermionic DM and Vector Mediator

In the case of a vector boson mediator V_μ, the Lagrangian reads

$$\mathcal{L} \supset \left[\left(\frac{1}{2}\right)\bar{\chi}\gamma^\mu(g_{\chi v} + g_{\chi a}\gamma^5)\chi + \bar{q}\gamma^\mu(g_{qv} + g_{qa}\gamma^5)q\right] V_\mu \, , \tag{2.3.65}$$

where the factor $1/2$ is applied in the Majorana case. In addition, the vector current vanishes for a Majorana fermion, resulting in $g_{\chi v} = 0$ (see Appendix A.2). In the Dirac case, we obtain

$$\sigma^{N,\mathrm{SI}}_{v,v} \approx \frac{\mu^2_{\chi N'}g^2_{\chi v}}{\pi m_V^4}\left(\frac{Z(2\tilde{b}_u + \tilde{b}_d) + (Z-A)(\tilde{b}_u + 2\tilde{b}_d)}{A}\right)^2 \tag{2.3.66}$$

$$\sigma^{N,\mathrm{SI}}_{a,v} \approx \frac{2\mu^2_{\chi N'}v^2}{m_\chi^2}\frac{\mu^2_{\chi N'}}{\mu^2_{\chi N}}\frac{\mu^2_{\chi N'}g^2_{\chi a}}{\pi m_V^4}\left(\frac{Z(2\tilde{b}_u + \tilde{b}_d) + (Z-A)(\tilde{b}_u + 2\tilde{b}_d)}{A}\right)^2 \tag{2.3.67}$$

$$\sigma^{N,\mathrm{SD}}_{v,a} \approx \frac{\mu^2_{\chi N'}}{\mu^2_{\chi N}}\frac{2g^2_{\chi v}v^2}{\pi m_v^4}\left(J_{N'}(J_{N'}+1)\frac{S_N(S_N+1)}{J^2_{N'}}\tilde{a}^2_N\right) \tag{2.3.68}$$

$$\sigma^{N,\mathrm{SD}}_{a,a} \approx \frac{4\mu^2_{\chi N'}g^2_{\chi a}}{\pi m_V^4}\left(J_{N'}(J_{N'}+1)\frac{S_N(S_N+1)}{J^2_{N'}}\tilde{a}^2_N\right) . \tag{2.3.69}$$

As it becomes apparent from Eqs. (2.3.66)-(2.3.69), the dominant SI contribution originates from (v,v), which is velocity unsuppressed. Analogously, the unsuppressed (a,a) contribution provides the leading order contribution to the SD DD cross section over (v,a).

Again, in the Majorana case, we have to make the substitution $g \to g/2$. It is worth noting at this stage that in the case where χ is a Majorana fermion the vector current $\bar{\chi}\gamma^\mu\chi$ vanishes and therefore the velocity suppressed (a,v) contribution becomes the dominant SI contribution. In these cases, it is possible that the SD limits are more stringent than the otherwise more constraining SI limits. This is an important feature in some model classes studied in Chapter 4.

2.3.3.4 s-channel Lagrangian and Fierz Identities

In the case of s-channel-type DM-quark interactions, the DM and quark/nucleon/nucleus operators do not factorize and the treatment according to Eq. (2.3.48) does not directly apply here. In this scenario, Fierz transformations can be used to relate the s-channel-type Lagrangian with a t-channel-type one. The Fierz identities can be expressed as [148]

$$\begin{aligned}(\Gamma^i_I)_{ab}(\Gamma_{iI})_{cd} &= \sum_K C_{IK}(\Gamma^j_K)_{ad}(\Gamma_{Kj})_{cb} \\ \text{with } C_{IJ} &= \frac{1}{16N_J}\,\mathrm{Tr}\left(\Gamma_{Jk}\Gamma^i_I\Gamma^k_J\Gamma_{Ii}\right)\ ,\end{aligned} \tag{2.3.70}$$

where N_J is the total number of Dirac matrices in each Γ ($N_s = N_p = 1$, $N_v = N_a = 4$, $N_t = 6$). This allows us to rewrite products of bilinears made of two distinct spinors as a linear combination of products of bilinears of the same type[20].

In two of the three model classes presented in Chapter 4, s-channel scalar mediated DD interactions are present and can be described by the effective Lagrangian [149]

$$\mathcal{L} \supset -\bar{\chi}(\lambda_s - \lambda_p\gamma^5)qA - \bar{q}(\lambda_s^* + \lambda_p^*\gamma^5)\chi A^\dagger \tag{2.3.71}$$

$$\begin{aligned}\Rightarrow \mathcal{L}_{\text{eff}} \supsetsim \frac{1}{m_A^2}\big[&|\lambda_s|^2(\bar{\chi}q)(\bar{q}\chi) - |\lambda_p|^2(\bar{\chi}\gamma^5 q)(\bar{q}\gamma^5\chi) \\ &+\lambda_s\lambda_p^*(\bar{\chi}q)(\bar{q}\gamma^5\chi) - \lambda_s^*\lambda_p(\bar{\chi}\gamma^5 q)(\bar{q}\chi)\big]\ .\end{aligned} \tag{2.3.72}$$

A manipulation with Fierz transformations yields

$$\begin{aligned}\mathcal{L}_{\text{eff}} \supsetsim \frac{1}{4m_A^2}\Big[&(|\lambda_s|^2-|\lambda_p|^2)(\bar{q}q\bar{\chi}\chi + \frac{1}{2}\bar{q}\sigma^{\mu\nu}q\bar{\chi}\sigma_{\mu\nu}\chi) \\ &+(|\lambda_s|^2+|\lambda_p|^2)(\bar{q}\gamma^\mu q\bar{\chi}\gamma_\mu\chi - \bar{q}\gamma^\mu\gamma^5 q\bar{\chi}\gamma_\mu\gamma^5\chi)\Big]\ ,\end{aligned} \tag{2.3.73}$$

where velocity suppressed combinations are neglected. Eq. (2.3.73) suggests that in the limit $|\lambda_s| = |\lambda_p|$, the ($s$,$s$) and ($t$,$t$) operators vanish completely.

The effective DM-nucleon cross sections can hence be calculated for every contribution according to Section 2.3.3.2.

Note also that in the case of χ being a Majorana fermion, both (v,v) and (t,t) contributions vanish.

---

[20] In fact, Fierz transformations can be used to express any kind of quadrilinears in terms of other orderings. Further details can also be found in [148].

2.3.4 Indirect Detection

Astrophysical searches for secondary particles created in DM annihilations or decays are summarized as indirect detection (ID). ID searches focus on large astrophysical structures, where an accumulation of DM is denser, such as the galactic center or the dwarf spheroidal satellite galaxies (dSphs) of the Milky Way, and DM interactions are thus more likely.

The nature of these secondary particles can be manifold and can in principle involve any kind of SM particle. However, only stable particles like leptons, protons and photons end up reaching Earth to induce a certain signal signature. This emission of stable particles can either occur via a cascade of decays of the initially induced heavy particles or via direct annihilation into these particles.

Standing out from the pool of possibilities are photons, as they can travel to the Earth on their straight path without being diverted by possible magnetic or electric fields[21]. This makes it easier to determine the place of their origin and therefore enhances the background estimate. This situation motivates experimental collaborations like Fermi-**L**arge **A**rea **T**elescope (LAT) [150] or HESS [151] to perform dedicated searches for DM in gamma ray signals from astrophysical sources. Fermi-LAT covers an energy range from $30\,\mathrm{MeV} - 300\,\mathrm{GeV}$, while HESS covers the high energy range of $300\,\mathrm{GeV} - 10\,\mathrm{TeV}$.

For annihilations of DM to photons (or similarly neutrinos), the expected flux can be parametrized as [150]

$$\begin{aligned}\phi(\Delta\Omega, E_{\min}, E_{\max}) = & \frac{1}{4\pi}\frac{\langle\sigma v\rangle}{2m_\chi^2}\int_{E_{\min}}^{E_{\max}}\frac{\mathrm{d}N_\gamma}{\mathrm{d}E_\gamma}\mathrm{d}E_\gamma \\ & \times \underbrace{\int_{\Delta\Omega}\int_{\mathrm{l.o.s.}}\rho^2(\vec{r}(l))\mathrm{d}l\mathrm{d}\Omega}_{\equiv J}\ ,\end{aligned} \tag{2.3.74}$$

where the so called *J-factor* encompasses the astrophysical parameters like the density profile, and $\mathrm{d}N_\gamma/\mathrm{d}E_\gamma$ is the differential gamma ray photon spectrum summed over all final states. Note that as a general rule of thumb, observations of dwarf spheroidal galaxies have less uncertainty in the J-factor, since the they involve integration over most of the dwarf galaxy's volume so that the details of the density profile are averaged out to a higher degree than in observations of the galactic core [152].

As becomes apparent in Eq. (2.3.74), the photon flux is directly proportional to the thermally averaged annihilation cross section $\langle\sigma v\rangle$ and thus limits on this quantity can be posed by ID experiments. The most stringent bounds involving photon-rich final state products generally come from the dSphs observed by Fermi-LAT, where bounds on the annihilation $\bar{\chi}\chi \to \bar{b}b/\tau^+\tau^-$ are derived [150, 152, 153]. Especially models that feature unsuppressed s-wave annihilation into these particles can be constrained. Since the velocity of DM particles today is much smaller than during the time of thermal freeze out, the velocity suppression is more severe in ID. For example typical WIMP models with strong annihilations into these channels, DM masses of $\lesssim 100\,\mathrm{GeV}$ are excluded[22].

The gamma ray spectrum created by the cascade-like annihilations described above is broad and smooth. Conversely, direct annihilations of DM into photons create monochromatic photons, which leads to a line-like feature in the spectrum near the kinematical endpoint. This

---

[21] Photon geodesics can in principle also be curved by galaxies, as observed by gravitational lensing experiments. However, this effect is orders of magnitude weaker than diversion of charged particles by the electromagnetic force.

[22] Note that for these kind of searches, it is generally unimportant if these models feature coannihilations, since the observations of the dSphs occur at times long after freeze-out, so that all coannihilation partner particles must have decayed already.

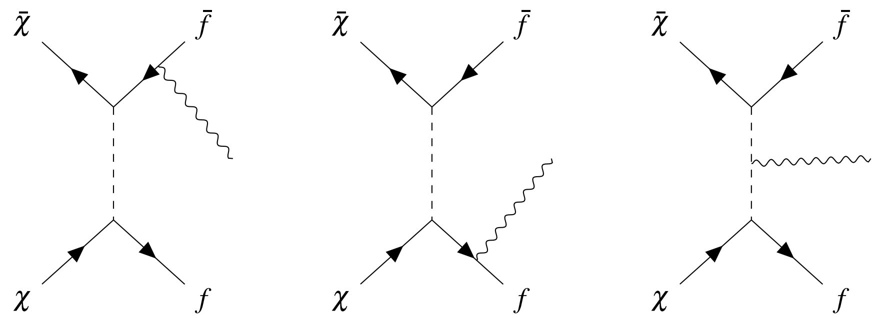

Figure 2.6: Feynman diagrams contributing to the amplitude of the three-body annihilation at leading order in an example with a scalar mediator.

signature is unexpected to originate from any astrophysical source and is thus considered to be a *smoking gun* for detection of DM. However, these direct annihilations are typically loop-suppressed and thus, they are expected to only make up a fraction of the total annihilation cross section of DM. The Fermi-LAT reports the 95% C.L. upper limits on $\langle\sigma v\rangle_{\gamma\gamma}$ for different density profiles from gamma ray searches from the galactic center region [154]. Furthermore, all-sky Fermi-LAT data has been analyzed and found to be weaker by up to one order of magnitude [155].

Another interesting, almost line-like spectral feature can be induced by DM annihilations into the three-body final states $\bar{\chi}\chi \to \bar{f}f\gamma$. Figure 2.6 shows the Feynman diagrams contributing to the three-body annihilation. The kind of interaction that drives the spectral feature is often referred to as virtual internal bremsstrahlung (VIB)[23], which is an effect that can occur in models with electrically charged (virtual) mediators. Note that the diagrams in Fig. 2.6 also contribute to the soft collinear final state radiation (FSR) and a clear distinction is only meaningful in an expansion of $\langle\sigma v\rangle$ in v and m_f [156]. Although this is a next-to-leading-order process in QED yielding a suppression by α_{em}, it is not loop-suppressed like the $\bar{\chi}\chi \to \gamma\gamma$ annihilation. It has been shown that the contribution can become as important - or even more so - than the annihilation into a pair of SM fermions because it can lift the helicity suppression $a \sim ({}^{m_f}/{}_{m_\chi})^2$ of the s-wave annihilation that is e.g. present in Majorana-DM models. This is especially true for relatively small mass gaps of DM and the mediator ${}^{m_{\text{med}}}/{}_{m_\chi} \lesssim 1.2$ [156, 157, 158, 159, 160, 161, 162, 163], which coincides with the coannihilation region described in Section 2.3.2. Limits from Fermi-LAT and HESS on VIB and line-like signals for DM models coupling to light fermions are derived in [164] for different mass gaps < 2 and applied to the Majorana-DM-type models presented in Chapter 4.

---

[23] Sometimes this phenomenon is called *internal bremsstrahlung (IB)* instead in the literature. The nomenclature is not consistent throughout the literature and sometimes includes final state radiation (FSR) and sometimes does not.

Chapter 3

Neutrino Oscillations with Altered Dispersion Relations as an Explanation for Neutrino Anomalies

In this chapter, we present a model that aims to solve the problems outlined in Section 2.1.3 with non-standard active-sterile neutrino oscillations. We base this chapter on the results published in [1][1].

In addition to the three active neutrinos, we introduce a number of sterile neutrinos featuring an altered dispersion relation (ADR). This means that the usual Hamiltonian is extended by an additional potential term, effectively altering the relationship between energy, momentum and mass of a certain particle.

As outlined in Section 2.1.4, the standard $(3{+}N)\nu$ active-sterile neutrino oscillation scenarios cannot explain the current neutrino anomalies, due to the strong disagreement between SBL and high-energy LBL experiments. The fundamental problem is the rigid dependence of the oscillation probability $P_{\nu_\alpha \to \nu_\beta}$ on the quotient L/E. This dependence can, however, be lifted in the presence of an ADR and subsequently energy-dependent mixing matrix entries.

The outline of the chapter is as follows: In Section 3.1, we present the general setup of the model. In Sections 3.2, we discuss specifically why a $(3{+}1)\nu$ version of this model cannot achieve the aim of the model. We discuss a $(3{+}3)\nu$ version of the model and present a phenomenological analysis in Section 3.2. Finally, we summarize our results in Section 3.4.

3.1 General Model Setup

The most widely-known example for such an ADR is induced by neutrino interactions with matter, where the dispersion relation of electron neutrinos is effectively altered and an effective potential is induced in the Hamiltonian. Due to the nature of the charged current interaction, this potential is independent from the neutrino energy. For more details on matter effects in neutrino oscillations, see Section 2.1.2.

In scenarios where the sterile neutrino ADR is induced by fundamental Lorentz violation, effective potentials in neutrino oscillations arise independently from the matter distribution and do not differentiate between neutrinos and anti neutrinos.

---

[1] Parts of the results presented in this thesis are also published in my collaborator's PhD thesis [165].

The ADR that is required for the realization of our model can e.g. be generated by setups similar to the model discussed in a series of papers [166, 167, 168, 169, 170, 171]. This model features one additional sterile neutrino and an asymmetrically warped[2] extra dimension [172, 173, 174] in a brane world scenario. The ADR is generated by an effective 'runtime difference' between active and sterile neutrinos. This can be pictured semi-classically in the following way: The sterile neutrino follows a geodesic in the bulk, oscillating around the brane and picking up a relative runtime advantage $\varepsilon := {}^{\delta t}\!/_{t}$ through the effectively higher velocity in the warped space, while the gauge-charged neutrino is tied to the SM-brane.

In such a scenario, the sterile neutrino Hamiltonian picks up a potential that is negatively proportional to this relative time difference ε, called the *shortcut parameter*. Conversely to matter effects, this potential also depends on the neutrino energy E [166, 167]. The shortcut parameter and the energy dependence of the potential depend on the spacetime geometry of the extra dimension, as discussed in [166, 175].

3.2 $(3+1)\nu$ Model

In the spirit of the model first presented in [166], we first introduce one additional sterile neutrino with an ADR. The mass of this neutrino lies at the eV-scale can e.g. be generated by a variant of the seesaw mechanism introduced in Sections 2.2.2 - 2.2.3 [176, 177, 178, 179, 180]. The resulting Hamiltonian in flavor space yields

$$\begin{aligned}
H_{\mathrm{F}} =& \frac{1}{2E} U \begin{pmatrix} m_1^2 & 0 & 0 & 0 \\ 0 & m_2^2 & 0 & 0 \\ 0 & 0 & m_3^2 & 0 \\ 0 & 0 & 0 & m_4^2 \end{pmatrix} U^\dagger - E \begin{pmatrix} 0 & 0 & 0 & 0 \\ 0 & 0 & 0 & 0 \\ 0 & 0 & 0 & 0 \\ 0 & 0 & 0 & \varepsilon \end{pmatrix} \\
\approx & \begin{pmatrix} & & & 0 \\ & V & & 0 \\ & & & 0 \\ 0 & 0 & 0 & 1 \end{pmatrix} \times \\
\times & \left[\frac{1}{2E} \begin{pmatrix} 1 & 0 & 0 & 0 \\ 0 & 1 & 0 & 0 \\ 0 & 0 & & \\ 0 & 0 & & R_{34} \end{pmatrix} \begin{pmatrix} 0 & 0 & 0 & 0 \\ 0 & 0 & 0 & 0 \\ 0 & 0 & 0 & 0 \\ 0 & 0 & 0 & \Delta m_{\mathrm{SBL}}^2 \end{pmatrix} \begin{pmatrix} 1 & 0 & 0 & 0 \\ 0 & 1 & 0 & 0 \\ 0 & 0 & & \\ 0 & 0 & & R_{34}^T \end{pmatrix} - E\varepsilon \begin{pmatrix} 0 & 0 & 0 & 0 \\ 0 & 0 & 0 & 0 \\ 0 & 0 & 0 & 0 \\ 0 & 0 & 0 & 1 \end{pmatrix} \right] \times \\
\times & \begin{pmatrix} & & & 0 \\ & V^\dagger & & 0 \\ & & & 0 \\ 0 & 0 & 0 & 1 \end{pmatrix},
\end{aligned} \tag{3.2.1}$$

where E denotes the neutrino energy, ε the shortcut parameter, and

$$U = \begin{pmatrix} & & & 0 \\ & V & & 0 \\ & & & 0 \\ 0 & 0 & 0 & 1 \end{pmatrix} \times \begin{pmatrix} 1 & 0 & 0 & 0 \\ 0 & 1 & 0 & 0 \\ 0 & 0 & & \\ 0 & 0 & & R_{34} \end{pmatrix}, \tag{3.2.2}$$

---

[2] This terminus refers to a warping, where bulk and time coordinates are warped non-factorizably. As opposed to symmetrically warped extra dimension, as in the the case of the *Randall-Sundrum model*, asymmetrically warped spacetimes are not vacuum solutions of the EFE and require an energy source.

the full 4×4 unitary mixing matrix. In the step from the first to the second line in Eq. (3.2.1), we used the approximations $m^2_{1/2/3}\approx 0$, $m_4^2 \approx m^2_{\mathrm{SBL}}$. The 3×3 matrix V corresponds to the standard PMNS matrix and R_{34} is the orthogonal rotation matrix

$$R_{34} = \begin{pmatrix} \cos\theta_{34} & \sin\theta_{34} \\ -\sin\theta_{34} & \cos\theta_{34} \end{pmatrix}\,, \tag{3.2.3}$$

which generates mixing in the 3-4 plane[3].

The eigenvalues of the Hamiltonian are [167]

$$\begin{aligned} \lambda_1 &= \lambda_2 = 0, \\ \lambda_\pm &= \frac{\Delta m^2_{\mathrm{SBL}}}{4E}\left(1-\cos 2\theta_{34}\left(\frac{E}{E_R}\right)^2 \pm \sqrt{\sin^2 2\theta_{34} + \cos^2 2\theta_{34}\left[1-\left(\frac{E}{E_R}\right)^2\right]^2}\,\right)\,, \end{aligned} \tag{3.2.4}$$

where

$$E_R = \sqrt{\frac{\Delta m^2_{\mathrm{SBL}}\cos 2\theta_{34}}{2\varepsilon}}\,. \tag{3.2.5}$$

is the *resonance energy*, where the level crossing of the neutrino eigenstates occurs.

Further following [167], we obtain the transition and survival probabilities $P_{\nu_\alpha\to\nu_\beta}$ and $P_{\nu_\alpha\to\nu_\alpha}$ for active flavors α,β as

$$\begin{aligned} P_{\nu_\alpha\to\nu_\beta} =& 4U^2_{\alpha 3}U^2_{\beta 3}\cdot\left[-\sin^2\left(\frac{L(\lambda_+-\lambda_-)}{2}\right)\sin^2\tilde\theta\cos^2\tilde\theta\right. \\ &\left.+\sin^2\left(\frac{L(\lambda_+)}{2}\right)\sin^2\tilde\theta + \sin^2\left(\frac{L(\lambda_-)}{2}\right)\cos^2\tilde\theta\right]\,, \end{aligned} \tag{3.2.6}$$

$$\begin{aligned} P_{\nu_\alpha\to\nu_\alpha} =& 1-4U^2_{\alpha 3}\cdot\left[\sin^2\left(\frac{L(\lambda_+-\lambda_-)}{2}\right)\sin^2\tilde\theta\cos^2\tilde\theta\, U^2_{\alpha 3}\right. \\ &\left.+\sin^2\left(\frac{L(\lambda_+)}{2}\right)\sin^2\tilde\theta\,(1-U^2_{\alpha 3}) + \sin^2\left(\frac{L(\lambda_-)}{2}\right)\cos^2\tilde\theta\,(1-U^2_{\alpha 3})\right]\,, \end{aligned} \tag{3.2.7}$$

where $\tilde\theta$ is the effective mixing angle defined via

$$\sin^2 2\tilde\theta = \frac{\sin^2 2\theta_{34}}{\sin^2 2\theta_{34} + \left(\cos 2\theta_{34} - \frac{2E^2\varepsilon}{\Delta m^2_{\mathrm{SBL}}}\right)^2}\,. \tag{3.2.8}$$

We note from Eq. (3.2.4) that the eigenvalue λ_+ vanishes at energies far above the resonance, as does $\cos^2\tilde\theta$, while $\sin^2\tilde\theta$ and λ_- are non-vanishing[4]. However, this limit is only meaningful in scenarios where L/E is comparably small. Comparing e.g. the setups of SBL experiments $\left(L/E|_{\mathrm{SBL}}\approx \mathcal{O}(10\text{-}1000\,\mathrm{m})/\mathcal{O}(1\mathrm{MeV}\text{-}1\,\mathrm{GeV})\right)$ and atmospheric experiments $\left(L/E|_{\mathrm{atm}}\approx \mathcal{O}(10^7\,\mathrm{m})/\mathcal{O}(0.1\text{-}1\,\mathrm{GeV})\right)$ we find that there are several orders of magnitude between these quantities and we can thus not apply the limit in every scenario. Rather than the eigenvalue of the Hamiltonian, the relevant quantity is the resulting mass-squared difference

$$m^2_\pm = 2E\cdot\lambda_\pm \tag{3.2.9}$$

---

[3] Note that this setup can be formulated in terms of a rotation with θ_{14} or θ_{24} analogously. However, if more than one of these angles is non-zero, the analytic formalism presented here is not applicable and we require a numerical analysis.

[4] Note that $\tilde\theta$ is defined in the second octant for energies $E > E_R$ and thus there is a common root of $\sin^2(2\tilde\theta)$ and $\cos^2\theta$ at $\pi/2$.

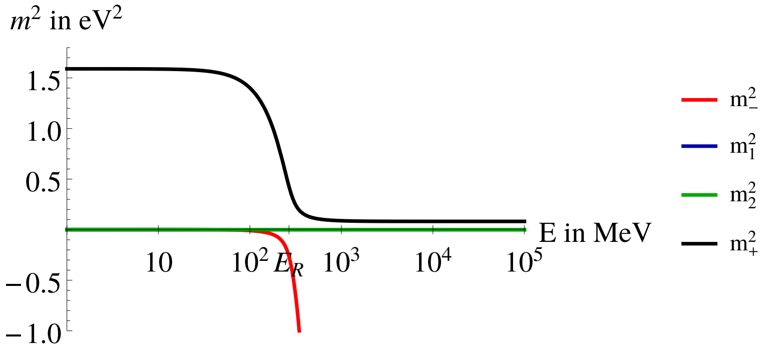

Figure 3.1: Effective squared masses as a function of the energy E in the $(3+1)\nu$+ADR model for a BSM parameter choice of $\sin^2\theta_{34}$, $\Delta m^2_{\mathrm{SBL}}$ and $\varepsilon = 5 \cdot 10^{-17}$.

giving rise to the oscillatory term $\sin^2(\Delta m^2_{\pm} L/2E)$.

As the limit of the mass-squared difference, conversely to the eigenvalue, does not approach zero but a constant value

$$\lim_{E\to\infty} m_+^2 = \Delta m^2_{\mathrm{SBL}} \cdot \frac{1-\cos 2\theta_{43}}{2}\,, \tag{3.2.10}$$

atmospheric experiments can in principle still detect an oscillation of this frequency. This is especially the case when the size of $\Delta m^2_{\mathrm{SBL}}$ is large enough to compensate the suppression of a small mixing angle θ_{34}.

Fig. 3.1 sketches the behavior of the effective squared masses with increasing energy. At the resonance energy E_R, we find the characteristic level crossing where maximal mixing occurs and the mass eigenstates swap their flavor content. At energies above the resonance, one of the squared masses diverges while the others approach a constant value.

While the deviations caused by the $(3+1)\nu$+ADR setup discussed above might elude detection by accelerator experiments like MINOS due to the relatively narrow energy spectrum, atmospheric neutrino experiments like IceCube and SK have high statistics at energies $\gtrsim 1\,\mathrm{GeV}$ and are thus able to rule out the deviation.

3.3 $(3+3)\nu$ Model

3.3.1 $(3+3)\nu$ Model with a Universal Potential

An effective mass-squared difference at energies far above the resonance emerging in the $(3+1)\nu$+ADR model can be averted in a setup with three instead of one sterile neutrino. In this model, we assume that each sterile state mixes with one of the predominantly active mass eigenstates, respectively. We also assume all sterile neutrinos to feature the same ADR. A universal potential for all sterile neutrinos leaves the mass-squared differences between the predominantly active neutrinos intact across the energy scales and no additional Δm^2 is generated as opposed to the $(3+1)\nu$+ADR model.

The 6×6 mixing matrix can be parametrized as[5]

$$U^{6\times 6} = U_{23}U_{13}U_{12}U_{14}U_{25}U_{36}\,. \tag{3.3.1}$$

---

[5] Note that the ordering of the sterile neutrino mixing matrices does not coincide with the usual parametrization.

We parametrize the bare squared masses as

$$\begin{aligned}
&\Delta m^2_{41} = \Delta m^2_{\mathrm{SBL}}\,, && \\
&\Delta m^2_{51} = \Delta m^2_{\mathrm{SBL}} + \Delta m^2_{21} &\quad\rightarrow\quad& \Delta m^2_{52} = \Delta m^2_{\mathrm{SBL}}\,, \\
&\Delta m^2_{61} = \Delta m^2_{\mathrm{SBL}} + \Delta m^2_{31} &\quad\rightarrow\quad& \Delta m^2_{63} = \Delta m^2_{\mathrm{SBL}}\,.
\end{aligned} \tag{3.3.2}$$

Since we assume a universal potential, meaning the same ε in all sterile neutrino potentials, the resonance energy E_R is universal. The effective potential reads

$$V_{\mathrm{eff}} = \begin{pmatrix} 0 & 0 & 0 & 0 & 0 & 0 \\ 0 & 0 & 0 & 0 & 0 & 0 \\ 0 & 0 & 0 & 0 & 0 & 0 \\ 0 & 0 & 0 & \varepsilon E & 0 & 0 \\ 0 & 0 & 0 & 0 & \varepsilon E & 0 \\ 0 & 0 & 0 & 0 & 0 & \varepsilon E \end{pmatrix}. \tag{3.3.3}$$

Since each mass eigenstate $\nu_{1,2,3}$ features an admixture with its own sterile state, the results from [167] discussed in Section 3.2 remain applicable. The mass eigenvalues are denoted by $m^2_{4\pm}$, $m^2_{5\pm}$, $m^2_{6\pm}$, which correspond to the $m^2_\pm$ mass eigenstates in Section 3.2. These eigenvalues are

$$m^2_{4\pm} \approx \frac{\Delta m^2_{\mathrm{SBL}}}{2}\left(1 - \cos 2\theta_{14}\left(\frac{E}{E_{R,4}}\right)^2 \mp \sqrt{\sin^2 2\theta_{14} + \cos^2 2\theta_{14}\left[1 - \left(\frac{E}{E_{R,4}}\right)^2\right]^2}\,\right), \tag{3.3.4}$$

$$m^2_{5\pm} \approx \frac{\Delta m^2_{\mathrm{SBL}}}{2}\left(1 - \cos 2\theta_{25}\left(\frac{E}{E_{R,5}}\right)^2 \mp \sqrt{\sin^2 2\theta_{25} + \cos^2 2\theta_{25}\left[1 - \left(\frac{E}{E_{R,5}}\right)^2\right]^2}\,\right), \tag{3.3.5}$$

$$m^2_{6\pm} \approx \frac{\Delta m^2_{\mathrm{SBL}}}{2}\left(1 - \cos 2\theta_{36}\left(\frac{E}{E_{R,6}}\right)^2 \mp \sqrt{\sin^2 2\theta_{36} + \cos^2 2\theta_{36}\left[1 - \left(\frac{E}{E_{R,6}}\right)^2\right]^2}\,\right), \tag{3.3.6}$$

with the corresponding resonance energies

$$E_{R,4} = \sqrt{\frac{\Delta m^2_{\mathrm{SBL}}\cos 2\theta_{14}}{2\varepsilon}}\,, \quad E_{R,5} = \sqrt{\frac{\Delta m^2_{\mathrm{SBL}}\cos 2\theta_{25}}{2\varepsilon}}\,, \quad E_{R,6} = \sqrt{\frac{\Delta m^2_{\mathrm{SBL}}\cos 2\theta_{36}}{2\varepsilon}}\,. \tag{3.3.7}$$

The squared masses Δm^2_{i-} decouple in the high energy limit $E \gg E_{R,i}$ and thus we study the high energy behavior of Δm^2_{i+}. We find

$$\lim_{E\to\infty} m^2_{4+} \approx \frac{1}{2}\left(\Delta m^2_{\mathrm{LSND}} \cdot \cos 2\theta_{14}\right)\,, \tag{3.3.8}$$

$$\lim_{E\to\infty} m^2_{5+} \approx \frac{1}{2}\left(\Delta m^2_{\mathrm{LSND}} \cdot \cos 2\theta_{25}\right)\,, \tag{3.3.9}$$

$$\lim_{E\to\infty} m^2_{6+} \approx \frac{1}{2}\left(\Delta m^2_{\mathrm{LSND}} \cdot \cos 2\theta_{36}\right)\,. \tag{3.3.10}$$

Therefore, the non-divergent mass-squared differences far above the resonance are

$$m_{5+}^2 - m_{4+}^2 \approx \frac{\Delta m_{\mathrm{LSND}}^2}{2} \left(\cos 2\theta_{14} - \cos 2\theta_{25}\right) , \tag{3.3.11}$$

$$m_{6+}^2 - m_{4+}^2 \approx \frac{\Delta m_{\mathrm{LSND}}^2}{2} \left(\cos 2\theta_{14} - \cos 2\theta_{36}\right) , \tag{3.3.12}$$

$$m_{6+}^2 - m_{5+}^2 \approx \frac{\Delta m_{\mathrm{LSND}}^2}{2} \left(\cos 2\theta_{25} - \cos 2\theta_{36}\right) . \tag{3.3.13}$$

Eqs. (3.3.11) - (3.3.13) suggest that the additional oscillation mode at high energies arising in the $(3+1)\nu$+ADR model can be avoided if we require the mixing angles to be equal to one another, i.e. $\theta_{14} = \theta_{25} = \theta_{36} \equiv \theta$. We call this scenario 'democratic mixing'. This mechanism allows the oscillations at very high energies to remain the way they are predicted in the standard 3ν model. This behavior is illustrated in Fig. 3.2, where we schematically show the evolution of the flavor content of the mass eigenstates in terms of the neutrino energy E.

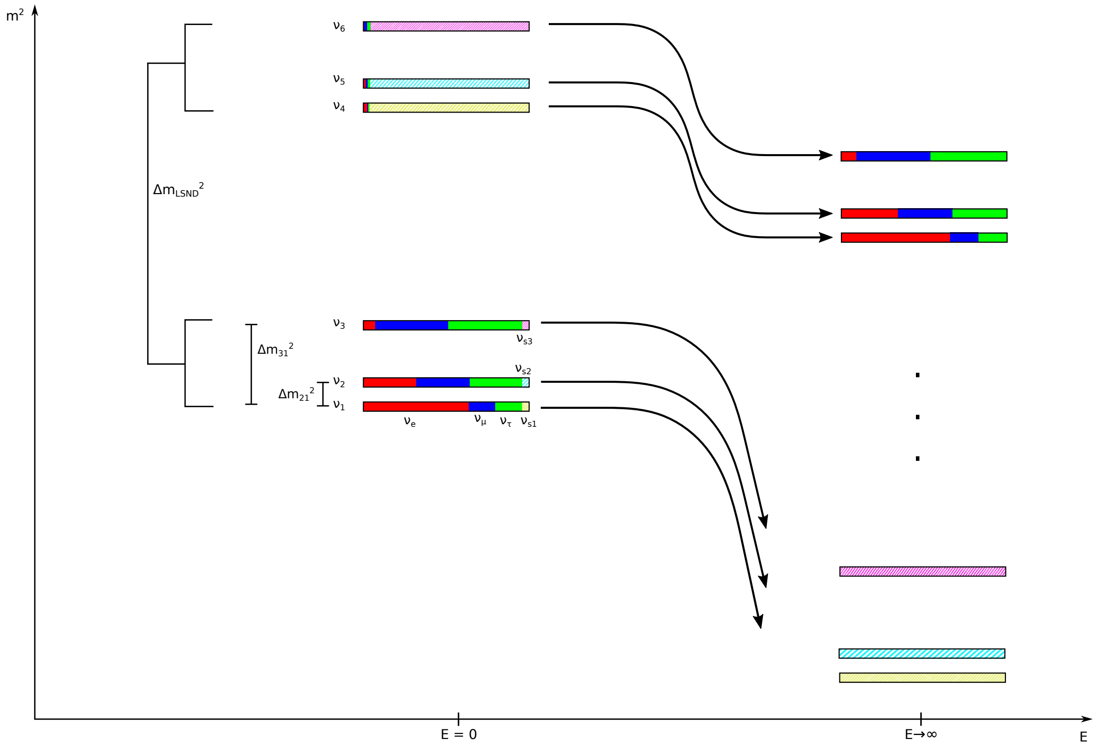

Figure 3.2: Schematic overview of mass eigenstates and their flavor content depending on the neutrino energy E.

Despite its desirable high energy limits, the $(3+3)\nu$+ADR model with a universal potential and democratic mixing is not able to solve the SBL anomalies. A major flaw of this setup is a vanishing appearance amplitude for the excess region in the MiniBooNE experiment.

The general electron neutrino appearance probability in a muon neutrino beam in the case of CP conservation is given by

$$P_{\nu_\mu \to \nu_e} = -4 \sum_{k>j} \tilde{U}_{\mu j} \tilde{U}_{\mu k} \tilde{U}_{ej} \tilde{U}_{ek} \sin^2\left(\Delta \tilde{m}_{kj}^2 \frac{L}{2E}\right) , \tag{3.3.14}$$

where $\tilde{U}$ and $\tilde{m}^2$ can be replaced with U and m^2 below the resonance.

Since SBL experiments like LSND and MiniBooNE are designed to probe the high Δm^2 region, only terms where $\Delta m^2 \approx \Delta m^2_{\text{SBL}}$ must be considered. According to Eq. (3.3.2), these mass-squared differences are $\Delta m^2_{4i}, \Delta m^2_{5i}$ and Δm^2_{6i}, where $i \in$ [1,2,3]. We can thus expand and simplify the probability given in Eq. (3.3.14) and obtain the factorized form

$$P_{\nu_\mu \to \nu_e} \sim -4 \sin^2 \left(\Delta m^2_{\text{SBL}} \frac{L}{2E} \right) \left(\sum_{i=1,2,3} U_{\mu i} U_{ei} \right) \left(\sum_{j=4,5,6} U_{\mu j} U_{ej} \right) . \tag{3.3.15}$$

For simplicity, we write the mixing matrix U in terms of U_0, which is the 6×6 enlargement

$$U_0 = \begin{pmatrix} U^{\text{SBL}}_{3\times3} & 0_{3\times3} \\ 0_{3\times3} & \mathbb{1}_{3\times3} \end{pmatrix} \tag{3.3.16}$$

of the unitary 3×3 PMNS matrix, as

$$\begin{aligned}
U^{6\times6} &= \underbrace{(U_{12}U_{13}U_{23})}_{U_0}(U_{14}U_{25}U_{36}) \\
&= U_0 \cdot \begin{pmatrix} c_\theta & 0 & 0 & s_\theta & 0 & 0 \\ 0 & 1 & 0 & 0 & 0 & 0 \\ 0 & 0 & 1 & 0 & 0 & 0 \\ -s_\theta & 0 & 0 & c_\theta & 0 & 0 \\ 0 & 0 & 0 & 0 & 1 & 0 \\ 0 & 0 & 0 & 0 & 0 & 1 \end{pmatrix} \cdot \begin{pmatrix} 1 & 0 & 0 & 0 & 0 & 0 \\ 0 & c_\theta & 0 & 0 & s_\theta & 0 \\ 0 & 0 & 1 & 0 & 0 & 0 \\ 0 & 0 & 0 & 1 & 0 & 0 \\ 0 & -s_\theta & 0 & 0 & c_\theta & 0 \\ 0 & 0 & 0 & 0 & 0 & 1 \end{pmatrix} \cdot \begin{pmatrix} 1 & 0 & 0 & 0 & 0 & 0 \\ 0 & 1 & 0 & 0 & 0 & 0 \\ 0 & 0 & c_\theta & 0 & 0 & s_\theta \\ 0 & 0 & 0 & 1 & 0 & 0 \\ 0 & 0 & 0 & 0 & 1 & 0 \\ 0 & 0 & -s_\theta & 0 & 0 & c_\theta \end{pmatrix} \\
&= U_0 \cdot \begin{pmatrix} c_\theta \cdot \mathbb{1}_{3\times3} & s_\theta \cdot \mathbb{1}_{3\times3} \\ -s_\theta \cdot \mathbb{1}_{3\times3} & c_\theta \cdot \mathbb{1}_{3\times3} \end{pmatrix} \\
&= \begin{pmatrix} c_\theta \cdot U^{\text{PMNS}}_{3\times3} & s_\theta \cdot U^{\text{PMNS}}_{3\times3} \\ -s_\theta \cdot \mathbb{1}_{3\times3} & c_\theta \cdot \mathbb{1}_{3\times3} \end{pmatrix} ,
\end{aligned} \tag{3.3.17}$$

where c_θ, s_θ are the (co)sine functions of the universal mixing angle θ.

Besides the overall unitarity condition $\sum_k^6 U_{\mu k} U_{ek} = 0$, the PMNS matrix $U^{\text{PMNS}}_{3\times3}$ is unitary itself in the sense that $\sum_k^3 U^{\text{PMNS}}_{\mu k} U^{\text{PMNS}}_{ek} = 0$ and thus both brackets in Eq. (3.3.15) vanish[6].

In conclusion of the results obtained in this section, the $(3+3)\nu$+universal ADR model can avoid oscillations far above the resonance in a democratic mixing setup. However, the same setup generates vanishing appearance probability at SBL experiments, which contradicts the experimental data and nullifies the main feature of the model. A realistic model therefore requires a different approach. In Section 3.3.2, we show that the issue of vanishing probability can be resolved by assuming different ADRs for each sterile neutrino.

3.3.2 $(3+3)\nu$ Model with Individual Potentials

Instead of assigning the same potential to all sterile neutrinos, there is a possibility to assign individual potentials to each sterile neutrino[7]. This leads to different resonance energies for different transitions. In the energy regime far above (or below) the resonances, however, the limits

---

[6] The bracket term is $\cos^2\theta\,(U^{\text{PMNS},(\mu\text{ row})}_{3\times3} \cdot U^{\text{PMNS},(e\text{ row})}_{3\times3} = 0)$, while the second bracket is $\sin^2\theta\,(U^{\text{PMNS},(\mu\text{ row})}_{3\times3} \cdot U^{\text{PMNS},(e\text{ row})}_{3\times3} = 0)$.

[7] In the extra dimensional setup mentioned in Section 3.1, this is possible by binding each sterile neutrino to a different extra dimension.

are independent of the resonance energies and the important features of the (3+3)ν+ADR model are recovered. Further, we expect a non-vanishing transition probability at SBL experiments due to the lack of exact unitarity cancellations in this setup.

We parametrize the effective, ubiquitous sterile neutrino potential as

$$V_{\text{eff}} = \begin{pmatrix} 0 & 0 & 0 & 0 & 0 & 0 \\ 0 & 0 & 0 & 0 & 0 & 0 \\ 0 & 0 & 0 & 0 & 0 & 0 \\ 0 & 0 & 0 & \eta \cdot \varepsilon E & 0 & 0 \\ 0 & 0 & 0 & 0 & \kappa \cdot \varepsilon E & 0 \\ 0 & 0 & 0 & 0 & 0 & \xi \cdot \varepsilon E \end{pmatrix}, \tag{3.3.18}$$

where η, κ and ξ are dimensionless scaling factors, controlling the relative size of the potentials. Since one of these factors can in principle be absorbed into the definition of ε, we effectively count two additional parameters compared to the setup in Section 3.3.1.

3.3.3 Below the Resonance

Additionally to the discussion about the high energy behavior of the model in Section 3.3.1, we briefly expand on the low energy limit in this section. This limit is especially interesting in the context of reactor experiments, which use low energy electron anti neutrinos from nuclear decays. Analogously to Eq. (3.3.15), we obtain

$$\begin{aligned} P_{\nu_e \to \nu_e} &\approx 1 - 4 \sin^2 \left(\Delta m^2_{\text{SBL}} \frac{L}{2E} \right) \left(\sum_{i=1,2,3} U^2_{ei} \right) \left(\sum_{j=4,5,6} U^2_{ej} \right) \\ &\approx 1 - 4 \sin^2 \left(\Delta m^2_{\text{SBL}} \frac{L}{2E} \right) \cos^2 \theta \sin^2 \theta \\ &\approx 1 - \sin^2 \left(\Delta m^2_{\text{SBL}} \frac{L}{2E} \right) \sin^2 2\theta \, . \end{aligned} \tag{3.3.19}$$

for the survival probability far below the resonance. This is the same expression obtained in Eq. (2.1.20) for the minimal $(3+1)\nu$ scenario discussed in Section 2.1.4. Indeed, there are hints in the data towards this kind of extra oscillation at low energies as suggested in Section 2.1.4 (see e.g. [99]).

Note, however, that this behavior only applies to energies far below the resonance. In the intermediate ranges, where the effective Δm^2s are not relaxed to their respective limiting cases, additional visible oscillation modes can in principle appear. This also applies to the high energy behavior and is highly dependent on the choice of resonance energies.

In our phenomenological analysis in Section 3.3.4, we include a discussion about the oscillation picture at short baseline reactor experiments like NEOS and DANSS and also the long baseline reactor experiment KamLAND, comparing the numerically obtained oscillation probability of the $(3+3)\nu$+ADR model with the simple $(3+1)\nu$ best fit oscillation probability from global fits.

3.3.4 Phenomenological Analysis

In this section, we present a numerical study of several benchmark points (BMPs) and show the phenomenological features of the $(3+3)\nu$+ADR model. We briefly describe the behavior of the effective mass-squared differences as a function of the neutrino energy for each BMP, allowing

BSM Parameter	BMP1	BMP2	BMP3	BMP4
Δm^2_{SBL}	$1.5\,\text{eV}^2$	$1.3\,\text{eV}^2$	$30\,\text{eV}^2$	$30\,\text{eV}^2$
$\sin^2 2\theta$	$1\cdot 10^{-2}$	$2\cdot 10^{-3}$	$1\cdot 10^{-4}$	$1\cdot 10^{-4}$
ε	$8\cdot 10^{-18}$	$1.5\cdot 10^{-17}$	$3\cdot 10^{-16}$	$3\cdot 10^{-16}$
η	1	10.9	10.1	100.9
κ	150	10.7	10	100.7
ξ	150	1	1	1

Table 3.1: Overview of the selection of BMPs chosen in this thesis.

us to extract intuitive information about the oscillation modes present in each energy regime. Moreover, we focus mainly on the SBL appearance experiments LSND and MiniBooNE, the low-energy disappearance experiments DANSS, NEOS and KamLAND, and the LBL accelerator experiment T2K. We also look at probabilities at KARMEN as well as at general atmospheric neutrino experiments (e.g. represented by IceCube and SK).

For the numerical analysis, we adopt the NO best-fit values from Table 2.1 for the standard 3ν PMNS parameters and mass-squared differences:

$$\begin{aligned} &\Delta m^2_{21} = 7.42\times 10^{-5}\text{eV}^2\,, \quad \Delta m^2_{31} = 2.514\times 10^{-3}\text{eV}^2\,, \\ &\sin^2\theta_{12} = 0.304\,, \quad \sin^2\theta_{13} = 0.0222\;, \quad \sin^2\theta_{23} = 0.570. \end{aligned} \tag{3.3.20}$$

Throughout this analysis, we neglect CP-violating phases and matter effects for all SBL experiments. However, we include them for LBL experiments and atmospheric experiments as they tend to play a more pronounced role in these setups.

Interpreting the MiniBooNE excess found as a resonance at $E \sim \mathcal{O}(100\,\text{MeV})$, different combinations of three BSM parameters can accomplish $E_R \sim \sqrt{\cos 2\theta\Delta m^2/\varepsilon}$. In this work, we present a selection of four BMPs where $\Delta m^2 = \mathcal{O}(1\,\text{eV}^2)$ and $\Delta m^2 = \mathcal{O}(10\,\text{eV}^2)$. We discuss phenomenological features of BMPs, aiming to provide the reader with an intuition of the parameter space available. We present BMPs that both can and cannot provide a possible explanation of the anomalies discussed in Section 2.1.3[8]. Note that in the case of one of the anomalies being a statistical fluctuation, an underestimation of a systematic error or not well enough understood nuclear physics effects, this model might still be able provide a good explanation for the global oscillation picture.

The BSM parameter choices of these BMPs are summarized in Table 3.1. Even though the BMPs are far from exhausting the five-dimensional parameter space of the model presented, they illustrate characteristic features and point out strategies to obtain a good fit to at least some of the neutrino anomalies. A fit to global neutrino data requires access to proprietary data of the experimental collaborations, which is beyond the scope of this work.

3.3.4.1 Oscillations at $\Delta m^2_{\textbf{SBL}} = \mathcal{O}(1\,\textbf{eV}^2)$

As indicated in Section 2.1.4, $1\,\text{eV}^2$-oscillations are indicated individually by analyses of the SBL and Gallium anomalies as well as the RAA. We present two BMPs and discuss their viability.

---

[8] The authors of [181] study this scenario and illustrate that it is generally not easy to find a good fit by hand. However, their analysis is restricted to a subset of the parameter space available.

Benchmark Point 1 The BSM parameters of this BMP are listed in Table 3.1 and the corresponding resonance energies are

$$\begin{aligned} E_{R,\eta} &= 303.1\,\text{MeV}, \\ E_{R,\kappa} &= 24.7\,\text{MeV}, \\ E_{R,\xi} &= 24.7\,\text{MeV}\,. \end{aligned} \tag{3.3.21}$$

Figs. 3.4 and 3.3 show the oscillation probabilities for BMP 1 at SBL experiments KARMEN, LSND and MiniBooNE plotted against the neutrino energy. We plot the probabilities of both the standard 3ν paradigm (black) as well as the $(3+3)\nu$+ADR model (red).

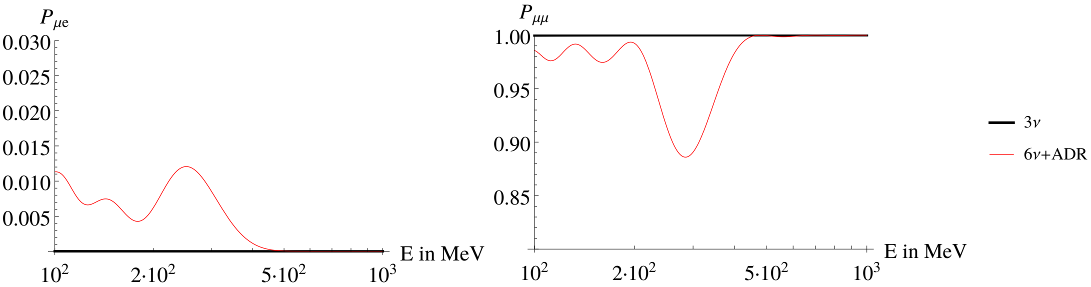

(a) $P_{\nu_\mu \to \nu_e}$ (b) $P_{\nu_\mu \to \nu_\mu}$

Figure 3.3: Appearance (a) and disappearance (b) probabilities at MiniBooNE for BMP 1.

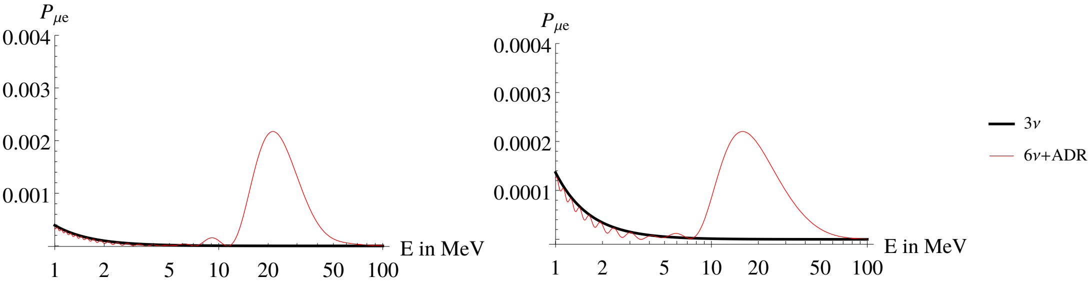

(a) $P_{\nu_\mu \to \nu_e}$@LSND (b) $P_{\nu_\mu \to \nu_e}$@KARMEN

Figure 3.4: LSND (a) and KARMEN (b) oscillation probabilities for BMP 1.

The oscillation probability at LSND features a resonant behavior, which we also find at KARMEN. However, the amplitude of the resonance is one order of magnitude smaller than the one featured at LSND. Since LSND reported on an excess whereas KARMEN did not, this feature is expected from the . At MiniBooNE, a broad resonance at $\sim 250\,\text{MeV}$ is visible. The suppression of $\nu_\mu \to \nu_e$ appearance probability due to the decoupling of the sterile states can be observed at energies $\gtrsim 400\,\text{MeV}$. Furthermore, MiniBooNE is not able to access lower energies than 200 MeV and thus the experiment cannot determine the broadness of the resonance extending to lower energies.

While BMP 1 possibly provides a good fit to both LSND and MiniBooNE, it is already excluded by reactor experiments such as KamLAND. As can be seen in Fig. 3.5, the main oscillation mode of the $(3+3)\nu$+ADR model (red) differs heavily from the standard Δm^2_{21} in the 3ν model (black), which is confirmed by experimental data. It also differs from the oscillation probability in the best fit, simple $(3+1)\nu$ scenario (blue), which features a slight modulation with the additional $\Delta m^2 = 1.3\,\text{eV}^2$.

A better understanding of the oscillation modes present at each energy scale can be gained from plotting all relevant mass-squared differences against the neutrino energy. In Fig. 3.6, we present a logarithmic plot from low energies of 10^{-2} MeV up to very high energies of 100 GeV, so that all relevant experiments are covered. We highlight the different energy regions of the experiments with a color code. The red region corresponds to the energy range of reactor and gallium experiments, the yellow region represents LSND, while the green and purple regions represent MiniBooNE and long baseline experiments, respectively.

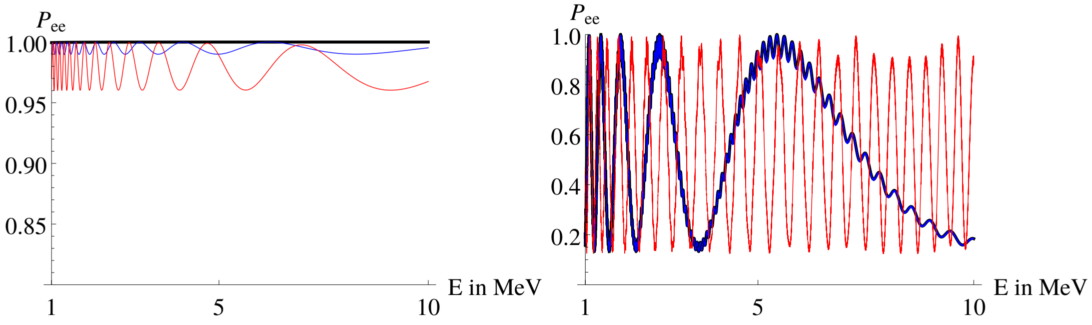

(a) $P_{\nu_e\to\nu_e}$@NEOS (b) $P_{\nu_e\to\nu_e}$@KamLAND

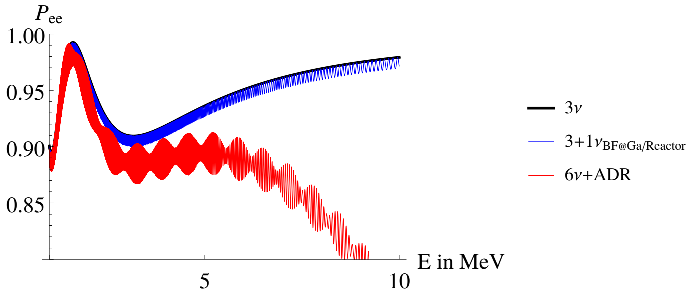

(c) $P_{\nu_e\to\nu_e}$@Daya-Bay

Figure 3.5: Disappearance probabilities at NEOS (a), KamLAND (b) and Daya-Bay (c) for BMP 1. The blue curve shows the global best fit point for a 3+1-scenario for reactor and gallium experiments found by [99] with $\Delta m^2_{\text{BF}} = 1.3\,\text{eV}^2$ and $\sin^2 2\theta_{14} = 0.01$.

Although the equations developed in the Section 3.3.3 still hold at low energies, Fig. 3.6 shows that the effective mass-squared differences have not fully converged at $E \sim \mathcal{O}(1\,\text{MeV})$. This is mainly due to the specific choice of resonance energies. However, an undesired kind of level crossing occurs in this scenario, where the effective Δm^2 drops to zero and the convergence behavior is significantly disturbed.

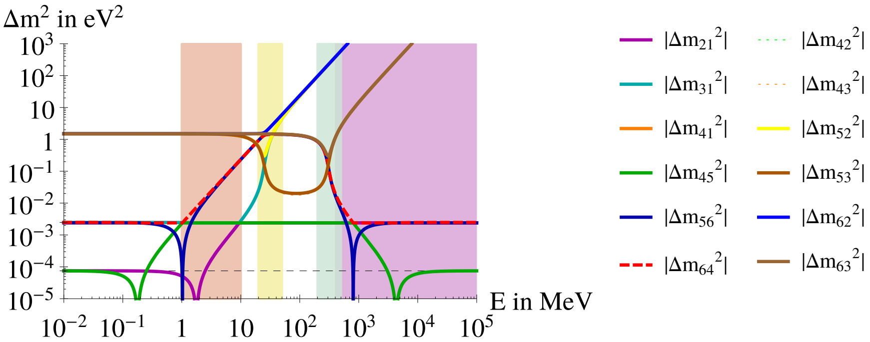

Figure 3.6: Effective Δm^2 depending on the neutrino energy E for BMP 1. The colored regions correspond to the energy ranges of certain experiments: red represents reactor and gallium experiments, yellow represents LSND, green represent MiniBooNE and purple represents long baseline experiments. The dashed black horizontal lines correspond to the standard Δm^2_{21} and Δm^2_{31} in the 3ν model.

This issue can be cured by re-ordering of the relative ADR parameters. In the case where $\eta > \kappa > \xi$, a $\Delta m^2 = 0$ can be avoided at all energies and the convergence behavior can be improved significantly as can be seen in Fig. 3.7. On the other hand, Fig. 3.7 shows that BMP 1 is still not viable with re-ordered parameters, as convergence to the high and low energy limits does not occur sufficiently fast. In order to increase the convergence, the mixing angle can e.g. be decreased or the resonance energies can be chosen close to each other.

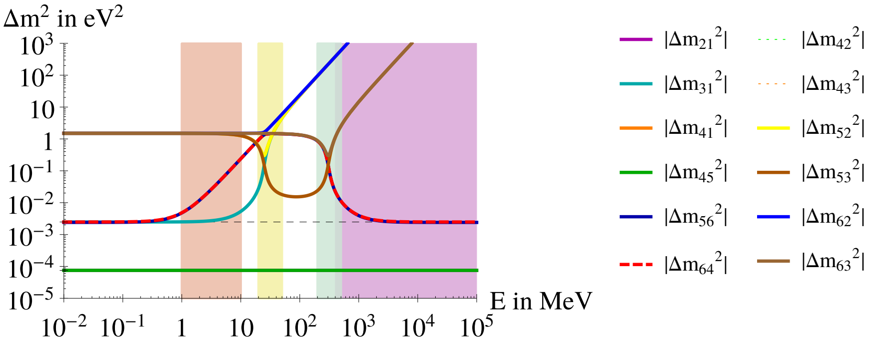

Figure 3.7: Effective Δm^2 depending on the energy E for BMP 1 with re-ordered ADR parameters $\eta > \kappa > \xi$.

Benchmark Point 2 BMP 2 features the BSM parameters listed in Table 3.1 and the corresponding resonance energies are

$$\begin{aligned} E_{R,\eta} &= 62.9\,\text{MeV}, \\ E_{R,\kappa} &= 63.5\,\text{MeV}, \\ E_{R,\xi} &= 207.8\,\text{MeV}\,. \end{aligned} \tag{3.3.22}$$

The corresponding $|\Delta m^2_{ij}(E)|$ are presented in Fig. 3.8.

This set of BSM parameters involves a mixing angle that is smaller by about one order of magnitude compared to BMP 1. The oscillation probabilities at the reactor experiments shown in Fig. 3.9 suggest that the $(3+3)\nu$+ADR model replicates the $(3+1)\nu$ modulation favored

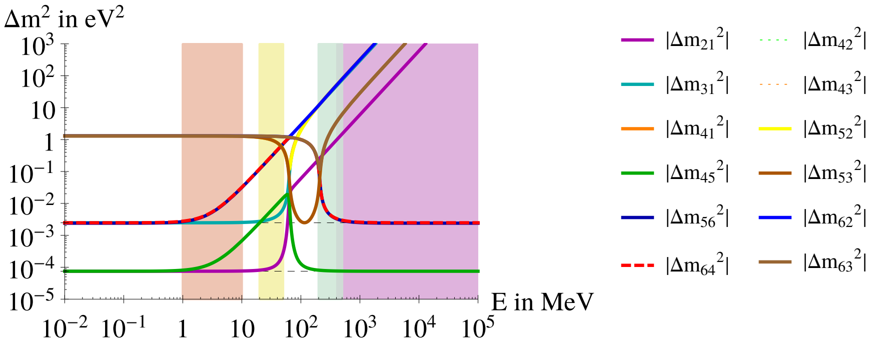

Figure 3.8: Effective Δm^2 depending on the energy E for BMP 2.

by gallium and reactor experiments because of the choice of $\Delta m^2_{\text{SBL}} = \Delta m^2_{\text{BF@Ga/Reactor}}$. This is indicated by the results presented in Fig. 3.8, as Δm^2_{21} completely converges to the standard solar mass-squared difference in the reactor regime (red region) and thus the considerations made in Section 3.3.3 apply.

At MiniBooNE, the resonance of the oscillation probability presented in Fig. 3.10, although at the correct position at $\sim 250\,\text{MeV}$, is heavily suppressed due to the small mixing angle and the subsequently low sterile-to-active conversion rate. The probability at LSND resembles the 3ν model in this scenario, as shown in Fig. 3.11.

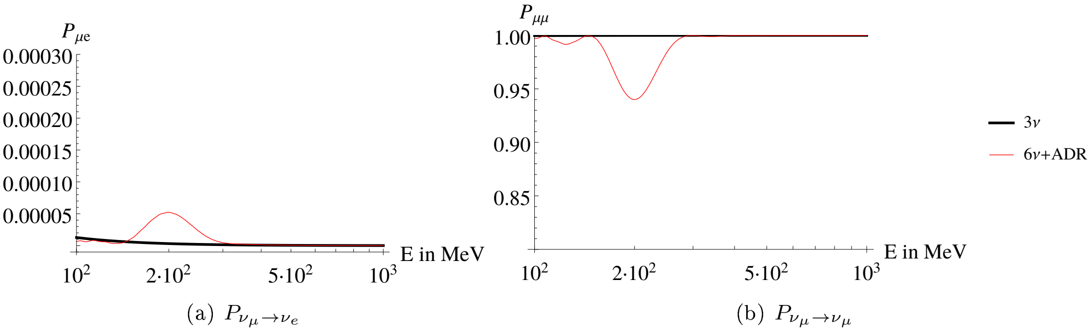

(a) $P_{\nu_\mu \to \nu_e}$

(b) $P_{\nu_\mu \to \nu_\mu}$

Figure 3.10: Appearance (a) and disappearance (b) probabilities at MiniBooNE for BMP 2.

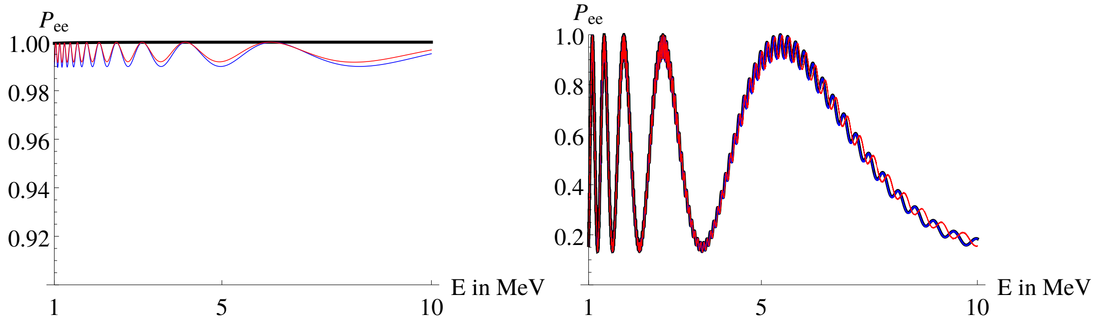

(a) $P_{\nu_e\to\nu_e}$@NEOS (b) $P_{\nu_e\to\nu_e}$@KamLAND

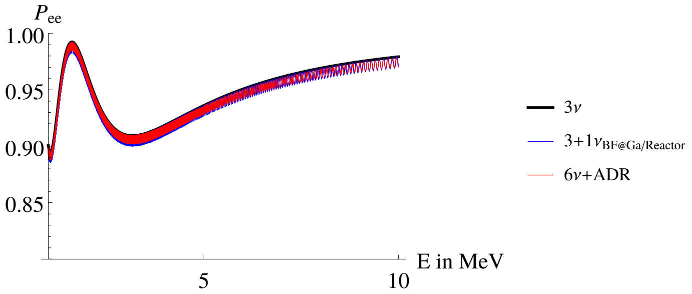

(c) $P_{\nu_e\to\nu_e}$@Daya-Bay

Figure 3.9: Disappearance probabilities at NEOS (a), KamLAND (b) and Daya-Bay (c) for BMP 2. The blue curve shows the global best fit point for a 3+1-scenario for reactor and gallium experiments found by [99] with $\Delta m^2_{\text{BF}} = 1.3\,\text{eV}^2$ and $\sin^2 2\theta_{14} = 0.01$.

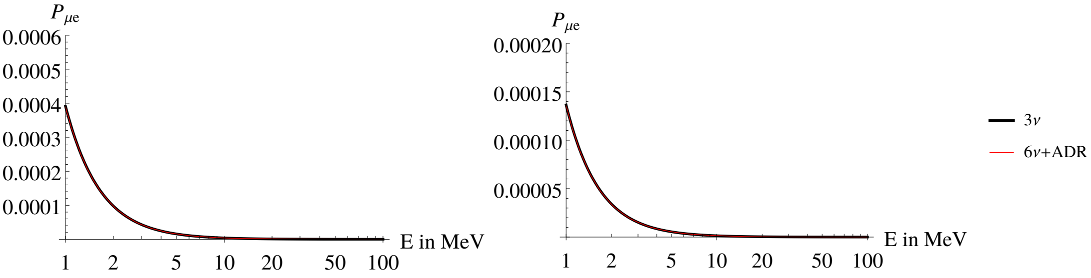

(a) $P_{\nu_\mu\to\nu_e}$@LSND (b) $P_{\nu_\mu\to\nu_e}$@KARMEN

Figure 3.11: LSND (a) and KARMEN (b) oscillation probabilities for BMP 2.

These considerations lead to the conclusion that BMP 2 cannot provide an explanation to the SBL anomalies. However, this set of parameters can still function as a viable candidate for a solution to the Ga/reactor anomaly, since Fig. 3.8 indicates that it is able to reconcile the low energy $(3+1)\nu$ oscillation with the high energy 3ν oscillation pattern. We aim to verify this claim by plotting the oscillation probability at LBL experiments like atmospheric experiments as well as accelerator experiments such as T2K. In Figs. 3.12 and 3.13, we present both appearance and disappearance probabilities. We employ the MCM density profile described in

Section 2.1.2 for atmospheric upward-going neutrinos and a constant density profile of Earth's crust with $\rho \approx 2.8\,{}^{\mathrm{g}}/_{\mathrm{cm}^3}$.

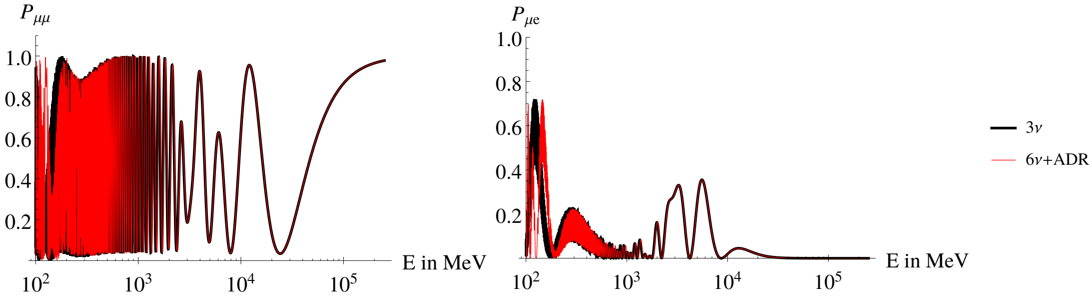

(a) $P_{\nu_\mu \to \nu_\mu}$ (b) $P_{\nu_\mu \to \nu_e}$

Figure 3.12: Disappearance and appearance probabilities of upward going neutrinos at atmospheric experiments for BMP 2 , where $L \sim d_{\mathrm{Earth}}$.

We find the oscillation probabilities of upward-going neutrinos at atmospheric experiments to be in agreement with the 3ν paradigm. The T2K experiment, however, has an increased potential to detect deviations of the ADR model from standard 3ν oscillations. This is due to the comparably low peak energy of the accelerator's neutrino energy spectrum at $E \sim 600\,\mathrm{MeV}$. Since we are inclined to locate the resonance energies at $\mathcal{O}(100\,\mathrm{MeV})$ by design of this model, the convergence behavior of the mass-squared difference at these energies is best constrained by the T2K experiment. The upper row of Fig. 3.13 shows a significant deviation on the level of the oscillation probability at T2K. However, the probability is not directly accessible because of the discrete energy resolution of the experiments. Within the finite energy bins, one typically encounters an averaging effect. We provide a plot of energy-binned versions T2K with a bin size of 200 MeV in the second row of Fig. 3.13. The individual bins do not show a strong deviation of the $(3+3)\nu$+ADR model from the standard 3ν one. This is especially true when we remind ourselves that the statistics of accelerator neutrinos with energies below the peak energy is strongly diminished. We argue that the averaging effect opens an interesting window for an interpretation of results but we acknowledge that a dedicated fit of this model to the T2K data is necessary to place final judgment on this issue.

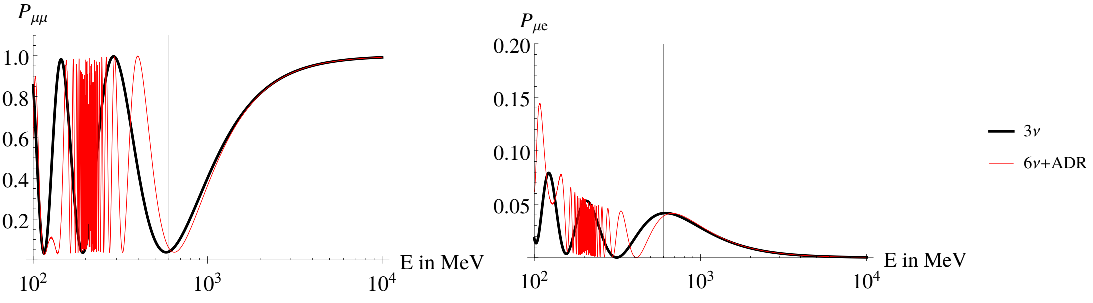

(a) $P_{\nu_\mu \to \nu_\mu}$ (b) $P_{\nu_\mu \to \nu_e}$

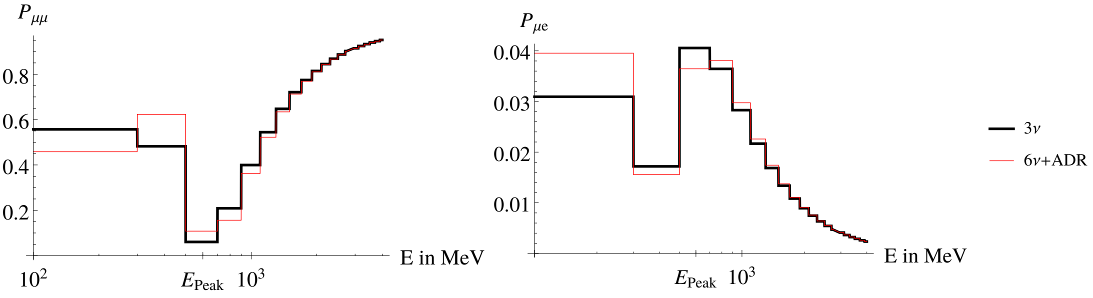

(c) $P_{\nu_\mu \to \nu_\mu}$ (d) $P_{\nu_\mu \to \nu_e}$

Figure 3.13: Disappearance a) and appearance b) probabilities at T2K for BMP 2 and their corresponding binned versions c) and d) with a bin-size of 200 MeV. The grey line indicates the peak energy of the accelerators neutrino spectrum.

3.3.4.2 Oscillations at $\Delta m^2_{\mathbf{SBL}} = \mathcal{O}(10\,\mathbf{eV}^2)$

In this section, we study the regime where $\Delta m^2 = \mathcal{O}(10\,\text{eV}^2)$. We present two BMPs, which provide a resonance at MiniBooNE while simultaneously aiming to respect bounds of LBL and low energy disappearance experiments. To ensure that the resonance energy for MiniBooNE stays at $\sim 250\,\text{MeV}$, the mixing angle θ is chosen smaller than in Section 3.3.4.1 according to Eq. (3.3.7).

Benchmark Point 3 The BSM parameters of BMP 3 are listed in Table 3.1 and the resonance energies in this scenario are

$$\begin{aligned} E_{R,\eta} &= 70.3\,\text{MeV}, \\ E_{R,\kappa} &= 70.7\,\text{MeV}, \\ E_{R,\xi} &= 223.6\,\text{MeV}\,. \end{aligned} \tag{3.3.23}$$

The corresponding mass-squared differences are shown in Fig. 3.14.

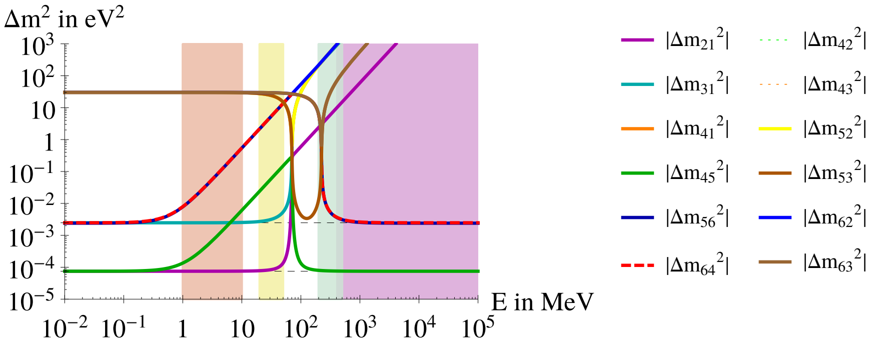

Figure 3.14: Effective Δm^2 depending on the energy E for BMP 3.

In this scenario, all level crossings happen considerably fast in comparison with $\Delta m^2 \sim \mathcal{O}(1\text{eV}^2)$ due to the small mixing angle, leading to a steep slope of $|\Delta m^2(E)|$ around the resonance energies. This behavior thus induces very distinct resonance peaks of the oscillation probability at SBL appearance experiments at these level crossings. Note that the BMP presented here does not aim to solve the LSND anomaly as the resonance energies are not in the required energy range but slightly above (see Fig. 3.16). However, at MiniBooNE we find a distinct resonance with significant amplitude at $E \sim 220\,\text{MeV}$ (see Fig. 3.15).

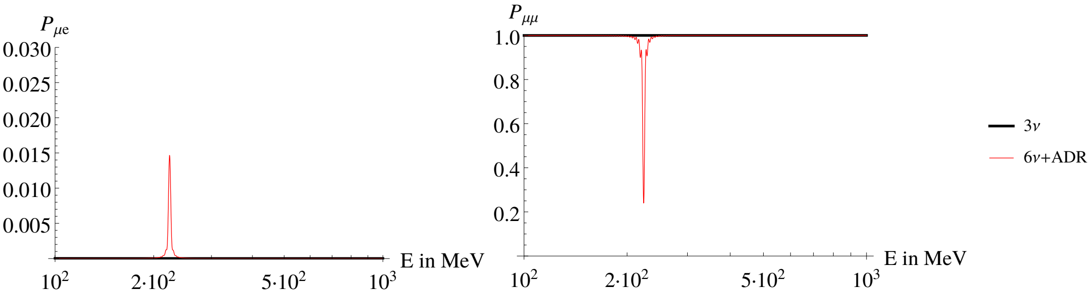

(a) $P_{\nu_\mu \to \nu_e}$ (b) $P_{\nu_\mu \to \nu_\mu}$

Figure 3.15: Appearance (a) and disappearance (b) probabilities at MiniBooNE for BMP 3.

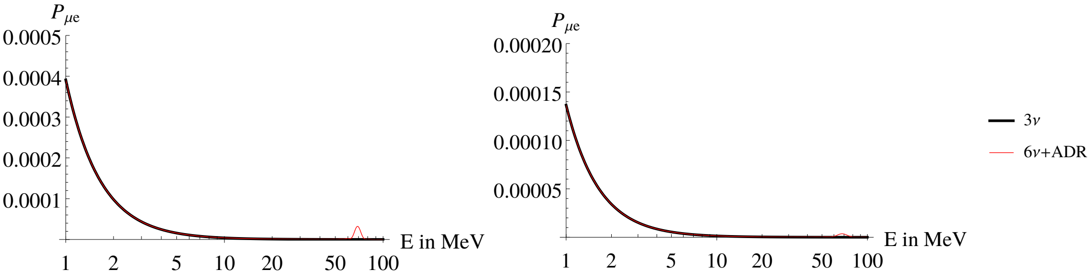

(a) $P_{\nu_\mu \to \nu_e}$@LSND (b) $P_{\nu_\mu \to \nu_e}$@KARMEN

Figure 3.16: LSND (a) and KARMEN (b) oscillation probabilities for BMP 3.

The bounds on the mixing matrix element $|U_{e4}|$ are respected as suggested by the oscillation probabilities at reactor experiments plotted in Fig. 3.17. Generally, the $(3+3)\nu$+ADR scenario behaves like a $(3+1)\nu$ scenario with weak mixing as is expected from Fig. 3.14. At NEOS and Daya-Bay, the 'extra' oscillation is hardly differentiable from the 3ν scenario because of the small amplitude of the modulation. Since KamLAND offers a larger base length, the differences between the $(3+3)\nu$+ADR and 3ν models is slightly more pronounced.

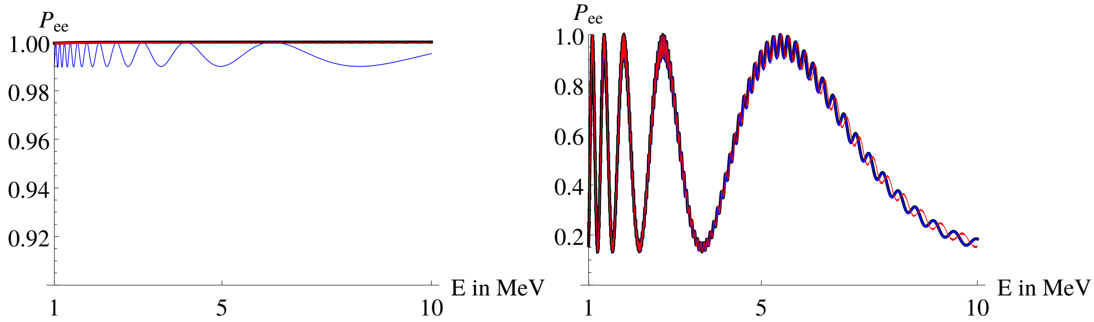

(a) $P_{\nu_e \to \nu_e}$@NEOS

(b) $P_{\nu_e \to \nu_e}$@KamLAND

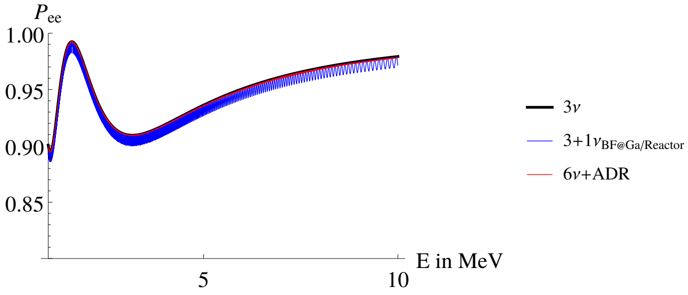

(c) $P_{\nu_e \to \nu_e}$@Daya-Bay

Figure 3.17: Disappearance probabilities at NEOS (a), KamLAND (b) and Daya-Bay (c) for BMP 3. The blue curve shows the global best fit point for a 3+1-scenario for reactor and gallium experiments found by [99] with $\Delta m^2_{\mathrm{BF}} = 1.3\,\mathrm{eV}^2$ and $\sin^2 2\theta_{14} = 0.01$.

The upward-going neutrino channel at atmospheric experiments, depicted in Fig. 3.18, is in good agreement with the standard 3ν oscillation probability. This is a similar trait compared to BMP 2. Another similarity is that averaging effects at T2K are able to conceal the effects of the ADR in the energy region $200 \lesssim E \lesssim 600\,\mathrm{MeV}$. This can be seen in Fig. 3.19.

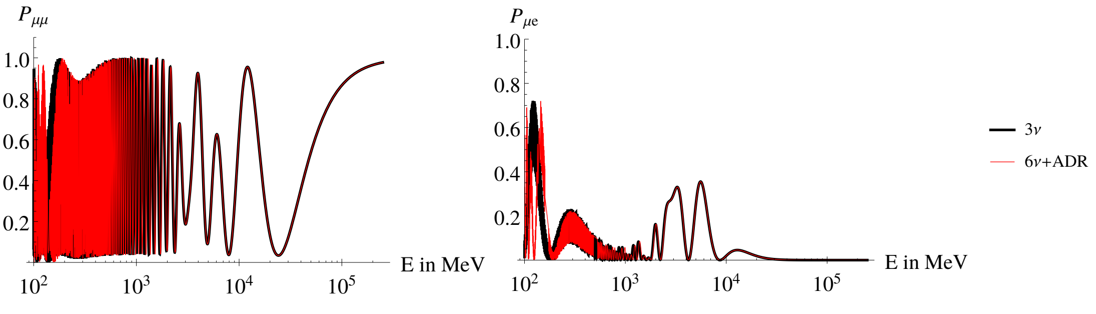

(a) $P_{\nu_\mu \to \nu_\mu}$ (b) $P_{\nu_\mu \to \nu_e}$

Figure 3.18: Disappearance and appearance probabilities of upward going neutrinos at atmospheric experiments for BMP 3 , where $L \sim d_{\text{Earth}}$.

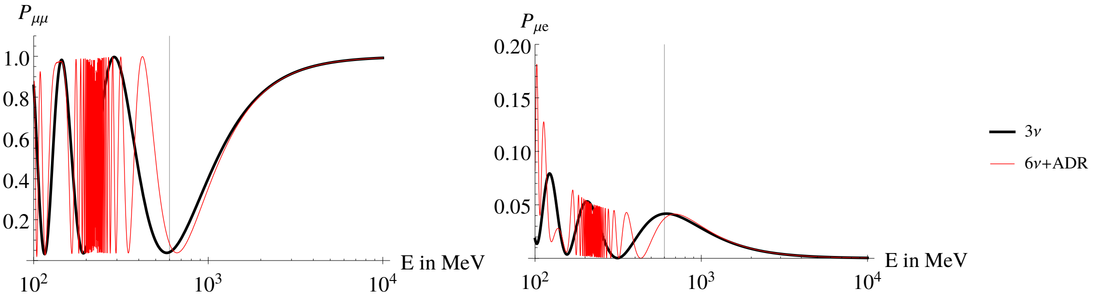

(a) $P_{\nu_\mu \to \nu_\mu}$ (b) $P_{\nu_\mu \to \nu_e}$

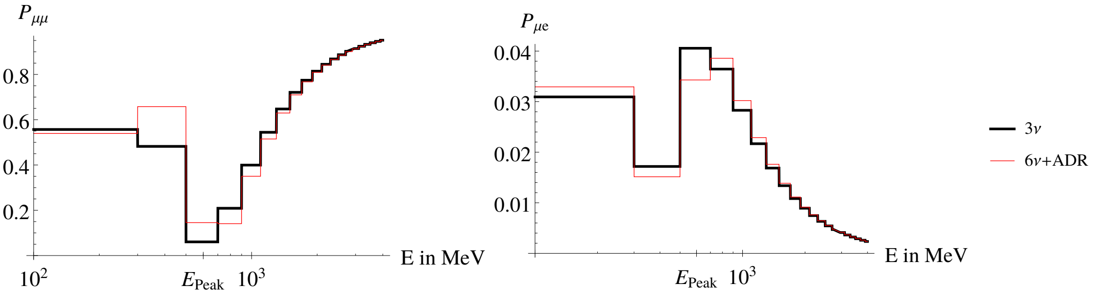

(c) $P_{\nu_\mu \to \nu_\mu}$ (d) $P_{\nu_\mu \to \nu_e}$

Figure 3.19: Disappearance a) and appearance b) probabilities at T2K for BMP 3 and their corresponding binned versions c) and d) with a bin-size of 200 MeV. The grey line indicates the peak energy of the accelerators neutrino spectrum.

Benchmark Point 4 For BMP 4, we choose the BSM parameters listed in Table 3.1 and the corresponding resonance energies are

$$\begin{aligned} E_{R,\eta} &= 22.3\,\text{MeV}, \\ E_{R,\kappa} &= 22.3\,\text{MeV}, \\ E_{R,\xi} &= 223.6\,\text{MeV}\,. \end{aligned} \tag{3.3.24}$$

The mass-squared differences obtained in this scenario are shown in Fig. 3.20.

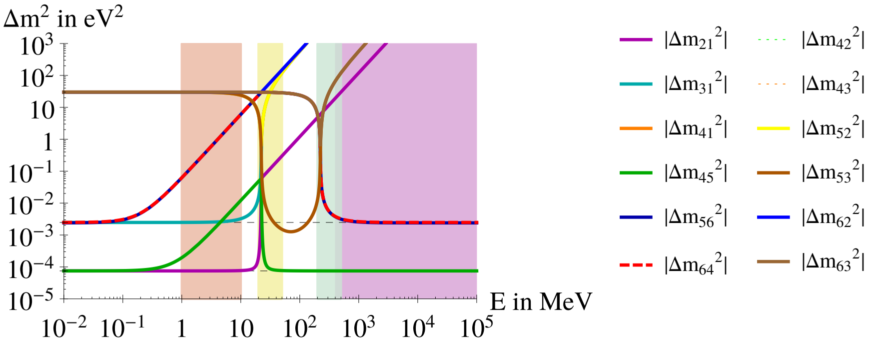

Figure 3.20: Effective Δm^2 depending on the energy E for BMP 4.

Conversely to BMP 3, this scenario features a resonance energy in the LSND range as well as MiniBooNE. KARMEN, as discussed for BMP 1, mirrors the narrow resonance behavior of LSND with ca. 10% of the amplitude. The oscillation probabilities of the SBL experiments are presented in Figs. 3.22 and 3.21. Moreover, the resonance at MiniBooNE is also narrow due to the miniscule mixing angle.

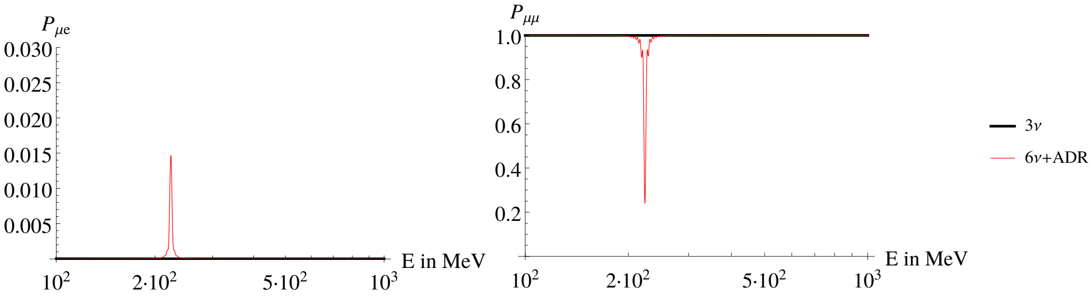

(a) $P_{\nu_\mu \to \nu_e}$

(b) $P_{\nu_\mu \to \nu_\mu}$

Figure 3.21: Appearance (a) and disappearance (b) probabilities at MiniBooNE for BMP 4.

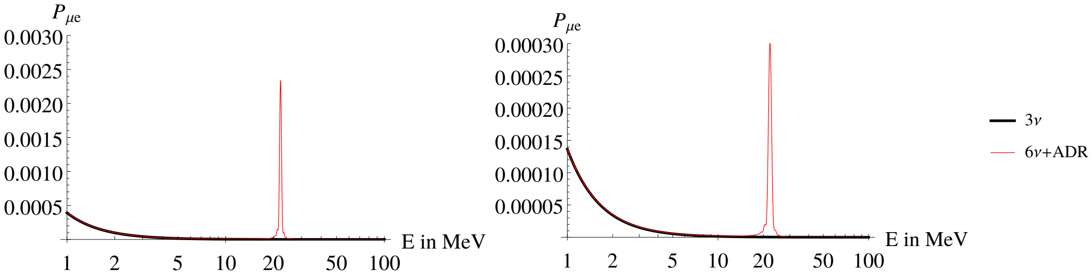

(a) $P_{\nu_\mu \to \nu_e}$@LSND

(b) $P_{\nu_\mu \to \nu_e}$@KARMEN

Figure 3.22: LSND (a) and KARMEN (b) oscillation probabilities for BMP 4.

Due to the level crossing at $E \sim 25\,\mathrm{MeV}$, the convergence in the range of $E \sim 5$-$10\,\mathrm{MeV}$ is not as unobstructed as it is in BMP 3. Thus, the oscillation probabilities at reactor experiments, shown in Fig. 3.23, do not closely resemble the simple $(3+1)\nu$ scenario. At Daya-Bay, for example, the $(3+3)\nu$+ADR average follows the $(3+1)\nu$ average. This way, a simple $(3+1)\nu$ scenario can be mimicked at an experiment like Daya-Bay and KamLAND, while the 3ν is resembled e.g. at NEOS.

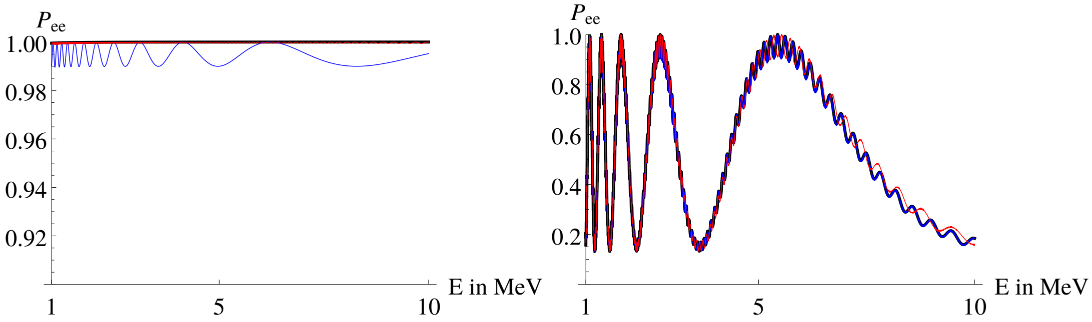

(a) $P_{\nu_e\to\nu_e}$@NEOS (b) $P_{\nu_e\to\nu_e}$@KamLAND

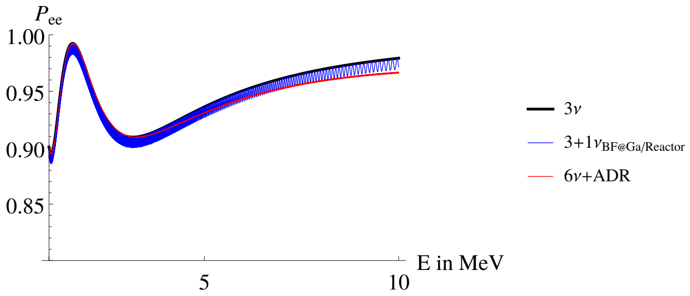

(c) $P_{\nu_e\to\nu_e}$@Daya-Bay

Figure 3.23: Disappearance probabilities at NEOS (a), KamLAND (b) and Daya-Bay (c) for BMP 4. The blue curve shows the global best fit point for a 3+1-scenario for reactor and gallium experiments found by [99] with $\Delta m^2_{\mathrm{BF}} = 1.3\,\mathrm{eV}^2$ and $\sin^2 2\theta_{14} = 0.01$.

The behavior at T2K and atmospheric experiments is the same as in the case of BMP 3. While atmospheric oscillations are the same as they are in the 3ν model, the T2K probability features fast oscillations which are averaged over the size of an energy bin. The numerical results are shown in Figs. 3.24 and 3.25.

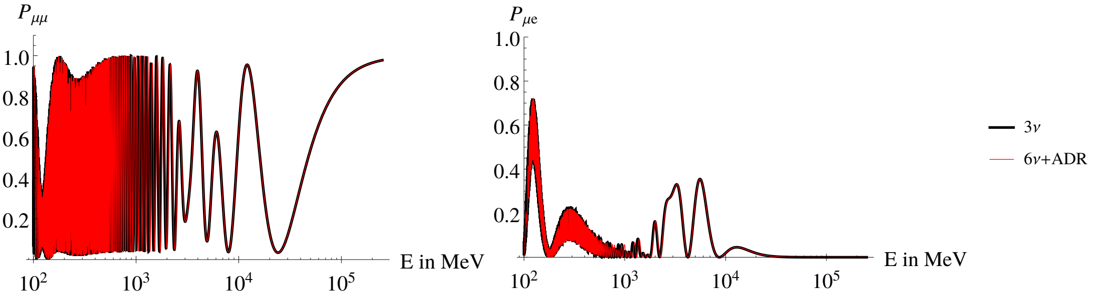

(a) $P_{\nu_\mu \to \nu_\mu}$ (b) $P_{\nu_\mu \to \nu_e}$

Figure 3.24: Disappearance and appearance probabilities of upward going neutrinos at atmospheric experiments for BMP 4 , where $L \sim d_{\text{Earth}}$.

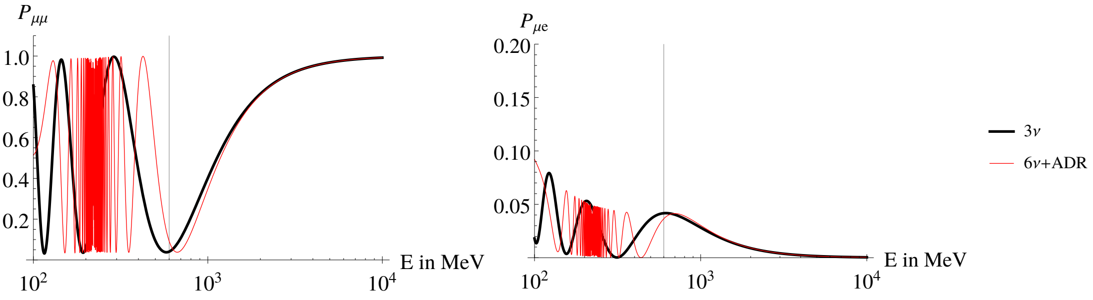

(a) $P_{\nu_\mu \to \nu_\mu}$ (b) $P_{\nu_\mu \to \nu_e}$

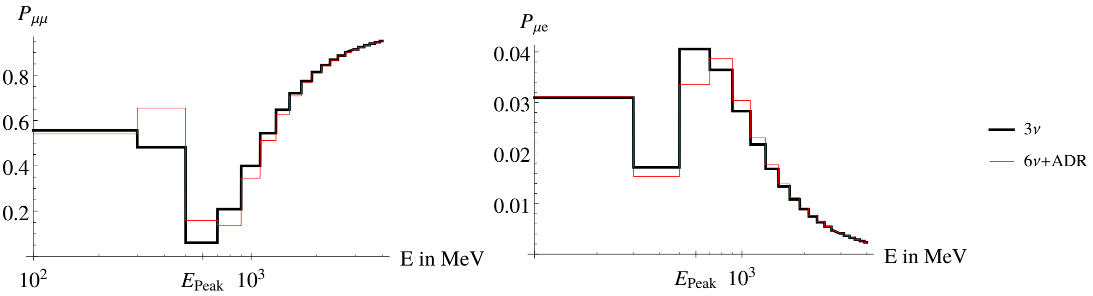

(c) $P_{\nu_\mu \to \nu_\mu}$ (d) $P_{\nu_\mu \to \nu_e}$

Figure 3.25: Disappearance a) and appearance b) probabilities at T2K for BMP 4 and their corresponding binned versions c) and d) with a bin-size of 200 MeV. The grey line indicates the peak energy of the accelerators neutrino spectrum.

3.3.5 Open Questions

In Section 3.3.4 we discussed that the proposed $(3+3)\nu$+ADR model recovers 3ν oscillations far above the resonance energies. However, due to the resonance at around 200 MeV inspired by the MiniBooNE result, the convergence of the effective mass-squared differences in the sub-GeV range at LBL experiments is not completed entirely. Thus, slight deviations from

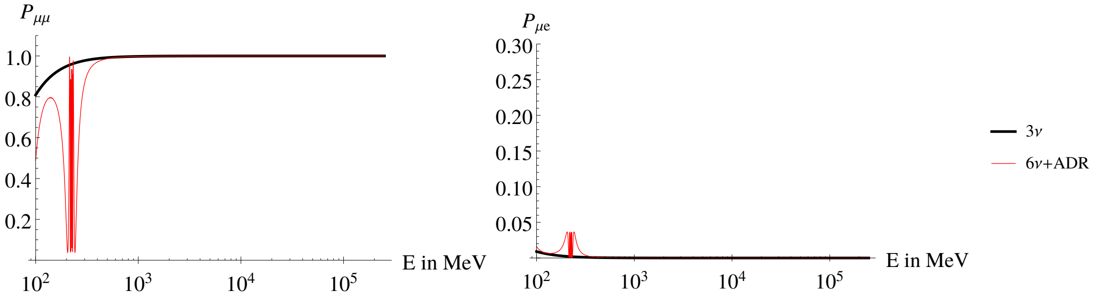

(a) Disappearance @ BMP3

(b) Appearance @ BMP3

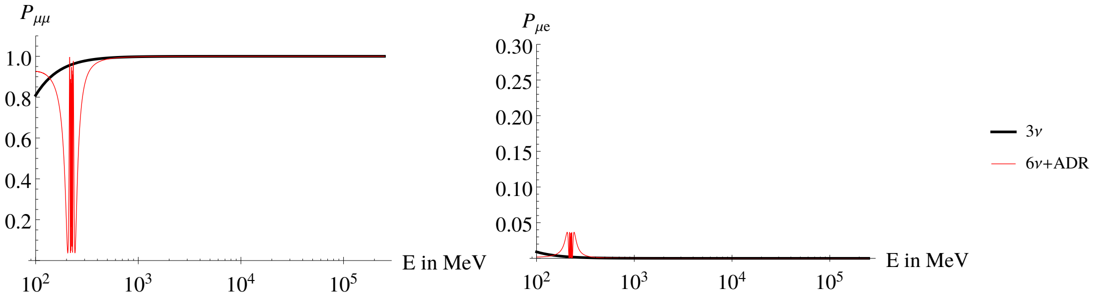

(c) Disappearance @ BMP4

(d) Appearance @ BMP4

Figure 3.26: Probabilities for downward-going neutrinos at atmospheric neutrino experiments that highlight the Sub-GeV to $\sim 100\,\mathrm{GeV}$ region.

the 3ν oscillation pattern can potentially arise. While the upward-going neutrino channels at atmospheric neutrino experiments like IceCube and SK are unperturbed due to the relatively strong matter effects within the earth that push the Δm^2s towards faster convergence, the downward-going neutrinos do not experience such effects.

The oscillation probabilities in this energy regime are presented in Fig. 3.26 for the BMPs 3 and 4. We show both the disappearance and appearance probabilities in comparison to each other. Due to the nature of fast oscillations, we also present a binned version of Fig. 3.26 in Fig. 3.27. The $(3+3)\nu$+ADR model indeed deviates from the simple 3ν pattern in the low sub-GeV range. However, at this stage, we contain ourselves from judging about whether the predicted oscillation patterns are excluded by current experiments. The exclusion limits proposed in the literature concerning the simple $(3+1)\nu$ model, analyzed in e.g. [182, 183], cannot be congruently applied for this model. Moreover, the energy spectra of neutrinos from recent analyses (e.g. [184]) indicate that there is very little statistics in the energy range below $200\,\mathrm{MeV}$ at SK. Additionally, a recent IceCube analysis [185] found hints towards an additional $\Delta m^2 \sim 8\,\mathrm{eV}^2$ oscillation. This might represent a slight indication of a deviation from the 3ν picture in the present data. Whether or not this model fits the atmospheric and accelerator data as well as the 3ν model in the sub-GeV region can be determined in a dedicated fit to the collaborations' data.

Furthermore, the CMB measurement is able to put bounds on the presence of eV-scale sterile neutrinos in the early universe in the framework of standard cosmology. As discussed in Section 2.3.1, the relativistic degrees of freedom $g_*(T)$ present during the radiation dominated era change the Hubble parameter $H \sim \sqrt{g_*(T)}$. More significantly, they can consequently influence the ratio abundances of light elements, which is well modeled by the standard theory

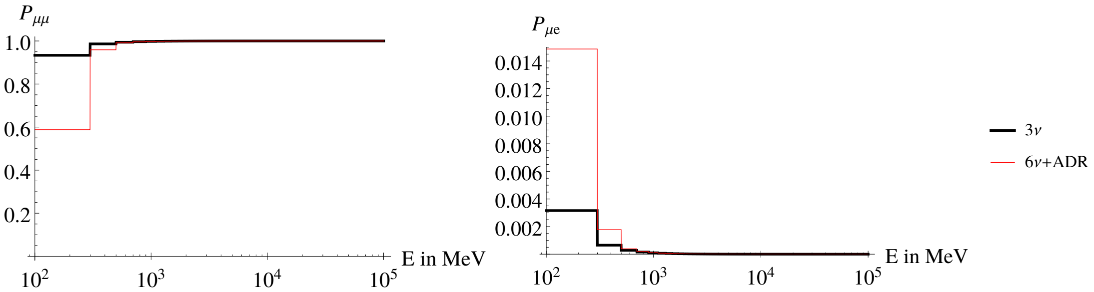

(a) Disappearance @ BMP3 with bins (b) Appearance @ BMP3 with bins

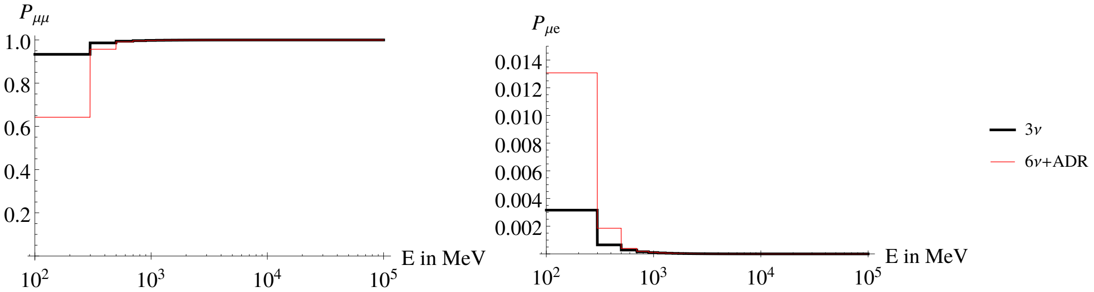

(c) Disappearance @ BMP4 with bins (d) Appearance @ BMP4 with bins

Figure 3.27: Probabilities for downward-going neutrinos at atmospheric neutrino experiments with finite energy resolution. Bin size is 200 MeV.

of BBN. Another constraint from the CMB measurement is the sum of the neutrino masses $\sum_i m_i < 0.12\,\text{eV}$, which is one order of magnitude below the eV scale.

As proposed in [166] and further studied in [171, 186], ADR scenarios effectively suppress the mixing of active and sterile neutrinos at energies above the resonance. This can act as a suppression mechanism of sterile neutrinos populations in the early universe. However, in the simplest resonance suppression scenario the resonance energies discussed in this work are too large in order to avoid a sterile neutrino population at the energy scales relevant for BBN and neutrino decoupling. Besides these concerns, it is conceivable that the ADR depends on temperature and density, as e.g. in extra-dimensional ADR models where the entries of the stress-energy tensor in the EFE obtain additional terms due to the large radiation density in the early universe. The resulting modifications in the metric can ultimately influence the dispersion relation and may help suppress the production of sterile neutrinos below the MeV scale. This mechanism is, however, strongly model dependent and not discussed in more detail in this thesis.

Furthermore, it was shown that large relic neutrino asymmetries of $L_\nu = {}^{(N_\nu - N_{\bar{\nu}})}\!/_{N_\gamma} \gtrsim 10^{-5}$ in the early universe can reconcile the simple sterile neutrino hypothesis with BBN bounds [187]. This is also consistent with the naïve bound of $L_\nu \lesssim 10^3$ from the upper limit on the universe's total energy density. Combining this mechanism with an ADR suppression mentioned above can possibly open large parts of the parameter space without obstructing successful BBN.

BMP	MiniBooNE	LSND	Ga/Reactor	Consistency with HE constraints
BMP1	✓	✓	✗	✗
BMP2	✗	✗	✓	✓
BMP3	✓	✗	✗	✓
BMP4	✓	✓	?	✓

Table 3.2: Overview of the phenomenological achievements of the BMPs chosen in this thesis. Ticks indicate that the BMP possess the main feature for a solution and crosses indicate that the model is ruled out.

3.4 Summary

In this work, we developed a $(3+3)\nu$ framework with an altered dispersion relation in order to explain combinations of the LSND, MiniBooNE, Reactor and Gallium anomalies.

We discussed the fatal flaws in the constructions of $(3+1)\nu$+ADR and $(3+3)\nu$++universal ADR models, leading to the proposed $(3+3)\nu$+individual ADRs model.

In a $(3+1)\nu$+ADR model, a relic oscillation at high energies persists although the predominantly sterile state decouples far above the resonance, ruling out the model due to non-observation of such a fast oscillation at atmospheric and LBL accelerator experiments.

To cure the issue of high energy relic oscillations, we first presented a $(3+3)\nu$ model with a universal ADR for all sterile states. We chose the respective mass differences of the six mass eigenstates to lie within two sets of the same mass differences found in the 3ν model. We found that no relic oscillation at high energy occurs if a democratic mixing scenario is employed, where the mixing angles $\theta_{41}, \theta_{52}, \theta_{63}$ are chosen to be the same. Due to an effective symmetric flavor swapping between the set of mass eigenstates that are predominantly sterile and the set of predominantly active mass eigenstates at the resonance, the 3ν mass-squared differences are preserved and the standard oscillation pattern re-emerges.

However, the main motivation for this work, a resonant neutrino oscillation solution of the SBL anomalies, is unattainable in such a scenario, since the oscillation probability at these experiments is miniscule due to unitarity cancellations. This fact led us to a modification of the model, allowing individual potentials for each sterile state. Subsequently, the modification led to different resonance energies, effectively lifting unitarity conditions that induce the vanishing of the amplitude at SBL experiments. The $(3+3)\nu+$ individual ADRs model possesses the same behavior far above the resonances and thus does not suffer from the flaws of the $(3+1)\nu$ model. It can also mimic a simple $(3+1)\nu$ model at low energies, which proves to be favored by current global fits to low energy reactor and gallium experiments.

We presented different BMPs that point out characteristic features of the model in the extended parameter space. While we did not present a parameter configuration which can explain all anomalies at once, resigning either the Ga-/Reactor-, LSND- or MiniBooNE anomaly can complete the rest of the picture. The achievements of each BMP are summarized in Table 3.2.

While it is possible that the various neutrino anomalies are due to our limited understanding of experimental backgrounds, this BSM scenario is testable by the upcoming MicroBooNE experiment, and may be observed first in sub-GeV atmospheric neutrino data.

Chapter 4

Fermionic Singlet Dark Matter in One-Loop Solutions to the R_K Anomaly: A Systematic Study

In this chapter, we present a systematic study of the DM phenomenology of the model class proposed in Reference [48], addressing the R_K (and also $(g-2)_\mu$) anomaly at one-loop level. We focus on models with fermionic singlet DM candidates and examine the compatibility of a solution to the R_K anomaly with bounds from DD and achieving the observed DM relic density (RD). The results of this work are published in [2] [1].

We structure this chapter in the following way: In Section 4.1, we review the model class presented in [48] and discuss constraints on the relevant couplings in Section 4.2. In Section 4.3, we briefly discuss the DM phenomenology of this model. We present the results of the numerical study in Section 4.4 and summarize them in Section 4.5.

4.1 The Model

Reference [48] analyzes a class of models introducing three new BSM fields that contribute to $b \to s\mu\mu$ transitions at one-loop level. These new fields can also add sizable contributions to the anomalous magnetic moment of the muon ($(g-2)_\mu$). The authors find that 48 different charge assignments can be made for the BSM field, allowing gauge group representations as far as the adjoint representation. The BSM particle content is implemented in two different ways. Realization a contains two scalars, ϕ_Q and ϕ_L, and one vector-like fermion ψ. Realization b on the other hand features one scalar field ϕ and two vector-like fermionic fields, ψ_Q and ψ_L. The indices Q and L indicate that these fields couple directly only to quarks or leptons, respectively, while the indexless fields have couplings to both types of SM fermions. The Lagrangians of both model realizations read

$$\mathcal{L}^{\text{a}}_{\text{int}} = \Gamma_{Q_i}\bar{Q}_i P_R \psi \phi_Q + \Gamma_{L_i}\bar{L}_i P_R \psi \phi_L + \text{h.c.} \tag{4.1.1}$$

$$\mathcal{L}^{\text{b}}_{\text{int}} = \Gamma_{Q_i}\bar{Q}_i P_R \psi_Q \phi + \Gamma_{L_i}\bar{L}_i P_R \psi_L \phi + \text{h.c.}\,, \tag{4.1.2}$$

---

[1] Two of the ten model studies presented in this work were also published in one of my collaborators' PhD thesis [188].

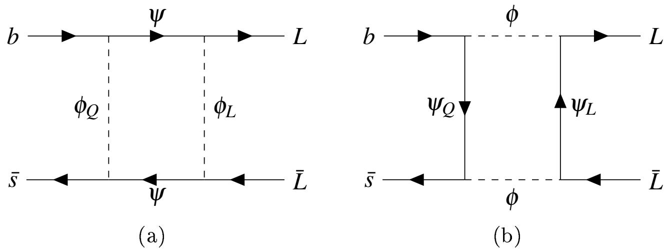

Figure 4.1: Box diagram contributions to $\mathcal{O}_9/\mathcal{O}_{10}$. a and b denote the different model realizations described by the Lagrangians in Eq. (4.1.1) and 4.1.2.

where L_i and Q_i are the left-handed lepton/quark doublets and i denotes the flavor index. Note that the Lagrangians in Eqs. (4.1.1) and (4.1.2) indicate that the BSM fields only couple to left-handed fermions of the SM. This feature is motivated by the fact that a scenario, where the Wilson coefficients $\mathcal{C}_9$ and $\mathcal{C}_{10}$ of the operators

$$\mathcal{O}_9 = (\bar{s}\gamma^\nu P_L b)(\bar{\mu}\gamma_\nu\mu), \quad \mathcal{O}_{10} = (\bar{s}\gamma^\nu P_L b)(\bar{\mu}\gamma_\nu\gamma^5\mu) \tag{4.1.3}$$

fulfill the requirement $\mathcal{C}_9 = -\mathcal{C}_{10}$, is one of the scenarios preferred by global fits to LFUV data (see e.g. [189, 190]). The operators are part of the operator basis that makes up the effective Hamiltonian

$$\mathcal{H}_{\text{eff}}^{b\to s\mu\mu} = -\frac{4G_F}{\sqrt{2}} V_{tb}V_{ts}^* \frac{\alpha_{\text{em}}}{4\pi} \sum \mathcal{C}_i\mathcal{O}_i\,. \tag{4.1.4}$$

This condition corresponds to a vector−axial-vector structure reproduced by couplings that are proportional to the left-handed chiral projector P_L. In this model, the operators obtain their main contribution from box diagrams depicted in Fig. 4.1. The contributions of photon penguin diagrams are demonstrated to be small in [48], so that $\mathcal{C}_9 \approx C_9^{\text{box}}$.

An important part of the coupling structure are the gauge group representations of the BSM fields. Table 4.1 presents all possible charge assignments up to the adjoint representation. Apart from the above mentioned realization type, which is denoted by a lower case Latin letter a or b, a model is classified by a roman numeral I-VI, which describes the $SU(2)_L$-representations of the BSM fields and a capital Latin letter A-D specifying the representations under $SU(3)_C$. For example, the model aIA contains the fields $\psi = (\mathbf{1},\mathbf{1})_X, \phi_L = (\mathbf{1},\mathbf{2})_{-X-1/2}, \phi = (\mathbf{3},\mathbf{2})_{-X+1/6}$. The possible combinations of these categories thus amount to $2 \times 6 \times 4 = 48$ different charge assignments.

Regarding the $U(1)_Y$ charge, Table 4.1 contains a free parameter X, which is defined as the hypercharge of ψ in model realization a or the negative hypercharge of ϕ in realization b. This parameter is w.l.o.g. chosen in units of $1/6$ in the interval $X \in [-1,1]$.

Since we are only interested in models containing a single particle DM candidate, which has to be colorless and electrically neutral, the $SU(3)_C$-representations of the categories C and D can be omitted from our analysis, since they do not contain a singlet representation. This requirement therefore effectively halves the number of viable models. Table 4.2 lists all models that contain a possible singlet DM candidate[2]. Since the fermionic singlet can either have Dirac or Majorana nature, $5 \times 2 = 10$ different models are studied in this work. Note that all BSM particles are assigned an odd charge under a discrete, DM-stabilizing $\mathcal{Z}_2$ symmetry, while SM particles are even.

---

[2] The model only contains a singlet if the parameter X is chosen such that the hypercharge of the DM candidate vanishes.

$SU(2)_L$	ϕ_Q,ψ_Q	ϕ_L,ψ_L	ψ,ϕ
I	**2**	**2**	**1**
II	**1**	**1**	**2**
III	**3**	**3**	**2**
IV	**2**	**2**	**3**
V	**3**	**1**	**2**
VI	**1**	**3**	**2**
$SU(3)_C$			
A	**3**	**1**	**1**
B	**1**	$\bar{\mathbf{3}}$	**3**
C	**3**	**8**	**8**
D	**8**	$\bar{\mathbf{3}}$	**3**
Y			
	$^1\!/_6 \mp X$	$-^1\!/_2 \mp X$	$\pm X$

Table 4.1: All possible choices for the combinations of representations of the BSM particles. The upper sign of ± belongs to a-type models, the lower to b-type models. The electric charge can be determined via $Q = T_3 + Y$, where T_3 is the third component of the weak isospin.

fermionic singlet	scalar singlet
aIA	aIIA
bIIA	aIIB
bIIB	aVA
bVA	aVIB
bVIB	bIA

Table 4.2: Models containing a singlet DM candidate. Only the models containing a fermionic singlet DM candidate, highlighted in red, are considered in this thesis.

4.2 Constraints on Couplings

In this section, we discuss the constraints on the couplings introduced in this model class. We consider the implications of the R_K and $(g-2)_\mu$ observables on the BSM Yukawa couplings Γ_{Q_i} and Γ_{L_i} as well as constraints for parameters of the extended scalar potential from requirements of vacuum stability and perturbativity.

4.2.1 Constraints on the BSM Yukawa

First of all, we assume that BSM Yukawa couplings Γ_d and Γ_e to the first generation are negligibly small[3]. This is a phenomenologically-driven feature, as it facilitates the explanation of R_K while simultaneously weakening mass bounds on BSM particles from colliders. Further following [48], we find the Wilson coefficients from the box diagram to be

$$\mathcal{C}_9^{\text{box,a/b}} = -\mathcal{C}_{10}^{\text{box,a/b}} \sim \frac{\Gamma_s \Gamma_b^* |\Gamma_\mu|^2}{M^2_{\psi/\phi}}\,. \tag{4.2.1}$$

---

[3] Note that the couplings $\Gamma_{d,s,b}$ are understood in the mass eigenbasis, while the couplings in Eqs. (4.1.1) and (4.1.2) are defined in the weak eigenbasis and can therefore be related via CKM rotations.

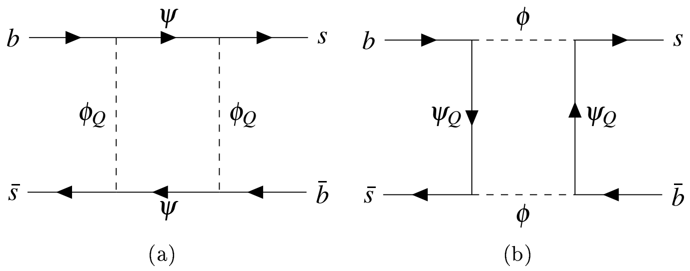

Figure 4.2: Box diagram contributions to B-$\bar{B}$ mixing. a and b denote the different model realizations.

The full expressions for the Wilson coefficients can be found in Appendix B. Global EFT fits [190] to the LFUV data constrain $\mathcal{C}_9 = -\mathcal{C}_{10}$ to be

$$\mathcal{C}_9 = -\mathcal{C}_{10} \in [-0.46, -0.29] \tag{4.2.2}$$

at the $2\,\sigma$ level. However, additional constraints on the couplings come from B-$\bar{B}$ meson mixing, which also receives contributions from box diagrams shown in Fig. 4.2 in this model. As this process does not involve leptons, the Wilson coefficient $\mathcal{C}_{B\bar{B}}$, which is defined as the coefficient of the only operator of

$$\mathcal{H}^{\text{eff}}_{B\bar{B}} = \mathcal{C}_{B\bar{B}}\,(\bar{s}_\alpha \gamma^\nu P_L b_\alpha)\,(\bar{s}_\beta \gamma_\nu P_L b_\beta)\ , \tag{4.2.3}$$

is only proportional to the quark BSM Yukawas as

$$\mathcal{C}^{\text{a/b}}_{B\bar{B}} \sim \frac{(\Gamma_s \Gamma_b^*)^2}{M^2_{\psi/\phi}}\,, \tag{4.2.4}$$

where the current bounds at $2\,\sigma$ are [191]

$$\mathcal{C}_{B\bar{B}} \in [-2.1{,}0.6] \cdot 10^{-5}\text{TeV}^{-2}\,. \tag{4.2.5}$$

With these premises, we can place an upper bound on the product of the quark Yukawas $\Gamma_s\Gamma_b^*$ from B-$\bar{B}$ mixing and use this to construct a lower bound on the leptonic coupling Γ_μ. These constraints are of the form

$$\Gamma_s \Gamma_b^* \leq \mathcal{B}^{\text{model}}_{bs}\,(\kappa)\,\frac{M_{\text{DM}}}{\text{GeV}}\,, \tag{4.2.6}$$

$$\Gamma_\mu \geq \mathcal{B}^{\text{model}}_{\mu}\,(\kappa)\,\sqrt{\frac{M_{\text{DM}}}{\text{GeV}}}\,, \tag{4.2.7}$$

where $\mathcal{B}^{\text{model}}_{\mu/bs}(\kappa)$ are model dependent coefficient functions. These functions are listed in Table 2 in Appendix B for each model .

Additionally, this model can induce sizable contributions to $\Delta a_\mu = {}^{(g-2)_\mu}/_2$ via the diagrams depicted in Fig. 4.3 [4]. These contributions generally scale like

$$\Delta a^{\text{a/b}}_\mu \sim \frac{m_\mu^2 |\Gamma_\mu|^2}{M^2_{\psi/\phi}}\,. \tag{4.2.8}$$

---

[4] Models that are similar to this setup can overcome parts of suppression with the small lepton mass e.g. by introducing a fourth BSM field ψ'/ϕ' that mixes with ψ/ϕ and induces a chirality flip in the loop [192].

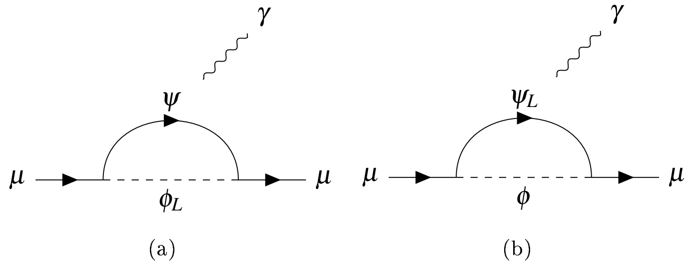

Figure 4.3: Loop diagram contributions to $(g-2)_\mu$ in this model. a and b denote the different model realizations.

Recently, the $g-2$ collaboration reported on a combined $4.2\,\sigma$ deviation of the measurements at Fermilab and BNL from the theoretical value obtained in the SM, where the difference $\Delta a_\mu \equiv \Delta a_\mu^{\text{Exp}} - \Delta a_\mu^{\text{SM}}$ amounts to [56]

$$\Delta a_\mu = (251 \pm 59) \cdot 10^{-11}\,. \tag{4.2.9}$$

This automatically translates into a DM mass dependent bound on the muon BSM Yukawa coupling Γ_μ. These bounds are also model dependent and are summarized in Table 3 in Appendix B.

We assume the non-DM BSM particles to be mass degenerate and we further introduce the dimensionless mass gap parameter

$$\kappa = \begin{cases} {}^{M_{\phi_Q}}\!/\!{}_{M_\psi} = {}^{M_{\phi_L}}\!/\!{}_{M_\psi}\,, & \text{in a-type models} \\ {}^{M_{\psi_Q}}\!/\!{}_{M_{\psi_L}} = {}^{M_\phi}\!/\!{}_{M_{\psi_L}}\,, & \text{in } \psi_L\text{-DM b-type models} \\ {}^{M_{\psi_L}}\!/\!{}_{M_{\psi_Q}} = {}^{M_\phi}\!/\!{}_{M_{\psi_Q}}\,, & \text{in } \psi_Q\text{-DM b-type models}\,, \end{cases} \tag{4.2.10}$$

which quantifies the the ratio between non-DM BSM- and DM particles in the model. As we mentioned earlier, our focus is on single-component fermionic singlet DM. To achieve this, we require the non-DM BSM particles to decay sufficiently fast. Therefore, the decay rate of these particles has a lower bound, which in turn translates to the condition [193]

$$(\kappa - 1) M_{\text{DM}} > m_\pi\,. \tag{4.2.11}$$

4.2.2 Constraints on Parameters of the Scalar Potential

Depending on the model realization, the scalar sector of the SM is extended by one (b) or two (a) scalar fields. With this extension, the scalar potential obtains additional mass and interaction terms, which introduce new mass parameters μ_i and quartic couplings λ_i. To preserve the DM stabilizing $\mathcal{Z}_2$-symmetry, we assume that no other scalar field than the $SU(2)_L$-doublet scalar field H acquires a vev. Throughout all our calculations, we demand perturbativity of all quartic couplings, which leads to

$$|\lambda_i| \leq (4\pi)^2\,. \tag{4.2.12}$$

We also restrict ourselves to models that respect vacuum stability at tree-level. This condition, however, is dependent on the field content of the model and thus we have to carry out a case analysis regarding the model realizations a and b.

a-Type Models Compared to the SM, a-type models feature two additional scalar fields. The most general scalar potential in this scenario is therefore

$$\begin{aligned}V_{\text{scalar}} =&\mu_H^2 H^\dagger H + \mu_{\phi_Q}^2 \phi_Q^\dagger \phi_Q + \mu_{\phi_L}^2 \phi_L^\dagger \phi_L \\ &+ \lambda_H \left(H^\dagger H\right)^2 + \lambda_{\phi_Q}\left(\phi_Q^\dagger\phi_Q\right)^2 + \lambda_{\phi_L}\left(\phi_L^\dagger\phi_L\right)^2 \\ &+ \lambda_{\phi_Q,H,1}\left(\phi_Q^\dagger\phi_Q\right)\left(H^\dagger H\right) + \lambda_{\phi_L,H,1}\left(\phi_L^\dagger\phi_L\right)\left(H^\dagger H\right) \\ &+ \lambda_{\phi_Q,H,2}\left(\phi_Q^\dagger H\right)\left(H^\dagger\phi_Q\right) + \lambda_{\phi_L,H,2}\left(\phi_L^\dagger H\right)\left(H^\dagger\phi_L\right) \\ &+ \lambda_{\phi_L,\phi_Q,1}\left(\phi_L^\dagger\phi_L\right)\left(\phi_Q^\dagger\phi_Q\right) + \lambda_{\phi_L,\phi_Q,2}\left(\phi_L^\dagger\phi_Q\right)\left(\phi_Q^\dagger\phi_L\right) \\ &+ \left[\lambda_{\phi_Q,H,3}\left(\phi_Q^\dagger H\right)^2 + \text{h.c.}\right] + \left[\lambda_{\phi_L,H,3}\left(\phi_L^\dagger H\right)^2 + \text{h.c.}\right] \\ &+ \left[\lambda_{\phi_L,\phi_Q,3}\left(\phi_Q^\dagger\phi_L\right)^2 + \text{h.c.}\right] .\end{aligned} \tag{4.2.13}$$

Adopting the limits from [194], the vacuum stability bounds at tree-level for this kind of potential read

$$\lambda_H,\lambda_{\phi_Q},\lambda_{\phi_L} > 0 \tag{4.2.14}$$

$$\begin{aligned}\lambda_{\phi_L,\phi_Q,1} + \lambda_{\phi_L,\phi_Q,2} &> -2\sqrt{\lambda_{\phi_Q}\lambda_{\phi_L}} \\ \lambda_{\phi_L,H,1} + \lambda_{\phi_L,H,2} &> -2\sqrt{\lambda_H\lambda_{\phi_L}} \\ \lambda_{\phi_Q,H,1} + \lambda_{\phi_Q,H,2} &> -2\sqrt{\lambda_{\phi_Q}\lambda_H} \\ \left|\lambda_{\phi_L,\phi_Q,3}\right| &< \left|\lambda_\alpha\right|, \left|\lambda_{\alpha,\beta,i}\right|\end{aligned} \tag{4.2.15}$$

where $\alpha \in [\phi_Q, \phi_L, H]$ and $i \in [1,2,3]$. Note that the assumption of mass degeneracy in the non-DM dark sector requires the Higgs portal couplings $\lambda_{\phi_L,H,2}$ and $\lambda_{\phi_Q,H,2}$ to vanish, as they contribute unevenly to the masses of the scalar degrees of freedom after EWSB. Moreover, for the $\mathcal{Z}_2$-symmetry to be intact after EWSB, we require the other Higgs portal couplings to satisfy the condition

$$\lambda_{\phi_L,H,1}, \lambda_{\phi_Q,H,1} < \frac{2}{v^2}\kappa^2 M_{\text{DM}}^2 . \tag{4.2.16}$$

b-Type Models In b-type models, there exists another scalar doublet ϕ in addition to H. The most general form of the scalar potential in this realization is consequently

$$\begin{aligned}V_{\text{scalar}} =&\mu_H^2 H^\dagger H + \mu_\phi^2 \phi^\dagger\phi + \lambda_H\left(H^\dagger H\right)^2 + \lambda_\phi\left(\phi^\dagger\phi\right)^2 \\ &+ \lambda_{\phi,H,1}\left(\phi^\dagger\phi\right)\left(H^\dagger H\right) + \lambda_{\phi,H,2}\left(\phi^\dagger H\right)\left(H^\dagger\phi\right) + \left[\lambda_{\phi,H,3}\left(\phi^\dagger H\right)^2 + \text{h.c.}\right] .\end{aligned} \tag{4.2.17}$$

We apply the vacuum stability limits of [195, 196], leading to the conditions

$$\begin{aligned}\lambda_\phi,\lambda_H &> 0, \\ \lambda_{\phi,H,1} &> -2\sqrt{\lambda_\phi\lambda_H}, \\ \lambda_{\phi,H,1} + \lambda_{\phi,H,2} - \left|2\lambda_{\phi,H,3}\right| &> -2\sqrt{\lambda_\phi\lambda_H} .\end{aligned} \tag{4.2.18}$$

Similarly to a-type models, we require the Higgs portal couplings to allow for mass degeneracy of the non-DM BSM particles and preserve the DM-stabilizing $\mathcal{Z}_2$. We obtain

$$\lambda_{\phi,H,1} < \frac{2}{v^2}\kappa^2 M_{\mathrm{DM}}^2 \tag{4.2.19}$$

$$\lambda_{\phi,H,2} = 0\,. \tag{4.2.20}$$

Note that since the Higgs portal term that is proportional to $\lambda_{\phi,H,3}$ vanishes in all models of our setup, we cannot create neutrino masses via the scotogenic radiative mass mechanism discussed in Section 2.2.4.

4.3 Dark Matter Phenomenology

In this section, we discuss estimates for DM observables in this model class. We can subdivide the models into three classes by their couplings to the SM particles: *leptophilic, quarkphilic* and *amphiphilic*. The full numerical results obtained with MICROMEGAs 5.0 are presented in Section 4.4.

4.3.1 Relic Density

As indicated in Eq. (2.3.39), the dark matter relic density (DMRD) is related to the effective annihilation cross section σ_{eff} of DM[5]. This cross section can be characterized solely by direct annihilations of DM particles or can alternatively receive large contributions from coannihilations of heavy dark sector particles, sometimes called coannihilation partners, in the case of a mass gap $\kappa \lesssim 1.2$. In some parts of the parameter space, these coannihilations can even become the dominant annihilation channels. If we assume that conversions among dark sector particles are efficient during freeze out and non-DM dark sector particles decay fast enough, it is possible to reduce the system of coupled Boltzmann equations to a single, effective Boltzmann equation.

$$\frac{\mathrm{d}Y_{\mathrm{DM}}}{\mathrm{d}x} = -\sqrt{\frac{\pi}{45}}\frac{M_{\mathrm{Pl}}\,M_{\mathrm{DM}}\,g_{*,\text{eff}}^{\frac{1}{2}}}{x^2}\langle\sigma_{\text{eff}}v\rangle\left(\tilde{Y}^2 - (\tilde{Y}^{\mathrm{eq}})^2\right)\,, \tag{4.3.1}$$

which is of the form described in Eq. (2.3.27) and where the overall yield $\tilde{Y}$ is defined as

$$\tilde{Y}^{\mathrm{eq}} = \begin{cases} \sum_{i=\phi_L,\phi_Q,\psi} Y_i^{\mathrm{eq}}, & \text{for a-type models} \\ \sum_{i=\psi_L,\psi_Q,\phi} Y_i^{\mathrm{eq}}, & \text{for b-type models}\,, \end{cases} \tag{4.3.2}$$

depending on the particle content of the model. The individual equilibrium yields can be expressed as

$$Y_{\mathrm{DM}}^{\mathrm{eq}} = \frac{90}{(2\pi)^{\frac{7}{2}}}\frac{g_{\mathrm{DM}}}{g_{*s}}x^{\frac{3}{2}}\exp\left(-x\right), \tag{4.3.3}$$

$$Y_{\text{non-DM}}^{\mathrm{eq}} = \frac{90}{(2\pi)^{\frac{7}{2}}}\frac{g_{\text{non-DM}}}{g_{*s}}\left(\kappa x\right)^{\frac{3}{2}}\exp\left(-\kappa x\right), \tag{4.3.4}$$

---

[5] Since the main interest of this work is the compatibility of DM with the R_K results, we require the muon BSM Yukawa coupling to be relatively large and thus DM is necessarily thermally produced via the freeze out mechanism.

where $g_{(\text{non-})\text{DM}}$ is the sum of degrees of freedom of (non-)DM particles. The effective thermally averaged cross section $\langle \sigma_{\text{eff}} v \rangle$ is described by the sum of the averaged cross sections of the various annihilation channels weighted by the ratio of the individual equilibrium densities and the summed equilibrium densities (see Eq. (2.3.43)).

In general, the DMRD is calculated numerically by solving the effective Boltzmann equation described in Eq. (4.3.1). In our setup, the heavier dark sector particles can have all sorts of representations under the SM gauge groups and can thus interact e.g. with gluons, EW vector bosons and the Higgs. These interactions can contribute to a large degree in coannihilation scenarios. In this work, we calculate the DMRD via the C++-based package micrOMEGAs [125, 126], which in turn calculates all particle physics matrix elements with the inbuilt calcHEP package [197]. The calcHEP model files are created with the calcHEP interface of FeynRules [198, 199].

However, in the simple case where there are there are only negligible contributions from coannihilations, the DMRD can be estimated from the leading order velocity contribution of the annihilation cross section of direct annihilations of DM[6]. Since we only consider fermionic singlet DM candidates, these direct annihilations are mediated by Yukawa interactions, which involve the new BSM Yukawa couplings Γ_i. Assuming that the DM particle is heavier than SM fermion pair that it annihilates into, we can express the leading order contribution to the thermally averaged cross section as

$$
\begin{aligned}
\sigma_{\text{eff},0} = {} & \frac{1}{4\pi M_{\text{DM}}^2} \frac{1}{\left(1+\kappa^2\right)^2} \left[C_l^m \Gamma_\mu^4 + 3 C_q^m \left(\Gamma_b^2 + \Gamma_s^2\right)^2 \right] \\
& \times \begin{cases} \frac{1}{4}, & \text{for Dirac DM} \\ \left(1+\kappa^4\right)\left(1+\kappa^2\right)^{-2}, & \text{for Majorana DM}\ , \end{cases}
\end{aligned}
\tag{4.3.5}
$$

where $\sigma_{\text{eff},0}$ is defined as the leading order coefficient of an expansion of $\langle \sigma_{\text{eff}} v \rangle$ in inverse powers of x (as discussed in Section 2.3.2) and $C_{l/q}^m$ are model dependent coefficients. The coefficients $C_l^{\text{bIIB}}, C_l^{\text{bVIB}}, C_q^{\text{bIIA}}$, and C_q^{bVA} vanish, while the remaining six coefficients are equal to 1.

Requiring the generation of the observed DMRD, we find the expression

$$
\begin{aligned}
\left[C_l^m \Gamma_\mu^4 + 3 C_q^m \left(\Gamma_b^2 + \Gamma_s^2\right)^2 \right] \approx {} & 1.65 \cdot 10^{-7} \left(\frac{M_{\text{DM}}}{\text{GeV}} \right)^2 \\
& \times \begin{cases} \left(1+\kappa^2\right)^2, & \text{for Dirac DM} \\ 5.6 \left(1+\kappa^4\right)^{-1} \left(1+\kappa^2\right)^4, & \text{for Majorana DM}\ . \end{cases}
\end{aligned}
\tag{4.3.6}
$$

Examining the properties of these considerations for different models, we find three different subclasses, leptophilic, quarkphilic and amphiphilic which can be characterized as the following

1. Leptophilic DM (bIIA,bVA)
   In this scenario Eq. (4.3.6) results in a scaling behavior $\Gamma_\mu = \mathcal{B}_{\text{RD}}^m(\kappa) \sqrt{M_{\text{DM}}/\text{GeV}}$, where $\mathcal{B}_{\text{RD}}^m(\kappa)$ is a model-dependent coefficient function. A comparison of this result with the lower bound on Γ_μ for a successful explanation of the R_K anomaly, given in Eq. (4.2.7), leads to a lower bound on the mass gap parameter $\kappa > \kappa_0^m$ for a possible simultaneous explanation of R_K and DM of

$$
\kappa_0^{\text{bIIA,Dir}} \approx 11.8\,, \quad \kappa_0^{\text{bIIA,Maj}} \approx 4.7\,, \quad \kappa_0^{\text{bVA,Dir}} \approx 26.5\,, \quad \kappa_0^{\text{bVA,Maj}} \approx 10.9 \tag{4.3.7}
$$

---

[6] Note further that in the case of Dirac DM, the relic density is given by the sum of particle and antiparticle contributions

2. Quarkphilic DM (bIIB,bVIB)
   In this subclass, the observed DMRD is achieved for $\left(\Gamma_s^2 + \Gamma_b^2\right) \sim \mathcal{B}_{\mathrm{RD}}^{m}(\kappa)\, ^{M_{\mathrm{DM}}}\!/_{\mathrm{GeV}}$. The product of Γ_s and Γ_b is constrained from above by $B - \bar{B}$-mixing, given in Eq. (4.2.6). The annihilation cross section is proportional to the sum $\Gamma_s^2 + \Gamma_b^2$ and can therefore not be constrained from B-$\bar{B}$ mixing, since either the second or third generation coupling can be chosen arbitrarily small. However, we obtain an upper bound on the annihilation cross section by setting $\Gamma_s \sim 0$ and $\Gamma_b = 4\pi$ at its perturbative limit [7]. We find $M_{\mathrm{DM}} \leq 16\pi^2 \cdot \left[\mathcal{B}_{\mathrm{RD}}^{m}(\kappa)\right]^{-1}$ GeV. For the four different configurations we find

$$M_{\mathrm{DM,max}}^{\mathrm{bIIB}} = M_{\mathrm{DM,max}}^{\mathrm{bVIB}} \approx \frac{674\,\mathrm{TeV}}{1+\kappa^2}\,, \quad M_{\mathrm{DM,max}}^{\mathrm{bIIB,Maj}} = M_{\mathrm{DM,max}}^{\mathrm{bVIB,Maj}} \approx \frac{254\,\mathrm{TeV}\sqrt{1+\kappa^4}}{\left(1+\kappa^2\right)^2} \tag{4.3.8}$$

3. Amphiphilic[8] DM (aIA)
   In this subclass, both couplings to leptons an quarks are present. We can apply the results derived in the two scenarios above if $\Gamma_\mu \gg \Gamma_q$ or $\Gamma_q \gg \Gamma_\mu$.

4.3.2 Direct Detection

The discussion in this section deals with the direct detection observables affected by the particles introduced in this model. We briefly discuss how we apply the limits set by DD experiments to our numerical analysis.

4.3.2.1 General Procedure

Depending on the subclass, tree-level contributions to the DM-nucleon cross section can arise (quarkphilic, amphiphilic) or be absent (leptophilic). However, these contributions are suppressed by parton distribution functions (PDFs), since the coupling to the first generation quarks tiny[9].

In all subclasses of models, DM-quark interactions mediated by t-channel-type interactions arise on one-loop level. Figure 4.4 schematically shows the interaction of the DM particle χ and quarks via t-channel exchange of the fundamental SM bosons.

In this work, we use FeynRules [198, 199] and its interface with FeynArts [200] and FormCalc [201] and/or FeynCalc to calculate effective vertices of the form $\bar{\chi}\,(H/Z_\mu/A_\mu)\,\chi$ in the zero-outer-momentum limit. For this, we use the explicit expressions for *Passarino-Veltman integrals* defined in [202]. We include these effective vertices in the calcHEP files, which are used by micrOMEGAs to calculate contributions to DM-nucleon cross sections up to one-loop level.

The estimates for the SI and SD DM-nucleon cross section can be extracted from Section 2.3.3.

The experimental bounds on the SI and SD DM-nucleon cross sections are stated under the assumption that the DM candidate in question constitutes all of the observed DMRD $\Omega_{\mathrm{DM}}h^2$. Therefore, if the produced RD $\Omega_\chi h^2$ of the DM candidate χ is smaller than the observed DMRD, the bounds have to be rescaled according to

$$\sigma_{\mathrm{DD}} \leq \frac{\Omega_{\mathrm{DM}}}{\Omega_\chi}\mathrm{Bound}(m_\chi) \tag{4.3.9}$$

---

[7] Note that the second generation BSM quark Yukawa coupling Γ_s cannot be chosen arbitrarily large, as it is constrained from D-$\bar{D}$ mixing.

[8] From Greek ἀμφί (*amphi*) eng.: on both sides and φιλία (*philia*) eng.: love, affection

[9] Even though Γ_d is assumed to vanish in this setup, a very small Γ_u is generated via CKM-rotations.

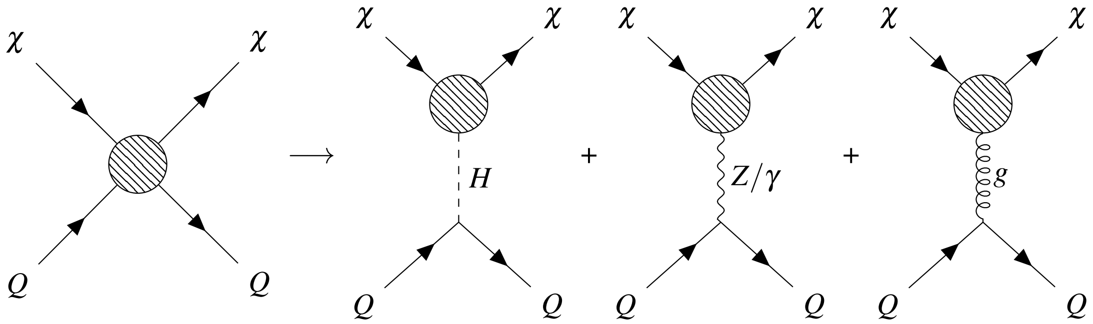

Figure 4.4: Schematic overview of several t-channel diagrams contributing to the DM-nucleon cross section.

to be consistent with the DD bounds presented by the experimental collaborations. As the rescale factor $\Omega_{\mathrm{DM}}/\Omega_\chi$ is > 1 for *underproduced* χ-DM, the DD bounds get *relaxed*. Note that technically, we tighten the DD bounds for overproduced DM with this definition of the rescaling. However, we do not regard parameter space that features overabundant DM as viable and thus the DD results in this region are of little interest in the first place[10].

4.3.2.2 Twist-2 Contributions to the SI DM-Nucleon Cross Section

In models where there is no unsuppressed contribution to the SI cross section from quark operators at leading order, twist-2 operators become important. While the twist-2 quark operators originate from a higher order expansion of the propagator of tree-level quark diagrams, gluonic twist-2 operators generated by the box-diagrams shown in Fig. 4.5 have to be considered.

The SI cross section receives additional contributions from these diagrams. The Wilson coefficients and the subsequent SI DM-nucleon cross section is derived in e.g. [204]. The DD phenomenology package of MICROMEGAS automatically takes the contributions of box diagrams to the SI DM-nucleon cross section into account.

$$\begin{aligned}
\sigma^{\mathrm{SI}} &\sim \left(\frac{m_\chi m_N}{m_{\mathrm{med}} + m_N}\right)^2 \left| -\frac{8\pi}{9\alpha_s} 0.8 f_G + \frac{3}{4} 0.416 \left(g_G^{(1)} + g_G^{(2)}\right)\right|^2 , \\
f_G &\approx \frac{\alpha_s \Gamma_{s/b}^2 m_\chi}{192\pi} \frac{m_\chi^2 - 2m_{\mathrm{med}}^2}{m_{\mathrm{med}}^2 \left(m_{\mathrm{med}}^2 - m_\chi^2\right)^2} , \\
g_G^{(1)} &\approx \frac{\alpha_s \Gamma_{s/b}^2}{96\pi m_\chi^3 (m_{\mathrm{med}}^2 - m_\chi^2)} \left[-2m_\chi^4 \log\left(\frac{m_q^2}{m_{\mathrm{med}}^2}\right) - m_\chi^2 (m_{\mathrm{med}}^2 + 3m_\chi^2) \right. \qquad (4.3.10) \\
&\quad \left. + (m_{\mathrm{med}}^2 - 3m_\chi^2)(m_{\mathrm{med}}^2 + m_\chi^2) \log\left(\frac{m_{\mathrm{med}}^2}{m_{\mathrm{med}}^2 - m_\chi^2}\right)\right] , \\
g_G^{(2)} &\approx \alpha_s \Gamma_{s/b}^2 \frac{-2m_{\mathrm{med}}^2 m_\chi^2 + 2(m_{\mathrm{med}}^2 - m_\chi^2)^2 \log\left(\frac{m_{\mathrm{med}}^2}{m_{\mathrm{med}}^2 - m_\chi^2}\right) + 3m_\chi^4}{48\pi m_\chi^3 (m_{\mathrm{med}}^2 - m_\chi^2)^2} .
\end{aligned}$$

The contributions play an important role in the SI direct detection procedure in quarkphilic/amphiphilic DM Majorana models, since they feature a strong suppression of the SI DM-quark interactions,

---

[10] Conversely to MICROMEGAS, some program packages like MADDM have an inbuilt rescaling of this kind. However, they do not tighten the bounds but rather use a step function [203]

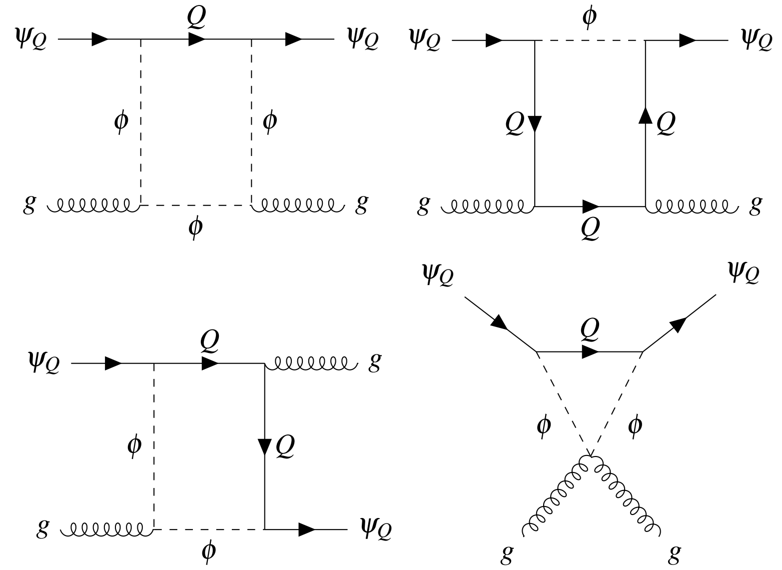

Figure 4.5: Leading order diagrams for DM-gluon scattering.

which are more severely constrained by experiments, and simultaneously feature direct vertices of DM and quarks and therefore also scalar particles that carry color charge.

4.3.3 Indirect Detection

We briefly address possible constraints on the parameter space from indirect detection in this section.

As described in Section 2.3.4, models that feature unsuppressed s-wave annihilation can be best constrained by photon searches from dSphs. In our set of models, this only applies to models with a Dirac-type DM candidate. The interesting parameter space of these models, i.e. the regions where a solution to R_K can potentially reside, is however already excluded by DD bounds. Conversely, models with Majorana-type DM candidates exhibit p-wave annihilation of DM $\sigma(\bar{\chi}\chi \to \bar{f}f) \sim v^2$ and thus cannot be constrained by broad photon spectrum searches from dSphs. Therefore, we do not consider these limits in Section 4.4.

However, we apply the limits found in searches for VIB spectral features in the photon spectrum, since the velocity suppression of DM annihilation is lifted in the channel $\bar{\chi}\chi \to \bar{f}f\gamma$ in Majorana models. We employ the limits on the thermally averaged cross section $\langle\sigma v\rangle_{\bar{f}f\gamma} + 2\langle\sigma v\rangle_{\gamma\gamma}$ obtained by [164] in an analysis of Fermi-LAT and HESS data. The authors present these limits in scenarios, where the mass ratio of DM and other dark sector particles is $\kappa = 1.01, 1.1, 2$. For κ larger than 2, VIB quickly becomes negligible since the cross section is proportional to κ^{-4}. We therefore do not investigate its impact on non-coannihilation scenarios.

Similarly to the DD case, we rescale the experimental constraints with the ratio of the observed DMRD and the RD of the DM candidate χ as

$$\sigma_{\mathrm{ID}} \leq \left(\frac{\Omega_{\mathrm{DM}}}{\Omega_\chi}\right)^2 \mathrm{Bound}(m_\chi)\,. \tag{4.3.11}$$

In this case, however, this ratio is squared, since the event rate of annihilations is proportional to the square of the number density of DM. This is intuitive, since the annihilation diagram features two DM particles in the initial state.

The results of our analysis show that the relevant parameter space *cannot* be constrained by VIB even for coannihilation scenarios. This is mainly due to the quadratic RD rescaling of the bounds. For large couplings Γ to SM fermions, the DM annihilation cross section can be sizable. However, the corresponding parameter points usually feature a strongly underproduced RD of the DM candidate in question, so that the bounds from ID via VIB are relaxed to a large degree. For the relevant plots, see Appendix C.

4.3.4 Collider Searches

In this section, we briefly review collider searches for particles contained in this work. Although the results of existing searches cannot be directly applied to the setup studied in this work, we can extract indications of the parameter space that is possibly exlcuded. We stress that in our analysis, we concentrate mainly on the DM observables and do not perform an extensive collider study on our own, as it is considered beyond the scope of this work.

In theory, b-type models that feature color-charged fermions can be constrained by displaced vertex (DV) + E_{miss}^T searches at colliders, if the values of the BSM Yukawa couplings Γ_i are small enough for these particles to be sufficiently long-lived on collider scales. Results of such searches [205] can be recast into limits on the mass and lifetime of the long-lived particle [206] (see Figure 6 of this reference). We translated the bounds in the M-$c\tau$-plane to limits in the M-Γ-plane by calculating the decay width of the long-lived particle depending on the Yukawa coupling Γ. The results of this analysis, however, suggests that we can only rule out Yukawa couplings in the range $\Gamma \in \left[10^{-5}, 10^{-2}\right]$ and masses up to 1.8 TeV. This due to the fact that the ATLAS detector has a finite size (lower limit on Γ) and also a finite resolution to detect a DV (upper limit on Γ). This region of BSM Yukawa couplings, however, proves to be uninteresting, as solutions for the R_K and $(g-2)_\mu$ typically require couplings $\mathcal{O}(10^{-1})$ (in amphiphilic models) or larger.

The most interesting collider signatures of leptophilic DM models involve decays of colored BSM particles that can be e.g. pair produced efficiently via gluon fusion. The process depicted in Fig. 4.6 can e.g. constrained by LHC searches for dilepton + jets + E_{miss}^T [207, 208]. The authors of Reference [209] e.g. suggest that masses of $M_{\psi_L} \lesssim 600$ GeV for $M_{\psi_Q} \lesssim 800$ GeV can be ruled out by dilepton searches.

In quarkphilic scenarios, ψ_Q-DM particles can be produced, besides other processes, by quark annihilation via a t-channel process mediated by the color-charged scalar ϕ. These scenarios can be constrained by LHC searches for monojet + E_{miss}^T signatures [210, 211]. Diagrams that induce such signatures in the quarkphilic DM subclass are shown in Fig. 4.7. A translation of these bounds to our model rules out a sizable area in the M_ϕ-M_{ψ_Q}-plane at $\Gamma_Q = 1$, where the highest ruled-out DM mass corresponds to the point $(M_{\psi_Q}, M_\phi) \approx (650\,\text{GeV}, 700\,\text{GeV})$, which corresponds to a coannihilation scenario with a mass gap of $\sim 8\%$. The highest constrained M_ϕ can be found at $M_\phi \approx 1.7\,\text{TeV}$ for very low DM masses, corresponding to a highly non-coannihilating scenario. For more details, see Figure 8 in Reference [211].

The only amphiphilic model that features a fermionic singlet DM candidate ψ, aIA, can also be constrained by the monojet + E_{miss}^T searches used to constrain the quarkphilic models, as it also features a color-charged scalar ϕ_Q. Thus, similar limits on the masses are expected.

4.4 Results

In this section, we present the results of our numerical analysis. At first, we discuss our analysis strategy before we address each model's results individually. We begin with the subclass of

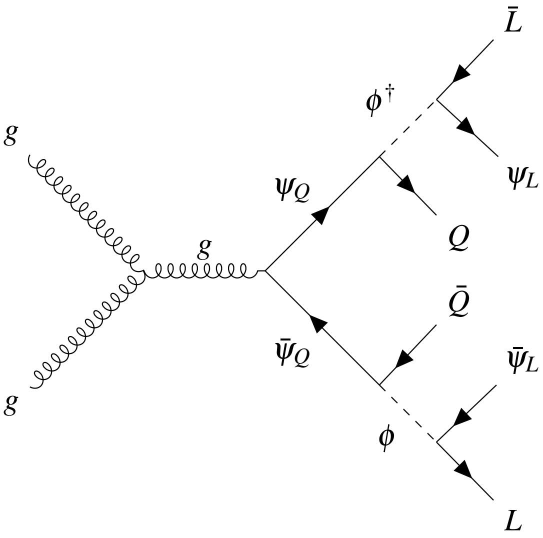

Figure 4.6: Possible detection channel in leptophilic DM models.

leptophilic models, proceed with quarkphilic models and end with amphiphilic models. We present the Dirac and Majorana versions of each model distinctly.

4.4.1 Analysis Strategy

The number of additional parameters in this model, which can vary between realizations a and b, is vast. We therefore have to make assumptions about a set of parameters in order to obtain useful results.

- We present all plots in the M_{DM}-Γ_μ plane. We scan logarithmically over 10^4 parameter sets in the $[100\,\text{GeV}, 40\,\text{TeV}] \times [10^{-5}, 4\pi]$ intervals.

- We require parameter set to not break the DM stabilizing symmetry and satisfy the vacuum stability conditions as well as perturbativity bounds discussed in Section 4.1. We do not, however, regard the bounds on R_K and $(g-2)_\mu$ realizations as stringent, since we perform scans over the whole DM mass and muon Yukawa coupling range.

- The product $\Gamma_s\Gamma_b^*$ is assumed to be at the upper bound (see Eq. 4.2.6). If the bound on Γ_μ set by R_K is exceeded, $\Gamma_s\Gamma_b^*$ is scaled down accordingly. This choice of parameter combination facilitates a solution to the R_K anomaly, since a smaller Γ_μ still tends to suffice in these constellations.

  We distinguish between two choices of coupling structures for the BSM quark Yukawas: democratic and hierarchical. In the democratic scenario, we choose the second and third generation couplings Γ_s and Γ_b to be almost identical[11], which implies that $\Gamma_s \approx \Gamma_b \approx \sqrt{\mathcal{B}_{bs}^{\text{model}}(\kappa) \cdot M_{\text{DM}}/\text{GeV}}$.

  In the hierarchical choice, we enforce the most extreme flavor structure. We choose Γ_b to be at its perturbative limit, which subsequently forces the coupling Γ_s to comply

---

[11] We choose the difference of these couplings to be as small as allowed by the constraints on Γ_s from D-$\bar{D}$ mixing. Typically, the difference is within $\mathcal{O}(1\%)$.

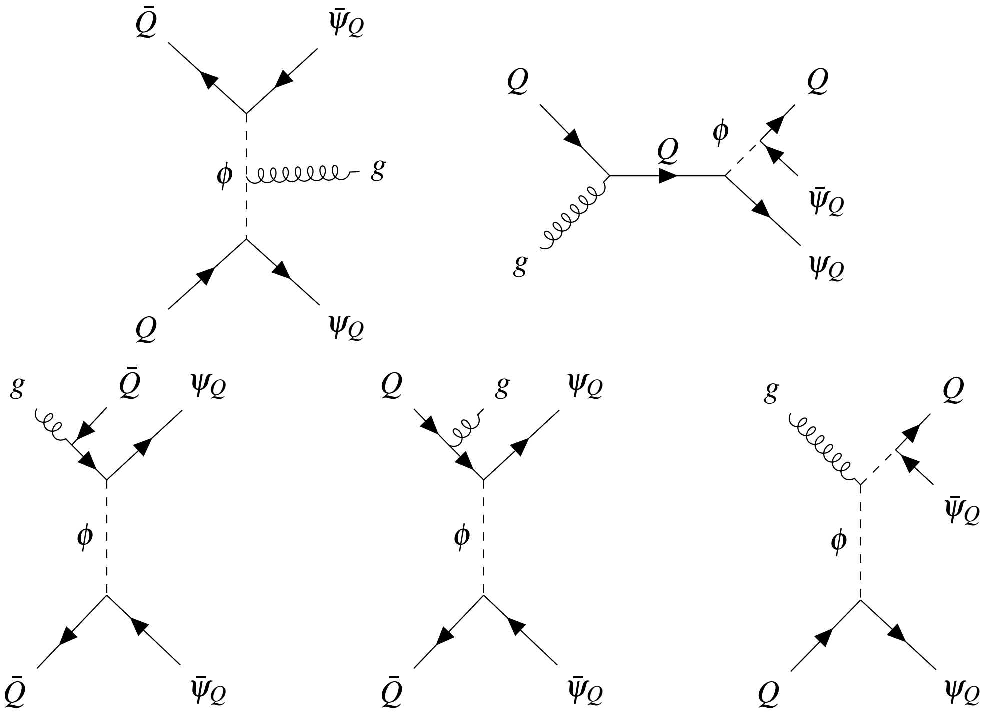

Figure 4.7: Diagrams inducing the monojet + E_{miss}^T signature in quarkphilic/amphiphilic DM models.

and fit the product $\Gamma_s\Gamma_b^*$ to be at the upper limit. Thus, we obtain $\Gamma_b = 4\pi \wedge \Gamma_s = \mathcal{B}_{bs}^{\text{model}}(\kappa)/4\pi \cdot M_{\text{DM}}/\text{GeV}$.

These two choices portray the most extreme scenarios regarding the flavor structure. Every other possible scenario lies on the spectrum between these two cases.

- Concerning the mass gaps, we present constellations where there is a 1% and 10% mass gap between DM and non-DM dark sector particles ($\kappa = 1.01, 1.1$). These scenarios feature strong coannihilations. We also present scenarios where those effects are absent ($\kappa = 5, 15$).
- We fix all Higgs portal couplings that are not required to vanish to ensure that mass degeneracy is upheld to 0.1, since they do not affect the DM phenomenology to a large degree.

All plots in this chapter show areas *allowed* by direct detection (DD,blue), R_K (gray), and muon $g-2$ (Δa_μ, green). This in turn means that areas that are left blank do not satisfy the bounds of these observables. The orange lines correspond to the observed relic density (RD) $\Omega_{\text{DM}}h^2 = 0.120 \pm 0.001$ in the universe[12]. The parameter space to the left of these lines features an underproduced RD, whereas the region to the right of the line features overproduction of DM and is therefore excluded.

---

[12] To be precise, the correct relic density is not only a line but a band, since it given with an experimental error. This band, however, is very narrow due to the relative error of $\sim 0.8\%$ and it is therefore reasonable to refer to a line in this case.

4.4.2 bIIA

Reminding ourselves of the model classification in Table 4.1, the representations of the BSM fields under $(SU(3)_C, SU(2)_L)_{U(1)_Y}$ in bIIA are

$$\begin{aligned} &\psi_L = (\mathbf{1},\mathbf{1})_0, \quad \psi_Q = (\mathbf{3},\mathbf{1})_{2/3}, \quad \phi = (\mathbf{1},\mathbf{2})_{-1/2} \\ \overset{\text{EWSB}}{\Rightarrow} \; &\psi_L \to \psi_L^0, \quad \psi_Q \to \psi_Q^{+2/3}, \quad \phi \to \begin{pmatrix} \frac{1}{\sqrt{2}}\left(\phi^0 + \phi^{0'}\right) \\ \phi^- \end{pmatrix}. \end{aligned} \tag{4.4.1}$$

Since ψ_L is the fermionic singlet DM candidate, this model qualifies as a leptophilic DM model.

4.4.2.1 Dirac DM

This section summarizes the results obtained for bIIA with a Dirac DM candidate. The numerical scan over the parameter space described in Section 4.4.1 yields the results summarized in Figure 4.8[13].

Most of the RD and R_K lines possess the same slope, meaning that they have the same scaling $\Gamma_\mu \sim \sqrt{M_{\psi_L}/\text{GeV}}$. This particular scaling is suggested by the R_K bounds in Eq. (4.2.7), while we show in Section 4.3.1 that the RD also scales like this in the case where DM annihilations into SM leptons dominate. While the mass scaling causes the lines to be parallel in the log-log plot, we can estimate the 'height' of the RD lines from the model dependent coefficient functions $\mathcal{B}_{\text{RD}}^{\text{model}}(\kappa)$.

The assumption of a dominant direct annihilation of DM into leptons is clearly valid in the case of non-coannihilation scenarios $\kappa = 5, 15$, but also for scenarios where $\kappa = 1.1$ or even $\kappa = 1.01$ when the muon BSM Yukawa is large ($\mathcal{O}(1)$) and the DM mass is well above a certain threshold. This threshold, which is clearly visible in Fig. 4.8, marks a smaller mass under which a successful generation of the observed DMRD is not possible. It stems from coannihilations of the color-charged ψ_Q via the quark BSM Yukawa interaction and into gluons interacting via the strong gauge coupling g_3. Also, interactions of ϕ via the Higgs portal contribute as well. Note that even if e.g. the quark BSM Yukawas and the Higgs portal coupling are chosen to be negligibly small, the threshold still exists since the gauge coupling constribution always exists. As suggested by the difference in lower mass thresholds between $\kappa = 1.1$ and $\kappa = 1.01$, the mass splitting in the dark sector κ strongly impacts the lower mass threshold since the efficiency of coannihilations is suppressed by the typical factor of $\exp(-2x_f\kappa)$ (see Eqs. (4.3.3)-(4.3.4), (2.3.43)). The subsequent decrease of $\langle\sigma v\rangle$ directly leads to an increase of the RD and the mass threshold thus shifts towards lower masses for an increasing κ.

In a hierarchical scenario, where the the BSM Yukawa coupling to the third generation Γ_b is at its perturbative limit, the mass thresholds of the coannihilation scenarios are shifted towards significantly higher DM mass values. This is due to the fact that the annihilation cross section into quarks scales like $\langle\sigma v\rangle \sim \Gamma_b^4 + 2\Gamma_b^2\Gamma_s^2 + \Gamma_s^4$, which is maximized for a Γ_b at the perturbative limit.

As suggested in Eq. (4.3.7), only the non-coannihilation scenario $\kappa = 15 > \kappa_0^{\text{bIIA,Dir}}$ could in principle produce the correct RD and solve the R_K anomaly at once in the bIIA Dirac model. This is confirmed by the numerical results in Fig. 4.8, where only the solid RD line lies within the gray R_K-area.

Furthermore, note that the RD lines of the coannihilation scenarios do not behave as expected from Eq. (4.3.5)[14]. In order to understand this behavior, we have to consider the effect

---

[13] Note that the legend displayed in Fig. 4.8 is valid for all forthcoming plots of this kind in this thesis and will not be repeated for the sake of saving space.

[14] Eq. (4.3.6) suggests a simple proportionality of the leptonic Yukawa coupling Γ_μ with regards to the mass gap parameter κ. By simple proportionality we mean that Γ_μ is a monotonically ascending function in κ.

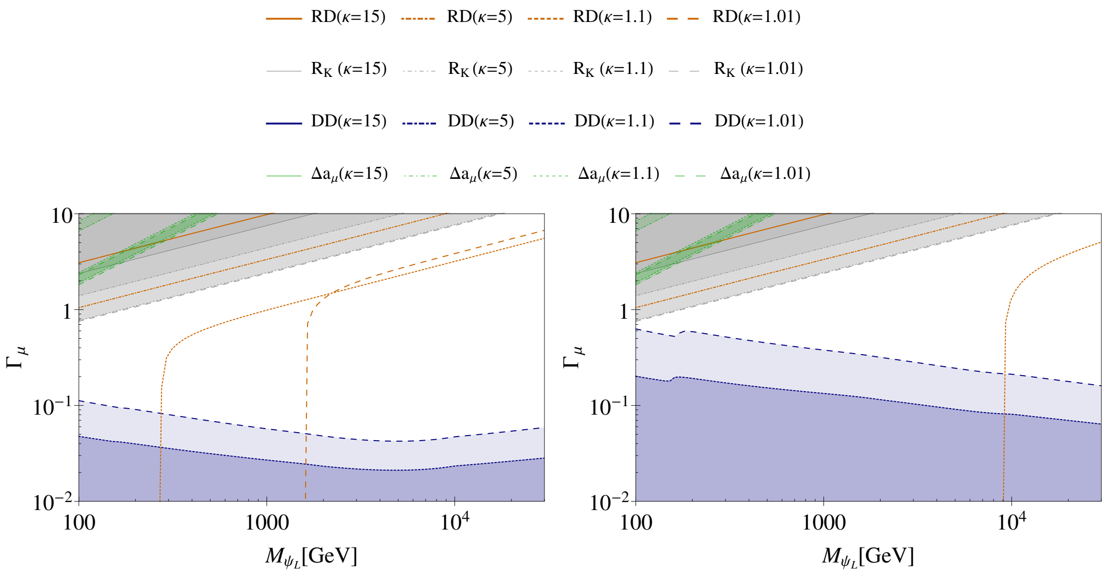

(a) democratic

(b) hierarchical

Figure 4.8: Summary plot for Dirac DM in bIIA. The plot provides all information about the R_K (R_K) and the anomalous magnetic moment of the muon (Δa_μ), as well as the DM observables relic density (RD) and direct detection (DD) for $\kappa = 1.01$ (dashed line), $\kappa = 1.1$ (dotted line), $\kappa = 5$ (dot-dashed line) and $\kappa = 15$ (solid line). The orange lines describe a correctly generated Ω_{DM}. Parameter regions to the left of these lines feature underproduced DM, whereas regions to the right overproduce DM. The gray area covers the region where the R_K anomaly can be solved at 2σ. Areas that show a green band are parameter regions where Δa_μ can be reproduced at 1σ. The area above the green bands lead to overly large contributions to Δa_μ and is therefore excluded. The blue region indicates the parameter space that is in agreement with direct detection bounds. Both SI and SD DM-nucleon cross section constraints are taken into account here.

of efficient conversions of dark sector particles. A discussion about this effect and the relevant values of κ can be found in Appendix D

In the following, we discuss the phenomenology of direct detection in this model, which is mediated at leading order on one-loop level by the processes depicted in Figure 4.9. First of all, note that the box diagram in Fig. 4.9 contains an additional heavy BSM particle propagator compared to any of the penguin diagrams. Moreover, it is also suppressed due to the vanishing first generation quark coupling and smaller fractions of second and third generation quark PDFs.

The results presented in Fig. 4.8 suggest that a simultaneous solution of R_K and DM is excluded in this model, as the allowed regions from DD and R_K are completely disjoint in both democratic and hierarchical versions. The statement can be formulated even more strictly, as the DD limits also rule out models that explain R_K with underproduced DM.

For coannihilation scenarios, there is open parameter space in regions where Γ_μ is small ($\Gamma_\mu \lesssim 10^{-1}$ in democratic, $\Gamma_\mu \lesssim 0.5$ in hierarchical), so that the observed DMRD can be reproduced while DD bounds are also respected.

The tightness of the DD constraints stems mainly from the large contributions of the effective vector coupling of ψ_L to the Z-boson in relation to the tight limits on the SI DM-nucleon cross section given by the XENON1T experiment.

Note that the DD constraint is weaker in coannihilation scenarios by $\sim$ 1-2 orders of mag-

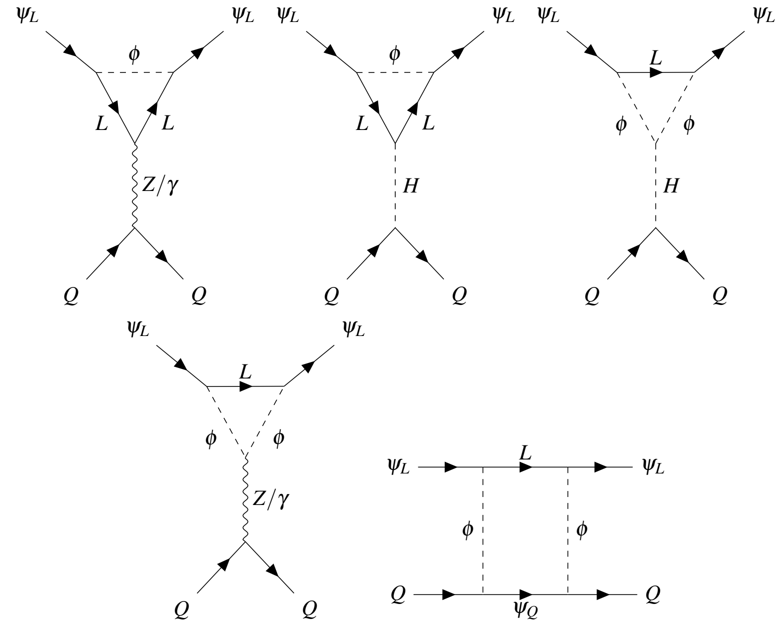

Figure 4.9: Leading order DM-quark diagrams contributing to the DD cross section of ψ_L DM.

nitude. In principle there are two effects acting in opposite directions. On the one hand, the effective $\bar{\psi}_L Z_\mu \psi_L$-coupling decreases with increasing κ because the masses of the BSM particles in the loops of the processes depicted in Fig. 4.9 increase proportional to κ, which leads to an alleviation of the bounds. On the other hand, an increasing κ also increases $\Omega_{\mathrm{DM}}h^2$ by enhancement of the mass suppression in the thermally averaged annihilation cross section $\langle \sigma v \rangle$. This in turn alters the DD limits for ψ_L-DM. As the experimental limits are rescaled with the fraction of ψ_L-DM compared in the observed DM density according to Eq. (4.3.9), the bounds are ultimately tightened[15].

Differences between the DD limits in the hierarchical and democratic implementations of bIIA Dirac are driven mainly by RD rescaling, as only the box diagram exhibits a $\Gamma_{s/b}$ dependence. This diagram, as discussed above, is subdominant. Coannihilation scenarios involve channels that feature a $\Gamma_{s/b}$-dependence and thus exhibit stronger underproduction of ψ_L-DM. This in turn leads to substantial relaxation of the DD limits.

Lastly, the region that signifies a solution of the $(g-2)_\mu$ anomaly exhibits a scaling behavior $\Gamma_\mu \sim M_{\psi_L}$ indicated by Eq. (4.2.8) and subsequently Table 3. In this model, all of the relevant parameter space is excluded by DD and thus no solution to the $(g-2)_\mu$ anomaly can be constructed.

4.4.2.2 Majorana DM

We summarize the results of the scan over the parameter space in the Majorana model (bIIA$^{\mathrm{Maj}}$) in Fig. 4.10.

In this version of bIIA, a simultaneous solution of R_K and RD can be achieved at smaller κ values, as suggested by $\kappa_0^{\mathrm{bIIA,\ Maj}} \approx 4.7$ derived in Eq. (4.3.7). This manifests itself in Fig. 4.10,

---

[15] Because of these competing effects, a flip of the hierarchy observed in Fig. 4.8 ($\mathrm{DD}(\kappa_1) > \mathrm{DD}(\kappa_2)$, $\kappa_1 < \kappa_2$) of the size of the limit is expected with increasing κ.

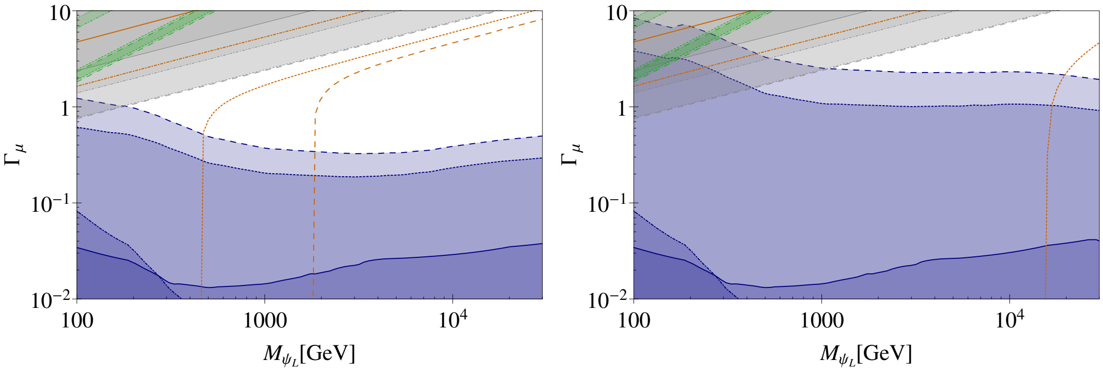

(a) democratic

(b) hierarchical

Figure 4.10: Summary plot for Majorana DM in bIIA. The legend and an explanation of the color scheme are given in Fig. 4.8.

where the RD of $\kappa = 5$ lies within the allowed R_K region. This is a consequence of the p-wave suppression of the annihilation cross section in Majorana models compared to the more efficient s-wave annihilations found in Dirac models. Subsequently, Majorana models require larger couplings to the muon in order to still achieve the observed DMRD, which causes the RD lines to enter the allowed R_K regions at smaller κ.

Note at this point that the RD lines in the coannihilation scenarios do not feature the intersecting behavior found in the Dirac version, which is mainly due to the change in the internal degrees of freedom of Majorana DM particles compared to Dirac DM and the p-wave nature of the direct annihilations compared to the s-wave nature of the coannihilations. The discussion in Appendix D contains more details about this topic.

Compared to the Dirac version of bIIA, the DD bounds on the muonic Yukawa coupling are relaxed by approximately one order of magnitude. This feature is plausible because the effective vector coupling of ψ_L to the Z-boson, which contributes to a large degree in the Dirac model is forbidden is the Majorana case, as demonstrated in Appendix A.2.

Here, the largest contribution comes from the SD DM-nucleon cross section generated by the axial vector current contribution to the $\bar{\psi} Z_\mu \psi$ vertex. This is an especially interesting feature, since the experimental limits on the SD DM-nucleon cross section are ~ 6 orders of magnitude weaker than the limits on the SI DM-nucleon cross section.

The most stringent bounds on the DM-proton cross section come from XENON [131], while the best bounds for the DM-proton cross section are presented by IceCube [136] in the mass range studied here. The smaller masses are typically constrained by the DM-neutron cross section in the region up to $\sim 300\,\text{GeV}$, whereas larger masses are often more constrained by the DM-proton cross section bounds from IceCube. In our analysis, we apply the strongest limits at any given mass[16].

Since the bounds are weakened by a large degree, there is significant overlap of R_K and DD regions and thus an explanation of R_K is potentially possible in this model. This, again, only holds for coannihilation scenarios, since they feature significantly weaker DD limits.

In the democratic scenario, we find an overlapping region at $M_{\psi_L} \lesssim 180\,\text{GeV}$, whereas in the hierarchical setup we find the mass window to extend to masses approximately one order of magnitude larger. In the case of $\kappa = 1.1$, DM masses range up to $\sim 420\,\text{GeV}$, while they

---

[16] In the discussion of the upcoming models, the mass regions where the aforementioned experiments are most constraining can vary slightly. However, we always apply the most stringent bounds automatically.

extend up to $\sim 1000\,\text{GeV}$ for $\kappa = 1.01$. Note, however, that these solutions always come with underprodcued DM, so that an additional, completely separate dark sector is required to solve the problem of the DMRD.

Furthermore, a solution of $(g-2)\mu$ is also possible. As in the case of R_K, a distinct flavor hierarchy $\Gamma_b \gg \Gamma_s$ is needed for the DM masses to be able to exceed $\sim 100\,\text{GeV}$. In the hierarchical setup, we find that the DM masses range up to $\sim 170\,\text{GeV}$ for $\kappa = 1.1$ and $\sim 290\,\text{GeV}$ in the case of $\kappa = 1.01$[17].

4.4.3 bVA

Following Table 4.1, the representations of the dark sector particles in bVA are

$$\begin{aligned} &\psi_L = (\mathbf{1},\mathbf{1})_0, \psi_Q = (\mathbf{3},\mathbf{3})_{2/3}, \phi = (\mathbf{1},\mathbf{2})_{-1/2} \\ \overset{\text{EWSB}}{\Rightarrow}\ &\psi_L \to \psi_L^0,\ \psi_Q \to \begin{pmatrix} \psi_Q^{+5/3} \\ \psi_Q^{+2/3} \\ \psi_Q^{-1/3} \end{pmatrix},\ \phi \to \begin{pmatrix} \frac{1}{\sqrt{2}}\left(\phi^0 + \phi^{0'}\right) \\ \phi^- \end{pmatrix}. \end{aligned} \tag{4.4.2}$$

This model is related with bIIA in the sense that it contains BSM fields with exactly the same set of representations under the SM gauge groups except ψ_Q being a triplet under $SU(2)_L$ instead of a singlet. This also qualifies bVA as a leptophilic DM model, for which we expect results similar to the ones obtained in bIIA.

4.4.3.1 Dirac DM

We summarize the numerical results of bVA Dirac in Fig. 4.11. Comparisons between the results of bIIA Dirac and this model (Figs. 4.8 and 4.11) show that there is no difference between the RDs in non-coannihilation scenarios. This is the case since the difference between the models lies in the coannihilation partner ψ_Q and thus, a change is only expected in the coannihilation scenarios.

Compared to bIIA, the effective annihilation cross section is enhanced and thus bVA features stronger underproduction of DM. At the same time, this also means that bVA exhibits larger mass thresholds than bIIA for both $\kappa = 1.1$ and $\kappa = 1.01$.

Regarding a simultaneous solution to the R_K anomaly and DM, this model requires a very large mass gap of $\kappa_0^{\text{bVA,Dir}} \approx 26.5$. This is due to the additional contributions to $b \to s l^- l^+$-transitions and B-$\bar{B}$ mixing.

Since the RD is more depleted in comparison to bIIA Dirac, the rescaling of the DD bounds according to Eq. (4.3.9) is more severe. The overall contributions to the DM-nucleon cross section, on the other hand, are not significantly altered since ψ_Q is only present in the suppressed box diagram depicted in Fig. 4.9. Overall, the effect on the DD limits is $\sim \mathcal{O}(10\%)$.

Combining the findings about the R_K, $(g-2)_\mu$ and DD regions in this models, we find that not even a single solution to either of the anomalies can be found, since DD rules out all of the potentially viable parameter space. This conclusion mirrors the one obtained for bIIA Dirac.

---

[17] Note that these mass regions are potentially excluded by colliders, as mentioned in the estimates made in Section 4.3.4. However, we require a fully dedicated collider analysis of this setup to make this statement with certainty.

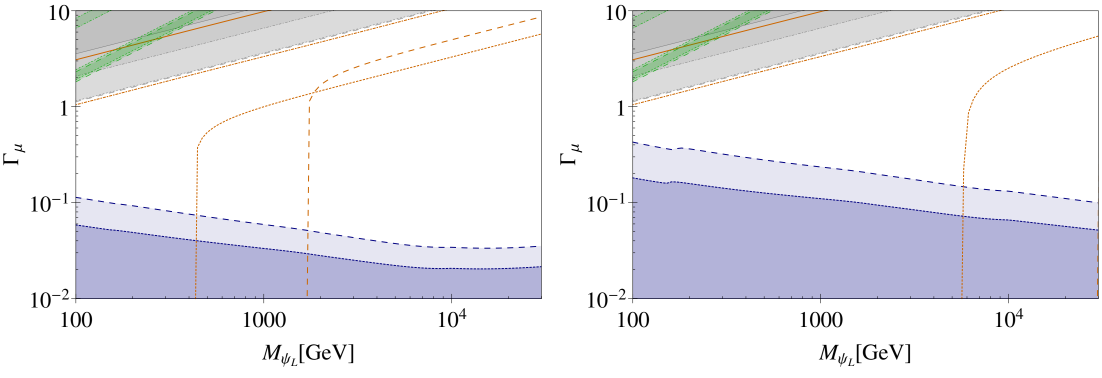

(a) democratic

(b) hierarchical

Figure 4.11: Summary plot for Dirac DM in bVA. The legend and an explanation of the color scheme are given in Fig. 4.8.

4.4.3.2 Majorana DM

The results of the scan over the parameter space in Majorana version of bVA are shown in Fig. 4.12. This model, also being a leptophilic Majorana DM model, possesses most features that are already discussed in the context of bIIA^{Maj}.

As discussed in Section 4.4.3.1, the region where a potential solution to the R_K anomaly can be achieved shrinks in this model compared to bIIA and thus the regions where a simultaneous solution is possible also decrease. The upper bound on the DM mass in this case is $\sim 260\,\text{GeV}$ for $\kappa = 1.1$ and $\sim 410\,\text{GeV}$ for $\kappa = 1.01$. Note that these regions are still underproducing RD.

Another minor but noteworthy effect in this model is that the RD lines of the coannihilation scenarios $\kappa = 1.1$ and $\kappa = 1.01$ intersect, although they do not intersect in bIIA^{Maj}. This can be understood by taking into account the alteration of the degrees of freedom of the color-charged fermion. This in turn affects the number density of the non-DM BSM particles. For more details on this topic see Appendix D.

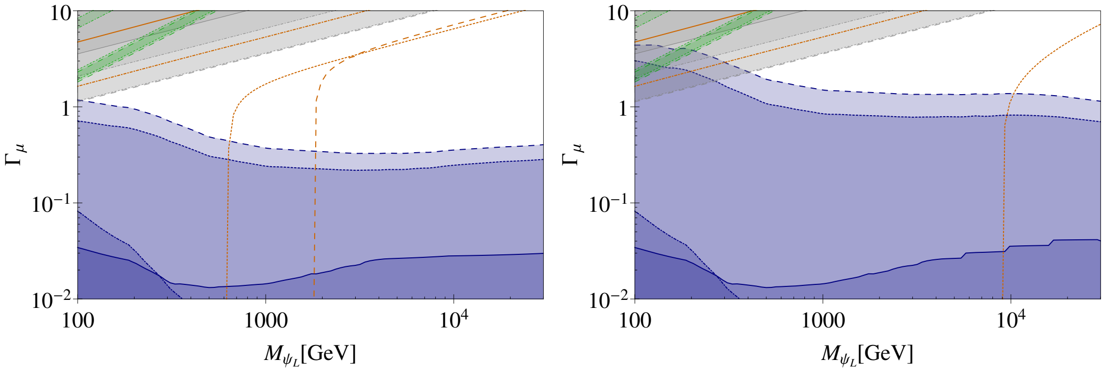

(a) democratic

(b) hierarchical

Figure 4.12: Summary plot for Majorana DM in bVA. The legend and an explanation of the color scheme are given in Fig. 4.8.

4.4.4 bIIB

Following Table 4.1, the representations of the dark sector particles in bIIB are

$$\begin{aligned} &\psi_L = (\bar{\mathbf{3}},\mathbf{1})_{-2/3}, \quad \psi_Q = (\mathbf{1},\mathbf{1})_0, \quad \phi = (\mathbf{3},\mathbf{2})_{1/6} \\ \overset{\text{EWSB}}{\Rightarrow} \quad &\psi_Q \to \psi_Q^0, \quad \psi_L \to \psi_L^{-2/3}, \quad \phi \to \begin{pmatrix} \phi^{+2/3} \\ \phi^{-1/3} \end{pmatrix} . \end{aligned} \tag{4.4.3}$$

The model bIIB qualifies as a quarkphilic DM models since the DM candidate ψ_Q couples directly to quarks. A notable consequence of this behavior and a significant difference to leptophilic models is that there are tree-level contributions to the DM-nucleon cross section.

4.4.4.1 Dirac DM

Figure 4.13 summarizes the results obtained for bIIB Dirac.

Since in this model, DM direct annihilation into SM particles proceeds via the Yukawa interaction with quarks, the muonic BSM Yukawa coupling only affects coannihilation scenarios. For both coupling structures, democratic and hierarchical, the non-coannihilation scenarios $\kappa = 5$ and $\kappa = 15$ are not able to generate the observed DMRD for $M_{\psi_Q} > 100\,\text{GeV}$. This is the case because the BSM Yukawa interaction with quarks alone is insufficient to keep ψ_Q in thermal equilibrium long enough to deplete the RD to the observed value.

In coannihilation scenarios, however, the exponential suppression factor $\exp(-x_f\kappa)$ is sufficiently small so that Γ_μ can contribute in the democratic model to the annihilation cross section. In the hierarchical scenario, the direct annihilation into b-quarks is so strong that Γ_μ does not play a role.

The shift of the mass threshold described in Section 4.4.2.1 is also visible in this model. We can compare the estimates $M_{\text{DM,max}}^{\text{bIIB}} \approx {}^{674\,\text{TeV}}/_{1+\kappa^2}$ made in Eq. (4.3.8) with the numerically obtained results in the hierarchical setup and remark that the obtained numbers $\approx 26\,\text{TeV}$ for $\kappa = 5$ and $\approx 3\,\text{TeV}$ for $\kappa = 15$ prove to be good estimates for all practical purposes.

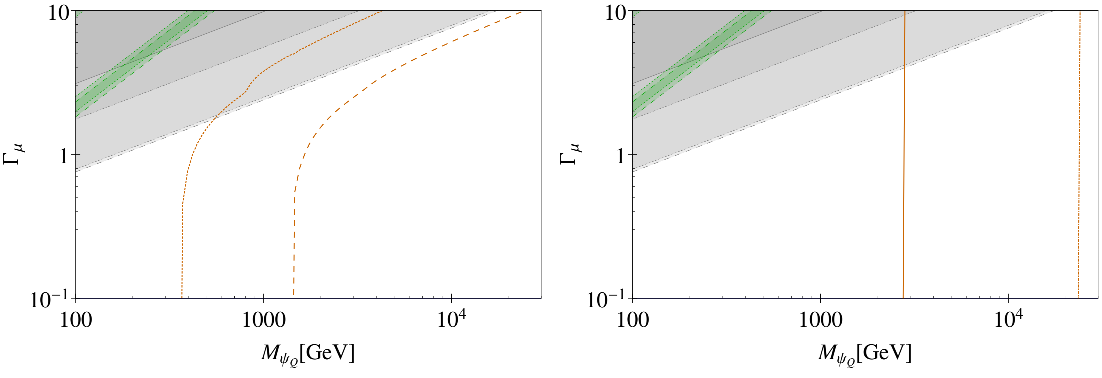

(a) democratic (b) hierarchical

Figure 4.13: Summary plot for Dirac DM in bIIB. The legend and an explanation of the color scheme are given in Fig. 4.8.

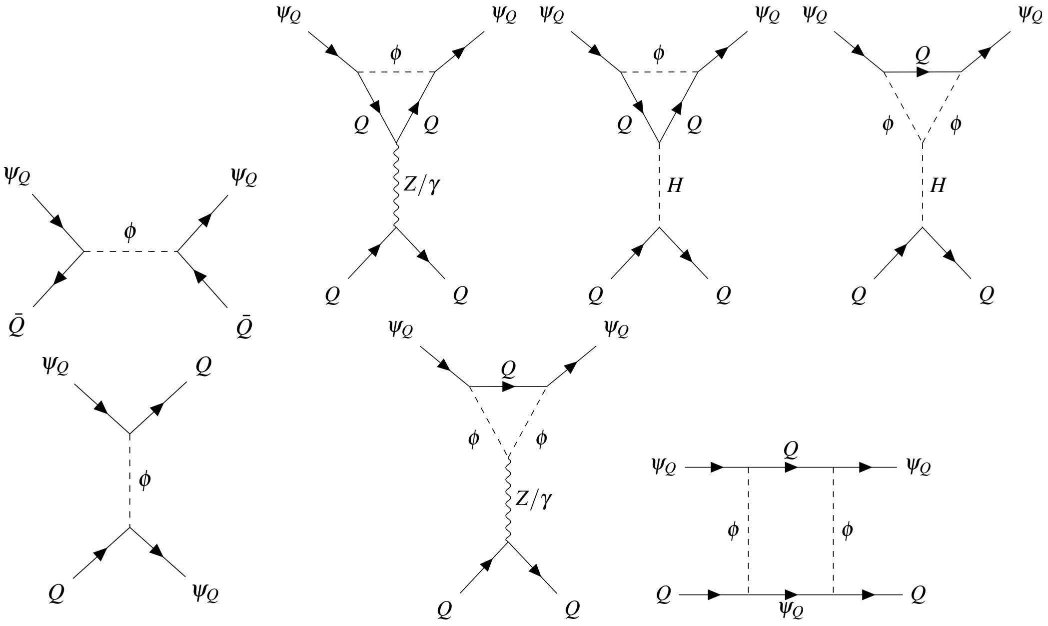

(a) tree-level (b) one-loop

Figure 4.14: Tree-level (a) and one-loop (b) DM-quark diagrams contributing to the DD cross section of ψ_Q DM. The legend and an explanation of the color scheme are given in Fig. 4.8.

All diagrams contributing to the DM-nucleon cross section up to one-loop level are depicted in Fig. 4.14. Although there are tree-level contributions, the SI DM-nucleon cross section is dominated by the vector current contribution to the effective $\bar{\psi}_Q Z \psi_Q$ vertex. This is the case because the tree-level diagrams are PDF-suppressed. Moreover, the Higgs mediated diagrams contribute to a larger degree than in the leptophilic DM models, since the top quark Yukawa $y_t \sim 1$ is significantly larger than the Yukawas of the leptons. Note here that the Higgs portal diagram is still suppressed by the additional heavy propagator.

In summary, the complete parameter space studied is excluded by DD and thus no solution to the R_K and $(g-2)_\mu$ anomalies or DM can be found in this model.

4.4.4.2 Majorana DM

In Fig. 4.15, we present the results of the numerical scan in $\mathrm{bIIB}^{\mathrm{Maj}}$.

In both Dirac and Majorana versions of bIIB, the RD results are similar in shape with the exception of a larger mass threshold for coannihilation scenarios and a lower mass threshold for non-coannihilation scenarios in the Majorana model. The lower mass threshold for non-coannihilation scenarios simply stems from the less efficient p-wave annihilation compared to the Dirac version's s-wave annihilation, since we encounter dominant direct annihilation into quarks. Coannihilations, on the other hand, are more efficient because the non-DM BSM particles occupy a larger percentage of the number density in the dark sector due to the reduced internal degrees of freedom of Majorana DM. Subsequently, DM is produced more efficiently by coannihilations than in the Dirac model and the mass threshold is shifted towards larger masses.

The estimates made in Eq. (4.3.8) for the Majorana model, $M_{\mathrm{DM,max}}^{\mathrm{bIIB,Maj}} \approx 254\,\mathrm{TeV}\,\frac{\sqrt{1+\kappa^4}}{(1+\kappa^2)^2}$, can also be compared to the numerical results. We obtain $\approx 9.4\,\mathrm{TeV}$ for $\kappa = 5$ and $\approx 1.1\,\mathrm{TeV}$ for $\kappa = 15$, which are also very useful estimates for the mass thresholds.

In stark contrast to the Dirac version, $\mathrm{bIIB}^{\mathrm{Maj}}$ offers viable parameter space regarding DD. In this model, the twist-2 operator contributions to the SI DM-nucleon cross section described in Section 4.3.2.2 become important. The reason for this is that the main contribution to the SI DM-nucleon cross section, which comes from the vector current contribution to the Z-boson-DM vertex, vanishes due to the Majorana nature of ψ_Q. Also the tree-level diagrams shown in Fig. 4.14 do not provide unsuppressed contributions to the SI DM-nucleon cross section. This is because both Feynman diagrams are of the s-channel structure $((\bar{\psi}_Q Q)(\bar{Q}\psi_Q))$ so that according to Section 2.3.3.4 a Fierz transformation yields $(v{,}v)$, $(v{,}a)$, $(a{,}v)$ and $(a{,}a)$ contributions, of which the $(v{,}v)$ contribution vanishes.

The effectively inverse scaling of the SI DM-nucleon cross section with the DM mass, estimated by using Eq. (4.3.10), and the XENON1T limit's approximately linear softening $\sim M_{\psi_Q}$ for masses $M_{\psi_Q} \gtrsim 30\,\mathrm{GeV}$ means that the SI twist-2 contributions generally provide stronger constraints in the lower mass regions. Concerning the behavior in κ, we find that the SI DM-nucleon cross section decreases with increasing κ, effectively dragging the DD threshold to smaller masses.

The mirrored shape of the excluded region in Fig. 4.15(a) originates from the RD rescaling effect, which is stronger at large Γ_μ and thus relaxes the limits with an increasing Γ_μ.

The complementarity of the bounds observed in Fig. 4.15 is, to a large extent, an effect of the positive rescaling of the DD bounds with the RD in an interplay with the different SI and SD DM-nucleon cross section scaling with the DM mass. In regions where the M_{ψ_Q} is large, we tend to find parameter space with overproduced ψ_Q-DM, leading to a rescale factor ${}^{\Omega_{\mathrm{DM}}}/{}_{\Omega_{\psi_Q}} < 1$, which tightens the bounds. The SD contributions coming from the one-loop diagrams are large enough to overcome the level of the tightened bounds and thus we observe an SD exclusion at masses beyond the RD line.

However, this parameter space is deemed uninteresting due to the overproduced RD. This is also the case for non-coannihilation scenarios, which are completely ruled out due to overproduction of DM.

The model possesses an interesting parameter space region at $M_{\psi_Q} \gtrsim 1.5\,\mathrm{TeV} \wedge \Gamma_\mu \gtrsim 3$ for $\kappa = 1.1$, since we find a simultaneous solution of the R_K anomaly and DM in this particular window[18]. Note, however, that this region is strongly dependent on the mass gap parameter κ,

---

[18] Note that in a setup that involves color-charged coannihilation partners there can potentially arise corrections

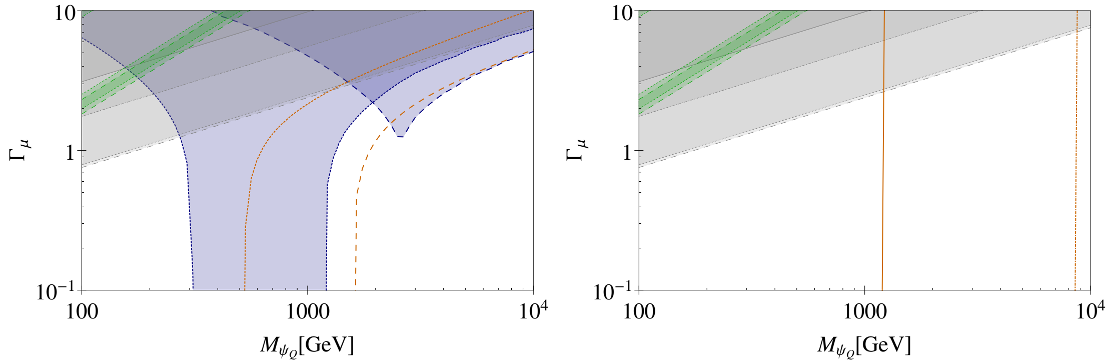

(a) democratic

(b) hierarchical

Figure 4.15: Summary plot for Majorana DM in bIIB. The legend and an explanation of the color scheme are given in Fig. 4.8.

as both smaller and larger values of κ studied in this work lead either lead to exclusion via DD and RD ($\kappa = 5$) or underproduces DM ($\kappa = 1.01$).

A simultaneous solution to $(g-2)_\mu$ and R_K is principally possible in the $\kappa = 1.1$ scenario in the region $150\,\text{GeV} \lesssim M_{\psi_Q} \lesssim 500\,\text{GeV}$ (and $400\,\text{GeV} \lesssim M_{\psi_Q} \lesssim 550\,\text{GeV}$ for $\kappa = 1.01$). Then again, this part of the parameter space underproduces DM. The solution is also unstable in κ, as smaller and larger values of κ tend to be excluded via DD.

The hierarchical scenario is completely ruled out. One the one hand, overproduction of the RD leads SD bounds to become more stringent after the mass threshold is surpassed. On the other hand, SI contributions from twist-2 operators are dependent on the BSM quark Yukawa couplings (see Fig. 4.5), of which Γ_b is at the perturbative limit in this setup. This leads the region to be excluded by SI limits to completely overlap with the region excluded by SD, subsequently rendering the complete parameter space studied unavailable. We also do not observe the relaxation of the SI bound in the Γ_μ direction, since it does not play a role in non-coannihilation scenario and Γ_b mediated interactions dominate severely.

4.4.5 bVIB

Following Table 4.1, the representations of the dark sector particles in bVIB are

$$\psi_L = (\mathbf{\bar{3}},\mathbf{3})_{-2/3}, \quad \psi_Q = (\mathbf{1},\mathbf{1})_0, \quad \phi = (\mathbf{3},\mathbf{2})_{1/6}$$

$$\overset{\text{EWSB}}{\Rightarrow} \; \psi_Q \to \psi_Q^0, \quad \psi_L \to \begin{pmatrix} \psi_L^{+1/3} \\ \psi_L^{-2/3} \\ \psi_L^{-5/3} \end{pmatrix}, \quad \phi \to \begin{pmatrix} \phi^{+2/3} \\ \phi^{-1/3} \end{pmatrix}. \tag{4.4.4}$$

The coannihilation partner ψ_L undergoes the same $SU(2)_L$-singlet → triplet shift from bIIB to bVIB that ψ_Q does from bIIA to bVA. This is why we consider bVIB the 'sibling' model to bIIB and expect similar results. Due to this fact, we can fall back on some explanations already established in Sections 4.4.3.1.

---

to the RD from non-perturbative effects such as *Sommerfeld enhancement* and *bound state formation*, e.g. described in [212]. As these features are not considered in MICROMEGAs 5.0, we consider an inclusion of them beyond the scope of this work.

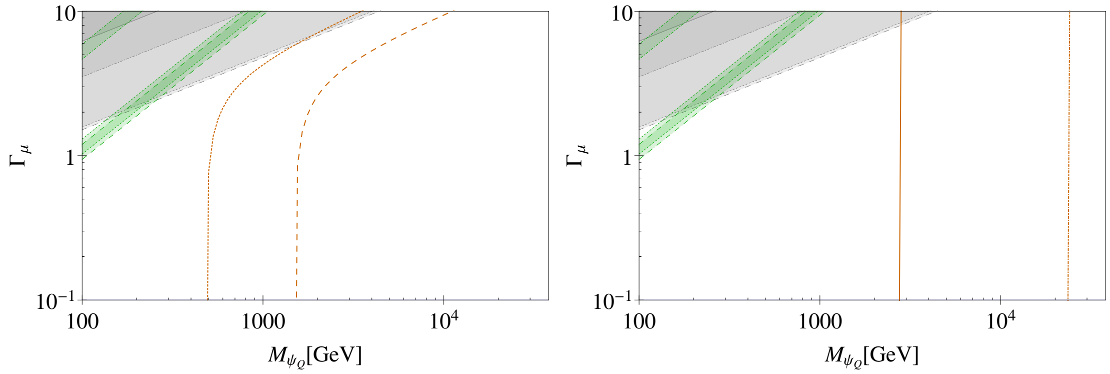

(a) democratic (b) hierarchical

Figure 4.16: Summary plot for Dirac DM in bVIB. The legend and an explanation of the color scheme are given in Fig. 4.8.

4.4.5.1 Dirac DM

The results of the scan over the parameter space in bVIB are presented in Fig. 4.16.

As already elaborated in Section 4.4.3.1, the singlet to triplet shift leads the mass thresholds in coannihilation scenarios to the increase from (bIIA Dirac to bVA Dirac) bIIB Dirac to bVIB Dirac. It also alters the contributions to the Wilson coefficients $\mathcal{C}_9$ and $\mathcal{C}_{B\bar{B}}$ according to Table 1, which leads to more stringent bounds on Γ_μ for a solution of the R_K anomaly.

We find strong similarities between the Dirac versions of bIIB and bVIB with respect to DD limits, as both models are completely ruled out for the parameter space studied in this work and the slight relaxation effects of the singlet-triplet shift does not suffice to open up any parameter space.

4.4.5.2 Majorana DM

We summarize the results of the parameter scan for the Majorana version of bVIB in Fig. 4.17. In general, many features of this model are shared with bIIB^{Maj}. The parameter space is excluded entirely in the hierarchical setup, which is again a feature of the overlap of SI and RD boosted SD limits.

The DD exclusion limits in the democratic setup are similar to bIIB^{Maj}, however, it does feature some differences. Note that the allowed area regarding DD for $\kappa = 5$ reaches values up to $\sim 120\,\text{GeV}$, which is due to the larger mass threshold for non-coannihilation scenarios compared to bIIB^{Maj}, where this threshold was just below the 100 GeV mark.

This has an effect on the feasibility of $(g-2)_\mu$ solutions for non-coannihaltion scenarios, which, mind a dedicated collider study, principally enter the mass range $\mathcal{O}(100\,\text{GeV})$. The allowed regions for a $(g-2)_\mu$ solution (with underproduced DM) in the coannihilation scenario $\kappa = 1.1$ are $350\,\text{GeV} \lesssim M_{\psi_Q} \lesssim 970\,\text{TeV}$ and $\Gamma_\mu \gtrsim 3.2$.

Conversely to bIIB, we do not find any viable windows for a simultaneous solution of the R_K anomaly and DM. The reason for this is that the allowed R_K region decreases substantially and the RD lines of the coannihilation scenarios do not extend into these regions anymore. This means that any viable solution to the R_K anomaly found in this model study exhibits underproduced DMRD.

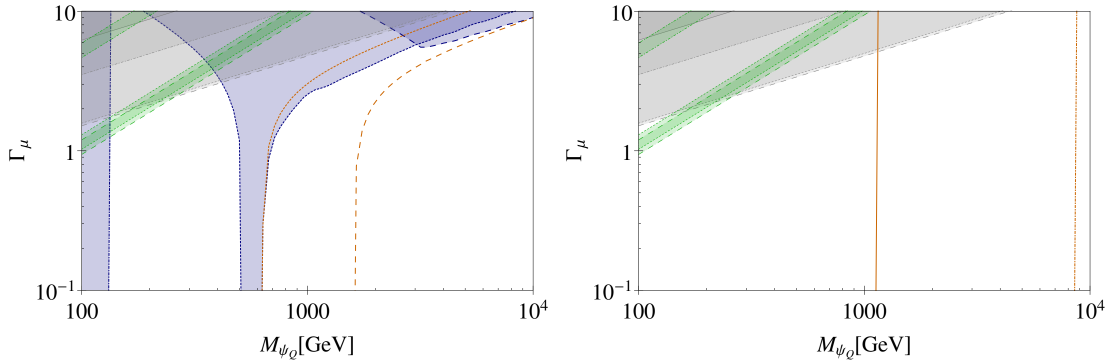

(a) democratic

(b) hierarchical

Figure 4.17: Summary plot for Majorana DM in bVIB. The legend and an explanation of the color scheme are given in Fig. 4.8.

4.4.6 aIA

The representations of the dark sector particles in aIA according to Table 4.1 are

$$\psi = (\mathbf{1},\mathbf{1})_0, \quad \phi_L = (\mathbf{1},\mathbf{2})_{-1/2}, \quad \phi_Q = (\mathbf{3},\mathbf{2})_{1/6}$$

$$\overset{\text{EWSB}}{\Rightarrow} \psi \to \psi^0, \quad \phi_L \to \begin{pmatrix} \frac{1}{\sqrt{2}}\left(\eta^0 + \eta^{0'}\right) \\ \eta^- \end{pmatrix}, \quad \phi_Q \to \begin{pmatrix} \sigma^{+2/3} \\ \sigma^{-1/3} \end{pmatrix}. \tag{4.4.5}$$

This model is the only representative of the amphiphilic DM subclass as far as fermionic DM models are concerned. This is the case because aIA is the only a-type model that contains a singlet ψ field, which couples to both leptons and quarks via a BSM Yukawa interaction.

4.4.6.1 Dirac DM

The results for aIA Dirac are shown in Figure 4.18.

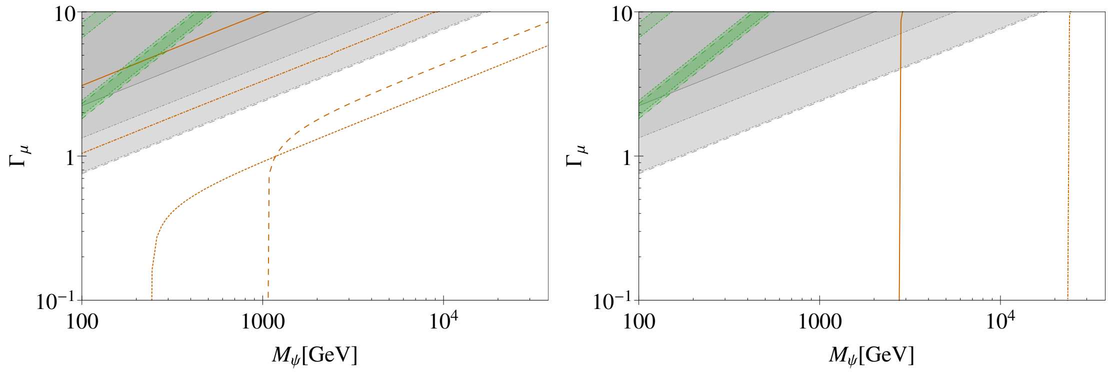

(a) democratic

(b) hierarchical

Figure 4.18: Summary plot for Dirac DM in aIA. The legend and an explanation of the color scheme are given in Fig. 4.8.

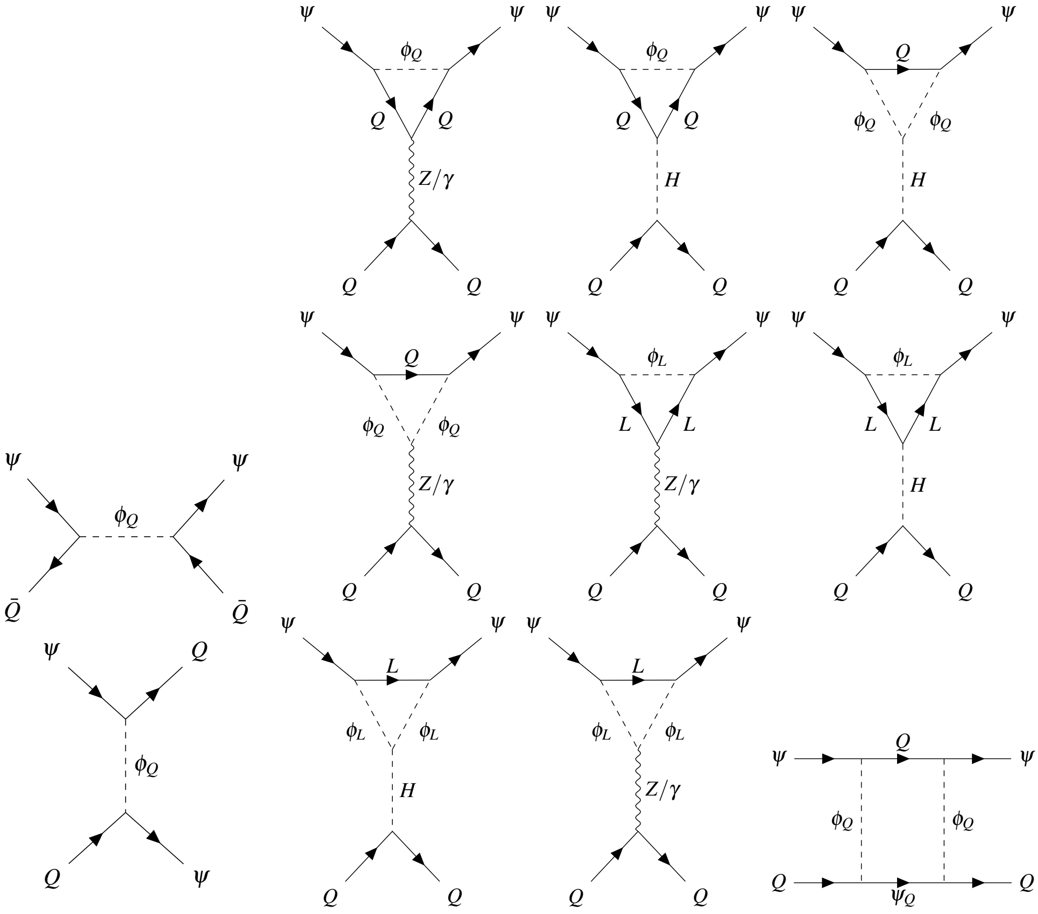

(a) tree-level

(b) one-loop

Figure 4.19: Tree-level (a) and one-loop (b) DM-quark diagrams contributing to the DD cross section of ψ_Q DM.

In the democratic setup, the behavior of the RD closely resembles that of leptophilic DM models like bIIA and bVA (see Figs. 4.8 and 4.11). Non-coannihilation scenarios are dominated by the leptonic BSM Yukawa coupling and therefore we observe the characteristic lines that follow $\Gamma_\mu \sim \sqrt{M_\psi/\mathrm{GeV}}$. Coannihilation scenarios feature the same scaling at large masses, whereas they also feature the mass threshold below which every parameter point underproduces DM. The hierarchical scenario exhibits the typically quarkphilic vertical RD lines in the non-coannihilation scenarios, also to be seen in Figs. 4.13 and 4.16. This hints towards the fact that direct annihilations into quarks dominate, as Γ_μ does not play a significant role in the RD generation.

In the Dirac version of this model, DD excludes all of the parameter space studied and thus the amphiphilic Dirac DM model shares this trait with quarkphilic DM models bIIB and bVIB. The principal reason for this is, again, the large contribution from the Z vector current that is allowed in Dirac DM models. Additionally, aIA also contains tree-level contributions. Fig. 4.19 shows all diagrams that contribute to DD cross sections in this model.

4.4.6.2 Majorana DM

The results of the scan over the parameter space in aIA Majorana are condensed in Fig. 4.20.

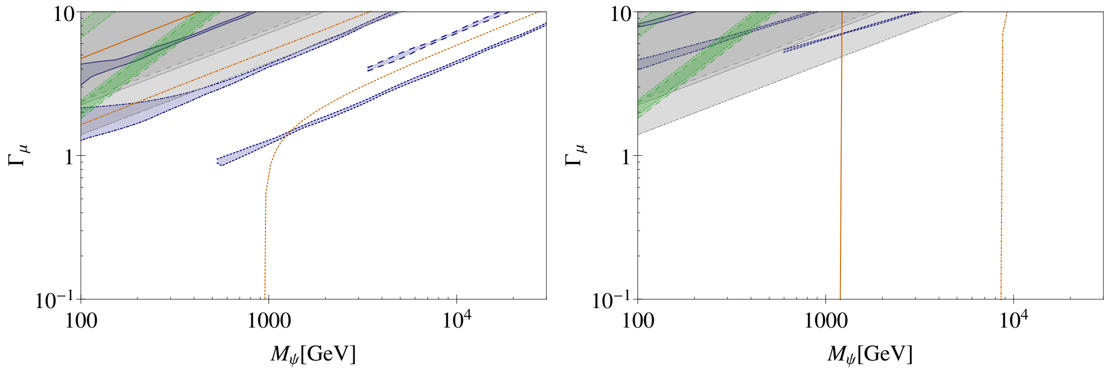

(a) democratic (b) hierarchical

Figure 4.20: Summary plot for Majorana DM in aIA. The legend and an explanation of the color scheme are given in Fig. 4.8.

For the reasons outlined in the Dirac version of this model, the RD structure in aIA Majorana resembles a leptophilic DM model in the democratic setup and a quarkphilic DM model in the hierarchical setup. The mass tresholds are shifted due to the p-wave DM annihilation at leading order, which is also an effect explained in earlier sections.

The allowed R_K region in aIA$^{\mathrm{Maj}}$ changes compared to the Dirac version. In our study, this is a feature that is unique to aIA, since it is the only model to allow for additional contributions from crossed box diagrams involving Majorana fermions to $b \to s l^+ l^-$ transitions and B-$\bar{B}$ mixing (see Fig. 1). This causes the ordering of the R_K regions to deviate from the usual $R_K(\kappa_1) > R_K(\kappa_2)$ for $\kappa_1 > \kappa_2$ and we find that the R_K bounds on Γ_μ of $\kappa = 1.01$ is more stringent than the one on $\kappa = 15$, while the bounds on $\kappa = 5$ and $\kappa = 1.1$ are the lowest bounds within an $\mathcal{O}(1\%)$ range of each other. We briefly review this effect in Appendix B.

Ignoring DD at first, potential solutions of R_K with the observed RD are conceivable for non-coannihilation scenarios in the democratic setup (see Fig. 4.20). In the hierarchical setup, only the non-coannihilation scenarios are potentially able to reproduce the observed Ω_{DM} within the parameter space studied.

Concerning the DD results, aIA$^{\mathrm{Maj}}$ exhibits an interesting behavior induced by a dynamic interplay between leptophilic and quarkphilic characteristics.

From the perspective of a leptophilic DM model, regions in which Γ_μ becomes large are generally excluded because the effective axial-vector-type vertex of DM with the mediator in question leads to contributions that push the SD DM-nucleon cross section beyond the allowed limits. In this mode, however, the regions allowed by DD are bounded from above *and* below. There are two major effects at play that induce this behavior.

Firstly, contributions to the SD DM-nucleon cross section from one-loop diagrams are prone to destructive interference between quark and lepton loop contributions because of a relative sign. This relative sign can be explained by the different hypercharge structures of these particles, leading to a different coupling with the $SU(2)_L \times U(1)_Y$ gauge bosons (the left-handed quark doublet has a weak hypercharge of $Y = 1/6$ and the left-handed lepton doublet has a weak hypercharge of $Y = -1/2$ according to Table 1.1). Conversely to purely quarkphilic/leptophilic models, this means that the contributions from both quark and lepton loops do not necessarily increase the DM-nucleon cross section but can also reduce it in some regions of the parameter space.

Secondly, the RD rescaling is severely altered by the additional direct annihilations of DM into quarks. In contrast to loops in DD diagrams, these additional contributions are additive due to the distinct final states. Due to this enhanced rescaling effect, the DD exclusion is more aligned to the RD in comparison to the purely leptophilic DM models. The visible blue DD areas in Fig. 4.20 are a product of a dynamic interplay between these effects.

Furthermore, contributions to the SI DM-nucleon cross section can also arise in this model. As described in Sections 4.4.4.2 and 4.4.5.2, these contributions exclude masses below a certain threshold due to the specific inverse mass scaling. In coannhihilation scenarios, this threshold extends into the DM mass range $M_{\mathrm{DM}} \sim \mathcal{O}(100\,\mathrm{GeV}\text{-}1\,\mathrm{TeV})$ so that the allowed regions exhibit a visible lower bound. In the hierarchical setup, the threshold for $\kappa = 1.1$ exceeds the mass at which of the region allowed by the SD bounds reaches the perturbative limit so that no viable parameter space is left for this mass gap.

We do not find any solutions to the $(g-2)_\mu$ anomaly in the parameter space studied in aIA Majorana for both coupling structures, democratic and hierarchical. This includes potential solutions that underproduce DM, as DD excludes the whole $(g-2)_\mu$ regions.

Although there are only small windows, both coannihilation and non-coannihilation scenarios provide windows for a solution to DM. However, only the non-coannihilation scenario can also solve the R_K anomaly. For $\kappa = 5$ we find a mass range of $M_\psi \lesssim 200\,\mathrm{GeV}$ (which might be further constrained by a collider analysis) and for $\kappa = 1.1$ we find a small window at $1.22\,\mathrm{TeV} \lesssim M_\psi \lesssim 1.32\,\mathrm{TeV}$.

4.5 Summary

In this chapter, we analyzed a class of models addressing the R_K anomaly at one-loop level with regards to its DM phenomenology. The model class extends the SM by three BSM fields, one vector-like fermion and two scalars in realization a or one scalar and two vector-like fermions in realization b. We restricted ourselves to models that contain a fermionic singlet DM candidate and assumed all BSM fields to be charged oddly under a discrete $\mathcal{Z}_2$-symmetry in order to stabilize the lightest BSM particle against a potential decay.

For our analysis, we chose parameter configurations that allowed to solve R_K anomaly at smaller BSM Yukawa couplings to muons Γ_μ by choosing the product of BSM quark Yukawa couplings $\Gamma_s \Gamma_b^*$ to be at its upper limit set by B-$\bar{B}$ mixing. Additionally, we assumed mass degeneracy between the two non-DM BSM particles, which are heavier than the DM candidate by a factor κ and required vacuum stability of the scalar potential at tree level and perturbativity for all parameter sets studied.

We found five configurations of SM gauge group charge assignments up until the adjoint representation that contain a fermionic singlet. For each of these configurations, we analyzed the parameter space in case of the fermionic singlet being a Dirac/Majorana particle. We further distinguished between two different flavor structures for the BSM quark Yukawa couplings: democratic ($\Gamma_s \approx \Gamma_b$) and hierarchical ($\Gamma_b \gg \Gamma_s$). Further, we investigated different mass hierarchies in the BSM sector including both coannihilation scenarios ($\kappa = 1.01, 1.1$) and non-coannihilation scenarios $\kappa = 5, 15$.

Moreover, we examined whether these configurations can also account for the $(g-2)_\mu$ anomaly.

The results of this analysis are summarized in Tables 4.3 and 4.4. Table 4.3 summarizes the models' ability to provide simultaneous solutions to more than one of the problems (observed RD, R_K, $(g-2)_\mu$), while Table 4.4 summarizes solutions to a single problem only.

		RD + R_K + Δa_μ	RD + R_K	RD + Δa_μ
leptophilic	bIIA	✗	✗	✗
	bIIA$^{\text{Maj}}$	✗	✗	✗
	bVA	✗	✗	✗
	bVA$^{\text{Maj}}$	✗	✗	✗
quarkphilic	bIIB	✗	✗	✗
	bIIB$^{\text{Maj}}$	✗	dem.: $M_{\psi_Q} \gtrsim 1.5\,\text{TeV}\,\vert_{\kappa=1.1}$	✗
	bVIB	✗	✗	✗
	bVIB$^{\text{Maj}}$	✗	✗	✗
amphiphilic	aIA	✗	✗	✗
	aIA$^{\text{Maj}}$	✗	dem.: $M_\psi \lesssim 200\,\text{GeV}\,\vert_{\kappa=5}$	✗

Table 4.3: Allowed mass regions for simultaneous solutions to RD, R_K and Δa_μ for each model.

Our study showed that we can further distinguish between three different subclasses of models, namely leptophilic, quarkphilic and amphiphilic DM models, depending on the direct DM vertices with SM fermions.

According to our analysis, all Dirac DM models are completely excluded by DD in the parameter space viable for an R_K or $(g-2)_\mu$ solution. We found that the principal reason for this exclusion is the kinematically unsuppressed (v,v)-type interaction in t-channel Z-boson interactions.

Majorana DM models, conversely to Dirac DM models, do not exhibit this kind of interaction due to the vanishing vector currents $\bar{\chi}\gamma^\mu\chi$ and are thus not as tightly constrained. These models provide potential for solutions of the aforementioned problems in different regions of the parameter space depending on the subclass.

We included an analysis of limits from ID and did not find any constraints on the parameter space of the Majorana models. Even characteristic features that can stem from s-wave DM annihilation in VIB processes do not not constrain our setup because of severe RD rescaling.

Leptophilic models have the potential to solve the R_K anomaly in the $M_{\psi_L} \lesssim 1000\,\text{GeV}$ region, while $(g-2)_\mu$ can be principally solved in the region $M_{\psi_L} \lesssim 290\,\text{GeV}$. These statements are valid for for coannihilation scenarios with underproduced DMRD. In these models, we found that the correct RD can only be achieved if the BSM Yukawa coupling is chosen to be very small in coannihilation scenarios. This statement is also uniquely true for leptophilic Dirac DM models as opposed to quark- and amphiphilic Dirac DM models.

In the quark and amphiphilic DM cases, we found that Majorana DM models have the potential to offer parameter space for simultaneous solutions of the observed RD and R_K.

The amphiphilic model aIA$^{\text{Maj}}$ provides a solution in the region $M_\psi \lesssim 200\,\text{GeV}$ for a non-coannihlation scenario. A small sweet spot in the region $1.22\,\text{TeV} \lesssim M_\psi \lesssim 1.32\,\text{TeV}$ for $\kappa = 1.1$ can also accommodate the observed DMRD, while not being able to solve the R_K anomaly. We also find several single solutions to the R_K anomaly with underproduced RD in both democratic and hierarchical scenarios. However, not one amphiphilic model setup could reproduce the required contributions to $(g-2)_\mu$.

We showed that democratic, coannihilating, quarkphilic Majorana DM models are relatively versatile in producing individual solutions to each of the problems addressed in this chapter. This is well documented by the entries for bIIB$^{\text{Maj}}$ and bVIB$^{\text{Maj}}$ in Table 4.4. In addition

		R_K only	RD only	Δa_μ only
leptophilic	bIIA	✗	dem.: $M_{\psi_L} \approx 270\,\mathrm{GeV}\,\vert_{\kappa=1.1}$, $M_{\psi_L} \approx 1.62\,\mathrm{TeV}\,\vert_{\kappa=1.01}$ hier.:$M_{\psi_L} \approx 9.1\,\mathrm{TeV}\,\vert_{\kappa=1.1}$	✗
	bIIA$^{\mathrm{Maj}}$	dem.: $M_{\psi_L} \lesssim 180\,\mathrm{GeV}\,\vert_{\kappa=1.01}$ hier.:$M_{\psi_L} \lesssim 420\,\mathrm{GeV}\,\vert_{\kappa=1.1}$, $M_{\psi_L} \lesssim 1000\,\mathrm{GeV}\,\vert_{\kappa=1.01}$	dem.:$M_{\psi_L} \approx 470\,\mathrm{GeV}\,\vert_{\kappa=1.1}$, $M_{\psi_L} \approx 1.85\,\mathrm{TeV}\,\vert_{\kappa=1.01}$ hier.: $M_{\psi_L} \lesssim 16.8\,\mathrm{TeV}\,\vert_{\kappa=1.1}$	hier.: $M_{\psi_L} \lesssim 170\,\mathrm{GeV}\,\vert_{\kappa=1.1}$, $M_{\psi_L} \lesssim 290\,\mathrm{GeV}\,\vert_{\kappa=1.01}$
	bVA	✗	dem.:$M_{\psi_L} \approx 440\,\mathrm{GeV}\,\vert_{\kappa=1.1}$,$M_{\psi_L} \approx 1.7\,\mathrm{TeV}\,\vert_{\kappa=1.01}$ hier.: $M_{\psi_L} \approx 5.7\,\mathrm{TeV}\,\vert_{\kappa=1.1}$,$M_{\psi_L} \approx 30\,\mathrm{TeV}\,\vert_{\kappa=1.01}$	✗
	bVA$^{\mathrm{Maj}}$	hier.: $M_{\psi_L} \lesssim 410\,\mathrm{GeV}\,\vert_{\kappa=1.01}$, $M_{\psi_L} \lesssim 260\,\mathrm{GeV}\,\vert_{\kappa=1.1}$	dem.: $M_{\psi_L} \lesssim 630\,\mathrm{GeV}\,\vert_{\kappa=1.1}$, $M_{\psi_L} \lesssim 1.85\,\mathrm{TeV}\,\vert_{\kappa=1.01}$ hier.: $M_{\psi_L} \lesssim 9\,\mathrm{TeV}\,\vert_{\kappa=1.1}$, $M_{\psi_L} \lesssim 32.4\,\mathrm{TeV}\,\vert_{\kappa=1.01}$	hier.: $M_{\psi_L} \lesssim 140\,\mathrm{GeV}\,\vert_{\kappa=1.1}$, $M_{\psi_L} \lesssim 210\,\mathrm{GeV}\,\vert_{\kappa=1.01}$
quarkphilic	bIIB	✗	✗	✗
	bIIB$^{\mathrm{Maj}}$	dem.:$M_{\psi_Q} \gtrsim 270\,\mathrm{GeV}\,\vert_{\kappa=1.1}$, $M_{\psi_Q} \gtrsim 1.5\,\mathrm{TeV}\,\vert_{\kappa=1.01}$	dem.: $M_{\psi_Q} \gtrsim 520\,\mathrm{GeV}\,\vert_{\kappa=1.1}$ $M_{\psi_Q} \gtrsim 2.32\,\mathrm{TeV}\,\vert_{\kappa=1.01}$	dem.: $M_{\psi_Q} \in [150{,}500]\,\mathrm{GeV}\,\vert_{\kappa=1.1}$, $M_{\psi_Q} \in [400{,}550]\,\mathrm{GeV}\,\vert_{\kappa=1.01}$
	bVIB	✗	✗	✗
	bVIB$^{\mathrm{Maj}}$	dem.: $M_{\psi_Q} \gtrsim 410\,\mathrm{GeV}\,\vert_{\kappa=1.1}$, $M_{\psi_Q} \gtrsim 2.4\,\mathrm{TeV}\,\vert_{\kappa=1.01}$	dem.: $M_{\psi_Q} \gtrsim 620\,\mathrm{GeV}\,\vert_{\kappa=1.1}$	dem.: $M_{\psi_Q} \in [350{,}970]\,\mathrm{GeV}\,\vert_{\kappa=1.1}$ $M_{\psi_Q} \lesssim 130\,\mathrm{GeV}\,\vert_{\kappa=5}$
amphi-philic	aIA	✗	✗	✗
	aIA$^{\mathrm{Maj}}$	dem.: $M_\psi \lesssim 860\,\mathrm{GeV}\,\vert_{\kappa=15}$, $M_\psi \lesssim 420\,\mathrm{GeV} \vee M_\psi \gtrsim 1.5\,\mathrm{TeV}\,\vert_{\kappa=5}$ hier.:$M_\psi \lesssim 200\,\mathrm{GeV}\,\vert_{\kappa=15}$, $M_\psi \lesssim 900\,\mathrm{GeV}\,\vert_{\kappa=5}$ $M_\psi \in [600\,\mathrm{GeV}, 3.2\,\mathrm{TeV}]\,\vert_{\kappa=1.1}$	dem: $M_\psi \in [1.22{,}1.32]\,\mathrm{TeV}\,\vert_{\kappa=1.1}$	✗

Table 4.4: Allowed mass regions for individual solutions to either RD, R_K and Δa_μ for each model.

to that, we also found a promising window at $M_{\psi_Q} \gtrsim 1.5\,\text{TeV}$ for $\kappa = 1.1$ in bIIB^{Maj}, which produces the observed Ω_{DM} and contributes correctly to R_K.

Many models feature the most interesting parameter windows in the TeV range or below, as summarized in Tables 4.3 and 4.4. Most of these scenarios include color-charged particles in the TeV range and earlier collider studies have shown that similar setups can be constrained up to TeV scale DM masses. A dedicated collider analysis beyond the content of Section 4.3.4 of the parameter space of interest is thus motivated by our DM phenomenology analysis.

Such a detailed collider analysis has been conducted e.g. in [213], where a similarly systematic study of this model class has been performed[19]. In their work, the authors choose an approach of presenting their results, which is complementary to the one chosen in this thesis. While they scan the available parameter space using assumptions that are more suitable for collider studies, effects of the flavor structure and coannihilation are not focused on as much as in this work.

Potential future work could also extend this study to different kinds of DM candidates apart from the fermionic singlet.

---

[19] This research article was published as a preprint just a few days before the article that this chapter is based on ([2]). The two independent articles discuss mainly the same topic but with fundamentally different approaches with regards to the analysis strategy. The authors study a different slice of the parameter space and perform a dedicated collider analysis with MadGraph, Pythia 8, DELPHES and CheckMATE. However, SD DD limits for Majorana models and RD rescaling of the DD bounds are not employed in their work. Another notable difference is that [213] does not thoroughly focus on fermionic singlet DM.

Chapter 5

Summary and Conclusion

In this thesis, we addressed current anomalies and inconsistencies of the SM such as hints towards LFUV in the B-meson decays, the existence of DM and anomalies in the neutrino sector in the context of BSM model building with additional neutral leptons.

In Chapter 1, we gave a brief overview of the existing frameworks of the SM and ΛCDM standard cosmology. Furthermore, we shortly outlined anomalies in the experimental data and possible shortcomings of these theories. In Chapter 2, we reviewed the theoretical frameworks of neutrino oscillations, neutrino mass generation, early universe thermodynamics and the production and detection of WIMP DM.

In Chapter 3, we introduced a model with additional sterile neutrinos and ADRs addressing the long-standing SBL anomalies as well as the Reactor- and Gallium anomalies. The ADR is introduced as a ubiquitous potential for the sterile neutrino state, potentially stemming from e.g. extradimensional setups.

We reviewed different approaches to constructing such a model. We discussed a $(3+1)\nu$+ADR model, a $(3+3)\nu$+universal ADR model and finally a $(3+3)\nu$+individual ADRs model. We showed that these models can in principle emulate an effective $(1+1)\nu$ model at low energies. Furthermore, we illustrated that both the $(3+1)\nu$+ADR model and the $(3+3)\nu$+universal ADR model are flawed in terms of their behavior at LBL disappearance experiments at high energies in combination with a non-vanishing oscillation amplitude at SBL experiments. The $(3+1)\nu$+ADR model always features a residual oscillation mode at high energies, which is not observed by atmospheric disappearance experiments. This issue can be avoided in a $(3+3)\nu$+ADR setup with democratic mixing. However, the $(3+3)\nu$+universal ADR model predicts a vanishing appearance probability at SBL experiments due to unitarity cancellations in this case. A $(3+3)\nu$+individual ADRs model does not suffer from this issue.

We explored the parameter space of the $(3+3)\nu$+individual ADRs model using four BMPs, pointing out characteristic imprints of the choices of the additional mass-squared difference $\Delta m^2_{\mathrm{SBL}}$, the mixing angle θ and the set of ADR parameters $\varepsilon, \eta, \kappa$ and ξ in the oscillation probabilities at several experiments. We found that the strongest constraints come from LBL accelerator experiments like T2K, which operate at energies $E \sim \mathcal{O}(100\,\mathrm{MeV}\text{-}1\,\mathrm{GeV})$, and sub-GeV data of atmospheric experiments like SK and IceCube. A potential fit to the world neutrino data and the forthcoming results of the MicroBooNE SBL experiment at Fermilab can provide a robust test for this model.

In Chapter 4, we studied a class of one-loop solutions to the B-anomalies and $(g-2)_\mu$ in the context of fermionic singlet DM phenomenology. This model class introduces three BSM fields, either one scalar and two vector-like fermions or vice versa. These particles interact with the SM quarks and leptons via Yukawa interactions, where couplings to the first generation are assumed to be negligible. The models are classified in terms of their representations under the SM gauge group up to the adjoint representation. Out of the 48 possible combinations we identified five setups with a fermionic singlet, which can be of either Dirac or Majorana nature.

We assume all BSM fields to be charged oddly (and SM particles evenly) under a $\mathcal{Z}_2$-symmetry in order to stabilize the DM candidate against a decay. We categorized these models in terms of the DM candidate's coupling to the SM, yielding four leptophilic, four quarkphilic and two amphiphilic DM models. For each of the ten different models, we studied the DM phenomenology for both democratic and hierarchical coupling structures in the quark sector. Furthermore, we investigated different mass differences in the dark sector including coannihilation and non-coannihilation scenarios. For our numerical scans, we took into account vacuum stability of the scalar potential and constraints on BSM Yukawas from B-$\bar{B}$-mixing.

Our results show that all Dirac models are ruled out by DD in the parameter space relevant for the solution of the B-anomalies and $(g-2)_\mu$ due to the strong effective interaction with the Z-boson. In Majorana models, we found several windows in the parameter space where individual solutions to the B-anomalies, DM or $(g-2)_\mu$ are allowed by DD. This is mainly due to vanishing vector current interaction in the effective DM-Z-boson vertex. We also found that VIB ID constraints are not sufficiently stringent to rule out these scenarios. In quarkphilic and amphiphilic DM models, we found a window for a simultaneous solution of DM and the B-anomalies. However, most of the parameter space viable in terms of DM phenomenology is located in the range $M_{\text{DM}} \lesssim 1\,\text{TeV}$, which could be in the range of current colliders. This result motivates future work on this topic including a dedicated collider study of this setup.

Appendix

A Useful Identities of Dirac Matrices, Spinors and Bilinears

A.1 Dirac Matrix Identities

A useful identity for Dirac matrices is

$$\gamma^0\gamma^\mu\gamma^0 = (\gamma^\mu)^\dagger\,, \tag{A.1}$$

which relates the Dirac matrices γ^μ with their hermitian conjugates. This is effectively a change of basis, since the the time-like Dirac matrix γ^0 is an involution, as

$$\gamma^0\gamma^0 = \mathbb{1}_4\,. \tag{A.2}$$

This in turn means that γ^0 is hermitian: $\gamma^0 = (\gamma^0)^\dagger$. It also means that the description of the Dirac matrices γ^μ and their hermitian conjugates $(\gamma^\mu)^\dagger$ is equivalent, as they are connected via a similarity transformation of the form $A\gamma^\mu A^{-1} = (\gamma^\mu)^\dagger$ and thus they can be shown to obey the same Clifford algebra. Using Eq. (A.1) and the definition of the Clifford algebra $\{\gamma^\mu, \gamma^\nu\} = 2\eta^{\mu\nu}$ made in Section 1.1, we find that the space-like Dirac matrices are anti-hermitian: $\gamma^\mu = -(\gamma^\mu)^\dagger$.

Another important similariy transformation for Dirac matrices is one, which involves the charge conjugation matrix C (which is more precisely defined in Section A.2) with

$$C\gamma^\mu C^{-1} = -(\gamma^\mu)^T\,. \tag{A.3}$$

This transformation shows that the negative transposed matrices $-(\gamma^\mu)^T$ also obey the same Clifford algebra.

A.2 Identities Involving Charge Conjugations

In this appendix we review some spinor identities following Section 3 in [73]. Let us assume that ψ is a four-component spinor. The charge conjugation is then defined as

$$\psi^C = C\bar{\psi}^T = \mathrm{i}\gamma^2\gamma^0\psi^* = \begin{pmatrix} 0 & -\mathrm{i}\sigma^2 \\ -\mathrm{i}\sigma^2 & 0 \end{pmatrix}\psi^* \tag{A.4}$$

in Dirac representation, so that C is antisymmetric, unitary and real, yielding

$$C^{-1} = -C = C^T = C^\dagger\,, \quad C\gamma^\mu C^{-1} = -(\gamma^\mu)^T\,. \tag{A.5}$$

Based on these properties of C, it can be shown that

$$\overline{\psi^C} = \psi^T C \tag{A.6}$$

and that the charge conjugation is an involution

$$(\psi^C)^C = \psi\,. \tag{A.7}$$

Useful properties of bilinears involving charge conjugation are

$$\begin{aligned} \overline{\psi_1}\psi_2^C &= \overline{\psi_2^C}\psi_1\,, && \text{(A.8)}\\ \overline{\psi_1}A\psi_2 &= \overline{\psi_2^C}(CA^TC^{-1})\psi_1^C\,, && \text{(A.9)} \end{aligned}$$

where A is an arbitrary 4×4 matrix.

Using Eqs. (A.9) and (A.3) it can be shown that the vector bilinear of a Majorana spinor vanishes

$$\begin{gathered} \bar{\psi}\gamma^\mu\psi = \overline{\psi^C}\gamma^\mu\psi^C = -\overline{\psi^C}\gamma^\mu\psi^C \\ \Rightarrow \bar{\psi}\gamma^\mu\psi = 0\,, \end{gathered} \tag{A.10}$$

where we used that the Majorana spinor obeys the Majorana equation

$$\psi = \psi^C\,. \tag{A.11}$$

Furthermore, [7] suggests also that the number operator $\int \mathrm{d}^3x\bar{\psi}\gamma^0\psi$ vanishes for Majorana particles.

B Wilson Coefficients and Loop Functions

Following [48], the $b \to s\mu\mu$ transition and B-$\bar{B}$ Wilson coefficients read

$$\begin{aligned} \mathcal{C}_9^{\text{box},a} = -\mathcal{C}_{10}^{\text{box},a} &= \frac{\sqrt{2}}{4G_FV_{tb}V_{ts}^*}\frac{\Gamma_s\Gamma_b^*|\Gamma_\mu|^2}{32\pi\alpha_{\text{em}}M_\psi^2}(\chi\eta F(x_Q,x_L) + 2\chi^M\eta^M G(x_Q,x_L))\,, && \text{(B.1)}\\ \mathcal{C}_9^{\text{box},b} = -\mathcal{C}_{10}^{\text{box},a} &= -\frac{\sqrt{2}}{4G_FV_{tb}V_{ts}^*}\frac{\Gamma_s\Gamma_b^*|\Gamma_\mu|^2}{32\pi\alpha_{\text{em}}M_\phi^2}(\chi\eta - \chi^M\eta^M)F(y_L,y_L)\,, && \text{(B.2)}\\ \mathcal{C}_{B\bar{B}}^a &= \frac{(\Gamma_s\Gamma_b^*)^2}{128\pi^2M_\psi^2}\left(\chi_{B\bar{B}}\eta_{B\bar{B}}F(x_Q,x_Q) + 2\chi_{B\bar{B}}^M\eta_{B\bar{B}}^M G(x_Q,x_Q)\right)\,, && \text{(B.3)}\\ \mathcal{C}_{B\bar{B}}^b &= \frac{(\Gamma_s\Gamma_b^*)^2}{128\pi^2M_\phi^2}\left(\chi_{B\bar{B}}\eta_{B\bar{B}} - \chi_{B\bar{B}}^M\eta_{B\bar{B}}^M\right)F(y_Q,y_Q)\,, && \text{(B.4)} \end{aligned}$$

where $x_{Q/L} = {}^{M^2_{\phi_{Q/L}}}\!/\!{}_{M^2_\psi}$ and $y_{Q/L} = {}^{M^2_{\psi_{Q/L}}}\!/\!{}_{M^2_\phi}$. F and G are the dimensionless loop-functions

$$\begin{aligned} F(x,y) &= \frac{1}{(1-x)(1-y)} + \frac{x^2\ln x}{(1-x)^2(1-y)} + \frac{y^2\ln y}{(1-x)(1-y)^2}\,, && \text{(B.5)}\\ G(x,y) &= \frac{1}{(1-x)(1-y)} + \frac{x\ln x}{(1-x)^2(1-y)} + \frac{y\ln y}{(1-x)(1-y)^2}\,. && \text{(B.6)} \end{aligned}$$

The $SU(2/3)$-factors $\eta^{(M)}_{(B\bar{B})}$,$\chi^{(M)}_{(B\bar{B})}$ can be extracted from Table 1.

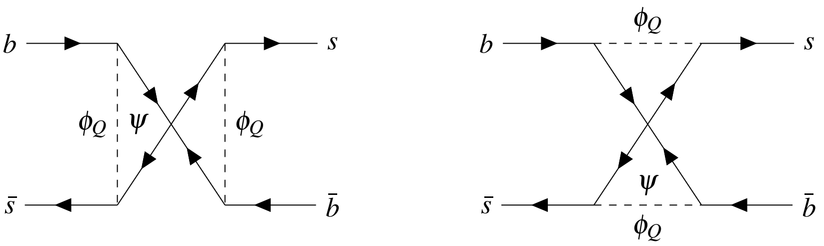

(a) B-$\bar{B}$ mixing

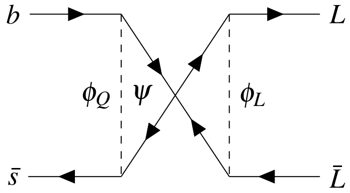

(b) $b \to s\,l^+l^-$ transitions

Figure 1: Crossed box-diagram contributions to (a) B-$\bar{B}$-mixing and (b) $b \to s\,l^+l^-$ in the case of ψ being a Majorana fermion.

$SU(2)_L$	η	η^M	$\eta_{B\bar{B}}$	$\eta^M_{B\bar{B}}$	η_{a_μ}	$\tilde{\eta}_{a_\mu}$
I	1	1	1	1	$-1 \mp X$	$\pm X$
II	1	0	1	0	$-\frac{1}{2} \mp X$	$-\frac{1}{2} \pm X$
III	$\frac{5}{16}$	0	$\frac{5}{16}$	0	$-\frac{7}{8} \mp \frac{3}{4}X$	$\frac{1}{8} \pm \frac{3}{4}X$
IV	$\frac{5}{16}$	$\frac{1}{16}$	$\frac{5}{16}$	$\frac{1}{16}$	$-\frac{1}{4} \mp \frac{3}{4}X$	$-\frac{1}{2} \pm \frac{3}{4}X$
V	$\frac{1}{4}$	0	$\frac{5}{16}$	0	$-\frac{1}{2} \mp X$	$-\frac{1}{2} \pm X$
VI	$\frac{1}{4}$	0	1	0	$-\frac{7}{8} \mp \frac{3}{4}X$	$\frac{1}{8} \pm \frac{3}{4}X$
$SU(3)_C$	χ	χ^M	$\chi_{B\bar{B}}$	$\chi^M_{B\bar{B}}$	χ_{a_μ}	
A	1	1	1	1	1	
B	1	0	1	0	3	

Table 1: $SU(2)$ and $SU(3)$ factors entering Wilson coefficients $\mathcal{C}_9^{\text{box}}$ and $\mathcal{C}_{B\bar{B}}$ [48]. X is defined as the (negative) weak hypercharge of ψ (ϕ).

We present the constraints on the Yukawa couplings $\Gamma_s\Gamma_b^*$ and Γ_μ from B-$\bar{B}$ and LFUV variables in Tables 2 and 3.

In the case of the model aIA$^{\text{Maj}}$, there are additonal diagrams that contribute to the Wilson coeffcients in $\mathcal{C}_9$ and $\mathcal{C}_{B\bar{B}}$, as indicated in Table 1. These diagrams are depicted in Fig. 1. As a consequence, the R_K bound is not monotonous in the mass ratio κ as opposed to all other models presented in this work. In Fig. 2, we show the R_K bound as a function of κ at an exemplary DM mass of $M_\psi = 100\,\text{GeV}$. We can see that at $\kappa_{\text{min}} \approx 1.777$, the function is minimal and therefore gives the weakest constraint. Furthermore, for the values chosen in this work, the hierarchy of the bounds reads

$$\text{Bound}_{R_K}(1.01) > \text{Bound}_{R_K}(15) > \text{Bound}_{R_K}(1.1) \approx \text{Bound}_{R_K}(5)\,. \tag{B.7}$$

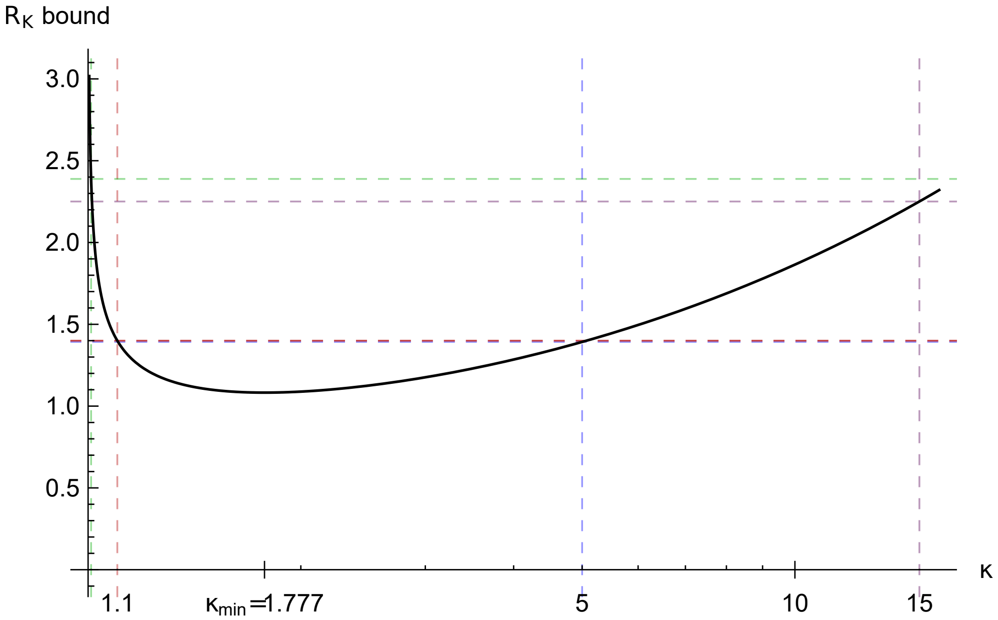

Figure 2: The R_K bound as a function of the mass ratio κ at $M_\psi = 100\,\text{GeV}$ for aIA$^{\text{Maj}}$. The minimum lies at $\kappa \approx 1.777$.

The contribution to $a_\mu = {}^{(g-2)_\mu}/_2$, which is defined via the effective operator

$$\mathcal{H}_{\text{eff}} = -a_\mu \frac{e}{4m_\mu}(\bar{\mu}\sigma^{\nu\rho}\mu)F_{\nu\rho} \tag{B.8}$$

yields

$$\Delta a_\mu^a = \frac{m_\mu^2 \left|\Gamma_\mu\right|^2}{8\pi^2 M_\psi^2}\chi_{a_\mu}\left[\eta_{a_\mu}F_7(x_L) - \tilde{\eta}_{a_\mu}\tilde{F}_7(x_L)\right] , \tag{B.9}$$

$$\Delta a_\mu^b = \frac{m_\mu^2 \left|\Gamma_\mu\right|^2}{8\pi^2 M_\phi^2}\chi_{a_\mu}\left[\tilde{\eta}_{a_\mu}\tilde{F}_7(y_L) - \eta_{a_\mu}F_7(y_L)\right] , \tag{B.10}$$

where the group factors $\tilde{\eta}_{a_\mu}/\eta_{a_\mu}$ and χ_{a_μ} can be extracted from Table 1 and the functions $F_7(x)$ and $\tilde{F}_7$ are characterized as

$$F_7(x) = \frac{x^3 - 6x^2 + 6x\log(x) + 3x + 2}{12(x-1)^4}, \quad \tilde{F}_7(x) = \frac{F_7(\frac{1}{x})}{x} . \tag{B.11}$$

The constraints on Γ_μ from $(g-2)_\mu$ are summarized in Table 3.

	$\mathcal{B}_{bs}^{\text{model}}(\kappa)$	$\mathcal{B}_{\mu}^{\text{model}}(\kappa)$
aIA	$2.45 \cdot 10^{-6} \left(\sqrt{(\frac{-0.000792+0.000792\kappa^4-0.001583\kappa^2 \log(\kappa^2)}{(\kappa^2-1)^3}}\right)^{-1}$	$0.0108 \left(\sqrt[4]{\frac{-0.000792+0.000792\kappa^4-0.001583\kappa^2 \log(\kappa^2)}{((\kappa^2-1)^3}}\right)^{-1}$
aIA$_{\mathrm{M}}$	$2.45 \cdot 10^{-6} \left(\sqrt{\frac{-0.003958+0.003166\kappa^2+0.0007916\kappa^4+(-0.001583-0.003166\kappa^2)\log(\kappa^2)}{(\kappa^2-1)^3}}\right)^{-1}$	$0.0108 \left(\sqrt[4]{\frac{-0.003958+0.003166\kappa^2+0.0007916\kappa^4+(-0.001583-0.003166\kappa^2)\log(\kappa^2)}{(\kappa^2-1)^3}}\right)^{-1}$
bIIA	0.000151κ	$0.608276 \left(\sqrt{\frac{\kappa(-230.909+307.878\kappa^2-76.970\kappa^4-153.939\log(\kappa^2))}{(\kappa^2-1)^3}}\right)^{-1}$
bVA	0.000270κ	$19.2354 \left(\sqrt{\frac{\kappa(-103.266+137.687\kappa^2-34.4218\kappa^4-68.8437\log(\kappa^2))}{(\kappa^2-1)^3}}\right)^{-1}$
bIIB	$0.000087 \left(\sqrt{\frac{-1+\kappa^4-2\kappa^2 \log(\kappa]^2)}{(\kappa^2-1)^3}}\right)^{-1}$	$2.8855 \sqrt[4]{(\kappa^2-1)^3} \left\lvert \sqrt{\frac{-3+4\kappa^2-\kappa^4-4\log(\kappa)}{\sqrt{-1+\kappa^4-4\kappa^2 \log(\kappa)}}} \right\rvert^{-1}$
bVIB	$2.45 \cdot 10^{-6} \left(\sqrt{\frac{-0.000791572+0.000791572\kappa^4-0.00158314\kappa^2 \log(\kappa^2)}{(\kappa^2-1)^3}}\right)^{-1}$	$19.2354 \left(\sqrt{\frac{-33.3288+44.4384\kappa^2-11.1096\kappa^4-22.2192\log(\kappa^2)}{(\kappa^2-1)^3\sqrt{\frac{-1+\kappa^4-2\kappa^2\log(\kappa^2)}{(\kappa^2-1)^3}}}}\right)^{-1}$

Table 2: Presented here are the constraints on new Yukawa coupling Γ_μ and the product $\Gamma_s\Gamma_b^*$. The entries of this table represent the upper bound on $\Gamma_s\Gamma_b^*$ from B-$\bar{B}$-mixing and thus a lower bound on Γ_μ from R_K.

	$\Gamma_\mu \in$
bIIA	$\frac{[0.0000386,0.0000568]M_{\psi_L}(1-\kappa^2)^2}{\sqrt{\lvert -0.0000235648-0.0000353472\kappa^2+0.0000706944\kappa^4-0.0000117824\kappa^6-0.0000706944\kappa^2\log(\kappa^2)\rvert}}$
bVA	$\frac{[0.0000386,0.0000568]M_{\psi_L}(1-\kappa^2)^2}{\sqrt{\lvert -0.0000235648-0.0000353472\kappa^2+0.0000706944\kappa^4-0.0000117824\kappa^6-0.0000706944\kappa^2\log(\kappa^2)\rvert}}$
bIIB	$[0.01590,0.02342]\kappa M_{\psi_Q}$
bVIB	$[0.00821,0.01209]\kappa M_{\psi_Q}$
aIA	$\frac{[0.0000386,0.0000568]M_{\psi}(1-\kappa^2)^2}{\sqrt{\lvert -0.0000235648-0.0000353472\kappa^2+0.0000706944\kappa^4-0.0000117824\kappa^6-0.0000706944\kappa^2\log(\kappa^2)\rvert}}$

Table 3: Presented here are the constraints on new Yukawa coupling Γ_μ for a solution of $(g-2)_\mu$. These constraints contain upper and lower bound on Γ_μ formulated as an interval.

C Relevant Plots of the DM Indirect Detection Results

In this appendix, we show the corresponding plots for the ID results from VIB discussed in Section 4.3.3. Figs. 3-7 show scans over the Γ_μ-M_{DM}-plane of the thermally averaged DM annihilation cross section into a fermion pair and an additional photon normalized by the bounds from Fermi-LAT/HESS [164]. In the scan, we make all assumptions about the model parameters stated in Section 4.4.1. In these figures, we include the RD rescaling according to Eq. (4.3.11) into the bound. Green-shaded points indicate that the VIB cross section is below the bounds and thus not excluded, whereas and purple-shaded areas are excluded.

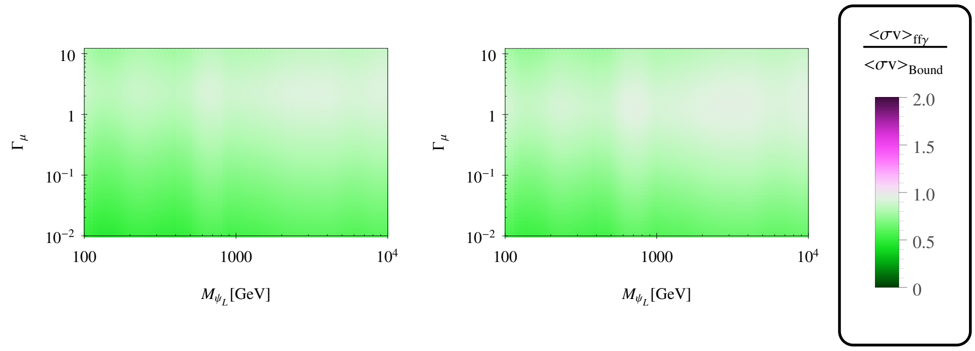

(a) $\kappa = 1.01$ (b) $\kappa = 1.1$

Figure 3: The thermally averaged VIB annihilation cross section normalized to the bound from Fermi-LAT and HESS $\langle\sigma v\rangle_{\bar f f\gamma}/\langle\sigma v\rangle_{\mathrm{Bound}}$ in the Γ_μ-M_{DM}-plane for the democratic scenario in bIIA Majorana. The ID bound is RD-rescaled. The color code indicates the exclusion of the parameter set, where green shades indicate non-exclusion and purple shades indicate excluded points. Since no purple areas exist in this setup, no constraints on the parameter space can be derived.

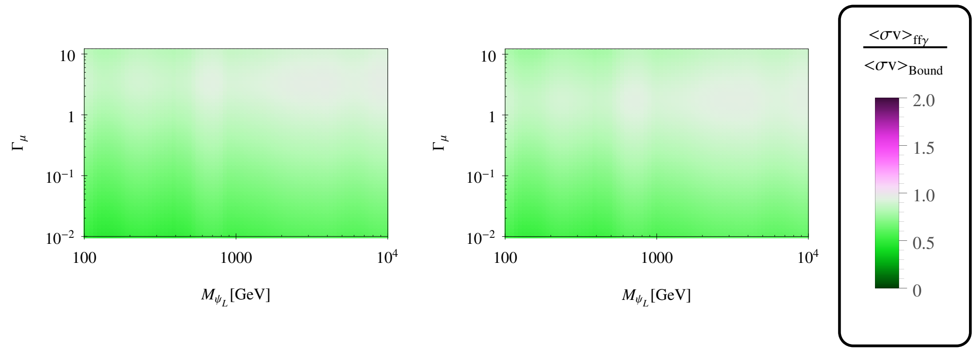

(a) $\kappa = 1.01$ (b) $\kappa = 1.1$

Figure 4: The thermally averaged VIB annihilation cross section normalized to the bound from Fermi-LAT and HESS $\langle\sigma v\rangle_{\bar f f\gamma}/\langle\sigma v\rangle_{\mathrm{Bound}}$ in the Γ_μ-M_{DM}-plane for the democratic scenario in bVA Majorana. The ID bound is RD-rescaled according to Eq. (4.3.11). The color code indicates the exclusion of the parameter set, where green shades indicate non-exclusion and purple shades indicate excluded points. Since no purple areas exist in this setup, no constraints on the parameter space can be derived.

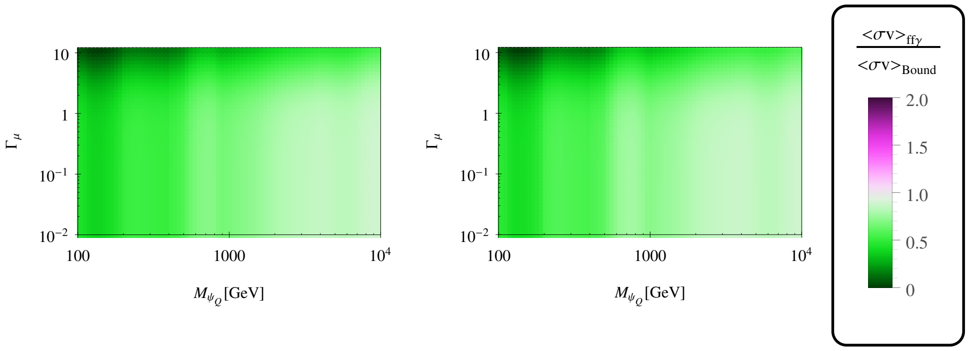

(a) $\kappa = 1.01$

(b) $\kappa = 1.1$

Figure 5: The thermally averaged VIB annihilation cross section normalized to the bound from Fermi-LAT and HESS $\langle\sigma v\rangle_{\bar{f}f\gamma}/\langle\sigma v\rangle_{\text{Bound}}$ in the Γ_μ-M_{DM}-plane for the democratic scenario in bIIB Majorana. The ID bound is RD-rescaled according to Eq. (4.3.11). The color code indicates the exclusion of the parameter set, where green shades indicate non-exclusion and purple shades indicate excluded points. Since no purple areas exist in this setup, no constraints on the parameter space can be derived.

The stripy pattern imprinted in all figures stems from the normalization to the mass-dependent limits from Fermi-LAT/HESS.

All figures show that the searches for VIB line-like signatures in the photon spectrum cannot place any constraints onto the parameter space. This is mainly due to the quadratic RD rescaling of the ID bound. Note that hierarchical scenarios tend to underproduce DM because of the large couplings to third generation quarks and the subsequently late freeze out. Thus, the ID bound for parameter points in a hierarchical scenario undergo an even more severe RD scaling than in democratic scenarios, which therefore become most constraining with regards to ID.

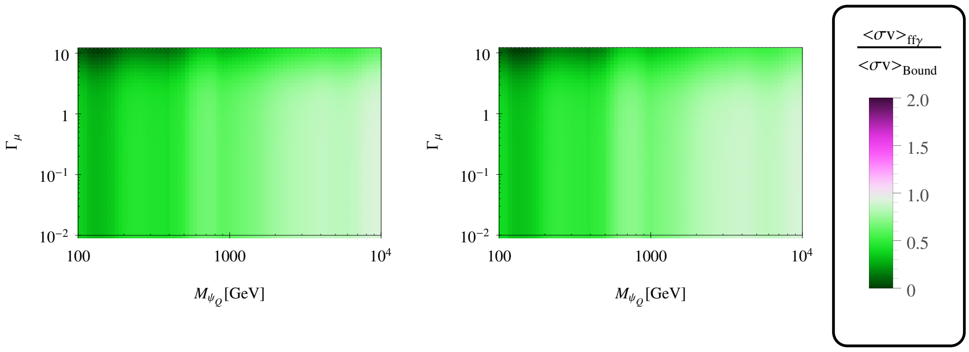

(a) $\kappa = 1.01$

(b) $\kappa = 1.1$

Figure 6: The thermally averaged VIB annihilation cross section normalized to the bound from Fermi-LAT and HESS $^{\langle\sigma v\rangle_{\bar{f}f\gamma}}/_{\langle\sigma v\rangle_{\text{Bound}}}$ in the Γ_μ-M_{DM}-plane for the democratic scenario in bVIB Majorana. The ID bound is RD-rescaled according to Eq. (4.3.11). The color code indicates the exclusion of the parameter set, where green shades indicate non-exclusion and purple shades indicate excluded points. Since no purple areas exist in this setup, no constraints on the parameter space can be derived.

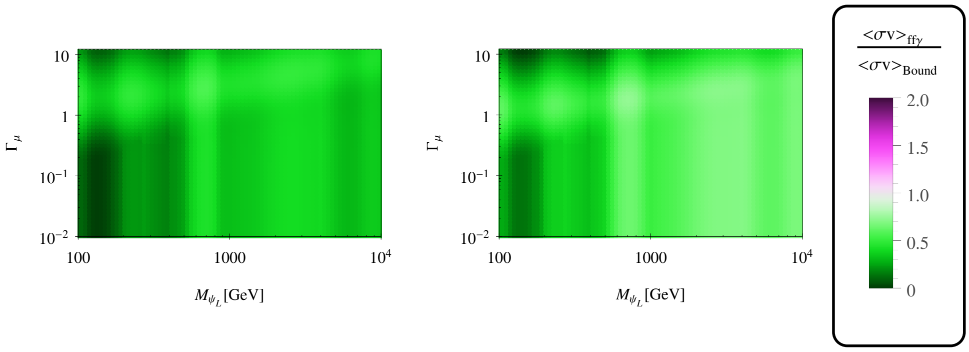

(a) $\kappa = 1.01$

(b) $\kappa = 1.1$

Figure 7: The thermally averaged VIB annihilation cross section normalized to the bound from Fermi-LAT and HESS $^{\langle\sigma v\rangle_{\bar{f}f\gamma}}/_{\langle\sigma v\rangle_{\text{Bound}}}$ in the Γ_μ-M_{DM}-plane for the democratic scenario in aIA Majorana. The ID bound is RD-rescaled according to Eq. (4.3.11). The color code indicates the exclusion of the parameter set, where green shades indicate non-exclusion and purple shades indicate excluded points. Since no purple areas exist in this setup, no constraints on the parameter space can be derived.

D Estimation of the DMRD in Coannihilation Scenarios

In addition to the discussion about the estimate for the relic density in the case of dominant direct annihilations in Section 4.3, we expand this discussion by giving a rough estimate of the RD in coannihilation scenarios ($\kappa \lesssim 1.2$) in this appendix.

Even in the scenario where only the direct annihilation of DM is relevant for the annihilation cross section, efficient conversions of dark sector particles can influence the *effective* annihilation cross section and thus the relic density significantly in the case of small mass splittings. This is done via an alteration of the ratio of equilibrium densities in Eq. (2.3.43).

Given the way we present the results in this work, we are most interested in the Yukawa coupling Γ_i required to produce the observed relic density for each ratio $\kappa \lesssim 1.2$.

Considering only the thermally averaged cross section of the direct annihilation of DM in Eq. (4.3.5), an increase in κ directly corresponds to a decrease of the cross section. As this is true for both Majorana and Dirac DM candidates. This is an intuitive result, since the non-DM BSM particle acts as a mediator of the annihilation diagram, for which an increasing mass implies a lower cross section.

However, if the ratio of equilibrium densities at the time of thermal freeze-out is considered, the κ dependence of the effective thermally averaged annihilation cross sectionis given by

$$\begin{aligned}\langle\sigma_{\text{eff}}v\rangle \approx{}& \frac{1}{\left(1+\kappa^2\right)^2}\left[1+\frac{g_{\text{non-DM}}}{g_{\text{DM}}}\kappa^{\frac{3}{2}}\exp\left(-\kappa x_f + x_f\right)\right]^{-2}\times\\ &\times\begin{cases} 1/8, & \text{for Dirac DM}\\ \left(1+\kappa^4\right)\left(1+\kappa^2\right)^{-2}, & \text{for Majorana DM}\end{cases}\,.\end{aligned} \tag{D.1}$$

This function is, conversely to Eq. (4.3.5) not monotonous in κ and develops a maximum at a finite κ_{max}. This means that there might be a value of κ_{max}, in whose case the observed relic density can be reproduced by the smallest Yukawa coupling Γ.

This effect can lead to the reversal of hierarchies of RD lines in a M_{DM}-Γ_μ diagram, since there can be a set of κ values, which require smaller Yukawa couplings than naïvely expected.

For example in the case of bIIA Dirac, the maximum of $\langle\sigma_{\text{eff}}v\rangle$ is reached at $\kappa_{\text{max}} \approx 1.15$. The corresponding behavior of the RD lines is shown in Fig. 4.8, where it is evident that the RD line of the $\kappa = 1.01$ scenario requires a larger Γ_μ than the $\kappa = 1.1$ scenario. A similar behavior can be observed in the results of the bVA and aIA Dirac scenarios, where the results are summarized in Figs. 4.11 and 4.18, respectively. Note that for purely quarkphilic DM scenarios, this effect cannot be observed in our analysis because the annihilation of DM into SM particles is dominated by annihilation into quark via $\Gamma_{s/b}$. However, we present our analysis in the M_{DM}-Γ_μ-plane and thus only the subdominant contribution of the coannihilation channels can be monitored directly.

In Majorana DM models, additional effects come into play. While DM direct annihilations are p-wave suppressed, coannihilations of the other BSM particles are s-wave and thus unsuppressed by velocity. Thus, in some parts of the parameter space, coannihilations can become dominant and Eq. (D.1), where we only consider DM direct annihilations, does not accurately describe the scenario anymore. Instead, the sum in Eq. (2.3.43) must be carried out entirely including coannihilations, yielding e.g.

$$
\begin{aligned}
\langle \sigma_{\text{eff}} v \rangle \approx \langle \sigma_{ann} v \rangle & \frac{\left(Y_{\text{DM}}\right)^2}{\left(Y_{\text{DM}} + Y_{\text{non-DM}}\right)^2} \\
& + \langle \sigma_{\text{coann},\phi_Q} v \rangle \frac{\left(Y_{\phi_Q}\right)^2}{\left(Y_{\text{DM}} + Y_{\text{non-DM}}\right)^2} + \langle \sigma_{\text{coann},\phi_L} v \rangle \frac{\left(Y_{\phi_L}\right)^2}{\left(Y_{\text{DM}} + Y_{\text{non-DM}}\right)^2} \\
& + \langle \sigma_{\text{coann},\phi_Q,\phi_L} v \rangle \frac{Y_{\phi_Q} Y_{\phi_L}}{\left(Y_{\text{DM}} + Y_{\text{non-DM}}\right)^2} ,
\end{aligned}
\tag{D.2}
$$

for a-type models, while b-type models are analogous.

In the case of leptophilic DM scenarios, e.g. , we find that for very a small mass splitting $\kappa = 1.01$ annihilations of the scalar doublet ϕ into SM leptons via Γ_μ is dominant. However, for a larger mass gap of $\kappa = 1.1$, direct annihilations of DM are again mainly responsible for setting the DMRD.

It is important to note that in the case of Majorana DM, the internal degrees of freedom of the fermionic singlet are halved compared to the Dirac case. This changes the relative composition of number densities in the dark sector, since the number density is directly proportional to g_i. Similarly, models that contain an $SU(2)_L$-triplet fermionic coannihilation partner have different internal degrees of freedom and subsequently a different composition of number densities than their $SU(2)_L$-singlet counterparts. So even in the case of dominant DM direct annihilations, this effect can affect the prediction of the DMRD via effective conversion, as discussed above.

In an exemplary comparison of bIIA^{Maj} and bVA^{Maj}, where the color-charged fermion ψ_Q makes the singlet → triplet shift, we can observe that the effective cross section of bIIA^{Maj} scales monotonically, while the one of bVA^{Maj} features a maximum in κ. As described above, this fact leads to the reordering of the RD line hierarchy.

Bibliography

[1] Dominik Döring, Heinrich Päs, Philipp Sicking, and Thomas J. Weiler. Sterile neutrinos with altered dispersion relations as an explanation for neutrino anomalies. *Eur. Phys. J. C*, 80(12):1202, 2020.

[2] Mathias Becker, Dominik Döring, Siddhartha Karmakar, and Heinrich Päs. Fermionic singlet dark matter in one-loop solutions to the R_K anomaly: a systematic study. *Eur. Phys. J. C*, 81(12):1053, 2021.

[3] Michael E. Peskin and Daniel V. Schroeder. *An Introduction to quantum field theory.* Addison-Wesley, Reading, USA, 1995.

[4] Steven Weinberg. *The Quantum theory of fields. Vol. 1: Foundations.* Cambridge University Press, 6 2005.

[5] Matthew D. Schwartz. *Quantum Field Theory and the Standard Model.* Cambridge University Press, 3 2014.

[6] M. Srednicki. *Quantum field theory.* Cambridge University Press, 1 2007.

[7] Utpal Sarkar. *Particle and astroparticle physics.* Series in high energy physics, cosmology, and gravitation. Taylor & Francis, New York, USA, 2008.

[8] P.A. Zyla et al. Review of Particle Physics. *PTEP*, 2020(8):083C01, 2020.

[9] J. Goldstone. Field Theories with Superconductor Solutions. *Nuovo Cim.*, 19:154–164, 1961.

[10] Jeffrey Goldstone, Abdus Salam, and Steven Weinberg. Broken Symmetries. *Phys. Rev.*, 127:965–970, 1962.

[11] UTFit-Collaboration. Fit results: Summer 18. `http://www.utfit.org/UTfit/Results`, 2018.

[12] Charles W. Misner, K.S. Thorne, and J.A. Wheeler. *Gravitation.* W. H. Freeman, San Francisco, 1973.

[13] Sean M. Carroll. *Spacetime and Geometry.* Cambridge University Press, 7 2019.

[14] Steven Weinberg. *Gravitation and Cosmology: Principles and Applications of the General Theory of Relativity.* John Wiley and Sons, New York, 1972.

[15] Steven Weinberg. *Cosmology.* 9 2008.

[16] Edward W. Kolb and Michael S. Turner. *The Early Universe*, volume 69. 1990.

[17] L. Bergstrom and A. Goobar. *Cosmology and particle astrophysics.* 2 1999.

[18] N. Aghanim et al. Planck 2018 results. VI. Cosmological parameters. *Astron. Astrophys.*, 641:A6, 2020.

[19] Alan H. Guth. The Inflationary Universe: A Possible Solution to the Horizon and Flatness Problems. *Adv. Ser. Astrophys. Cosmol.*, 3:139–148, 1987.

[20] Meghnad Saha. Ionization in the solar chromosphere. *The London, Edinburgh, and Dublin Philosophical Magazine and Journal of Science*, 40(238):472–488, 1920.

[21] Bruce T. Cleveland, Timothy Daily, Jr. Raymond Davis, James R. Distel, Kenneth Lande, C. K. Lee, Paul S. Wildenhain, and Jack Ullman. Measurement of the solar electron neutrino flux with the homestake chlorine detector. *The Astrophysical Journal*, 496(1):505–526, mar 1998.

[22] John N. Bahcall. Standard solar models. *Nucl. Phys. B Proc. Suppl.*, 77:64–72, 1999.

[23] Palash B. Pal. Particle physics confronts the solar neutrino problem. *Int. J. Mod. Phys. A*, 7:5387–5460, 1992.

[24] B. Pontecorvo. Mesonium and anti-mesonium. *Sov. Phys. JETP*, 6:429, 1957.

[25] V. N. Gribov and B. Pontecorvo. Neutrino astronomy and lepton charge. *Phys. Lett. B*, 28:493, 1969.

[26] Y. Fukuda et al. Evidence for oscillation of atmospheric neutrinos. *Phys. Rev. Lett.*, 81:1562–1567, 1998.

[27] Q. R. Ahmad et al. Direct evidence for neutrino flavor transformation from neutral current interactions in the Sudbury Neutrino Observatory. *Phys. Rev. Lett.*, 89:011301, 2002.

[28] M. Aker et al. Improved Upper Limit on the Neutrino Mass from a Direct Kinematic Method by KATRIN. *Phys. Rev. Lett.*, 123(22):221802, 2019.

[29] Steven Weinberg. The Cosmological Constant Problem. *Rev. Mod. Phys.*, 61:1–23, 1989.

[30] Vera C. Rubin, W. Kent Ford, Jr., and Norbert Thonnard. Extended rotation curves of high-luminosity spiral galaxies. IV. Systematic dynamical properties, Sa through Sc. *Astrophys. J. Lett.*, 225:L107–L111, 1978.

[31] Emily E. Richards et al. Baryonic distributions in the dark matter halo of NGC 5005. *Mon. Not. Roy. Astron. Soc.*, 449(4):3981–3996, 2015.

[32] Mordehai Milgrom. Dynamics with a non-standard inertia-acceleration relation: an alternative to dark matter. *Annals Phys.*, 229:384–415, 1994.

[33] Albert Einstein. Lens-Like Action of a Star by the Deviation of Light in the Gravitational Field. *Science*, 84:506–507, 1936.

[34] Douglas Clowe, Anthony Gonzalez, and Maxim Markevitch. Weak lensing mass reconstruction of the interacting cluster 1E0657-558: Direct evidence for the existence of dark matter. *Astrophys. J.*, 604:596–603, 2004.

[35] Douglas Clowe, Marusa Bradac, Anthony H. Gonzalez, Maxim Markevitch, Scott W. Randall, Christine Jones, and Dennis Zaritsky. A direct empirical proof of the existence of dark matter. *Astrophys. J. Lett.*, 648:L109–L113, 2006.

[36] Brian Fields and Subir Sarkar. Big-Bang nucleosynthesis (2006 Particle Data Group mini-review). 1 2006. arXiv:astro-ph/0601514.

[37] A. Ringwald. Axions and Axion-Like Particles. In *49th Rencontres de Moriond on Electroweak Interactions and Unified Theories*, 7 2014.

[38] Gudrun Hiller and Frank Kruger. More model-independent analysis of $b \to s$ processes. *Phys. Rev. D*, 69:074020, 2004.

[39] Marzia Bordone, Gino Isidori, and Andrea Pattori. On the Standard Model predictions for R_K and R_{K^*}. *Eur. Phys. J. C*, 76(8):440, 2016.

[40] Roel Aaij et al. Search for lepton-universality violation in $B^+ \to K^+\ell^+\ell^-$ decays. *Phys. Rev. Lett.*, 122(19):191801, 2019.

[41] Roel Aaij et al. Test of lepton universality in beauty-quark decays. 3 2021. arXiv:hep-ex/2103.11769.

[42] Gudrun Hiller, Dennis Loose, and Kay Schönwald. Leptoquark Flavor Patterns \& B Decay Anomalies. *JHEP*, 12:027, 2016.

[43] Svjetlana Fajfer and Nejc Košnik. Vector leptoquark resolution of R_K and $R_{D^{(*)}}$ puzzles. *Phys. Lett. B*, 755:270–274, 2016.

[44] Claudia Cornella, Javier Fuentes-Martin, and Gino Isidori. Revisiting the vector leptoquark explanation of the B-physics anomalies. *JHEP*, 07:168, 2019.

[45] Ligong Bian, Soo-Min Choi, Yoo-Jin Kang, and Hyun Min Lee. A minimal flavored $U(1)'$ for B-meson anomalies. *Phys. Rev. D*, 96(7):075038, 2017.

[46] Wolfgang Altmannshofer, Stefania Gori, Maxim Pospelov, and Itay Yavin. Quark flavor transitions in $L_\mu - L_\tau$ models. *Phys. Rev. D*, 89:095033, 2014.

[47] Andreas Crivellin, Giancarlo D'Ambrosio, and Julian Heeck. Explaining $h \to \mu^\pm\tau^\mp$, $B \to K^*\mu^+\mu^-$ and $B \to K\mu^+\mu^-/B \to Ke^+e^-$ in a two-Higgs-doublet model with gauged $L_\mu - L_\tau$. *Phys. Rev. Lett.*, 114:151801, 2015.

[48] Pere Arnan, Lars Hofer, Federico Mescia, and Andreas Crivellin. Loop effects of heavy new scalars and fermions in $b \to s\mu^+\mu^-$. *JHEP*, 04:043, 2017.

[49] G. W. Bennett et al. Final Report of the Muon E821 Anomalous Magnetic Moment Measurement at BNL. *Phys. Rev. D*, 73:072003, 2006.

[50] B. Abi et al. Measurement of the Positive Muon Anomalous Magnetic Moment to 0.46 ppm. *Phys. Rev. Lett.*, 126(14):141801, 2021.

[51] M. Knecht. The Anomalous magnetic moment of the muon: A Theoretical introduction. *Lect. Notes Phys.*, 629:37–84, 2004.

[52] Prateek Agrawal. (g-2) in qed and beyond. lecture at fermilab, 'the allure of ultrasensitive experiments' series, september 17th, 2014. `https://indico.fnal.gov/event/7309/contributions/101335/attachments/66130/79359/notes-3.pdf`. Accessed: 01.06.2021.

[53] Julian S. Schwinger. On Quantum electrodynamics and the magnetic moment of the electron. *Phys. Rev.*, 73:416–417, 1948.

[54] Fred Jegerlehner and Andreas Nyffeler. The Muon g-2. *Phys. Rept.*, 477:1–110, 2009.

[55] Joshua Ellis. TikZ-Feynman: Feynman diagrams with TikZ. *Comput. Phys. Commun.*, 210:103–123, 2017.

[56] B. Abi et al. Measurement of the Positive Muon Anomalous Magnetic Moment to 0.46 ppm. *Phys. Rev. Lett.*, 126(14):141801, 2021.

[57] Alessandro Broggio, Eung Jin Chun, Massimo Passera, Ketan M. Patel, and Sudhir K. Vempati. Limiting two-Higgs-doublet models. *JHEP*, 11:058, 2014.

[58] Debrupa Chakraverty, Debajyoti Choudhury, and Anindya Datta. A Nonsupersymmetric resolution of the anomalous muon magnetic moment. *Phys. Lett. B*, 506:103–108, 2001.

[59] Carla Biggio and Marzia Bordone. Minimal muon anomalous magnetic moment. *JHEP*, 02:099, 2015.

[60] Gi-Chol Cho, Kaoru Hagiwara, Yu Matsumoto, and Daisuke Nomura. The MSSM confronts the precision electroweak data and the muon g-2. *JHEP*, 11:068, 2011.

[61] Motoi Endo, Koichi Hamaguchi, Sho Iwamoto, and Takahiro Yoshinaga. Muon g-2 vs LHC in Supersymmetric Models. *JHEP*, 01:123, 2014.

[62] Kamila Kowalska, Leszek Roszkowski, Enrico Maria Sessolo, and Andrew J. Williams. GUT-inspired SUSY and the muon g − 2 anomaly: prospects for LHC 14 TeV. *JHEP*, 06:020, 2015.

[63] Peter Athron, Csaba Balázs, Douglas Hj Jacob, Wojciech Kotlarski, Dominik Stöckinger, and Hyejung Stöckinger-Kim. New physics explanations of a_μ in light of the FNAL muon $g-2$ measurement. 4 2021.

[64] H. Georgi and S. L. Glashow. Unity of All Elementary Particle Forces. *Phys. Rev. Lett.*, 32:438–441, 1974.

[65] Jogesh C. Pati and Abdus Salam. Lepton Number as the Fourth Color. *Phys. Rev. D*, 10:275–289, 1974. [Erratum: Phys.Rev.D 11, 703–703 (1975)].

[66] Harald Fritzsch and Peter Minkowski. Unified Interactions of Leptons and Hadrons. *Annals Phys.*, 93:193–266, 1975.

[67] C. Abel et al. Measurement of the permanent electric dipole moment of the neutron. *Phys. Rev. Lett.*, 124(8):081803, 2020.

[68] R. D. Peccei and Helen R. Quinn. CP Conservation in the Presence of Instantons. *Phys. Rev. Lett.*, 38:1440–1443, 1977.

[69] A. D. Sakharov. Violation of CP Invariance, C asymmetry, and baryon asymmetry of the universe. *Pisma Zh. Eksp. Teor. Fiz.*, 5:32–35, 1967.

[70] Ryan J. Cooke, Max Pettini, and Charles C. Steidel. One Percent Determination of the Primordial Deuterium Abundance. *Astrophys. J.*, 855(2):102, 2018.

[71] Michael Dine and Alexander Kusenko. The Origin of the matter - antimatter asymmetry. *Rev. Mod. Phys.*, 76:1, 2003.

[72] W. Buchmuller, R. D. Peccei, and T. Yanagida. Leptogenesis as the origin of matter. *Ann. Rev. Nucl. Part. Sci.*, 55:311–355, 2005.

[73] Evgeny K. Akhmedov. Neutrino physics. In *ICTP Summer School in Particle Physics*, pages 103–164, 6 1999.

[74] Andre de Gouvea. TASI lectures on neutrino physics. In *Theoretical Advanced Study Institute in Elementary Particle Physics: Physics in D* $\geqq 4$, pages 197–258, 11 2004.

[75] M. Fukugita and T. Yanagida. *Physics of neutrinos and applications to astrophysics.* 2003.

[76] M. Tanabashi et al. Review of Particle Physics. *Phys. Rev. D*, 98(3):030001, 2018.

[77] V. Alan Kostelecky and Matthew Mewes. Lorentz and CPT violation in the neutrino sector. *Phys. Rev. D*, 70:031902, 2004.

[78] Evgeny Kh. Akhmedov and Alexei Yu. Smirnov. Paradoxes of neutrino oscillations. *Phys. Atom. Nucl.*, 72:1363–1381, 2009.

[79] C. Giunti. Coherence and wave packets in neutrino oscillations. *Found. Phys. Lett.*, 17:103–124, 2004.

[80] Ivan Esteban, M. C. Gonzalez-Garcia, Michele Maltoni, Thomas Schwetz, and Albert Zhou. The fate of hints: updated global analysis of three-flavor neutrino oscillations. *JHEP*, 09:178, 2020.

[81] NuFit-Collaboration. Fit results: Summer 18. `http://www.nu-fit.org/`, 2020.

[82] J. Linder. Derivation of neutrino matter potentials induced by earth. 4 2005. arXiv:hep-ph/0504264.

[83] S. P. Mikheev and A. Yu. Smirnov. Resonant amplification of neutrino oscillations in matter and solar neutrino spectroscopy. *Nuovo Cim. C*, 9:17–26, 1986.

[84] L. Wolfenstein. Neutrino Oscillations in Matter. *Phys. Rev. D*, 17:2369–2374, 1978.

[85] X. Qian and P. Vogel. Neutrino Mass Hierarchy. *Prog. Part. Nucl. Phys.*, 83:1–30, 2015.

[86] R. B. Patterson. Prospects for Measurement of the Neutrino Mass Hierarchy. *Ann. Rev. Nucl. Part. Sci.*, 65:177–192, 2015.

[87] A. M. Dziewonski and D. L. Anderson. Preliminary reference earth model. *Phys. Earth Planet. Interiors*, 25:297–356, 1981.

[88] Joachim Kopp. Phenomenology of Three-Flavour Neutrino Oscillations. Master's thesis, Technische Universität München, 2006. https://www.staff.uni-mainz.de/jkopp/pdf/diploma-thesis.pdf , Acessed on 01.07.2021.

[89] A. Aguilar-Arevalo et al. Evidence for neutrino oscillations from the observation of $\bar{\nu}_e$ appearance in a $\bar{\nu}_\mu$ beam. *Phys. Rev. D*, 64:112007, 2001.

[90] A. A. Aguilar-Arevalo et al. Updated MiniBooNE neutrino oscillation results with increased data and new background studies. *Phys. Rev. D*, 103(5):052002, 2021.

[91] A. A. Aguilar-Arevalo et al. Significant Excess of ElectronLike Events in the MiniBooNE Short-Baseline Neutrino Experiment. *Phys. Rev. Lett.*, 121(22):221801, 2018.

[92] G. Mention, M. Fechner, Th. Lasserre, Th. A. Mueller, D. Lhuillier, M. Cribier, and A. Letourneau. The Reactor Antineutrino Anomaly. *Phys. Rev. D*, 83:073006, 2011.

[93] Carlo Giunti and Marco Laveder. Statistical Significance of the Gallium Anomaly. *Phys. Rev. C*, 83:065504, 2011.

[94] Joel Kostensalo, Jouni Suhonen, Carlo Giunti, and Praveen C. Srivastava. The gallium anomaly revisited. *Phys. Lett. B*, 795:542–547, 2019.

[95] K. N. Abazajian et al. Light Sterile Neutrinos: A White Paper. 4 2012.

[96] Janet M. Conrad, William C. Louis, and Michael H. Shaevitz. The LSND and MiniBooNE Oscillation Searches at High Δm^2. *Ann. Rev. Nucl. Part. Sci.*, 63:45–67, 2013.

[97] L. J. Wen J. Cao and Y. F. Wang. Reactor Neutrino Experiments: Present and Future. *Ann. Rev. Nucl. Part. Sci.*, 67:183–211, 2017.

[98] Carlo Giunti and Chung W. Kim. *Fundamentals of Neutrino Physics and Astrophysics.* 2007. ISBN: 978-0-19-850871-7.

[99] Mona Dentler, Álvaro Hernández-Cabezudo, Joachim Kopp, Pedro A. N. Machado, Michele Maltoni, Ivan Martinez-Soler, and Thomas Schwetz. Updated Global Analysis of Neutrino Oscillations in the Presence of eV-Scale Sterile Neutrinos. *JHEP*, 08:010, 2018.

[100] S. Schael et al. Precision electroweak measurements on the Z resonance. *Phys. Rept.*, 427:257–454, 2006.

[101] O. L. G. Peres and A. Yu. Smirnov. (3+1) spectrum of neutrino masses: A Chance for LSND? *Nucl. Phys. B*, 599:3, 2001.

[102] C. Giunti and E. M. Zavanin. Appearance–disappearance relation in $3+N_s$ short-baseline neutrino oscillations. *Mod. Phys. Lett. A*, 31(01):1650003, 2015.

[103] S. Gariazzo, C. Giunti, M. Laveder, and Y. F. Li. Updated Global 3+1 Analysis of Short-BaseLine Neutrino Oscillations. *JHEP*, 06:135, 2017.

[104] Yi Cai, Juan Herrero-García, Michael A. Schmidt, Avelino Vicente, and Raymond R. Volkas. From the trees to the forest: a review of radiative neutrino mass models. *Front. in Phys.*, 5:63, 2017.

[105] André de Gouvêa. Neutrino mass models. *Annual Review of Nuclear and Particle Science*, 66(1):197–217, 2016.

[106] S. F. King. Neutrino mass models. *Rept. Prog. Phys.*, 67:107–158, 2004.

[107] Gerard 't Hooft. Naturalness, chiral symmetry, and spontaneous chiral symmetry breaking. *NATO Sci. Ser. B*, 59:135–157, 1980.

[108] R. Primulando, J. Julio, and P. Uttayarat. Scalar phenomenology in type-II seesaw model. *JHEP*, 08:024, 2019.

[109] Stefan Antusch, Oliver Fischer, A. Hammad, and Christiane Scherb. Low scale type II seesaw: Present constraints and prospects for displaced vertex searches. *JHEP*, 02:157, 2019.

[110] Roberto Franceschini, Thomas Hambye, and Alessandro Strumia. Type-III see-saw at LHC. *Phys. Rev. D*, 78:033002, 2008.

[111] Arindam Das and Sanjoy Mandal. Bounds on the triplet fermions in type-III seesaw and implications for collider searches. *Nucl. Phys. B*, 966:115374, 2021.

[112] Deepanjali Goswami and P. Poulose. Direct searches of Type III seesaw triplet fermions at high energy e^+e^- collider. *Eur. Phys. J. C*, 78(1):42, 2018.

[113] Georges Aad et al. Search for type-III seesaw heavy leptons in dilepton final states in pp collisions at $\sqrt{s} = 13$ TeV with the ATLAS detector. *Eur. Phys. J. C*, 81(3):218, 2021.

[114] Ernest Ma. Verifiable radiative seesaw mechanism of neutrino mass and dark matter. *Phys. Rev. D*, 73:077301, 2006.

[115] A. Zee. A Theory of Lepton Number Violation, Neutrino Majorana Mass, and Oscillation. *Phys. Lett. B*, 93:389, 1980. [Erratum: Phys.Lett.B 95, 461 (1980)].

[116] Lincoln Wolfenstein. A Theoretical Pattern for Neutrino Oscillations. *Nucl. Phys. B*, 175:93–96, 1980.

[117] K. S. Babu and C. Macesanu. Two loop neutrino mass generation and its experimental consequences. *Phys. Rev. D*, 67:073010, 2003.

[118] A. Zee. Quantum Numbers of Majorana Neutrino Masses. *Nucl. Phys. B*, 264:99–110, 1986.

[119] Lawrence M. Krauss, Salah Nasri, and Mark Trodden. A Model for neutrino masses and dark matter. *Phys. Rev. D*, 67:085002, 2003.

[120] Paolo Gondolo and Graciela Gelmini. Cosmic abundances of stable particles: Improved analysis. *Nucl. Phys. B*, 360:145–179, 1991.

[121] G. F. Giudice, A. Notari, M. Raidal, A. Riotto, and A. Strumia. Towards a complete theory of thermal leptogenesis in the SM and MSSM. *Nucl. Phys. B*, 685:89–149, 2004.

[122] Mariangela Lisanti. Lectures on Dark Matter Physics. In *Theoretical Advanced Study Institute in Elementary Particle Physics: New Frontiers in Fields and Strings*, 3 2016.

[123] David G. Cerdeño. Dark matter 101: From production to detection. lecture at ippp durham. `https://www.ippp.dur.ac.uk/~dcerdeno/Dark_Matter_Lab_files/DM.pdf`. Accessed: 11.04.2021.

[124] Robert J. Scherrer and Michael S. Turner. On the Relic, Cosmic Abundance of Stable Weakly Interacting Massive Particles. *Phys. Rev. D*, 33:1585, 1986. [Erratum: Phys.Rev.D 34, 3263 (1986)].

[125] G. Belanger, F. Boudjema, A. Pukhov, and A. Semenov. micrOMEGAs_3: A program for calculating dark matter observables. *Comput. Phys. Commun.*, 185:960–985, 2014.

[126] Geneviève Bélanger, Fawzi Boudjema, Andreas Goudelis, Alexander Pukhov, and Bryan Zaldivar. micrOMEGAs5.0 : Freeze-in. *Comput. Phys. Commun.*, 231:173–186, 2018.

[127] Federico Ambrogi, Chiara Arina, Mihailo Backovic, Jan Heisig, Fabio Maltoni, Luca Mantani, Olivier Mattelaer, and Gopolang Mohlabeng. MadDM v.3.0: a Comprehensive Tool for Dark Matter Studies. *Phys. Dark Univ.*, 24:100249, 2019.

[128] Kim Griest and David Seckel. Three exceptions in the calculation of relic abundances. *Phys. Rev. D*, 43:3191–3203, 1991.

[129] Joakim Edsjo and Paolo Gondolo. Neutralino relic density including coannihilations. *Phys. Rev. D*, 56:1879–1894, 1997.

[130] E. Aprile et al. Dark Matter Search Results from a One Ton-Year Exposure of XENON1T. *Phys. Rev. Lett.*, 121(11):111302, 2018.

[131] E. Aprile et al. Constraining the spin-dependent WIMP-nucleon cross sections with XENON1T. *Phys. Rev. Lett.*, 122(14):141301, 2019.

[132] D. S. Akerib et al. An Effective Field Theory Analysis of the First LUX Dark Matter Search. 3 2020.

[133] C. Amole et al. Dark Matter Search Results from the Complete Exposure of the PICO-60 C_3F_8 Bubble Chamber. *Phys. Rev. D*, 100(2):022001, 2019.

[134] F. Petricca et al. First results on low-mass dark matter from the CRESST-III experiment. *J. Phys. Conf. Ser.*, 1342(1):012076, 2020.

[135] I. Alkhatib et al. Light Dark Matter Search with a High-Resolution Athermal Phonon Detector Operated Above Ground. 7 2020. arXiv:hep-ex/2007.14289.

[136] M. G. Aartsen et al. Search for annihilating dark matter in the Sun with 3 years of IceCube data. *Eur. Phys. J. C*, 77(3):146, 2017. [Erratum: Eur.Phys.J.C 79, 214 (2019)].

[137] Marc Schumann. Direct Detection of WIMP Dark Matter: Concepts and Status. *J. Phys. G*, 46(10):103003, 2019.

[138] Mariangela Lisanti, Louis E. Strigari, Jay G. Wacker, and Risa H. Wechsler. The Dark Matter at the End of the Galaxy. *Phys. Rev. D*, 83:023519, 2011.

[139] Julio F. Navarro, Carlos S. Frenk, and Simon D. M. White. The Structure of cold dark matter halos. *Astrophys. J.*, 462:563–575, 1996.

[140] Martin C. Smith et al. The RAVE Survey: Constraining the Local Galactic Escape Speed. *Mon. Not. Roy. Astron. Soc.*, 379:755–772, 2007.

[141] Felix Karl David Kahlhoefer. *Complementarity of Searches for Dark Matter*. PhD thesis, Oxford U., 2014.

[142] David G. Cerdeño and Anne M. Green. Direct detection of WIMPs. 2 2010.

[143] Asher Berlin, Dan Hooper, and Samuel D. McDermott. Simplified Dark Matter Models for the Galactic Center Gamma-Ray Excess. *Phys. Rev. D*, 89(11):115022, 2014.

[144] Marco Cirelli, Eugenio Del Nobile, and Paolo Panci. Tools for model-independent bounds in direct dark matter searches. *JCAP*, 10:019, 2013.

[145] Felix Karl David Kahlhöfer. Sensitivität von Flüssig-Xenon-Detektoren für Leichte Dunkle Materie. Master's thesis, Ruprecht-Karls-Universität Heidelberg, 2010. https://web.physik.rwth-aachen.de/user/kahlhoefer/master_felixkahlhoefer.pdf Acessed on 15.04.2021.

[146] Hai-Yang Cheng and Cheng-Wei Chiang. Revisiting Scalar and Pseudoscalar Couplings with Nucleons. *JHEP*, 07:009, 2012.

[147] Parikshit Junnarkar and Andre Walker-Loud. Scalar strange content of the nucleon from lattice QCD. *Phys. Rev. D*, 87:114510, 2013.

[148] Jose F. Nieves and Palash B. Pal. Generalized Fierz identities. *Am. J. Phys.*, 72:1100–1108, 2004.

[149] Prateek Agrawal, Zackaria Chacko, Can Kilic, and Rashmish K. Mishra. A Classification of Dark Matter Candidates with Primarily Spin-Dependent Interactions with Matter. 3 2010. arXiv:hep-ph/1003.1912.

[150] A. Albert et al. Searching for Dark Matter Annihilation in Recently Discovered Milky Way Satellites with Fermi-LAT. *Astrophys. J.*, 834(2):110, 2017.

[151] A. Abramowski et al. Search for a Dark Matter annihilation signal from the Galactic Center halo with H.E.S.S. *Phys. Rev. Lett.*, 106:161301, 2011.

[152] Tracy R. Slatyer. Indirect Detection of Dark Matter. In *Theoretical Advanced Study Institute in Elementary Particle Physics: Anticipating the Next Discoveries in Particle Physics*, 10 2017.

[153] M. Ackermann et al. Searching for Dark Matter Annihilation from Milky Way Dwarf Spheroidal Galaxies with Six Years of Fermi Large Area Telescope Data. *Phys. Rev. Lett.*, 115(23):231301, 2015.

[154] M. Ackermann et al. Updated search for spectral lines from Galactic dark matter interactions with pass 8 data from the Fermi Large Area Telescope. *Phys. Rev. D*, 91(12):122002, 2015.

[155] Shang Li, Zi-Qing Xia, Yun-Feng Liang, Kai-Kai Duan, Zhao-Qiang Shen, Xiang Li, Lei Feng, Qiang Yuan, Yi-Zhong Fan, and Jin Chang. Search for line-like signals in the all-sky Fermi-LAT data. *Phys. Rev. D*, 99(12):123519, 2019.

[156] Stefan Vogl. *Majorana Dark Matter: The Power of Direct, Indirect and Collider Searches.* PhD thesis, Technische Universität München, 6 2014.

[157] Paolo Ciafaloni, Marco Cirelli, Denis Comelli, Andrea De Simone, Antonio Riotto, and Alfredo Urbano. On the Importance of Electroweak Corrections for Majorana Dark Matter Indirect Detection. *JCAP*, 06:018, 2011.

[158] Torsten Bringmann, Xiaoyuan Huang, Alejandro Ibarra, Stefan Vogl, and Christoph Weniger. Fermi LAT Search for Internal Bremsstrahlung Signatures from Dark Matter Annihilation. *JCAP*, 07:054, 2012.

[159] Mathias Garny, Alejandro Ibarra, and Stefan Vogl. Signatures of Majorana dark matter with t-channel mediators. *Int. J. Mod. Phys. D*, 24(07):1530019, 2015.

[160] Lars Bergstrom. Radiative Processes in Dark Matter Photino Annihilation. *Phys. Lett. B*, 225:372–380, 1989.

[161] Lars Bergstrom, Torsten Bringmann, Martin Eriksson, and Michael Gustafsson. Gamma rays from heavy neutralino dark matter. *Phys. Rev. Lett.*, 95:241301, 2005.

[162] Torsten Bringmann, Lars Bergstrom, and Joakim Edsjo. New Gamma-Ray Contributions to Supersymmetric Dark Matter Annihilation. *JHEP*, 01:049, 2008.

[163] Lars Bergstrom, Torsten Bringmann, and Joakim Edsjo. New Positron Spectral Features from Supersymmetric Dark Matter - a Way to Explain the PAMELA Data? *Phys. Rev. D*, 78:103520, 2008.

[164] Mathias Garny, Alejandro Ibarra, Miguel Pato, and Stefan Vogl. Internal bremsstrahlung signatures in light of direct dark matter searches. *JCAP*, 12:046, 2013.

[165] Philipp Sicking. *Searches for new physics with neutrino oscillations in the high precision era*. PhD thesis, Technische Universität Dortmund, 2019.

[166] Heinrich Pas, Sandip Pakvasa, and Thomas J. Weiler. Sterile-active neutrino oscillations and shortcuts in the extra dimension. *Phys. Rev. D*, 72:095017, 2005.

[167] D. Marfatia, H. Pas, S. Pakvasa, and T. J. Weiler. A model of superluminal neutrinos. *Phys. Lett. B*, 707:553–557, 2012.

[168] Sebastian Hollenberg and Heinrich Pas. Resonant active-sterile neutrino mixing in the presence of matter potentials and altered dispersion relations. 4 2009.

[169] Sebastian Hollenberg, Octavian Micu, Heinrich Pas, and Thomas J. Weiler. Baseline-dependent neutrino oscillations with extra-dimensional shortcuts. *Phys. Rev. D*, 80:093005, 2009.

[170] Elke Aeikens, Heinrich Päs, Sandip Pakvasa, and Philipp Sicking. Flavor ratios of extragalactic neutrinos and neutrino shortcuts in extra dimensions. *JCAP*, 10:005, 2015.

[171] Elke Aeikens, Heinrich Päs, Sandip Pakvasa, and Thomas J. Weiler. Suppression of cosmological sterile neutrino production by altered dispersion relations. *Phys. Rev. D*, 94(11):113010, 2016.

[172] Daniel J. H. Chung and Katherine Freese. Cosmological challenges in theories with extra dimensions and remarks on the horizon problem. *Phys. Rev. D*, 61:023511, 2000.

[173] Daniel J. H. Chung and Katherine Freese. Can geodesics in extra dimensions solve the cosmological horizon problem? *Phys. Rev. D*, 62:063513, 2000.

[174] Csaba Csaki, Joshua Erlich, and Christophe Grojean. Gravitational Lorentz violations and adjustment of the cosmological constant in asymmetrically warped space-times. *Nucl. Phys. B*, 604:312–342, 2001.

[175] Dominik Döring and Heinrich Päs. Sterile Neutrino Shortcuts in Asymmetrically Warped Extra Dimensions. *Eur. Phys. J. C*, 79(7):604, 2019.

[176] Yoshio Koide. Neutrino masses and mixings in a universal seesaw mass matrix model. *Phys. Rev. D*, 57:5836–5843, 1998.

[177] Yoshio Koide and Hideo Fusaoka. Universal seesaw mass matrix model with three light pseudoDirac neutrinos. *Phys. Rev. D*, 59:053004, 1999.

[178] E. J. Chun, C. W. Kim, and U. W. Lee. Three neutrino Delta m**2 scales and singular seesaw mechanism. *Phys. Rev. D*, 58:093003, 1998.

[179] G. C. Branco, J. T. Penedo, Pedro M. F. Pereira, M. N. Rebelo, and J. I. Silva-Marcos. Type-I Seesaw with eV-Scale Neutrinos. *JHEP*, 07:164, 2020.

[180] Shinsuke Kawai and Nobuchika Okada. eV-scale sterile neutrinos from an extra dimension. *Phys. Rev. D*, 100(11):115043, 2019.

[181] Gabriela A Barenboim, Pablo Martínez-Miravé, Christoph Andreas Ternes, and Maria Amparo Tórtola. Sterile neutrinos with altered dispersion relations revisited. *JHEP*, 03:070, 2020.

[182] M. G. Aartsen et al. Searches for Sterile Neutrinos with the IceCube Detector. *Phys. Rev. Lett.*, 117(7):071801, 2016.

[183] K. Abe et al. Limits on sterile neutrino mixing using atmospheric neutrinos in Super-Kamiokande. *Phys. Rev. D*, 91:052019, 2015.

[184] K. Abe et al. Atmospheric neutrino oscillation analysis with external constraints in Super-Kamiokande I-IV. *Phys. Rev. D*, 97(7):072001, 2018.

[185] M. G. Aartsen et al. eV-Scale Sterile Neutrino Search Using Eight Years of Atmospheric Muon Neutrino Data from the IceCube Neutrino Observatory. *Phys. Rev. Lett.*, 125(14):141801, 2020.

[186] Dukjae Jang, Motohiko Kusakabe, and Myung-Ki Cheoun. Effects of sterile neutrinos and an extra dimension on big bang nucleosynthesis. *Phys. Rev. D*, 97(4):043005, 2018.

[187] Robert Foot and R. R. Volkas. Reconciling sterile neutrinos with big bang nucleosynthesis. *Phys. Rev. Lett.*, 75:4350, 1995.

[188] Mathias Becker. *Dark Matter Models: The Neutrino and Flavor Portals.* PhD thesis, Technische Universität Dortmund, 2020.

[189] Marcel Algueró, Bernat Capdevila, Andreas Crivellin, Sébastien Descotes-Genon, Pere Masjuan, Joaquim Matias, Martín Novoa Brunet, and Javier Virto. Emerging patterns of New Physics with and without Lepton Flavour Universal contributions. *Eur. Phys. J. C*, 79(8):714, 2019. [Addendum: Eur.Phys.J.C 80, 511 (2020)].

[190] Marcel Algueró, Bernat Capdevila, Sébastien Descotes-Genon, Joaquim Matias, and Martín Novoa-Brunet. $\boldsymbol{b \to s\ell\ell}$ global fits after Moriond 2021 results. In *55th Rencontres de Moriond on QCD and High Energy Interactions*, 4 2021.

[191] A. Bazavov et al. $B^0_{(s)}$-mixing matrix elements from lattice QCD for the Standard Model and beyond. *Phys. Rev. D*, 93(11):113016, 2016.

[192] Giorgio Arcadi, Lorenzo Calibbi, Marco Fedele, and Federico Mescia. Muon $g-2$ and B-anomalies from Dark Matter. 4 2021. arXiv:hep-ph/2104.03228.

[193] Marco Cirelli, Nicolao Fornengo, and Alessandro Strumia. Minimal dark matter. *Nucl. Phys. B*, 753:178–194, 2006.

[194] Venus Keus, Stephen F. King, and Stefano Moretti. Phenomenology of the inert (2+1) and (4+2) Higgs doublet models. *Phys. Rev. D*, 90(7):075015, 2014.

[195] G. C. Branco, P. M. Ferreira, L. Lavoura, M. N. Rebelo, Marc Sher, and Joao P. Silva. Theory and phenomenology of two-Higgs-doublet models. *Phys. Rept.*, 516:1–102, 2012.

[196] Manfred Lindner, Moritz Platscher, Carlos E. Yaguna, and Alexander Merle. Fermionic WIMPs and vacuum stability in the scotogenic model. *Phys. Rev. D*, 94(11):115027, 2016.

[197] Alexander Belyaev, Neil D. Christensen, and Alexander Pukhov. CalcHEP 3.4 for collider physics within and beyond the Standard Model. *Comput. Phys. Commun.*, 184:1729–1769, 2013.

[198] Adam Alloul, Neil D. Christensen, Céline Degrande, Claude Duhr, and Benjamin Fuks. FeynRules 2.0 - A complete toolbox for tree-level phenomenology. *Comput. Phys. Commun.*, 185:2250–2300, 2014.

[199] Neil D. Christensen, Priscila de Aquino, Celine Degrande, Claude Duhr, Benjamin Fuks, Michel Herquet, Fabio Maltoni, and Steffen Schumann. A Comprehensive approach to new physics simulations. *Eur. Phys. J. C*, 71:1541, 2011.

[200] Thomas Hahn. Generating Feynman diagrams and amplitudes with FeynArts 3. *Comput. Phys. Commun.*, 140:418–431, 2001.

[201] T. Hahn and M. Perez-Victoria. Automatized one loop calculations in four-dimensions and D-dimensions. *Comput. Phys. Commun.*, 118:153–165, 1999.

[202] Jorge C. Romão. Modern techniques for one-loop calculations, personal notes. https://porthos.tecnico.ulisboa.pt/Public/textos/one-loop.pdf.

[203] Mihailo Backović, Antony Martini, Olivier Mattelaer, Kyoungchul Kong, and Gopolang Mohlabeng. Direct Detection of Dark Matter with MadDM v.2.0. *Phys. Dark Univ.*, 9-10:37–50, 5 2015.

[204] Kirtimaan A. Mohan, Dipan Sengupta, Tim M. P. Tait, Bin Yan, and C. P. Yuan. Direct detection and LHC constraints on a t-channel simplified model of Majorana dark matter at one loop. *JHEP*, 05:115, 2019.

[205] Morad Aaboud et al. Search for long-lived, massive particles in events with displaced vertices and missing transverse momentum in $\sqrt{s} = 13$ TeV pp collisions with the ATLAS detector. *Phys. Rev. D*, 97(5):052012, 2018.

[206] G. Bélanger et al. LHC-friendly minimal freeze-in models. *JHEP*, 02:186, 2019.

[207] Search for top squarks in final states with one isolated lepton, jets, and missing transverse momentum in $\sqrt{s} = 13$ TeV pp collisions with the ATLAS detector. 8 2016.

[208] Albert M Sirunyan et al. Search for top squark pair production using dilepton final states in pp collision data collected at $\sqrt{s} = 13\,\text{TeV}$. *Eur. Phys. J. C*, 81(1):3, 2021.

[209] James M. Cline and Jonathan M. Cornell. $R(K^{(*)})$ from dark matter exchange. *Phys. Lett. B*, 782:232–237, 2018.

[210] Davide Racco, Andrea Wulzer, and Fabio Zwirner. Robust collider limits on heavy-mediator Dark Matter. *JHEP*, 05:009, 2015.

[211] Morad Aaboud et al. Search for dark matter and other new phenomena in events with an energetic jet and large missing transverse momentum using the ATLAS detector. *JHEP*, 01:126, 2018.

[212] Julia Harz and Kalliopi Petraki. Radiative bound-state formation in unbroken perturbative non-Abelian theories and implications for dark matter. *JHEP*, 07:096, 2018.

[213] Giorgio Arcadi, Lorenzo Calibbi, Marco Fedele, and Federico Mescia. Systematic approach to B-physics anomalies and t-channel dark matter. 3 2021. arXiv:hep-ph/2103.09835.

List of Figures

List of Tables